Detecting Small Signals: Near-Infrared Studies of Substellar Companions

Thesis by

Camillus Francis Buzard

In Partial Fulfillment of the Requirements for the
Degree of
Doctor of Philosophy

Caltech

CALIFORNIA INSTITUTE OF TECHNOLOGY
Pasadena, California

2022
Defended May 10, 2022

Camillus Francis Buzard
ORCID: 0000-0002-9943-6124

ACKNOWLEDGEMENTS

Science is a collaborative process, and my scientific journey would not have been possible without the many people who've supported me along the way. Thank you first to Professor Geoffrey Blake, who has been a kind and supportive advisor, for always seeing the best in me and believing me to be capable. Thanks also to my committee members, Professors Heather Knutson, Mitchio Okumura, and Ryan Hadt, for encouraging me to think in new ways.

The Barnard Chemistry Department is really responsible for cultivating my interest in physical chemistry, and I thank them for the journey they set me on. Drs. John Magyar, Dina Merrer, and Andrew Crowther, in particular, exposed me to the beauty of chemistry and inspired me to take the next step in my scientific career. Drs. Kelle Cruz, Emily Rice, and Jacqueline Faherty at the American Museum of Natural History turned my interests to astronomy and taught me what it meant to be a member of the greater scientific community.

I am so thankful for the Caltech and Keck employees who supported my scientific and personal life along the way. Thanks to Scott A. Dungan, the GPS Senior Systems Administrator, for always knowing how to fix my code and for coming to the rescue when I accidentally deleted months of work. To Dr. Greg Doppman, at the Keck Observatory, for so patiently teaching me how to drive NIRSPEC, even in the moments when I thought I'd broken the telescope. Thanks especially to Erin-Kate Escobar and Monique Thomas from the Caltech Center for Inclusion and Diversity for offering friendship and a much-needed reprieve from science. Thanks to the GPS administrative staff—Irma Black, Ulrika Terrones, Margaret Carlos, Ruth Loisel, Stephanie Petty, and Loreta Young—for making the office a place I wanted to be (and missed during the pandemic!) with Thanksgiving lunches, post-grant submission cookies, and friendly conversations in the hallways. Thanks to Cruz Martinez for his tireless work cleaning the office and for being the only one to venture back to greet me at my hidden desk many mornings.

To the students I've worked with along the way, thank you for always reconnecting me to the joy of math and science, even when it was hard to find in my research. Thank you to Liz Jackman from Caltech Rise and to Bernadette Ruby Lopez from the Los Angeles LGBT Center Education Department for coordinating such incredible programs for these students.

Many thanks to the Blake group members who have been with me for all of the highs and lows of the last five and a half years. Thanks to the senior generation of grad students when I arrived—Ian Finneran, Danielle Piskorz, Brandon Carroll, Masha Kleshcheva, and Dana Anderson—for welcoming me to the group and getting me started on both the servers and the science. Thanks especially to Danielle who spent her last year sending me code, sitting with me as I tried to get it running, and answering every little question I could come up with and to Masha who sat with me through the emotional side of grad school. To those Blake group members with whom I spent the most time—Griffin Mead, Olivia Wilkins, Alex Froebel, Kyle Virgil, Haw-Wei Lin, Sadie Dutton, and Maria Camarca—thank you. Even though I was the group's lone planetary astronomer, you were there with advice for each and every science and coding challenge I faced. Thanks too to the Planetary Science grad students—Nancy Thomas, Nicole Wallack, Shreyas Vissapragada, Aida Behmard—for adopting me as an honorary Planetary Science grad student and letting me take advantage of the full GPS experience. Thank you all, along with Alex and Günther Sauers, for all the holiday parties, movie nights, and coffee breaks that kept me going along the way.

Thank you, Dena Williams, for giving me a home and a family in California. Thank you for all the ways you've challenged and comforted me. Thanks to Kasseiopeia the cat for all the cuddles.

Finally, growing up, I was taught that in a moment like this, it's only appropriate to say, "I owe it all to my mom." My mom, Ina Lipkowitz, has been a constant friend, teacher, and source of support. Thank you, Mom, and Gary, Natt, Noah, and Dylan for putting up with my being three thousand miles away and for always being a joyous crowd to come back to.

ABSTRACT

As the number of known exoplanets, or planets in other solar systems, grows, we have become empowered to ask deeper and more specific questions about the possibilities presented by our universe. A group of giant gaseous planets called "hot Jupiters" spurred us to think in new ways about giant planet formation. The diversity of solar system architectures, exoplanet sizes, atmospheric composition and dynamics expands our perspective on the many possible outcomes resulting from the same primordial ingredients in different amounts and in different environments. To fully answer these questions, we need to look directly into exoplanet atmospheres. Infrared spectra can reveal atmospheres' molecular content and certain physical processes, such as winds and rotation effects. From spectoscopic measurements, we can test theories of planet formation, evolution, and habitability. Unfortunately, most current direct exoplanet characterization techniques are limited to certain populations, whether planets with specific orbital geometries or planets either very far from or very near their host stars. These well-established methods miss a key population of exoplanets, specifically those that are non-transiting and with orbital separations between roughly 0.15 and 5 AU. This group contains around 19% of the exoplanets known today (a percentage which will only increase in the coming extreme precision radial velocity era) and will almost certainly include the nearest potentially habitable world. This dissertation presents two projects. In the first, we work to further a direct exoplanet characterization approach that will be sensitive to these elusive planets by identifying and reducing an insidious source of structured noise—in the process, making it easier to directly detect planetary emission. With advancements promised by the simulation framework presented in this dissertation, our multi-epoch direct detection approach, in combination with planet-to-star contrast gains enabled by high-contrast imaging technology, will be uniquely capable of characterizing ever smaller, cooler, and more complex planetary atmospheres. In the second project, we apply the direct detection method to a particularly interesting substellar object, a brown dwarf in a very close ($<$ 2 hour) orbit around a white dwarf, in order to understand how gaseous atmospheres behave in exotic irradiation environments. Together, these projects demonstrate the capacity of multi-epoch spectroscopic observations to serve as a window into gaseous atmospheres and a pathway to potentially habitable worlds.

PUBLISHED CONTENT AND CONTRIBUTIONS

Buzard, C., Finnerty, L., Piskorz, D., et al. (2020). Simulating the Multi-Epoch Direct Detection Technique to Isolate the Thermal Emission of the Non-Transiting Hot Jupiter HD187123b. *The Astronomical Journal*, 160(1). DOI: 10.3847/1538-3881/ab8f9c
C.B., L.F., D.P., N.W., and O.W. participated in the data collection. C.B. led the data reduction and analysis, generated the simulation framework, and wrote the manuscript. S.P. and B.B. provided planetary atmospheric models.

Buzard, C., Pelletier, S., Piskorz, D., Benneke, B., & Blake, G. A. (2021a). Primary Velocity and Orbital Phase Effects on Planetary Detectability from Small Epoch Number Data Sets. *The Astronomical Journal*, 162(26). DOI: 10.3847/1538-3881/abf7b9
C.B. generated the simulation framework, performed the analysis, and wrote the manuscript. S.P. provided planetary spectral models. C.B. and D.P. collected and reduced the NIRSPEC data.

Buzard, C., Piskorz, D., Lockwood, A. C., et al. (2021b). Reinvestigation of the Multi-Epoch Direct Detections of HD 88133 b and Upsilon Andromedae b. *The Astronomical Journal*, 162(269), DOI: 10.3847/1538-3881/ac2a2c
C.B. reanalyzed data originally presented by D.P., ran the simulations, and wrote the manuscript. T.S.B. and B.B. provided the planetary spectral models and J.S.C. provided a stellar spectral model.

Buzard, C., Casewell, S., Lothringer, J., et al. (2022). Near-Infrared Spectra of the Inflated Post-Common Envelope Brown Dwarf NLTT 5306 B. *The Astronomical Journal*, 163(262), DOI: 10.3847/1538-3881/ac6508
C.B. and G.A.B participated in data collection. C.B. analyzed the data and wrote the manuscript. J.L. provided the irradiated substellar spectral models and S.C. provided crucial feedback on and context for the manuscript.

TABLE OF CONTENTS

LIST OF ILLUSTRATIONS

LIST OF TABLES

Chapter 1

INTRODUCTION

Astronomers and the public alike were shocked to learn in the mid-1990s that our solar system was not all that unique; there were planets both like and very unlike our own orbiting distant stars. While our system has close-in terrestrial planets, followed by more distant gas and ice giants, the newly discovered exoplanets included close-in gas giants, a preponderance of super-Earths in the mass range between our terrestrial planets and ice giants, and more. These discoveries emboldened us to ask new sorts of questions: How and where do planets actually form? With the multitude of newly discovered planets, is there life beyond Earth?

Before these discoveries, we had used the particular cases of our gas giants, Jupiter and Saturn, to understand planet formation. Jupiter and Saturn exist at large orbital separations, far beyond ~ 2.7 AU, where the water snow line would have fallen in our primordial disk (Martin & Livio, 2012). It therefore seemed logical to assume that gas giants in general must form far out in their protoplanetary disks, where there would be enough gas and dust to explain the planets' large masses. The two dominant theories for the formation of these planets, core accretion and disk instability, both require large separations. Core accretion, as described by Rice & Armitage 2003, involves the growth of a solid core followed by rapid accretion of a gas envelope. Disk instability, on the other hand, describes a process in which disk material collapses under its own weight to form a planet (Boss, 1997).

The discovery of the first few planets, hot Jupiters, threw the assumption of giant planet formation at large separations into question. Hot Jupiters, as their name suggests, are approximately Jupiter-mass planets that are hot because of their close separations ($P \approx 3-5$ days) to their host stars. As they were first detected, theorists came up with a range of ideas about how they could form at large separations and subsequently migrate in to their current-day positions; researchers considered mechanisms from planet-disk interactions (e.g., Goldreich & Tremaine, 1980), to dynamical models like planet-planet scattering (e.g., Nagasawa et al., 2008) and Kozai migration (e.g., Malmberg et al., 2007). It was not until much more recently that Batygin et al. 2016 proposed that rather than forming at large separations and migrating in, hot Jupiters may be able to form on their present-day close-in orbits.

In addition to our Solar System-centric assumptions about giant planet formation, with only the set of planets in our system to reference, we assumed that Earth was the only life-hosting planet, it being the only one that could currently sustain liquid water, after all. As exoplanet surveys using instruments from the Transiting Exoplanet Survey Satellite (TESS) to the Habitable Planet Finder (HPF) on the Hobby-Eberly Telescope detect ever more terrestrial planets in their host stars' so-called "habitable zones" (Kasting et al., 1993), the chances we are alone seem to diminish.

Ultimately, exoplanet atmospheres will be the key to answering our questions into planetary formation and habitability. If hot Jupiters form via core accretion, and if the amount of solids accreted into the planetary envelope and atmosphere is negligible, their atmospheric carbon-to-oxygen ratios should reflect where they formed within their protoplanetary disks with respect to snow lines of water, carbon monoxide, and carbon dioxide (Öberg et al., 2011). Planetary atmospheres' bulk carbon-to-oxygen ratios could be accurately measured by spectrally resolved near-infrared CO and H_2O lines, as CO and H_2O are virtually unaffected by non-equilibrium effects at the level probed by near-infrared spectroscopy (below 1 μbar) (Line et al., 2011; Moses et al., 2013). Conversely, if solid accretion into planetary envelopes is not negligible—a possibility considered by Espinoza et al. 2017 and seemingly the case for the Solar System giants (e.g., Owen et al., 1999)—it might in fact be the solid composition that could encode evidence of planets' formation locations (e.g., Öberg & Wordsworth, 2019). Either way, using spectroscopy to detect and measure abundances of various molecular species in exoplanet atmospheres, we can get a sense of where, and even how, giant planets form. Molecular spectroscopy too can investigate giant planets' present-day (thermal) structure and dynamics, including global wind patterns (Snellen et al., 2010) and rotation rates (Brogi et al., 2016; Bryan et al., 2018).

Further, atmospheric composition can indicate a planet's potential for life. Researchers have postulated that the metabolic processes that characterize life would be required to explain the presence of substantial redox disequilibrium, such as would be demonstrated by the simultaneous detection of O_2 and a reduced gas, like CH_4 (Lovelock, 1965). Such chemical disequilibrium in a planet's atmosphere could then be strong evidence for life.

While spectroscopy will presumably be our gateway to understanding the habitability of remote worlds, one challenge in gleaning evidence of life from these distant planets is how faint they are relative to their much brighter host stars. For example, approximating both as blackbody radiators, at 3 μm, an Earth-like planet would be only $\sim 10^{-11}$ times as bright as a Solar type star. An Earth-like planet orbiting even the faintest, M type, star would still be at a planet-to-star contrast of only $\sim 10^{-9}$.

Substantial ongoing work is asking how we can observe these low-contrast planetary signals. High-contrast imaging (HCI) systems combine extreme adaptive optics with coronagraphy to suppress starlight and increase planet-to-star contrasts. Current HCI instruments, like the Gemini Planet Imager (Macintosh et al., 2014) at the Gemini South telescope and the Spectro-Polarimetric High contrast imager for Exoplanets REsearch (SPHERE, Beuzit et al. 2019) at the Very Large Telescope, have already shown sunlight suppression of $\sim 10^4 - 10^6$ at planet-star separations within ~ 1 arcsecond (Hinkley et al., 2021). Suppression will be even further amplified on the next generation of extremely large telescopes.

High-contrast imaging does not, however, need to make up the low planet-to-star contrasts of Earth-like planets orbiting Solar-, or even M-, type stars all on its own. High-dispersion coronagraphy (HDC) was presented as a collaboration between HCI and high-resolution spectroscopy (e.g., Sparks & Ford, 2002; Wang et al., 2017). The idea was that high-resolution ($R \sim 10^4 - 10^5$) spectroscopic techniques could reach down to detect planetary signals a few orders of magnitude below their host stars, and in doing so, could relax the need for starlight suppression by these few orders of magnitude. For HDC to be effective, development and refinement of high-resolution spectroscopic techniques is just as crucial, and must run alongside, the development and refinement of HCI technology.

In this dissertation, we work to develop and further an observational approach which aims to directly detect and characterize planetary atmospheres. We first target bright, hot Jupiters ($\sim 10^{-4}$ times their host stars at 3 μm), which both are compelling in their own right and allow us to refine our method for the eventual application, on data from next generation spectrometers, to potentially habitable, terrestrial exoplanets. In the short term, these studies will teach us about giant planet formation and present-day structure and composition. In the long term, they may be our key to discovering we are not alone.

This dissertation is organized as follows. We describe our high-resolution method in Chapter 2. Next, as detailed in Chapter 3, we use this technique to detect emission from the hot Jupiter, HD 187123b. For the first time, we generate simulations to mirror the data. These simulations allow us to identify and remove noise structure obscuring the planetary signal, and in doing so, substantially increase the planetary detection significance. In Chapter 4, we use this same simulation framework to predict observing strategies that could lead to stronger planetary detections. Chapter 5 demonstrates the importance of understanding sources of noise or interference in exoplanet studies by revisiting two previously reported hot Jupiter detections. Building off this reanalysis, Chapter 6 identifies some areas for further improvement in the technique moving forward. The refinements described in this work, mainly the introduction and application of the simulation framework, will lead the way, in collaboration with the parallel improvements in high-contrast imaging technology, to the confident detections of low-contrast planetary atmospheres.

Finally, Chapter 7 diverges from the low-contrast targets, focusing instead on a different kind of spectroscopic binary, the $<$ 2-hour orbital period white dwarf/brown dwarf binary, NLTT5306. Though in this case not applied to a planetary system, astronomical spectroscopy proves again to be an incredible tool in understanding the historical and current states of substellar bodies. In Chapter 8, we summarize our findings and discuss future steps that will be made possible by upcoming infrared instruments.

References

Batygin, K., Bodenheimer, P. H., & Laughlin, G. P. 2016, *ApJ*, 829, 114, doi: 10.3847/0004-637X/829/2/114

Beuzit, J. L., Vigan, A., Mouillet, D., et al. 2019, *A&A*, 631, A155, doi: 10.1051/0004-6361/201935251

Boss, A. P. 1997, Science, 276, 1836, doi: 10.1126/science.276.5320.1836

Brogi, M., de Kok, R. J., Albrecht, S., et al. 2016, *ApJ*, 817, 106, doi: 10.3847/0004-637X/817/2/106

Bryan, M. L., Benneke, B., Knutson, H. A., Batygin, K., & Bowler, B. P. 2018, Nature Astronomy, 2, 138, doi: 10.1038/s41550-017-0325-8

Espinoza, N., Fortney, J. J., Miguel, Y., Thorngren, D., & Murray-Clay, R. 2017, *ApJL*, 838, L9, doi: 10.3847/2041-8213/aa65ca

Goldreich, P., & Tremaine, S. 1980, *ApJ*, 241, 425, doi: 10.1086/158356

Hinkley, S., Vigan, A., Kasper, M., Quanz, S. P., & Lacour, S. 2021, in ExoFrontiers; Big Questions in Exoplanetary Science, ed. N. Madhusudhan, 5–1

Kasting, J. F., Whitmire, D. P., & Reynolds, R. T. 1993, , 101, 108, doi: 10.1006/icar.1993.1010

Line, M. R., Vasisht, G., Chen, P., Angerhausen, D., & Yung, Y. L. 2011, *ApJ*, 738, 32, doi: 10.1088/0004-637X/738/1/32

Lovelock, J. E. 1965, *Nature*, 207, 568, doi: 10.1038/207568a0

Macintosh, B., Graham, J. R., Ingraham, P., et al. 2014, Proceedings of the National Academy of Science, 111, 12661, doi: 10.1073/pnas.1304215111

Malmberg, D., Davies, M. B., & Chambers, J. E. 2007, *MNRAS*, 377, L1, doi: 10.1111/j.1745-3933.2007.00291.x

Martin, R. G., & Livio, M. 2012, *MNRAS*, 425, L6, doi: 10.1111/j.1745-3933.2012.01290.x

Moses, J. I., Line, M. R., Visscher, C., et al. 2013, *ApJ*, 777, 34, doi: 10.1088/0004-637X/777/1/34

Nagasawa, M., Ida, S., & Bessho, T. 2008, *ApJ*, 678, 498, doi: 10.1086/529369

Öberg, K. I., Murray-Clay, R., & Bergin, E. A. 2011, *ApJL*, 743, L16, doi: 10.1088/2041-8205/743/1/L16

Öberg, K. I., & Wordsworth, R. 2019, *AJ*, 158, 194, doi: 10.3847/1538-3881/ab46a8

Owen, T., Mahaffy, P., Niemann, H. B., et al. 1999, *Nature*, 402, 269, doi: 10.1038/46232

Rice, W. K. M., & Armitage, P. J. 2003, *ApJL*, 598, L55, doi: 10.1086/380390

Snellen, I. A. G., de Kok, R. J., de Mooij, E. J. W., & Albrecht, S. 2010, *Nature*, 465, 1049, doi: 10.1038/nature09111

Sparks, W. B., & Ford, H. C. 2002, *ApJ*, 578, 543, doi: 10.1086/342401

Wang, J., Mawet, D., Ruane, G., Hu, R., & Benneke, B. 2017, *AJ*, 153, 183, doi: 10.3847/1538-3881/aa6474

Chapter 2

MULTI-EPOCH OBSERVATIONAL APPROACH AND SIMULATION FRAMEWORK

2.1 Introduction

Since the 1990s, thousands of exoplanets have been detected orbiting stars beyond our own Sun. The majority of these exoplanets have been detected through two observational approaches: the transit method and the radial velocity approach. The transit approach looks for dips in stellar light as a planet passes in front of its host and the radial velocity approach looks for the velocity shifting characteristic of a star being tugged around by its planetary companion. Both of these approaches are *indirect*. They do not collect photons from planets directly, but rather look for evidence of a planet's presence through its influence on its host star. As we aim to learn more about these planets, including clues into both the diversity of giant planet atmospheres and the potential for habitability on terrestrial exoplanets, we must develop observational approaches that can *directly* probe exoplanet atmospheres.

2.2 Direct Planetary Detection Methods

Researchers have developed *direct* approaches that leverage the changing radial velocity of the exoplanet itself. In short, when two bodies are bound, the two will orbit the center-of-mass of the system. In the case of planets and stars, because the star is much more massive than the planet, the system's center-of-mass will lie much closer to the star, but the star will orbit it nonetheless. The traditional radial velocity approach which *indirectly* detects planets looks for the characteristic Doppler shifting of the stellar spectrum as it is pulled around the system's center-of-mass. *Direct* radial velocity approaches instead look for Doppler shifting of the planetary spectrum itself.

Because planets are much cooler and smaller than stars, the light we receive directly from them is many times fainter the light from the star, making this technique very difficult. As an example, the difference in planet and star brightnesses can be approximated as a ratio between $R^2 B_\lambda(T)$ of each of the two objects, where R is the body's radius and B_λ is the Planck function at temperature T and wavelength λ. A typical hot Jupiter could be as much as ten thousand times fainter than a Sun-like star ($\sim 10^{-3} - 10^{-4}$ at 3 μm), and cooler and smaller planets like the Earth would be much fainter still ($\sim 10^{-11}$ at 3 μm).

Two general variations of a direct radial velocity (RV) approach have been introduced, the observational strategies of which are illustrated in Figure 2.1. In this dissertation, we focus on what we will call the "multi-epoch approach." Like the traditional (or stellar) radial velocity approach, we aim to observe the system at multiple epochs and combine the single-point velocities measured during those epochs to measure the overall planetary velocity. This approach was first presented by Lockwood et al. 2014 using Keck/NIRSPEC data and was further developed by Piskorz 2018. The alternative direct RV variation, we will call either the "CRIRES approach," because it was first applied to VLT/CRIRES data (Snellen et al., 2010), or the "single-night approach," because it can be applied to a single night of data whereas the multi-epoch approach requires multiple nights of observations. Rather than seeking out multiple epochs with single-point planetary velocities, the CRIRES approach targets longer observations that allow for the planetary velocity to change. Since its first application to CRIRES data, this innovative technique has become quite popular, with many following CRIRES studies (e.g., Brogi et al., 2012; Rodler et al., 2012; Brogi et al., 2013; Birkby et al., 2013; de Kok et al., 2013; Brogi et al., 2014; Snellen et al., 2014; Schwarz et al., 2015; Brogi et al., 2016, 2017; Birkby et al., 2017; Hawker et al., 2018; Cabot et al., 2019; Flowers et al., 2019; Webb et al., 2020; Beltz et al., 2021), as well as studies with data from several other high-resolution ground-based spectrometers, including ESO/HARPS (Martins et al., 2015; Allart et al., 2017), CFHT/ESPaDOnS (Esteves et al., 2017), TNG/GIANO (Brogi et al., 2018; Guilluy et al., 2019; Giacobbe et al., 2021), Subaru/HDS (Nugroho et al., 2017), Subaru/IRD (Nugroho et al., 2021), CARMENES (Alonso-Floriano et al., 2019; Sánchez-López et al., 2019, 2020), IGRINS (Flagg et al., 2019), CFHT/SPIRou (Pelletier et al., 2021; Boucher et al., 2021), and Gemini-North/MAROON-X (Kasper et al., 2021). Section 2.3 describes the basis of these two techniques and the fundamental way in which they differ.

2.3 Multi-Epoch vs. CRIRES Approaches

Common Basis of Direct Radial Velocity Approaches

As radial velocity (RV) techniques, both the multi-epoch and the CRIRES approaches aim to measure the overall velocity of the planet. To do so, both measure line-of-sight planetary (secondary) velocities, v_{sec}, at different epochs. The CRIRES approach measures a span of different v_{sec} in a single night, while the multi-epoch approach measures a single v_{sec} per observation. These v_{sec} values are shown as

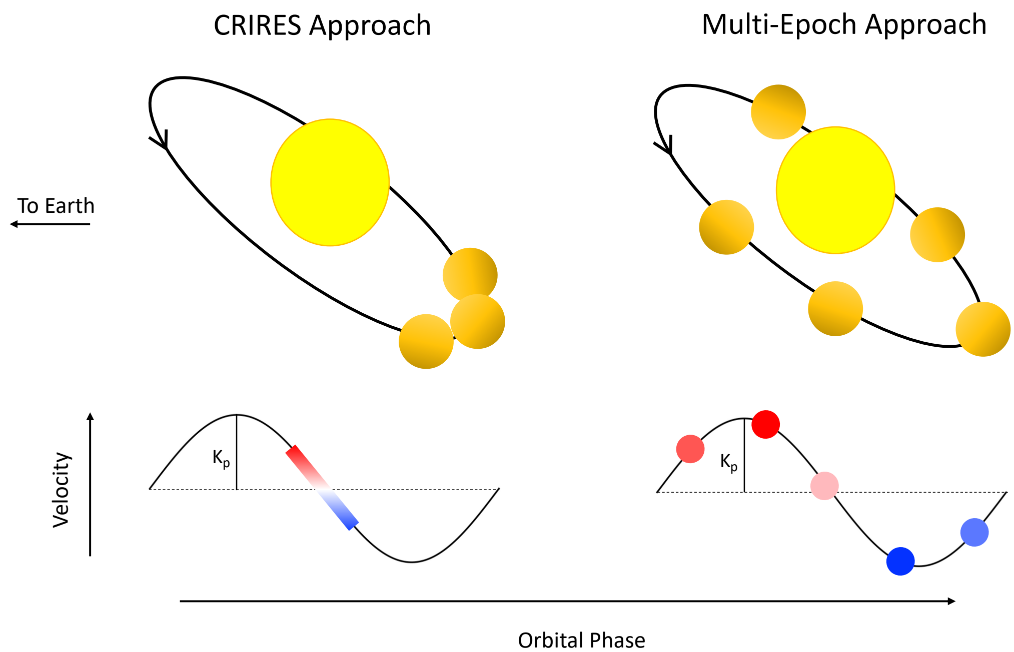

Figure 2.1: Illustration of the differences between the CRIRES (left) and the multi-epoch (right) approaches. The CRIRES approach relies on long ($\sim 5-8$ hour) observations during which the planetary line-of-sight velocity changes. The approach could target, as in the example shown, a time span that corresponds with a planet moving through superior conjunction; in which case, the planetary spectral lines would vary from red- to blue-shifted (represented by the diagonal line which runs from positive to negative velocities). The multi-epoch approach, on the other hand, uses shorter ($\sim 2-3$ hour) observations during which the planetary line-of-sight velocity is constant and a single-velocity measurement can be made (the points each represent a single epoch). Both approaches aim to measure the amplitude of the velocity curves, which we call the Keplerian orbital velocity, K_p.

the red-to-blue diagonal line and the red and blue points on the velocity axes in the schematic diagram in Figure 2.1. The information from these multiple data points can be combined to constrain the amplitude of the sinusoidal velocity function, or the planet's Keplerian orbital velocity, K_p. The line-of-sight planetary velocity can be described according to the function

$$v_{sec} = -K_p(\cos(f+\omega) + e\sin(\omega)) + v_{pri}, \tag{2.1}$$

or, if the orbit can be assumed circular, according to the slightly altered functional form,

$$v_{sec} = K_p \sin(M) + v_{pri}. \tag{2.2}$$

In these equations, e and ω are the orbital eccentricity and argument of periastron, respectively, parameters that are measured in traditional, stellar, RV studies. The planet's orbital position is introduced into the equations as f and M, the true and mean anomalies, though as written here, M has a zero-point at the planet's inferior conjunction and f has its zero-point at periastron. The primary velocity, v_{pri}, or more accurately, the velocity of the center-of-mass of the system, is made up of the systemic velocity and barycentric velocity. It sets the baseline around which the planetary velocity oscillates.

Lastly, the Keplerian orbital veloctiy, K_p, describes the amplitude of planetary velocity oscillation. A measure of K_p signifies of direct detection of the planetary emission. From K_p, we can directly measure the orbital inclination and planetary mass that are left degenerate from stellar RV measurements alone. Once K_p has been constrained, the planetary mass can be measured as

$$M_p = \frac{M_s K_s}{K_p}, \tag{2.3}$$

where M_s is the stellar mass, which, for bright, main-sequence FGKM stars, can be measured to $\sim$ 5% from Hipparcos data and precise spectral synthesis (Lovis & Fischer, 2010), and K_s is the stellar velocity semi-amplitude, which is measured from stellar RV data. Then, the orbital inclination, i, can be calculated from the newly measured planetary mass and planetary minimum mass, $M_p \sin(i)$, which is a stellar RV parameter, as

$$i = \arcsin\left(\frac{M_p \sin(i)}{M_p}\right). \tag{2.4}$$

Direct measurements of planetary masses and orbital inclinations could inform theories of planet formation, migration, and potential for habitability. Beyond masses and inclinations, once planetary emission has been directly detected through these RV approaches, different planetary spectral models can be tested against the data to constrain atmospheric parameters such as the molecular composition (e.g., Birkby et al., 2013; Lockwood et al., 2014; Piskorz et al., 2018; Guilluy et al., 2019; Buzard et al., 2020), wind speed (Snellen et al., 2014), rotation (Brogi et al., 2016), and temperature/pressure profiles (e.g., Schwarz et al., 2015; Pelletier et al., 2021). This critical insight into planetary atmospheres could never be reached with *indirect* observation techniques, like the traditional stellar RV approach, alone.

Fundamental Difference Between Multi-Epoch and CRIRES Approaches

While the multi-epoch approach and the CRIRES approach both aim to measure the Keplerian orbital velocity, K_p, of a planet, they do so in different ways. As described above, the CRIRES technique aims for long observations in a single night during which the planetary line-of-sight velocity will change and the planetary signal will shift across pixels on the detector. The multi-epoch technique, on the other hand, uses short observations from different nights that individually allow no change in planetary velocity.

The technical implications are that the two approaches rely on quite different methods for separating the planetary signal from the telluric and stellar signals. In CRIRES-style data, as the planetary velocity changes, the planetary signal moves across detector pixels. If a CRIRES data set is set up in a observation time (or nod number) vs. wavelength matrix, as displayed in Figure 2.2, each planetary line will shift column-by-column diagonally down the matrix. The telluric and stellar features, on the other hand, because they show no change in velocity, will remain in the same column. Correcting out the median of each column will remove the telluric and stellar features and leave behind the planetary signal. A one-dimensional cross correlation can easily then find the planetary velocities at each nod. This constitutes a simple, highly effective way of separating the planetary signal from the much stronger components of the data set.

In multi-epoch style data, with no change in planetary line-of-sight velocity, the planetary features, like the telluric and stellar features, remain in the same columns down the data matrix of a single epoch. This makes telluric and stellar correction substantially more challenging. In short, we use a telluric model followed by principal component analysis to remove the majority of the telluric contribution to the data set. A two-dimensional cross correlation then detects the stellar and planetary velocities in the data set. This procedure must then be repeated for each of the epochs observed, and the individual epochs combined to yield K_p. A more in depth description of the multi-epoch technical process can be found in the coming chapters, with Chapter 6 in particular describing the important decision points along the multi-epoch pathway.

Table 2.1 lists the main points points at which the two techniques diverge.

2.4 Comparison to Other Techniques

Despite the multi-epoch technique's technical difficulties, its development and use will be especially important moving forward because it will be able to target a range of planets not yet accessible with any other technique. Figure 2.3 illustrates which regions of exoplanet parameter space are accessible to each of the main

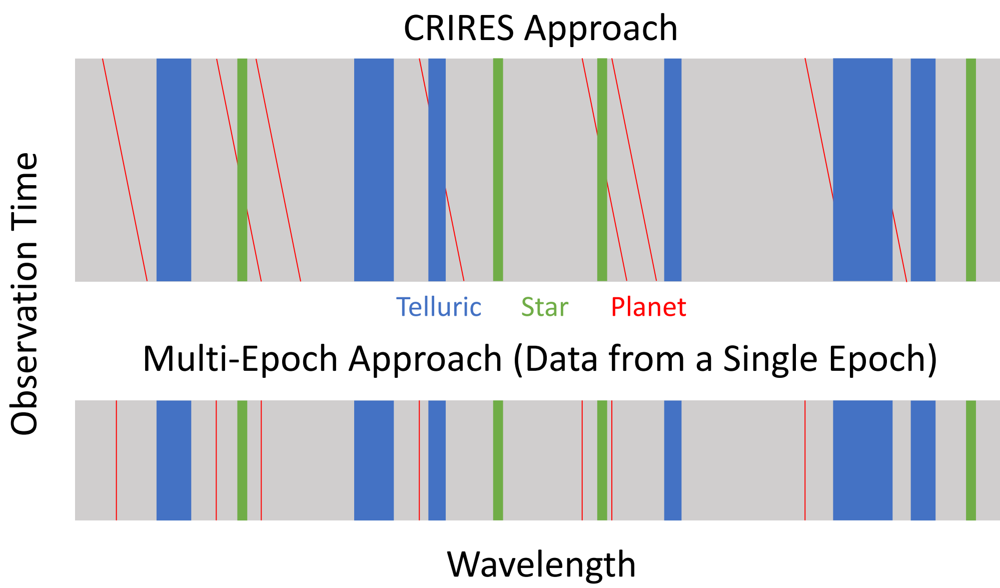

Figure 2.2: Representation of one night of CRIRES-style and multi-epoch style data. The blue and green lines represent stationary telluric and stellar spectral features. The red lines represent planetary features that shift across pixels in a CRIRES data set and remain stationary in a single epoch of multi-epoch style data. The lack of time variation in the planetary signal of the multi-epoch data makes it harder to distinguish from the telluric and stellar signals than in the CRIRES approach.

Table 2.1: CRIRES vs. Multi-Epoch Analyses

	CRIRES Approach	**Multi-Epoch Approach**
Observation length	5–8 hrs	2–3 hrs per epoch
Spectral resolution	70–100,000	25–40,000 (or less)
Target orbital position	Eclipse/Conjunction	Quadrature
Telluric correction approach	Stripe out median by column	Model + PCA
Use of PCA	Identifies moving planetary signal	Removes variable telluric contamination
Cross correlation	1-D	2-D

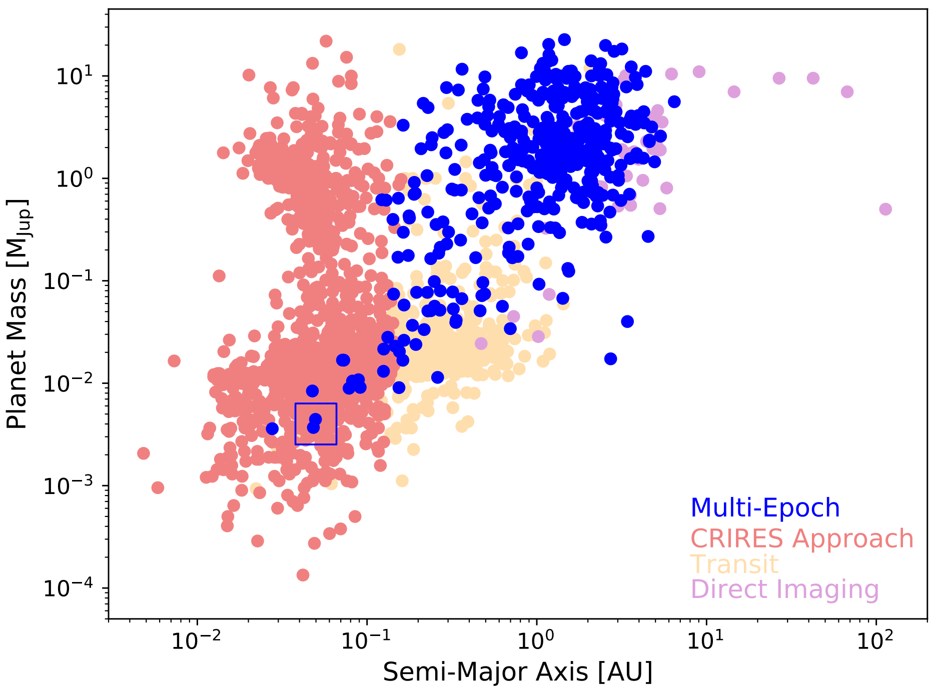

Figure 2.3: Known planets from Exoplanets Data Explorer (www.exoplanets.org; Han et al. 2014) as of October 20, 2021, that are accessible by each of the major characterization techniques. The planets shown in peach could be detected with the CRIRES technique, assuming they are in transiting geometries, with an 8-hour observation on a $R = 100,000$ spectrometer. The planets in yellow are transiting, and could be studied with transmission or secondary eclipse spectroscopy. The pink planets are on orbits beyond $0''.1$, so could (ultimately) be directly imaged. Those only accessible by the multi-epoch technique are in blue. This population includes such planets as Proxima b and Ross 128 b, the two closest known exo-Earths, shown in the blue box.

characterization approaches.

The CRIRES approach could feasibly study each of the planets shown in peach. Each of these planets (generously assumed to be transiting) could cross 3 resolution elements on a $R = \lambda/\Delta\lambda = 100,000$ spectrometer in an 8-hour observation centered on conjunction, when the planet's velocity changes the most rapidly. Even with these liberal constraints, further described in Section 6.3, the CRIRES approach is strictly limited to exoplanets on very close orbits, within ~0.15 AU of their host stars. CRIRES studies often aim for planets that cross more than 3 resolution elements (e.g., 15 pixels ≈ 6 resolution elements, Birkby et al., 2017), which would bring the right-hand edge of the peach planet population to even shorter semi-major axes. Additionally, any inclination from a transiting geometry could substantially reduce the change in velocity over a night, and transform these peach points into blue, multi-epoch detectable, planets.

Direct imaging, in which a planet and its star can be spatially resolved on a spectrometer, has offered fascinating insight into planetary atmospheric chemistry and physics, for example in the cases of Konopacky et al. 2013, Snellen et al. 2014, Schwarz et al. 2016, Bryan et al. 2018, and Wang et al. 2021. Planets must be beyond $\sim 0''.1$ to be spatially resolved from their host stars though, even on the largest existing telescopes. These direct imaging accesible planets are shown in pink at large semi-major axes.

The yellow portion in the center of the graph represents planets that could be studied with transmission and secondary eclipse spectroscopy (e.g., Knutson et al., 2014; Sing et al., 2016). While missions like Kepler and TESS, that target transiting exoplanets, have resulted in transiting planets making up $\sim$80% of those known today[1], statistically, only $\sim$0.1% of hot Jupiters and $\sim 0.5\eta$% of planets at 1 AU around Sun-like stars, where η is the fraction of Sun-like stars with a planet at 1 AU to begin with, are expected to be in transiting geometries (Winn, 2010). Relying on only transmission/secondary eclipse spectroscopy would severely limit what we could learn from the full exoplanet population. Further, we will need to be sensitive to non-transiting planets to target our nearest potentially habitable neighbors; while statistically the nearest potentially habitable *transiting* Earth-sized planet is 10.6 pc away, the nearest *non-transiting* one is only 2.6 pc away (Dressing & Charbonneau, 2015). While the particular yellow points correspond to transiting planets, it is highly possible that many more non-transiting planets are yet to be detected in the yellow portion of the graph. With masses below 0.01 M, non-transiting planets in this region would require Extreme Precision Radial Velocity (EPRV) instruments such as NEID on the WIYN Telescope at Kitt Peak National Observatory (Schwab et al., 2016) and The Habitable Zone Planet Finder (HPF) on the Hobby-Eberly Telescope (Mahadevan et al., 2012, 2014) to be *indirectly* detected and multi-epoch analyses to be *directly* detected. The detection of such planets would add blue points at an even lower mass region than they currently inhabit.

Finally, the blue points in Figure 2.3 show those planets which are currently *only* accessible via the multi-epoch technique. While those planets shown in peach, pink,

[1]www.exoplanets.org.

and yellow can be targeted by other direct approaches, multi-epoch analyses too are capable of detecting them. The only inherent obstacle that the multi-epoch technique cannot overcome is a face-on orbital geometry. A planet on a completely face-on ($i = 0°$) orbit will show no line-of-sight velocity, and therefore will not be detectable by any radial velocity-dependent method. All other obstacles, the most challenging of which will be extremely low planet/star contrast, should be surmountable with sufficient data, high-precision telluric correction routines, and star suppression from high-contrast imaging technology.

The two multi-epoch accessible planets shown in a box in Figure 2.3 are Proxima b and Ross 128 b, the two closest known exo-Earths, both orbiting M stars. Both planets are estimated to be within their host stars' habitable zones. Proxima b orbits the Sun's closest neighbor in the star's traditionally defined habitable zone (Anglada-Escudé et al., 2016). Orbiting a fairly active star, Proxima b's potential for habitability, and, in fact, retention of an atmosphere, have been the subjects of much debate. Direct multi-epoch study of the planet could answer fundamental questions about atmospheric evolution and habitability around M dwarfs. Ross 128, on the other hand, rotates slowly and has weak magnetic activity, suggesting Ross 128 b's atmosphere has not eroded, a positive sign for habitability (Bonfils et al., 2018). With a maximal 15 mas planet-star separation, the temperate planet will be resolvable by the 39 m European ELT (E-ELT) at optical wavelengths ($> 3\lambda/D$ in the O_2 bands). With data from the E-ELT (planned first light in 2027), multi-epoch analyses like ours will be capable of targeting the temperate, habitable-zone planet Ross 128 b. With its ability to target our closest neighboring M dwarf habitable-zone planets, the multi-epoch approach could hold the key to our understanding how atmospheres evolve and what is necessary, from a planetary perspective, for the appearance of life.

2.5 Simulations

Finally, we want to take this chance to briefly introduce the Keck/NIRSPEC multi-epoch simulation framework that is an important component of this dissertation and describe a few of its benefits and challenges. Such simulations can be very useful analytic tools because they can give us an idea of how both planetary signals and structured, or non-random, noise should appear. With this knowledge, we can be confident not to assign a noise peak, or structured residuals, as a planet. Further, we can consider ways to reduce the level of structured noise and use this information to plan future observations and techniques.

Our simulations are generated according to the following steps. Details on how the simulation code is run can be found in Appendix D.

1. **Spectral Models:** We start off with high-resolution spectral models covering the desired wavelength regime. We have mainly relied on SCARLET planetary models (Benneke, 2015) and PHOENIX stellar models (Husser et al., 2013). While other spectral models can, and should, be tested through the simulation code, they must represent the spectrum, with its expected continuum shape, in non-normalized flux units.

2. **Contrast:** To achieve the desired contrast, we scale each model by its respective object's relative surface area, πR^2. The radii R can either be pulled from literature sources or input as desired. The temperature component of the contrast is already accounted for in the spectral model fluxes.

3. **Velocity shift:** The stellar and planetary wavelength axes are each replaced with axes shifted to the expected velocities at the epoch. The stellar velocity is predicted as $v_{pri} = v_{sys} - v_{bary}$, where v_{sys} is the systemic velocity and v_{bary} is the barycentric velocity toward the system at the observation date. The planetary velocity can be estimated from either Equation 2.1 or 2.2.

4. **Combine:** The stellar model is interpolated onto the planetary wavelength axis and the two model fluxes are added.

5. **Continuum removal:** The simulated data is normalized and the continuum shape is removed. For L band wavelengths, we typically fit a third-order polynomial to the simulated data in wavenumber space between 2.8 and 4.0 μm. Dividing the simulated data by this polynomial fit corrects for the continuum shape.

6. **Broaden:** We broaden the spectrum to the instrumental resolution of the data we are simulating using the instrumental profile fit from the data. Our instrumental profile usually consists of just one central Gaussian kernel. To generate predictive simulations centered in wavenumber space on $\tilde{\nu}_{cent}$, the desired instrumental resolution R can be achieved via a Gaussian kernel with $\sigma = \frac{\tilde{\nu}_{cent}}{2.355R}$. Any broadening of the planetary spectrum due to rotation is introduced prior to Step 4 when the two models are combined.

7. **White Noise:** Next, random noise per pixel is added at shot noise level in the observed data.

8. **Wavelength axis:** At this point, the simulated data are linearly interpolated onto the wavelength array from each order of observed data. Prior to the NIRSPEC upgrade, there were 1024 pixels per order, while after the upgrade, there were 2048 pixels per order.

9. **Saturated tellurics:** Lastly, we remove the pixels that were lost in the data to saturated tellurics and edge effects. To do so, we match each order of simulated data with the corresponding observed order and, column-by-column, replace simulated flux values with `NaN`s when present in the observed data.

At this stage, the simulated spectra of each epoch are saved and input into the two-dimensional cross correlation routine in the same procedure applied to real data. The planetary cut of the two-dimensional cross correlation surface from the simulated spectra can be compared to that from the real spectra.

The benefits of such a simulation framework are substantial and are investigated in the following chapters. Simulated results can be used to identify structure that arises from non-random noise vs. structure that is tied to the planetary signal (e.g., Buzard et al., 2020). Once identified, this non-random structure can be accounted for to elucidate the true detection peak. Simulations can also allow us to compare the levels of random and non-random noise to determine whether, even with the reduction of non-random noise, planetary signals should be detectable within a given data set (Buzard et al., 2021b). They can also be used to optimize observing strategies (e.g., Buzard et al., 2021a), allowing for stronger planetary detections and more efficient use of telescope time. Finally, simulations can be used to find the optimal analytic procedures for constraining interesting atmospheric parameters such as carbon-to-oxygen (C/O) ratio and equilibrium temperature (Finnerty et al., 2021). A well-constructed simulation framework can be a crucial component of an analytic procedure such as the multi-epoch technique, and can be extremely useful both in analyzing existing data and in directing future observations and analyses.

While the simulation framework presented in this dissertation has allowed for the exciting results described in the coming chapters, it is a very simple simulation and has substantial room for growth. Our simulation framework generates spectra analogous to those achieved after full reduction from the raw two-dimensional telescope images, wavelength correction, and telluric correction. The simulated data run through only the cross-correlation analysis in the same way as real data. As such, our simulations do not show any noise structure that would arise from inaccuracies in the reduction, wavelength solution, or telluric residuals left behind. Saturated tellurics are considered, as will be discussed below. The structured noise that arises in our simulation results, then, arises from correlations between the planetary spectral model used to correlate the simulated spectra and the portion of the stellar spectral model used to generate the simulated spectra that is not masked out by saturated tellurics. Balance between random (shot) noise structure and non-random noise structure in our simulations is therefore only sensitive to this specific source of non-random noise. Any random or non-random noise arising from reduction inaccuracies, wavelength calibration issues, or residual tellurics will not appear in our simulations. Following, our simulations almost certainly give too optimistic an estimation of a planet's detectability. However, because their prediction is so optimistic, they can set an absolute baseline below which a planet will be undetectable. For instance, in Buzard et al. 2021a, we consider different configurations of epochs that would allow for the strongest planet detections. In the best cases, a real data set would not result in a detection of the strength predicted by simulations unless treated with perfect analytic technique. On the other hand, it is clear to avoid the worst cases as even with perfect technique, planets will prove undetectable in such data sets. As useful as our simple simulations may be, it is important to keep in mind the sources of noise they consider and those they do not.

Additionally, because correlation between planetary and stellar spectral models gives rise to the structured noise in our simulated results, the accuracy and completeness of the spectral models themselves is another important factor. The less similar the spectral models are to the spectra of the star and planet in question, the less the noise structure in the simulated result will approximate even that one source of structured noise in the real data results. Spectral linelists and temperature profiles can significantly alter spectral shapes; to most closely simulate real results, accurate linelists (such as from the latest version of HITRAN, Gordon et al. 2022) and appropriate temperature profiles must be adopted in the input spectral models.

A final challenge comes from the removal of saturated telluric absorption features from the simulated spectra. In Steps 8 and 9 of the simulation procedure, we interpolate our simulated spectrum onto the wavelength axis pulled from a corresponding order of data and mask out the flux points corresponding to those lost to saturated tellurics in the real data. Both of these steps require existing data on which the simulations can be built. In Step 6, we make use of Gaussian kernels, also fit from data, to broaden our simulated data to an appropriate instrumental resolution. Since these kernels can be effectively approximated, though, data-derived kernels are not as important as data-derived wavelength axes and saturated telluric positions for producing accurate simulations. In Figure 2.4, we compare simulations that are equivalent except in Steps 8 and 9. The simulated result shown in red was interpolated onto the wavelength axes of each of five epochs on NIRSPEC1.0 data of HD187123 and the same pixels were masked as were lost to tellurics in real data from Buzard et al. 2020. The simulated results shown in gray were instead interpolated onto wavelength axes with 1024 linearly spaced pixels covering approximately the same orders, with bounds determined using the NIRSPEC Echelle Format Simulator. Different telluric abundances of H_2O, CO_2, and CH_4 were used to determine the position of saturated telluric pixels in the different gray curves. White noise is not introduced into any of the simulated data. While each simulation roughly retrieves the input K_p of 60 km/s, there are some major differences in the shape and position of the structured noise in the red curve as opposed to in the gray curves. Notably, the red simulation shows a side peak near 30 km/s that is absent in the gray curves. This structured noise peak is likely related to the 40 km/s side-peak that obscured the planetary signal in the real data presented in Buzard et al. 2020. If the gray simulated curves, built on telluric models rather than on existing data, had been compared to the real results, the $\sim 30 - 40$ km/s peak could not have identified as noise and ruled out. This illustrates the precision necessary to generate simulations with strong predictive power. Unfortunately, it limits our simulations to spectral regions for which we have existing Keck/NIRSPEC data. Neither multi-epoch analyses nor simulations have been yet attempted on other instruments. To extend the domain for our multi-epoch NIRSPEC simulations, on July 28, 2020, we obtained nearly continuous, K, L, and M band ($\approx 2.15 - 5.53\mu$m) NIRSPEC2.0 high resolution, high signal-to-noise data from two standard stars, one A and one B. These data would provide the basis for high-precision, multi-wavelength simulations that could guide us toward the best observational set-ups and strategies for the detection of cooler planets and the constraints of atmospheric properties like molecular composition (including C/O ratio). Longer wavelength studies, potentially into the M band, will allow us to target black body peak emission from cooler, habitable-zone planets; our precise simulations will enable and streamline this transition.

2.6 Summary

While the multi-epoch approach is quite technically challenging, it will access a population of planets currently out of the range of every other characterization

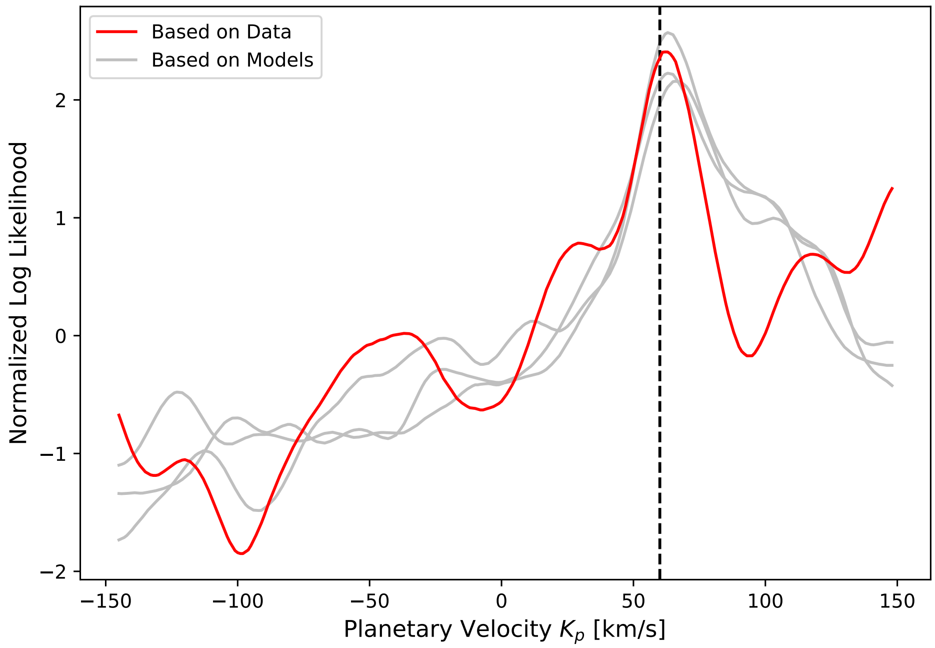

Figure 2.4: Multi-epoch simulations with the wavelength scale and saturated telluric positions taken directly from observed data vs. estimated from tellurics models. In red, the simulated data adopted the wavelength axis and saturated pixel positions from real NIRSPEC1.0 data, while the simulated results shown in gray estimated the saturated pixel positions from telluric models assuming different relative amounts of H_2O, CO_2, and CH_4. The differing structure, namely the red side-peak near ~ 30 km/s not present in the gray curves, shows the importance of using real data to guide the conception of precisely simulated data.

method. This subset includes habitable-zone planets such as Proxima b and Ross 128 b and potentially many others yet to be discovered by upcoming Extreme Precision Radial Velocity instruments such as WIYN/NEID (RV precision < 50 cm/s, Robertson et al. 2019; first light in January 2020) and HET/HPF (RV precision ~ 1.53 m/s, Metcalf et al. 2019; science operations began in late 2018). This crucial characterization technique deserves further development and improvement. In the following chapters, we use the multi-epoch approach to detect the non-transiting hot Jupiter HD187123 b, and introduce simulations that aid in the detection of this planet and present guidelines for more efficient multi-epoch observations. While ultimately, a wavelength-stabilized high-resolution instrument in space would make a world of difference in what we can learn about planetary atmospheres, the simulation framework presented in this dissertation promises to lead us to the best uses of the ground-based instruments available currently or in the near future.

References

Allart, R., Lovis, C., Pino, L., et al. 2017, *A&A*, 606, A144, doi: 10.1051/0004-6361/201730814

Alonso-Floriano, F. J., Sánchez-López, A., Snellen, I. A. G., et al. 2019, *A&A*, 621, A74, doi: 10.1051/0004-6361/201834339

Anglada-Escudé, G., Amado, P. J., Barnes, J., et al. 2016, *Nature*, 536, 437, doi: 10.1038/nature19106

Beltz, H., Rauscher, E., Brogi, M., & Kempton, E. M. R. 2021, *AJ*, 161, 1, doi: 10.3847/1538-3881/abb67b

Benneke, B. 2015, arXiv e-prints, arXiv:1504.07655. https://arxiv.org/abs/1504.07655

Birkby, J. L., de Kok, R. J., Brogi, M., et al. 2013, *MNRAS*, 436, L35, doi: 10.1093/mnrasl/slt107

Birkby, J. L., de Kok, R. J., Brogi, M., Schwarz, H., & Snellen, I. A. G. 2017, *AJ*, 153, 138, doi: 10.3847/1538-3881/aa5c87

Bonfils, X., Astudillo-Defru, N., Díaz, R., et al. 2018, *A&A*, 613, A25, doi: 10.1051/0004-6361/201731973

Boucher, A., Darveau-Bernier, A., Pelletier, S., et al. 2021, *AJ*, 162, 233, doi: 10.3847/1538-3881/ac1f8e

Brogi, M., de Kok, R. J., Albrecht, S., et al. 2016, *ApJ*, 817, 106, doi: 10.3847/0004-637X/817/2/106

Brogi, M., de Kok, R. J., Birkby, J. L., Schwarz, H., & Snellen, I. A. G. 2014, *A&A*, 565, A124, doi: 10.1051/0004-6361/201423537

Brogi, M., Giacobbe, P., Guilluy, G., et al. 2018, *A&A*, 615, A16, doi: 10.1051/0004-6361/201732189

Brogi, M., Line, M., Bean, J., Désert, J. M., & Schwarz, H. 2017, *ApJL*, 839, L2, doi: 10.3847/2041-8213/aa6933

Brogi, M., Snellen, I. A. G., de Kok, R. J., et al. 2012, *Nature*, 486, 502, doi: 10.1038/nature11161

Brogi, M., Snellen, I. A. G., de Kok, R. J., et al. 2013, *ApJ*, 767, 27, doi: 10.1088/0004-637X/767/1/27

Bryan, M. L., Benneke, B., Knutson, H. A., Batygin, K., & Bowler, B. P. 2018, Nature Astronomy, 2, 138, doi: 10.1038/s41550-017-0325-8

Buzard, C., Pelletier, S., Piskorz, D., Benneke, B., & Blake, G. A. 2021a, *AJ*, 162, 26, doi: 10.3847/1538-3881/abf7b9

Buzard, C., Piskorz, D., Lockwood, A. C., et al. 2021b, *AJ*, 162, 269, doi: 10.3847/1538-3881/ac2a2c

Buzard, C., Finnerty, L., Piskorz, D., et al. 2020, *AJ*, 160, 1, doi: 10.3847/1538-3881/ab8f9c

Cabot, S. H. C., Madhusudhan, N., Hawker, G. A., & Gandhi, S. 2019, *MNRAS*, 482, 4422, doi: 10.1093/mnras/sty2994

de Kok, R. J., Brogi, M., Snellen, I. A. G., et al. 2013, *A&A*, 554, A82, doi: 10.1051/0004-6361/201321381

Dressing, C. D., & Charbonneau, D. 2015, *ApJ*, 807, 45, doi: 10.1088/0004-637X/807/1/45

Esteves, L. J., de Mooij, E. J. W., Jayawardhana, R., Watson, C., & de Kok, R. 2017, *AJ*, 153, 268, doi: 10.3847/1538-3881/aa7133

Finnerty, L., Buzard, C., Pelletier, S., et al. 2021, *AJ*, 161, 104, doi: 10.3847/1538-3881/abd6ec

Flagg, L., Johns-Krull, C. M., Nofi, L., et al. 2019, *ApJL*, 878, L37, doi: 10.3847/2041-8213/ab276d

Flowers, E., Brogi, M., Rauscher, E., Kempton, E. M. R., & Chiavassa, A. 2019, *AJ*, 157, 209, doi: 10.3847/1538-3881/ab164c

Giacobbe, P., Brogi, M., Gandhi, S., et al. 2021, *Nature*, 592, 205, doi: 10.1038/s41586-021-03381-x

Gordon, I. E., Rothman, L. S., Hargreaves, R. J., et al. 2022, *J. Quant. Spec. Radiat. Transf.*, 277, 107949, doi: 10.1016/j.jqsrt.2021.107949

Guilluy, G., Sozzetti, A., Brogi, M., et al. 2019, *A&A*, 625, A107, doi: 10.1051/0004-6361/201834615

Han, E., Wang, S. X., Wright, J. T., et al. 2014, *PASP*, 126, 827, doi: 10.1086/678447

Hawker, G. A., Madhusudhan, N., Cabot, S. H. C., & Gandhi, S. 2018, *ApJL*, 863, L11, doi: 10.3847/2041-8213/aac49d

Husser, T. O., Wende-von Berg, S., Dreizler, S., et al. 2013, *A&A*, 553, A6, doi: 10.1051/0004-6361/201219058

Kasper, D., Bean, J. L., Line, M. R., et al. 2021, *ApJL*, 921, L18, doi: 10.3847/2041-8213/ac30e1

Knutson, H. A., Benneke, B., Deming, D., & Homeier, D. 2014, *Nature*, 505, 66, doi: 10.1038/nature12887

Konopacky, Q. M., Barman, T. S., Macintosh, B. A., & Marois, C. 2013, Science, 339, 1398, doi: 10.1126/science.1232003

Lockwood, A. C., Johnson, J. A., Bender, C. F., et al. 2014, *ApJL*, 783, L29, doi: 10.1088/2041-8205/783/2/L29

Lovis, C., & Fischer, D. 2010, Radial Velocity Techniques for Exoplanets, ed. S. Seager, 27–53

Mahadevan, S., Ramsey, L., Bender, C., et al. 2012, in Society of Photo-Optical Instrumentation Engineers (SPIE) Conference Series, Vol. 8446, Ground-based and Airborne Instrumentation for Astronomy IV, ed. I. S. McLean, S. K. Ramsay, & H. Takami, 84461S

Mahadevan, S., Ramsey, L. W., Terrien, R., et al. 2014, in Society of Photo-Optical Instrumentation Engineers (SPIE) Conference Series, Vol. 9147, Ground-based and Airborne Instrumentation for Astronomy V, ed. S. K. Ramsay, I. S. McLean, & H. Takami, 91471G

Martins, J. H. C., Santos, N. C., Figueira, P., et al. 2015, *A&A*, 576, A134, doi: 10.1051/0004-6361/201425298

Metcalf, A. J., Anderson, T., Bender, C. F., et al. 2019, Optica, 6, 233, doi: 10.1364/OPTICA.6.000233

Nugroho, S. K., Kawahara, H., Masuda, K., et al. 2017, *AJ*, 154, 221, doi: 10.3847/1538-3881/aa9433

Nugroho, S. K., Kawahara, H., Gibson, N. P., et al. 2021, *ApJL*, 910, L9, doi: 10.3847/2041-8213/abec71

Pelletier, S., Benneke, B., Darveau-Bernier, A., et al. 2021, *AJ*, 162, 73, doi: 10.3847/1538-3881/ac0428

Piskorz, D., Buzard, C., Line, M. R., et al. 2018, *AJ*, 156, 133, doi: 10.3847/1538-3881/aad781

Piskorz, D. F. 2018, PhD thesis, California Institute of Technology, United States

Robertson, P., Anderson, T., Stefansson, G., et al. 2019, Journal of Astronomical Telescopes, Instruments, and Systems, 5, 015003, doi: 10.1117/1.JATIS.5.1.015003

Rodler, F., Lopez-Morales, M., & Ribas, I. 2012, *ApJL*, 753, L25, doi: 10.1088/2041-8205/753/1/L25

Sánchez-López, A., Alonso-Floriano, F. J., López-Puertas, M., et al. 2019, *A&A*, 630, A53, doi: 10.1051/0004-6361/201936084

Sánchez-López, A., López-Puertas, M., Snellen, I. A. G., et al. 2020, *A&A*, 643, A24, doi: 10.1051/0004-6361/202038629

Schwab, C., Rakich, A., Gong, Q., et al. 2016, in Society of Photo-Optical Instrumentation Engineers (SPIE) Conference Series, Vol. 9908, Ground-based and Airborne Instrumentation for Astronomy VI, ed. C. J. Evans, L. Simard, & H. Takami, 99087H

Schwarz, H., Brogi, M., de Kok, R., Birkby, J., & Snellen, I. 2015, *A&A*, 576, A111, doi: 10.1051/0004-6361/201425170

Schwarz, H., Ginski, C., de Kok, R. J., et al. 2016, *A&A*, 593, A74, doi: 10.1051/0004-6361/201628908

Sing, D. K., Fortney, J. J., Nikolov, N., et al. 2016, *Nature*, 529, 59, doi: 10.1038/nature16068

Snellen, I. A. G., Brandl, B. R., de Kok, R. J., et al. 2014, *Nature*, 509, 63, doi: 10.1038/nature13253

Snellen, I. A. G., de Kok, R. J., de Mooij, E. J. W., & Albrecht, S. 2010, *Nature*, 465, 1049, doi: 10.1038/nature09111

Wang, J. J., Ruffio, J.-B., Morris, E., et al. 2021, *AJ*, 162, 148, doi: 10.3847/1538-3881/ac1349

Webb, R. K., Brogi, M., Gandhi, S., et al. 2020, *MNRAS*, 494, 108, doi: 10.1093/mnras/staa715

Winn, J. N. 2010, arXiv e-prints, arXiv:1001.2010. https://arxiv.org/abs/1001.2010

Chapter 3

SIMULATING THE MULTI-EPOCH DIRECT DETECTION TECHNIQUE TO ISOLATE THE THERMAL EMISSION OF THE NON-TRANSITING HOT JUPITER HD187123B

This chapter is adapted from work previously published as

Buzard, C., Finnerty, L., Piskorz, D., et al. 2020, *The Astronomical Journal*, 160, 1, doi: 10.3847/1538-3881/ab8f9c

3.1 Introduction

To date, over four-thousand extrasolar planets have been discovered with a range of vastly different orbital and atmospheric properties. The most detailed follow-up characterizations of these planets have been provided by the transit technique. While the transit technique can give invaluable insight into the atmospheres of these planets (e.g., Madhusudhan et al., 2014), it is restricted to systems with a very narrow range of orbital inclinations that allow them to transit with respect to our line-of-sight from Earth. Though ~10% of typical hot Jupiters around Sun-like stars can be expected to transit, as we move to habitable-zone planets around M stars and Sun-like stars, the transit probabilities drop to ~9% and 0.5%, respectively. Direct imaging has also provided information on the atmospheric content and relative molecular abundances of planets at large separation (e.g., Konopacky et al., 2013), but these techniques are not yet sensitive to planets within $\sim 0.1''$ (e.g., Snellen et al., 2014; Schwarz et al., 2016), which excludes habitable zone planets around even the closest M stars.

Recent work has developed high-resolution cross-correlation techniques that aim to target the much larger sample of non-transiting, yet close-in, planets by separating the stellar and planetary signals by radial velocity rather than by flux variation, as in the transit technique, or by spatial separation, as in the direct imaging technique (e.g., Snellen et al., 2010; Lockwood et al., 2014). These direct detection techniques work by treating a star/planet system as a spectroscopic binary and measuring the radial velocity signature of the planet. This signature will have an opposite phase to the stellar radial velocity curve (see Figure 3.1), and by combining its amplitude, which we call K_p, the planetary Keplerian line-of-sight velocity, with the stellar radial velocity amplitude K, we can break the mass/inclination degeneracy left by the stellar radial velocity technique and further characterize the planet's atmosphere (e.g., Brogi et al., 2012, 2013, 2014; Lockwood et al., 2014; Piskorz et al., 2016, 2017; Birkby et al., 2017; Piskorz et al., 2018). These techniques have been used to detect the presence of H_2O (e.g., Birkby et al., 2017), CO (e.g., Brogi et al., 2012), TiO (Nugroho et al., 2017), HCN (e.g., Hawker et al., 2018), and CH_4 (Guilluy et al., 2019) in planetary atmospheres, as well as winds (Snellen et al., 2010) and planetary rotation rate (Brogi et al., 2016). They have been applied using data from VLT/CRIRES (e.g., Snellen et al., 2010), Keck/NIRSPEC (e.g., Lockwood et al., 2014), ESO/HARPS (e.g., Martins et al., 2015), CFHT/ESPaDOnS (e.g., Esteves et al., 2017), GIANO (e.g., Brogi et al., 2018), and CARMENES (e.g., Alonso-Floriano et al., 2019) to study about 10 hot Jupiters.

There are two main methods that have been applied to measure planetary Keplerian orbital velocites K_p: a single-night version and a multi-epoch version. The single-night version (e.g., Snellen et al., 2010) observes the systems over a full night (~5-7 hours) when the planet is near superior or inferior conjunction, where its line-of-sight velocity changes most rapidly, and watches for the planetary lines to move across detector pixels as the stellar and telluric lines remain stationary. This technique can also be applied to multiple partial nights as long as the planet lines move across the detector's pixels in the partial nights (e.g., HD 179949, Brogi et al., 2014). The single-night method has provided several high-confidence detections of planetary emission and molecular features, but requires the planetary lines to move by tens of km/s over a ~5–7 hour observation window, and so is limited to close-in planets. The multi-epoch method (e.g., Lockwood et al., 2014), rather than looking for shifting planetary lines in a single night, observes at multiple epochs around the planet's orbit for ~2–3 hours per epoch. These times are chosen to be long enough to maximize the signal-to-noise on the system and to allow for a principal component analysis telluric correction (as described in Section 3.2) but short enough that the planetary lines stay fixed, and so are not removed by the telluric correction. Because the multi-epoch technique does not require the planetary lines to move in a short time period, it is applicable to the future study of planets at larger orbital radii, including those in habitable zones. It could study planets in M-dwarf habitable zones out to those in K-dwarf and solar habitable zones that are too far out for the single-night method but too close in for direct imaging techniques with current adaptive optics capabilities.

As such, improvements on the multi-epoch technique are timely and critical. Here, we apply the multi-epoch method to the hot Jupiter HD187123b, using simulations to understand the limiting factors in our detection. As one of only two known systems with a hot Jupiter (gas giant with $P < 10$ days and $M \sin i > 0.1 M_{\text{Jup}}$) and a very-long period planet ($P > 5$ yrs) in a well-determined orbit (Feng et al., 2015), this system could hold valuable clues to understanding planetary migration. The system is orbiting the Sun-like G2V star HD187123A. HD187123b, the hot Jupiter, has a minimum mass of 0.51 M_{Jup} and an orbital period of 3.10 days. HD187123c is the Jupiter-analogue in the system. It is on an eccentric ($e = 0.280$) orbit with a period of 9.1 yrs and a minimum mass of 1.8 M_{Jup} (Feng et al., 2015). HD187123b was first discovered by Butler et al. 1998 and the most up-to-date Keck/HIRES radial velocity data set was analyzed by Feng et al. 2015 (see Figure 3.1). The relevant properties of HD187123A and HD187123b are given in Table 3.1.

In Section 3.2, we describe the Keck/NIRSPEC data sets and their reduction. In Section 3.3, we describe how we simulate multi-epoch data. We use our simulation framework to measure the K_p of HD187123b along with its mass and inclination in Section 3.4. We consider the trade-off between signal-to-noise (S/N) per epoch and orbital coverage in Section 3.5, and discuss and conclude in Sections 3.6 and 3.7, respectively.

3.2 NIRSPEC Observations and Data Reduction

Observations

We observed the HD187123 system for seven nights in the L band using NIRSPEC (Near InfraRed SPECtrometer; McLean et al. 1998) at the Keck Observatory. Two of the nights were obtained with the upgraded NIRSPEC instrument (Martin et al., 2018), while the rest were taken with the original. We used an ABBA nodding pattern and obtained spectral resolutions of ~25,000 pre-upgrade with the $0.432'' \times 24''$ slit setup and ~41,000 in L post-upgrade with the $0.288'' \times 24''$ slit setup. Before the instrument upgrade, we used echelle settings to obtain orders typically covering 3.4022–3.4550, 3.2549–3.3055, 3.1200–3.1685, 2.9959–3.0424 μm. Our post-upgrade L band settings covered 3.6292–3.6965, 3.4630–3.5292, 3.3131–3.3764, 3.1758–3.2364, 3.0495–3.1075, 2.9330–2.9886 μm. Note that the band settings before and after the upgrade do not overlap. Table 3.2 gives the details of these observations.

Table 3.1: HD187123 System Properties

Property	Value	Ref.
HD187123A		
Mass, $M_\star$	$1.037 \pm 0.025\ M_\odot$	(1)
Radius, $R_\star$	$1.143 \pm 0.039 R_\odot$	(2)
Effective temperature, $T_{\rm eff}$	5815 ± 44 K	(3)
Metallicity, [Fe/H]	0.121 ± 0.30	(3)
Surface gravity, $\log g$	4.359 ± 0.060	(3)
Rotational velocity, $v \sin i$	2.15 ± 0.50 km/s	(3)
Systemic velocity, v_{sys}	-16.965 ± 0.0503 km/s	(4)
K band magnitude, K_{mag}	6.337	(5)
HD187123b		
Velocity semi-amplitude, K	$69.04^{+0.42}_{-0.43}$ m/s	(6)
Line-of-sight orbital velocity, K_P	53 ± 13 km/s	(6)
Minimum mass, $M_p \sin i$	$0.5077^{+0.0087}_{-0.0088}\ M_J$	(6)
Mass, M_p	$1.4^{+0.5}_{-0.3}\ M_J$	(6)
Inclination, i	$21 \pm 5^\circ$	(6)
Semi-major axis, a	0.04209 ± 0.00034 AU	(6)
Period, P	$3.0965885^{+0.0000051}_{-0.0000052}$ days	(6)
Eccentricity, e	$0.0076^{+0.0060}_{-0.0049}$	(6)
Time of periastron, T_{peri}	2454342.87 ± 0.30 JD	(2)
Argument of periastron, ω	$360 \pm 200^\circ$	(2)
Time of inferior conjunction, T_o	$2454343.6765^{+0.0064}_{-0.0074}$ JD	(6)

Refs: (1) Takeda et al. 2007, (2) Feng et al. 2015, (3) Valenti & Fischer 2005, (4) Soubiran et al. 2013, (5) Cutri et al. 2003, (6) This work.

Table 3.2: NIRSPEC Observations of HD187123

Date	Julian Date[a] ($-2,400,000$ days)	Shifted mean anomaly $M'^{\rm a,b}$	Barycentric velocity v_{bary} (km/s)	Integration time (min)	S/N$_L^{\rm c}$
2011 May 21	55703.105	0.01	16.16	56	1724
2011 Aug 10	55783.829	0.08	-2.48	108	1713
2013 Oct 27	56592.759	0.31	-17.44	44	1283
2013 Oct 29	56594.738	0.95	-17.50	80	2050
2017 Sep 7	58003.774	0.98	-10.15	96	2409
2019 Apr 3[d]	58577.140	0.14	15.49	84	2298
2019 Apr 8[d]	58582.131	0.75	16.09	64	3417

[a]Julian date and shifted mean anomaly refer to the middle of the observing sequence.

[b]We report a shifted mean anomaly (M') that is defined from inferior conjunction, rather than from pericenter, and runs from 0 to 1.

[c]S/N$_L$ is calculated at 3.0 μm. Each S/N calculation is for a single channel (i.e., resolution element) for the whole observation.

[d]These observations were taken with the upgraded NIRSPEC instrument.

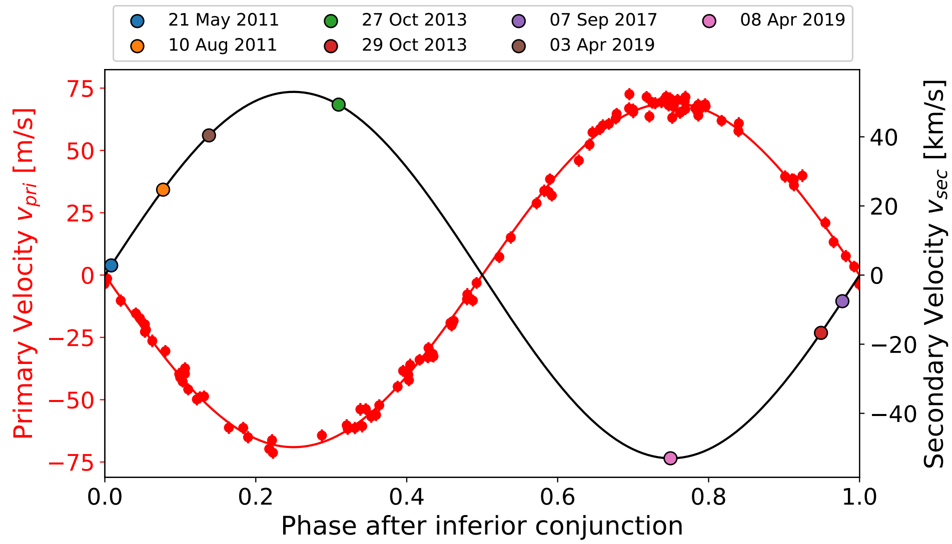

Figure 3.1: Model showing the spectroscopic binary nature of the HD187123 system. The red curve and points show the stellar radial velocity model and measurements (Feng et al., 2015), respectively, and the black curve shows the planetary velocity signature with the colored circles showing the planet's phase at each of our observations with v_{sec} given by our measured K_p of 53 km/s.

NIRSPEC Data Reduction

We reduce our NIRSPEC data using the Python pipeline described by Piskorz et al. 2016, adapting the pipeline where necessary to reduce the 2 nights of data from the upgraded NIRSPEC instrument. The two-dimensional images are flat-fielded and dark-subtracted according to Boogert et al. 2002. The extracted one-dimensional spectra are then wavelength-calibrated with a fourth-order polynomial fit according to model telluric lines.

After the 1-D spectra are extracted and wavelength-calibrated, a model-guided principal component analysis (PCA) is used to remove time-variable components from the data. We use the ESO tool `Molecfit` (Kausch et al., 2014) to fit the initial telluric model to each night of data. In addition to fitting the telluric abundances and continuum, `Molecfit` uses a Gaussian fit to determine the resolution of the data. It reports the full-width at half maximum (FWHM) of the Gaussian kernel, which we later use to broaden the stellar and planetary templates for cross correlation. After the best-fit model is removed from each nod in the data set, PCA is used to identify the dominant sources of variance, following the technique developed in Piskorz et al. 2016. Typically, the majority of the variance is accounted for in the first few principal components. These components typically contain variance due to changes in telluric abundances, in airmass, in the continuum, and in instrument response. After these first few components are removed, a clean stellar/planetary spectrum is left behind. Figure 3.2 shows the third order of the data from September 7, 2017 with its initial telluric fit, the first three principal components, and the clean stellar+planetary spectrum. We specifically limit our observation times so that the planetary signal does not move across pixels in the course of a single night observation, to ensure that PCA will not remove the planetary signal. For the rest of this work, we use spectra with three components and five fringes removed. We also mask out pixels in which telluric absorption features are stronger than 25%. This results in between 9 and 68% of each order being lost. Panel E of Figure 3.2 shows an order from September 7, 2017 with these regions masked out.

3.3 Simulating NIRSPEC Observations

After telluric correction, we use a two-dimensional cross-correlation technique to detect the planetary velocity each night. Because of the difficulty in detecting the planetary velocity in only one epoch, due to the planet's low contrast relative to the star, the correlations from the different nights are combined. This is what allows us to detect the true planetary line-of-sight Keplerian orbital velocity. In order to run the cross correlation, we need high-resolution, high-fidelity stellar and planetary spectral models. We also need a reliable method of combining the correlations from different nights. Before describing the analysis of our HD187123b data, we first describe the spectral models used for the cross correlation in Section 3.3 and describe how we simulate the data at each epoch to help determine the true planetary velocity in Section 3.3. We describe the math behind the three different approaches to combining cross correlations in the Appendix.

High-Resolution Spectral Models

We use an R = 250,000 high-resolution thermal emission model of HD187123b generated using the SCARLET framework (Benneke, 2015). The model computes both the equilibrium chemistry and temperature structure of HD187123b assuming a solar elemental composition, perfect heat redistribution, and an internal heat flux of 75 K. The spectrum is calculated assuming an atmosphere with a metallicity equal to that of the Sun and a C/O ratio of 0.54. The default temperature structure used in this work is inverted due to the inclusion of short wavelength absorbers TiO and VO. The SCARLET model framework includes molecular opacities of H_2O, CH_4, HCN, CO, CO_2, NH_3, and TiO from the ExoMol database (Tennyson & Yurchenko 2012),

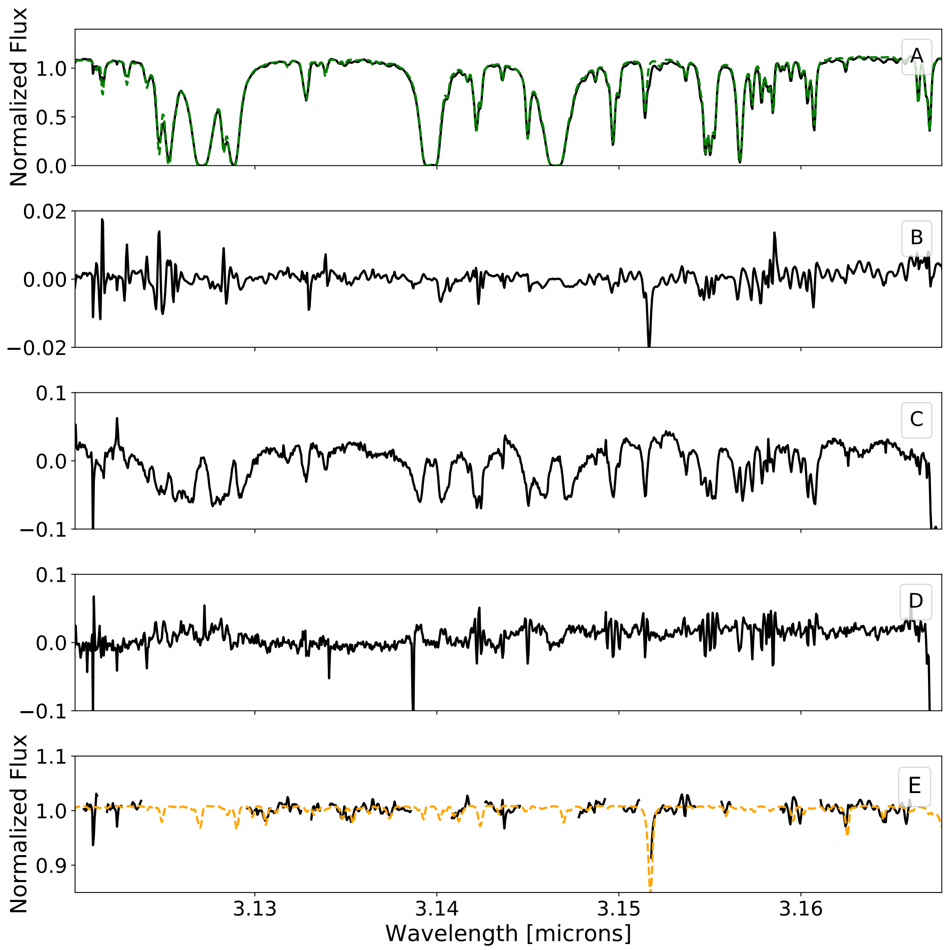

Figure 3.2: Demonstration of PCA telluric removal approach. (A): Raw spectrum of HD187123 from September 7, 2017 with the initial telluric model fit shown in green. (B–D): The first three principal components identified in arbitrary units. These describe changes in the airmass, molecular abundances in the Earth's atmosphere, and plate scale over the course of the observation. (E): Same as A, but without the initial telluric model fit and the first five principal components. A stellar model is overplotted in orange.

molecular opacities of O_2, O_3, OH, C_2H_2, C_2H_4, C_2H_6, H_2O_2, and HO_2 (HITRAN database by Rothman et al. 2009), alkali metal absorptions (VALD database by Piskunov et al. 1995), H_2 broadening (Burrows & Volobuyev, 2003), and collision-induced broadening from H_2/H_2 and H_2/He collisions (Borysow, 2002). We broaden the planetary model with the instrument profiles fit to the data. The L-band portion of the spectral model, covering our data, is dominated by water emission features.

We use a stellar model obtained by interpolating PHOENIX models (Husser et al., 2013) to the effective temperature $T_{\rm eff}$, surface gravity $\log(g)$, and metallicity [Fe/H] values for HD187123A listed in Table 3.1. Instrumental broadening is ultimately determined by the size of the intrument's pixels. The original L band NIRSPEC pixels covered ~5 km/s, and the upgraded L band pixels cover ~3.1 km/s. Because HD187123A is a slow rotator, with a rotational velocity of only 2.15 km/s, instrumental broadening will dominate over rotational broadening and, as such, we broaden the stellar model with only the kernels determined in Section 3.2.

Simulating Multi-Epoch Data

In this work, we simulate the multi-epoch data to better understand the strengths and weaknesses of the technique. To do this, we start with the high-resolution SCARLET planetary and PHOENIX stellar models described in Section 3.3. We scale each model by its relative surface area–that is, its radius squared. The stellar radius is well measured (see Table 3.1), but because it is a non-transiting system, the planetary radius is not. We assume a radius of 1.0 R_J. With this planetary radius, the simulated data has an average spectroscopic planet/star contrast of 1.4×10^{-3} in the L band.

After the stellar and planetary models are appropriately scaled, they are shifted to the nightly velocities. The stellar spectrum is shifted by

$$v_{pri} = v_{sys} - v_{bary}, \tag{3.1}$$

where v_{sys} is the systemic radial velocity and v_{bary} is the nightly barycentric velocity in the direction of the system. The planetary spectrum is shifted by

$$v_{sec} = K_p \sin\left(\frac{2\pi}{P}(T_{obs} - T_o)\right) + v_{pri}, \tag{3.2}$$

where K_p is the line-of-sight Keplerian velocity of the planet, P is the orbital period, T_o is the time of inferior conjunction, and T_{obs} is the midpoint of the observation in Julian date. Unless otherwise stated, P, T_o, and v_{sys} are set as the values in

Table 3.1. The P and T_o values reported were measured using `RadVel` (Fulton et al., 2018) to refit the radial velocity data from Feng et al. 2015. We measure equivalent values of P, e, K, and using the same stellar mass estimate from Takeda et al. 2007, $M_p \sin i$ and a to those found in Feng et al. 2015. However, by refitting the data, we can directly measure the time of inferior conjunction, T_o, and its uncertainty. The uncertainty we measure on T_o is only ~0.2% of the orbital period, meaning that we have a very good sense of where the planet is on its orbit during each epoch. While this would not make much of a difference to the detection ability of the simulations, it will be important for detecting the planet in the real data (described in Section 3.4). The T_{obs} and v_{bary} values are from Table 3.2. K_p is a free parameter.

Next, the stellar model is linearly interpolated onto the planetary model wavelength axis and the two models are added. The stellar continuum is then removed using a third-order polynomial fit to the combined spectrum in wavenumber space from 2.8 to 4 μm. The stellar spectral template used to cross correlate the data (and simulated data) is continuum normalized in the same way (Section 3.4).

The spectra are then broadened according to the instrument profiles fit to the data and interpolated onto the wavelength axes for each of the orders and nights. The same pixels that are clipped from the data (described in Section 3.2) are clipped from these simulated data as well. Lastly, random Gaussian noise is added to the simulated data at the level measured from the real data and reported in Table 3.2.

These simulations account for sections of the data that have to be clipped, but assume that the PCA routine effectively removes all residual telluric structure from the data.

3.4 NIRSPEC Data Analysis and Results

We use two-dimensional cross correlations to determine the stellar and planetary velocities in each epoch of data. While the stellar velocities are readily apparent from single epochs, we must combine cross correlations from multiple epochs to detect the planetary velocity. Cross correlations can be combined as log likelihoods. Throughout this paper, we will call the process of converting cross correlations to log likelihoods "CC-to-log(L)." Zucker 2003 presented an approach to converting cross correlations into log likelihoods that can be applied in two ways which we will call the Zucker log(L) and Zucker maximimum likelihood (ML) approaches. Brogi & Line 2019 recently presented a new CC-to-log(L) approach. The math of these three approaches is described in the Appendix. We use each of these three approaches to combine the seven epochs of HD187123 data and compare the results each gives.

Now that we have presented the stellar and planetary spectral models and introduced the different CC-to-log(L) approaches, we describe our analysis of the HD187123b data.

Two-Dimensional Cross Correlation

We measure the stellar and planetary velocities using the two-dimensional cross-correlation technique (TODCOR, Equation 3.8) from Zucker & Mazeh 1994 and the stellar and planetary spectral models described in Section 3.3. In each night of data, we detect the star's velocity as expected (see Panel A of Figure 3.3). Panels B-H of Figure 3.3 show the log likelihoods from each of the nights combined using each of the three CC-to-log(L) approaches: Zucker log(L) (blue), Zucker ML (green), and Brogi & Line (maroon). The log likelihoods are normalized so that they fit on the same scale, but the relative heights of the log likelihoods between the nights for each CC-to-log(L) approach are maintained. The Zucker log(L) and Zucker ML log likelihoods have the same functional shapes, but the different nights are weighted differently. In each panel, the vertical dashed red line represents the velocity of the star during that epoch, which would correspond to the planetary velocity if the system were face-on. The white region, which illustrates the range of possible planetary velocities each night, begins there and extends until it reaches the maximum orbital velocity (given by $2\pi a/P$), which would represent an edge-on system. The planet's mass and inclination will determine where the peak will be within the white region.

Panels G and H are from the NIRSPEC2 data. The increased resolution of the upgraded instrument can easily be seen in the more resolved structure in these panels as compared to Panels B–F.

The sizes of the white regions also illustrate that some epochs have better constraining power than others. When the planet is near inferior or superior conjunction (M~0, 0.5), as on May 21, 2011, the nightly planetary velocity (v_{sec}) will be largely independent of K_p. When the planet is near quadrature (M~0.25, 0.75), however, as on April 8, 2019, the nightly planetary velocity changes significantly as a function of K_p. Thus, quadrature epochs are more useful for constraining K_p than are those near conjuncture. We note that the opposite is true for the single-night technique. While the multi-epoch technique is most sensitive to epochs with the largest separation between the planetary and stellar velocities (quadrature), the single-night technique is most sensitive to orbital positions that give access to the largest change in planetary velocity over a short time period (near superior/inferior conjunction).

Planet Mass and Orbital Solution

Because the planetary velocities cannot be reliably measured from single epochs, we combine the seven epochs to measure the K_p of HD187123. As described in the Appendix, the log likelihoods from different epochs are combined by converting them from v_{sec} to K_p space using Equation 3.2 and then summing them.

Panel A of Figure 3.4 shows the combined log likelihoods using the three different CC-to-log(L) methods. The three methods each produce a significant peak between around 45 to 60 km/s. To determine the correct Keplerian velocity, we simulate the effect of a 1.0 R_J HD187123b-like planet at 44 and 57 km/s (shown in Panels B and C of Figure 3.4). We see that while both CC-to-log(L) approaches can uniquely detect the planet at 44 km/s, when the planet is shifted to 57 km/s, a side peak appears around 44 km/s. In the Brogi & Line approach, this side peak is stronger than the real peak at 57 km/s while in both Zucker approaches the 57 km/s peak is broadened. We see a similar pattern when we compare these results to the log likelihoods derived from the data (Panel A). The Zucker log(L) approach shows two approximately equal height peaks at ~40 and ~57 km/s while the Brogi & Line approach has a dominant peak at 44 km/s with a much weaker side peak at ~63 km/s.

Both sets of simulations also show a bump at around ~135 km/s, which is also seen in the data. The Zucker 2003 log(L) and Brogi & Line 2019 log(L) approaches do give rise to a small peak at about 100 km/s in the data that does not appear in the simulations. This side peak does not appear in the Zucker 2003 ML approach on the data however. We therefore can rule out the peak at ~100 km/s as the true planetary velocity.

One difference between the simulated results and the data results is the magnitude of the log likelihood variation. We show scaled log likelihood curves in Figure 3.4 so that the curves can be plotted on the same axes. In general, the variation in the simulated log likelihoods from -150 to 150 km/s is $\sim 5\times$ the variation in the data log likelihood curves. We have found that varying the spectroscopic contrast α, which is a function of the planetary radius, used to run the 2D cross correlation (described in the Appendix), changes the magnitude, but not the shape, of the resulting log likelihood curves. Therefore, the magnitude difference is likely due

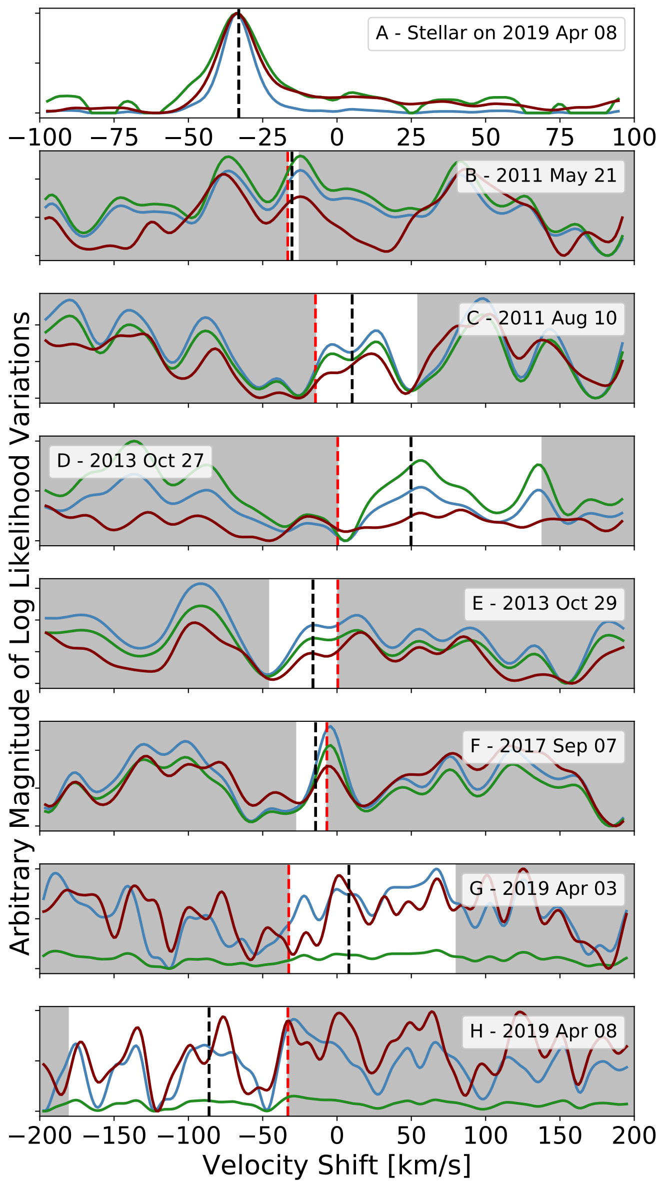

Figure 3.3: Log likelihood functions for all 7 epochs of NIRSPEC data on HD187123. (A): The stellar correlation from April 8, 2019. (B–H): The planetary likelihoods for each of the epochs. The colors represent different CC-to-log(L) approaches with Zucker log(L) in blue, Zucker ML in green, and Brogi & Line in maroon. The curves are normalized, so the y-magnitude is arbitrary, but the relative heights between epochs combined the same way are maintained. The white regions show the allowable velocities, defined between face-on (red dashed line) and edge-on configurations, for each epoch given the known orbital position. The planetary mass/inclination of the system would determine where the planet would fall within the allowed regions.

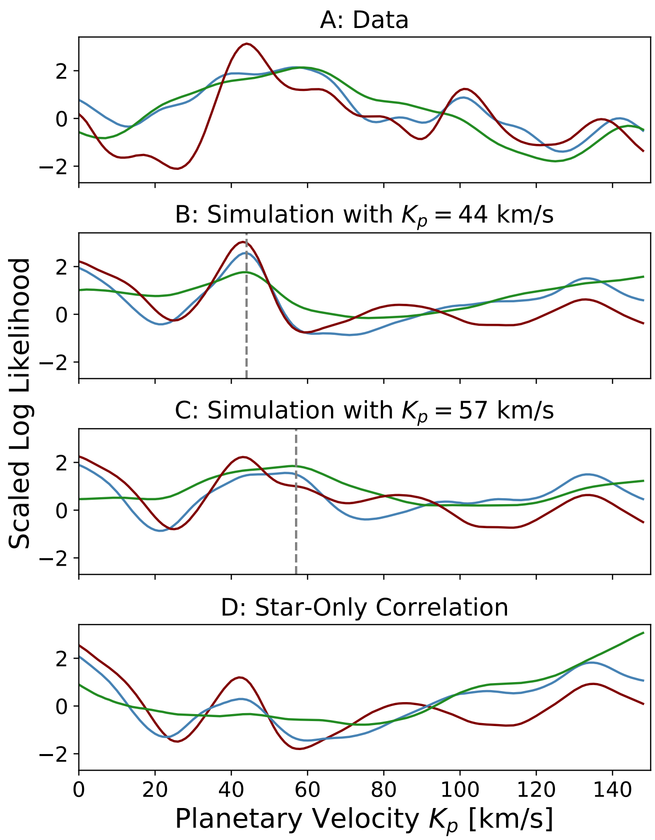

Figure 3.4: Normalized log likelihoods as a function of Keplerian orbital velocity K_p. The Zucker log(L), Zucker ML, and Brogi & Line CC-to-log(L) combination techniques are shown in blue, green, and maroon, respectively. (A): The results of the data. (B–C): The results of the system simulations with a K_p of 44 km/s and 57 km/s, respectively. These simulations both consider a 1 R_{Jup} planet. The results of the simulations in Panel C match the data results in Panel A much better than do the simulation results in Panel B. (D): Similar to Figure 3.4B and 3.4C, but with no injected planetary signal. All structure represents unwanted correlation between stellar model and planetary model spectral lines.

to the uncertainty in the planetary radius and lapse rate. We also note that the simulations seem to show a larger rise toward 0 km/s than is seen in the data. This is likely from correlation between the stellar component of the simulated data and the star model template that leaked into the second dimension of the correlation. In the simulated data, we use the same stellar model spectrum to generate the simulated data and to correlate it. In the real data on the other hand, the real stellar spectrum could be slightly different from the stellar spectral model used to correlate it. For instance, the stellar spectral model does not consider any starspots that could introduce a lower temperature component to the real stellar spectrum. The better match between the stellar template and the stellar component in the simulated data than in the real data would explain why the peak at 0 km/s is stronger in the simulated cases than in the real case.

There are several factors in addition to a lack of modeled starspots that could be leading to a discrepancy between our data results and our modeled results. One stems from inaccuracies in the molecular opacities in both our planetary and stellar spectral models. The ExoMol database uses the MARVEL (Furtenbacher et al., 2007) procedure to correct theoretical calculations of transition frequencies and line shapes using laboratory experiments. The MARVEL framework has only been applied to a few molecules, however, including H_2O and TiO, but notably missing CH_4 and CO_2[1]. The molecules not corrected by MARVEL have errors in transition frequencies around 0.1 cm^{-1}, which is around the resolution element of NIRSPEC. These errors, which are accounted for in the simulated results since the same planetary spectral model is used to generate the simulated data as to correlate it, are not accounted for in the real data and so could cause discrepancies between the two results. Inaccuracies in the stellar line lists could produce similar discrepancies.

An additional source of discrepancy between the simulated and real results could be from our use of the literature value of v_{sys} to combine the data from different epochs. Again, the same systemic (and barycentric) velocities are used to simulate the data as to cross correlate it. However, there are several sources (e.g., rotation, winds, Zhang et al., 2017) that are known to shift the real planetary emission a few km/s from the systemic velocity measured from star. We choose to only consider the planetary cut along the known stellar velocity, though, and so this could account for some discrepancy between the data and simulated results.

We consider the peak at ~57 km/s to be the true planetary detection. To test if we

[1]http://kkrk.chem.elte.hu/Marvelonline/molecules.php.

could determine where the extra correlation peaks (notably the one at 44 km/s) come from, we ran additional simulations with no planet present in the simulated data. These are set up the same way as the simulations shown in the Panels B and C of Figure 3.4, but this time there is no planet model added in to the simulated data. We then run the two-dimensional cross correlation, as above, and show the results of the combined planetary log likelihoods in Figure 3.4D. Because there is no planetary signal in the simulated data, the second dimension of the cross correlation, which involves correlating the data with a planetary model, shows the correlation between the stellar lines in the data and the planetary model. Figure 3.4D shows that this unintended star/planet correlation gives rise to both the peak at 44 km/s and the bump at ~135 km/s. We also see from the flatness of the green curve that the Zucker ML approach is least affected by planet/star correlation. These results support our conclusion that the true K_p is at 57 km/s rather than at 44 km/s.

In general, we find that the two Zucker methods do not have as large peaks at incorrect values of K_p as the Brogi & Line method does for this data set. Figure 3.3 shows the log likelihoods computed for each epoch from each of the three combination approaches. We note that the Brogi & Line method gives more weighting to the two NIRSPEC2 epochs (G, H) than to the five NIRSPEC1 epochs (B–F) while the Zucker log(L) approach gives more even weighting to all of the seven epochs. The Brogi & Line combinations of the two NIRSPEC2 epochs each show a peak that corresponds to a K_p of 44 km/s (just next to the black dashed lines in the direction of the red dashed lines in Panels G and H of Figure 3.3), that does not appear in the five NIRSPEC1 epochs. Since the NIRSPEC1 and NIRSPEC2 L band settings cover slightly different wavelength regions (see Section 3.2), this extraneous peak could be the result of correlation between stellar and planetary lines present in the NIRSPEC2 wavelength regions that are not in the NIRSPEC1 regions. Because the Brogi & Line approach gives more weight to these epochs, the extraneous peak is not diluted by the NIRSPEC1 epochs as much as it is in the Zucker log(L) combination approach. On the other hand, the Zucker ML approach gives more weight to the NIRSPEC1 epochs than the NIRSPEC2 epochs, so it does not benefit from the improved resolution of the NIRSPEC2 data in the same way that the Zucker log(L) approach does.

This suggests that the Zucker log(L) approach is better suited for heterogeneous data sets than either the Brogi & Line or the Zucker ML methods are. To test this hypothesis, we simulate the seven data epochs but as a homogeneous data set, i.e.,

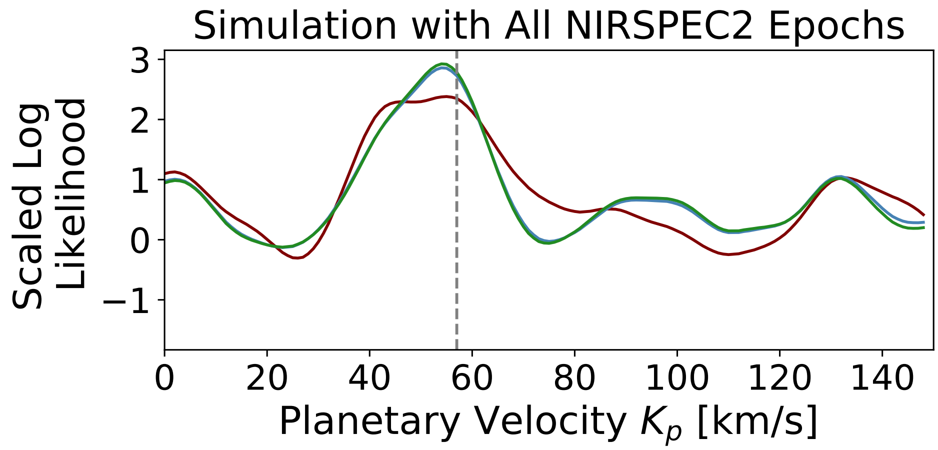

Figure 3.5: Similar to Figure 3.4C, but seven NIRSPEC2 epochs rather than five NIRSPEC1 and two NIRSPEC2 epochs. The three combination approaches give much more similar results on this homogeneous data set than on the heterogeneous data set shown in Figure 3.4C. This suggests that while all of the methods can detect the true peak in a homogeneous data set, the Zucker log(L) approach (blue) performs better on heterogeneous data sets, like our HD187123b one.

with all NIRSPEC2 epochs rather than with five NIRSPEC1 and two NIRSPEC2 epochs. The NIRSPEC version determines the number of pixels per order, the number of orders, the instrument resolution, and the exact wavelength regions covered. We leave the S/N per epoch, planetary orbital phases, and barycentric velocities the same as in the real data set. Figure 3.5 shows that with a homogeneous data set the two Zucker methods and the Brogi & Line approach give much more equivalent results than they do with a heterogeneous data set, though the Brogi & Line method still shows a side peak at ~44 km/s that is not in the Zucker results. In other words, the Brogi & Line approach is more sensitive to unwanted star/planet correlation than the Zucker approaches when applied to homogeneous data sets, but this effect is exaggerated with heterogeneous data. The Brogi & Line log(L) function contains the variance of the data, which suggests that it should account for the variable noise across orders and epochs. Because of this, it may be surprising that it seems to perform worse on the heterogeneous data set than the Zucker log(L) method does. However, the make-up of each epoch (e.g., the specific wavelength range covered, the instrument profile, the orbital position, the barycentric velocity) could affect the level of per-epoch structured noise (e.g., planet/star correlation), a phenomenon to be investigated in future work. While the Brogi & Line formalism accounts for differing levels of random noise between the epochs, it does not account for differing levels of structured, non-random noise. This could explain why it may not be performing as well on the heterogeneous data set as we may have expected it to.

Because the Zucker log(L) method seems to produce the best results for our heterogeneous data set, we use it moving forward. We do, however, stress that further simulations of both different systems and inclination angles and heterogeneous data sets (different wavelength regions, different instruments) are needed to assess the robustness of log likelihood combination approaches.

To further investigate the validity of the peak at 57 km/s, we fit the simulations (as in panels of B and C of Figure 3.4) to the data and report the standard likelihood function

$$\log L = \sum_k \left(\log \frac{1}{\sqrt{2\pi}\sigma_k} - \frac{(M_k - D_k)^2}{2\sigma_k^2} \right), \tag{3.3}$$

where M_k are the simulated pixels, D_k are the data result pixels, and σ_k is the uncertainty on the data results by pixel. To estimate our uncertainty on K_p, we use jack-knife sampling. Jack-knife sampling involves sequentially removing one epoch of data from the combination. The error is then equal to the $\sqrt{N-1}$ × standard deviation of the N different combinations (where N is the total number of epochs). The jack-knife error bars are shown on the Zucker log(L) curve in Figure 3.6A. As described in Piskorz et al. 2016, jack-knife sampling is only one way of estimating error, which often actually overestimates the error because high variance between jack-knife samples drives a high standard deviation, which produces large error intervals. Before fitting the simulations to the data, we normalize the simulated results by the ratio of the standard deviation of the data results and the standard deviation of the simulated results to account for the magnitude difference resulting from the uncertainty in planetary radius and lapse rate. A more sophisticated way of treating structured noise, for instance a Gaussian processes approach, is not yet computationally feasible for such high-resolution data sets.

We test simulations from 0 to 150 km/s in steps of 5 km/s. The normalized likelihood is shown in Figure 3.6B. Fitting the simulations to the results allows us to remove unintended structure in the likelihood surface. In comparing the data result, shown in light blue in Figure 3.6A to the likelihood result in Figure 3.6B, we can see how much of the unwanted structure, including that near 0 and between ~90 and 150 km/s, is depleted. This indicates that the extraneous structure is not random, and can be removed by simulating multi-epoch data sets.

To determine the uncertainty on K_p, we fit Gaussian functions to the results of both

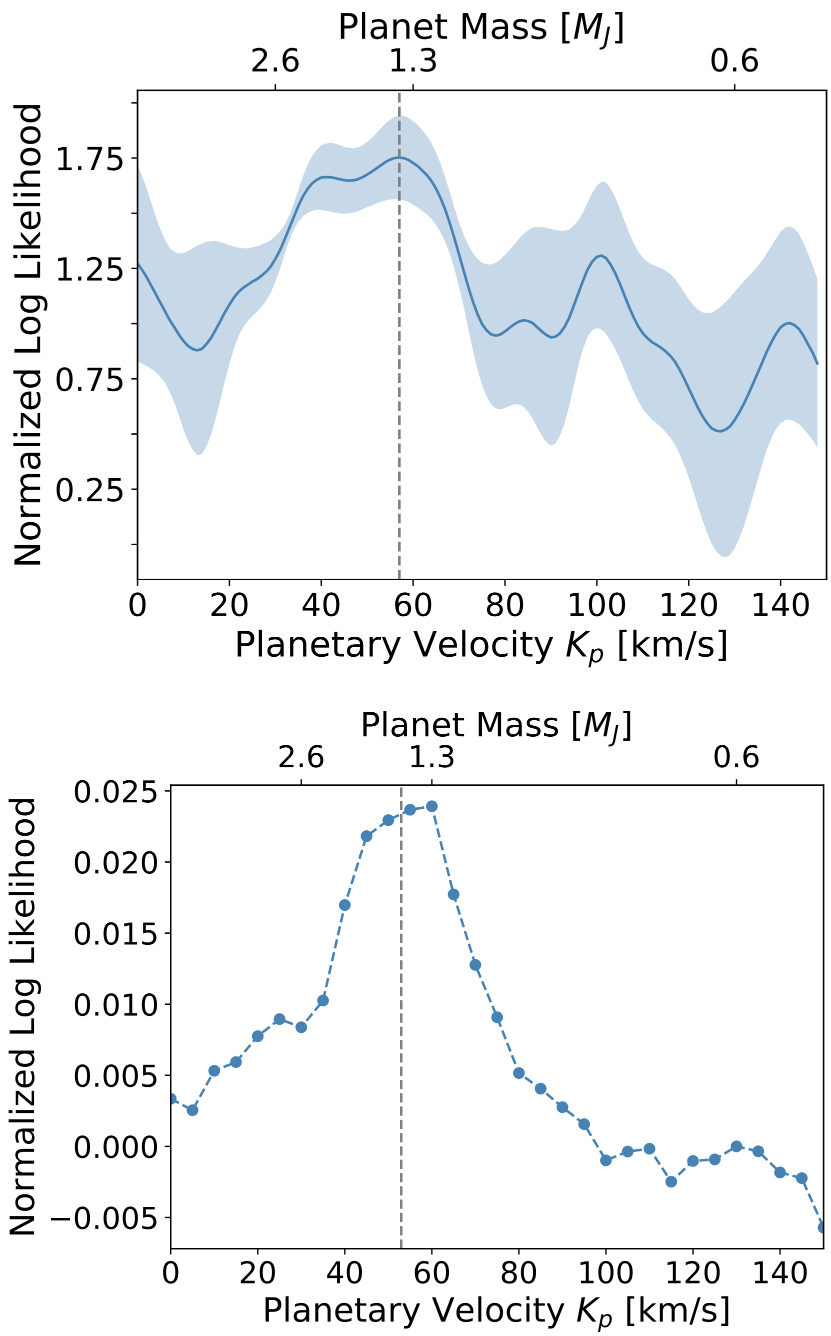

Figure 3.6: (A) Normalized log likelihood as a function of Keplerian orbital velocity K_p for the HD187123b data using the Zucker 2003 log(L) CC-to-log(L) approach. The normalized log likelihoods plotted here and in subsequent figures are normalized by subtracting the mean of the log(L) from -150 to 150 km/s and adding 1. The curve shows the data results with the shaded region indicating the uncertainty ranges resulting from a jack-knife analysis of the data. (B) Normalized log likelihood as a function of Keplerian orbital velocity K_p between the data results and the simulated results using the Zucker log(L) cross correlation combination approach.

the raw data and the simulation fit to data results. From the raw data (shown in light blue in Figure 3.6A), we measure a K_p of 57 ± 15 km/s from the Zucker 2003 log(L) approach, while the simulation fit (Figure 3.6B) yields a K_p of 53 ± 13 km/s.

We determine the significance of the detection from the likelihood fit between the simulations and the data results, i.e., the function shown in Figure 3.6B, since real structure is minimized here and we can assume the variation at the baseline is from unstructured noise. We determine the noise level from the standard deviation of points beyond 2σ from the peak. This gives a significance of 6.5σ at 53 km/s.

Previous multi-epoch detection works (e.g., Piskorz et al., 2018) have reported significance by comparing the likelihood of a Gaussian fit (representing a detection) vs. a linear fit (representing a non-detection) to the peak. This method has given significances of hot Jupiter detections in the range of 3–4σ. This method was used previously because it was clear that the structure at off-peak velocities was not random and so an accurate noise level could not be obtained from it. Applying this technique to the raw data result, we measure a 3.6σ detection from the Zucker log(L) approach. However, we were able to reduce the level of non-random off-peak structure, which allows us to determine the significance in a more straightforward way. While the two values of significance are not directly comparable, we do find a large increase in detection confidence by using simulations to correct out real off-peak structure.

This K_p of 53 ± 13 km/s corresponds to a planetary mass of $1.4^{+0.5}_{-0.3}$ M_J and an orbital inclination of 21 ± 5° at 6.5σ. We correlate the data with planetary models containing the spectral lines of only one molecule (H_2O, CO, or CH_4) and find that the log(L) surface is completely made from correlation with water lines. Therefore, we also report the 6.5σ detection of water in the atmosphere of HD187123b. The log(L) curves produced from CO and CH_4 spectral models do not show peaks at the true K_p. This is not surprising, however, because CO does not have any spectral lines in the L-band wavelengths our data cover, and equilibrium chemistry predicts CO as the major carbon-bearing species in hot Jupiter atmospheres rather than CH_4.

3.5 Signal to Noise vs. Orbital Coverage

Signal to Noise per Epoch

The simulations used to fit the data (the results of which are shown in Figure 3.6B) elucidated the true planetary peak by reducing off-peak structure from correlation between the planetary and stellar spectral models. Though we could reduce this structured noise to a large extent, the detection significance is far from shot noise limited. Since this is the case, we investigate how the planet detectability would change with lower S/N epochs. To do so, we run simulations with the same parameters in the HD187123b data set described in Table 3.2, but decreasing S/N per epoch. To simplify these simulations we spread the total S/N evenly across the seven epochs, so each epoch has a S/N of 2220 to make up the total S/N of 5874 that we obtained in the data. The even distribution of S/N across epochs does not change the results much from the S/N distribution measured in the data as can be seen by the orange (data-like S/N distribution) and black (even S/N distribution) curves in Figure 3.7A. The rest of the curves in the figure show decreasing S/N per epoch. Interestingly, we see that the S/N per epoch can be degraded from 2220 per pixel to 1500 without any noticeable change in the height of the likelihood peak. Furthermore, the off-peak structure also remains the same until the S/N has degraded beyond a S/N of ~500, confirming that this structure is real and not the result of random noise.

To further test these results, we chop the data into lower S/N epochs and test whether we see the same trend. By reducing the number of nods per epoch, we diminish the data set to seven epochs with average S/N per epoch of 1490 and 530 as well as the full average 2220 per epoch. We run PCA to remove telluric contamination after chopping the data, to approximate the results if we had truly only obtained the seven 1490 or 530 S/N epochs. In Figure 3.7B, the data set with 1490 S/N epochs produces a very similar shape to the full 2220 S/N epochs. The green curve, representing an average S/N of only 530 per epoch, also shows similar off-peak structure, for instance around ~100 and ~140 km/s, but the real peak is much diminished here. These results agree with those found using simulations, as seen in Figure 3.7A. These results, in both the simulations and the data, suggest that indeed, our detection is not shot-noise limited, and shorter epochs could be as effective for detecting planetary emission.

One feature seen in the data that is not seen in the simulations is the increase toward 0 km/s in the average S/N 530 epoch case. This set only considered two nods, which is the minimum possible to run a PCA-based telluric correction. Without a large offset in time between the two nods, there would not be as much change in the tellurics (airmass, abundances, plate scale, etc.), meaning that PCA could not remove the telluric contamination as effectively as it could in the higher S/N, more nod cases. The increase toward 0 km/s in the green curve is likely from correlation

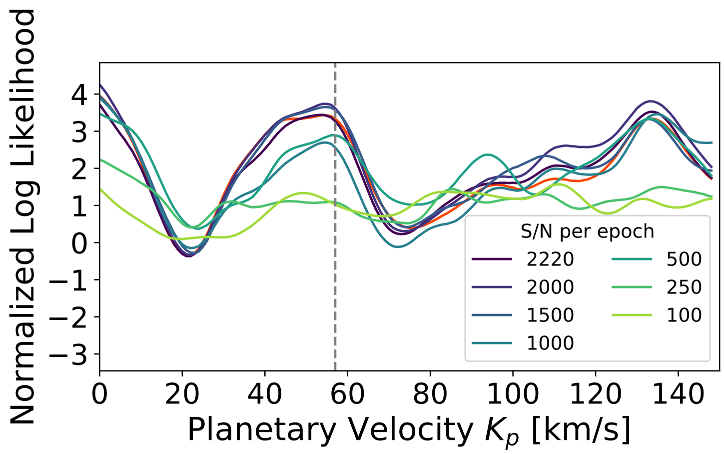

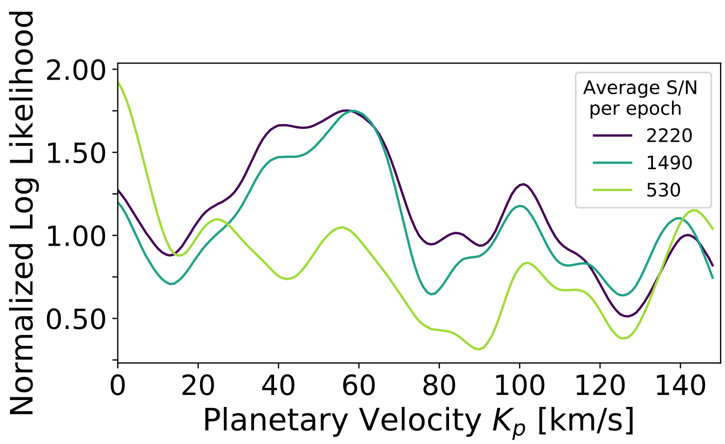

Figure 3.7: (A) Simulations showing how the K_p detection decreases with decreasing S/N per epoch. The S/N is evenly distributed across the seven epochs. The 2220 S/N per epoch simulation has the same total S/N as the data results (shown in orange) that have an uneven S/N distribution, as described in Table 3.2. The similarity between the black, 2220 S/N per epoch curve and the orange curve demonstrated that the different distributions of the total S/N does not have a large effect on the structure of the final results. (B) Normalized log likelihood as a function of K_p showing how chopping the data into lower S/N epochs affects the detection. The purple curve shows the results of the data with its full S/N per epoch, and the teal and green curves show the results when the data is chopped up such that there is an average S/N per epoch of 1490 and 530 respectively. As in the simulations shown in Figure 3.7A, we can see that the data epochs can be dropped from 2220 to ~1500 while retaining quite similar peak and off-peak structure.

between the planetary spectral model and telluric contamination in the data. This sets a limit on how short the exposure time per epoch can be as long as a PCA-based approach is used to remove telluric contamination.

Orbital Coverage

We have seen that currently our detection confidence is limited by structured noise resulting from the correlation between stellar and planetary spectral models. Because we are not in the shot-noise limited case, and could achieve similar detections with lower S/N epochs, we test whether there is a more efficient way of using the full S/N that could help to remove the off-peak structured noise.

To test how we can reduce this structure, we run a simulation with the same total S/N as we obtained in the seven data epochs, but instead we spread that S/N evenly across 20 epochs. These 20 epochs are evenly spaced across the orbit and with primary velocities evenly spaced between the maximum (v_{sys}−min(v_{bary})) and minimum (v_{sys}−max(v_{bary})). They have a S/N of 1313 per epoch as opposed to the average 2220 per epoch in the data. We use the NIRSPEC2 wavelength coverage and resolution to create the twenty epochs.

The results of these simulations are shown in Figure 3.8. The light blue curve represents the data-like simulations, the dark blue curve represents the data-like simulations, but with the wavelength coverage and resolution of NIRSPEC2, and the black curve shows the results of the 20 epoch simulations. Clearly, the twenty epochs result in a much stronger detection than do the seven epochs (whether as observed or with all NIRSPEC2 epochs), even with the same total S/N. More epochs give us access to different wavelength shifts between both (1) the planet and the star and (2) the planet and the Earth's atmosphere, thus significantly reducing the correlation between the planet and star spectral models. It also reduces the the amount of the planetary spectrum that is lost to saturated tellurics because wavelengths that are lost to saturated tellurics will vary as the planet moves around its orbit and its spectrum is Doppler shifted relative to the stationary telluric lines. These simulations suggest that it would be more effective to spread the same total S/N over many epochs across the orbit rather than to obtain just a few isolated higher S/N epochs.

3.6 Discussion

The multi-epoch technique is a promising method for studying hot Jupiters and, in the future, cooler, further separated exoplanets, including those in habitable zones. It can access a much wider sample of planets than the transit technique can, and does not require the quickly changing line-of-sight planetary velocity that the single night technique does, or the spatial separation that direct imaging programs do. Multi-epoch detections are currently limited by structured noise arising from correlation

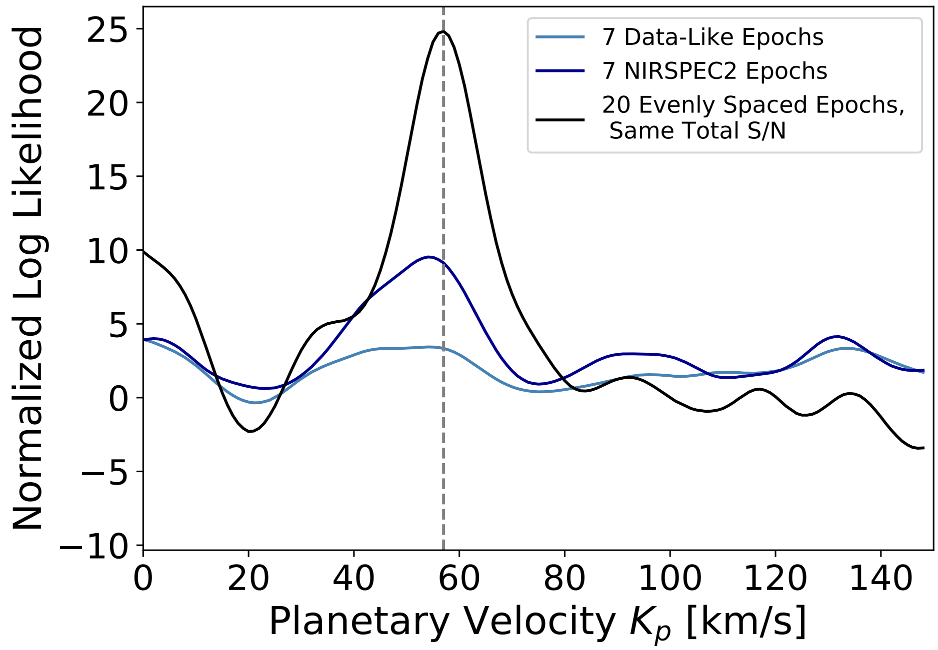

Figure 3.8: Simulations showing the trade-off between S/N per epoch and number of epochs. The light blue curve represents the simulations approximating our data set, with the same S/N per epoch, number of epochs, and epoch orbital positions. The dark blue curve, likewise, represents our data set, but all seven of the epochs are simulated assuming NIRSPEC2 wavelength coverage and resolution. The black curve shows the results of simulations with 20 epochs evenly spaced across the orbit, but the same total S/N. The much stronger peak in the black curve implies that more, lower S/N epochs, i.e., greater orbital coverage, would give a much stronger detection than fewer, higher S/N epochs.

between the planetary models and the stellar component of the data. In this work, we investigate several ways of trying to reduce this unwanted structure.

The multi-epoch technique falls under the category of high-resolution cross-correlation techniques that must combine information from cross correlations of different segments of data. Zucker 2003 and Brogi & Line 2019 each presented ways to convert cross correlations to log likelihoods so that they can be combined. We find that, for this heterogeneous data set, the Brogi & Line 2019 version gives more weight to the unwanted planet/star correlation at ~44 km/s than either of the two Zucker 2003 versions do. This suggests that the Zucker 2003 combination method is better suited than the Brogi & Line 2019 for the two-dimensional cross correlation used in the multi-epoch technique, particularly for heterogeneous data sets (consisting of epochs with different resolutions, wavelength regions, number of orders, etc.). Future work comparing the three combination versions on two-dimensional cross correlations would be useful for really understanding the benefits and weaknesses of each technique, and for determining which would provide the strongest multi-epoch results moving forward.

We also present simulations that can reproduce the off-peak structure in the multi-epoch detection of HD187123b. We find that the detection is far from shot-noise limited and that in both simulations and data, the S/N per epoch could be reduced from 2220 to 1500 without a significant change in the shape of the normalized log likelihood vs. K_p curve. We see that if we obtained many, lower S/N epochs rather than a few, higher S/N epochs, there would be a large increase in detection confidence, even without needing to fit the data results with simulated results.

Being able to obtain useful information from lower S/N epochs could actually have a large impact on multi-epoch observing strategy. Since S/N increases with the square root of time, pushing from 2220 S/N epochs to 1500 S/N epochs, or from a total S/N of 5874 to 3968 per resolution element, we could save a factor of 2.2 in time. This suggests that a more traditional stellar radial velocity observation approach, such as a dedicated program on a smaller ground based telescope that could obtain many lower S/N epochs of data from many hot Jupiter systems, could be successful.

The multi-epoch technique aims to learn about the bulk and atmospheric properties of exoplanets through directly detecting their Keplerian line-of-sight orbital velocity, K_p. More confident and constrained measurements of K_p, obtained through data sets with many, lower S/N epoch data sets, would provide more precise measurements of mass and inclination. Additionally, confident detections of K_p will be critical for using multi-epoch detections to constrain atmospheric parameters, including metallicity and C/O. Öberg et al. 2011 found that, for giant planets that form via core accretion, the C/O ratio of the planet's atmosphere could be an indicator of whether it formed beyond the water snowline, where the gaseous C/O ratio is enriched relative to the stellar value, or within the water snowline, where the gaseous C/O ratio equals the stellar value. Such a measurement for a system like HD187123, with both a hot Jupiter and a Jupiter-analogue, could help to elucidate the processes of planetary formation and migration.

We do note that a C/O measurement would likely require either K or M band data, in addition to the L band data presented here, as the L band contains H_2O lines while the K and M bands have prominent CO features. Future work to investigate whether many, lower S/N epochs could similarly improve K and M band detections, and how these improvements would affect constraints on C/O, would be illuminating.

3.7 Conclusion

In this chapter, we present a simulation framework that enables us to reduce the structured noise from multi-epoch direct detection campaigns (as in Lockwood et al. 2014; Piskorz et al. 2016, 2017, 2018) and elucidate the true planetary detection. Using this framework, we report the 6.5σ detection of the thermal emission from the hot Jupiter HD187123b, and constrain its Keplerian orbital velocity to 53 ± 13 km/s. This allows us to measure the true planetary mass and orbital inclination of $1.4^{+0.5}_{-0.3}$ M_J and 21 ± 5°, respectively. We also report the presence of water in its atmosphere. We use these data sets to compare three methods of converting cross correlations to log likelihoods in order to combine them (Zucker, 2003; Brogi & Line, 2019) on multi-epoch data, and show that the Zucker log(L) approach is least affected by unwanted planet/star correlation for this data set. We also show that an observing strategy that spreads the total S/N across a planet's orbit rather than isolating it into a few, higher S/N epochs would inherently reduce this unwanted structure. The simulation framework presented here, and the optimized observing strategies it will permit, could provide a path from the atmospheres of non-transiting hot Jupiters down to those of habitable zone, Earth-sized planets.

3.8 Appendix

Combining Cross Correlations

As high-resolution cross correlation (CC) spectroscopy becomes more and more widely used to detect and characterize exoplanets, the questions of how to combine both (1) different segments of high-resolution data and (2) high- (e.g., NIRSPEC, CRIRES) and low- (e.g., Spitzer, JWST) resolution data become important. Zucker 2003 introduced an approach to convert cross correlations to log likelihoods (CC-to-log(L)) that can be applied in two ways. We will call these two versions of the Zucker 2003 approach (1) the Zucker log(L) method and (2) the Zucker maximum likelihood or ML method. Previous multi-epoch detections of hot Jupiters (Lockwood et al., 2014; Piskorz et al., 2016, 2017, 2018) have used the Zucker ML method. Brogi & Line 2019 recently presented a new CC-to-log(L) routine.

In this work, and for the multi-epoch technique in general, we use two-dimensional cross correlations (2D CC) to detect the unchanging stellar and planetary velocities during each epoch (see Section 3.4). Once the 2D cross correlations are calculated, we test each of the three different approaches to converting these cross correlations to log likelihoods. We first describe how the 2D CC is calculated, and then describe each of the approaches to converting these 2D cross correlations to log likelihoods.

One- and Two-Dimensional Cross Correlations

When there is only one dominant spectral component in the data, the data can be described by the model

$$f(n) = ag(n-s) + d_n, \tag{3.4}$$

where a is a scaling factor, $g(n)$ is a template spectrum in the same reference frame as the data, s is a wavelength shift, and d_n is the noise at bin n. In this case, a one-dimensional cross correlation function $C(s)$ is sufficient to match the model to the data and can be computed as

$$C(s) = \frac{\sum_n f(n)g(n-s)}{N\sqrt{\sigma_f^2\sigma_g^2}}, \tag{3.5}$$

where $f(n)$ and $g(n)$ are the target and template spectra, respectively, and the variances of the target (σ_f) and the template (σ_g) are given by

$$\sigma_i^2 = \frac{1}{N}\sum_n i^2(n). \tag{3.6}$$

When there is more than one spectral component in the data, however, as is the case in the multi-epoch technique, the model described by Equation 3.4 can no longer accurately describe the data. Rather, a model considering two components is necessary,

$$f(n) = a[g_1(n-s_1) + \alpha g_2(n-s_2)] + d_n. \tag{3.7}$$

As above, a is a scaling factor and d_n is the noise at bin n. The two spectral templates are given by g_1 and g_2 with wavelength shifts of s_1 and s_2, respectively. The scaling factor α accounts for the intensity ratio between the two template models. For this work, we set α equal to 0.0014, which is the spectroscopic contrast given by our stellar and planetary models and assuming a planetary radius of 1 R_J. We have found, however, that the *shape* of the resulting log likelihood surfaces, from both data and simulations, is independent of α in the range of 1.4×10^{-3} to 10^{-9}. This is consistent with what was seen by Lockwood et al. 2014 and Piskorz et al. 2016.

Zucker & Mazeh 1994 showed that a 2D CC $R(s_1, s_2, \alpha)$ could be calculated as

$$R(s_1, s_2, \alpha) = \frac{\sum_n f(n)[g_1(n-s_1) + \alpha g_2(n-s_2)]}{N\sigma_f\sigma_g(s_1, s_2)}, \tag{3.8}$$

where σ_f is the same as described above, but $\sigma_g(s_1, s_2)$ can now be calculated as

$$\sigma_g = \sqrt{\sigma_{g1}^2 + 2\alpha\sigma_{g1}\sigma_{g2}C_{12}(s_2 - s_1) + \alpha^2\sigma_{g2}^2}. \tag{3.9}$$

C_{12} is the correlation between the two templates.

In all of the CC-to-log(L) approaches described below, we combine 2D CCs rather than 1D CCs. This involves replacing $(C(s))$ with $(R(s_1, s_2, \alpha))$ and using σ_g calculated by Equation 3.9 rather than by Equation 3.6.

Once we have calculated the 2D log(L) surface for each epoch, we reduce to the one-dimensional log likelihood functions (e.g., as seen in Figure 3.3) by taking a cut along the maximum stellar velocity, which we check matches the expected stellar velocity from the combined systemic and barycentric velocities.

Zucker (2003) log(L) Approach

First, all correlations from a single night (segments from all orders after the saturated tellurics are removed) are combined using the approach from Zucker (2003). This considers the observed spectrum $f(n)$ and a model $g(n)$ with a scaling factor (a), a shift (s), and random white Gaussian noise (σ). Expressions for a, σ, and s can be found that maximize the log(L) between the observed spectrum and the model(s). By substituting these expressions in to log(L) equation, Zucker 2003 showed that cross correlations can be related to log likelihoods (log(L)) as

$$\log(L) = -\frac{N}{2}\log(1 - R^2). \tag{3.10}$$

The individual cross correlations are converted to log likelihoods and summed for each epoch. The fact that the cross correlation R is squared in this operation means that a negative correlation would provide the same log likelihood as a positive correlation. In other words, a model would give the same log likelihood when fit to the data at a given velocity whether it were multiplied by 1 or -1. This could be concerning because, while planetary absorption and emission lines are not merely related by a sign-flip, correlation between an absorption line in the data with an emission line in the model, or vice versa, would produce an anticorrelation, which, if the baseline correlation were at zero, would be given the same likelihood as a corresponding positive correlation by Equation 3.10. The pressure/temperature profile of a planet's atmosphere, whether inverted or non-inverted, determines whether lines will show up in absorption vs. emission, and so not being able to distinguish between the two cases would severely limit our ability to understand atmospheres.

In our multi-epoch data sets, however, stellar lines are the dominant component and the real planetary signal must correspond with the correct stellar velocity. In other words, we can only detect the planetary signal once the model and data stellar lines are matched up. Therefore, the variation in the planetary correlation is around the mean stellar correlation peak, which is well above zero. Because the planetary correlation values will never reach down to, or below, zero, anticorrelation between the planetary lines in the data and model will be distinguishable from correlation because it will result in smaller (i.e., below the stellar correlation baseline), but still positive, correlation values. We demonstrate the technique's ability to distinguish between inverted and non-inverted planetary atmospheres in Section 6.4.

As a further step in processing the correlations, we correct any negative correlation values to zero. These negative correlation values correspond to incorrect stellar velocities, and so correcting them will not affect the planetary curves. This negative correlation correction is done by calculating $\log(L)$ as

$$
\begin{aligned}
y_i(s) &= \left\{ \begin{array}{ll} N_i \log(1 - R_i(s)^2) & R_i(s) \geq 0 \\ N_i \log(1 + R_i(s)^2) & R_i(s) < 0 \end{array} \right\} \\
\log(L(s)) &= \left\{ \begin{array}{ll} -\frac{1}{2} \sum_i y_i(s) & \sum_i y_i(s) < 0 \\ 0 & \sum_i y_i(s) \geq 0 \end{array} \right\}.
\end{aligned}
\tag{3.11}
$$

Applying this correction after summing the y_i functions, rather than for each negative R_i, accounts only for heavily weighted negative correlations. That is, we do not set negative values in the individual R_i functions equal to zero before combining them because we wish to retain the information from negative R_i functions that arise from noise or uncertainty in the spectra. By waiting until the y_i functions are combined to make this cut, we avoid automatically losing both small negative values in the R_i functions or negative values in an R_i function that have very small relative weighting (N_i). This correction creates the horizontal portions at zero of the stellar log likelihood curve in Panel A of Figure 3.3. This method of correcting negative correlations has been used in previous multi-epoch analyses (e.g., Piskorz et al., 2016, 2017, 2018), and we describe it here for transparency.

We want to stress that negative correlations should not be corrected when using a one-dimensional cross correlation or when the two spectral components in a two-dimensional cross correlation are of similar strength. Doing so would artificially alter the distribution of likelihood values which would invalidate the uncertainties given by the resulting likelihood surface.

Then, the log(L) from different nights of data are converted from v_{sec} to K_p space according to Equation 3.2. Finally, the log likelihoods are summed to find the most likely K_p.

Zucker (2003) ML Approach

The Zucker ML method follows the Zucker log(L) method up to Equation 3.10. However, rather than combining the likelihoods at this point, Zucker 2003 shows that individual correlations can be combined into an "effective" correlation value, ML, as follows:

$$N_{tot} \log[1 - \mathrm{ML}^2(s)] = \sum_i N_i \log[1 - R_i^2(s)], \tag{3.12}$$

where the right side is the sum of the log(L)'s of individual segments and the left side is the log(L) of the full data set (from a single night where the planetary velocity is constant). The R_i's and N_i's are the 2D cross correlations and number of pixels of each of the segments, respectively, and N_{tot} is the total number of pixels. By analogy, ML is the effective correlation of the full data set. Because ML is an effective correlation, we rename it $R(s)$ and evaluate it as,

$$R(s) = \sqrt{1 - \exp\left(\frac{1}{N_{tot}} \sum_i N_i \log[1 - R_i^2(s)]\right)}. \tag{3.13}$$

This gives us an effective correlation for each epoch. We correct for negative correlation values here in an analogous fashion to that described for the Zucker log(L) approach. The effective cross correlations can then be converted to log(L) following Lockwood et al. 2014:

$$\log(L) = \mathrm{const} + R(s). \tag{3.14}$$

Finally, the log(L)'s from different nights are converted from v_{sec} to K_p space, as in the other approaches, and summed.

This was the CC-to-log(L) approach used in the previous NIRSPEC multi-epoch detection papers (Lockwood et al., 2014; Piskorz et al., 2016, 2017, 2018).

Brogi & Line (2019) Approach

Brogi & Line (2019) recently presented a new approach to converting cross correlations to log(L). Instead of substituting the expression for a that maximizes the log(L) between an observed spectrum and a model, they set a equal to 1. Setting a to 1 allows for discrimination between correlation and anticorrelation, or between emission and absorption lines, in a 1D cross correlation routine.

By setting $a = 1$, Brogi & Line (2019) derive the expression

$$\log(L) = -\frac{N}{2}\left\{ \log(\sigma_f \sigma_g) + \log\left[\frac{\sigma_f}{\sigma_g} + \frac{\sigma_g}{\sigma_f} - 2R(s)\right]\right\}. \tag{3.15}$$

We stress that since our approach uses two-dimensional cross correlations, in applying this conversion to our data, $R(s)$ and σ_g are the two-dimensional variants described in Equations 3.8 and 3.9, rather than the one-dimensional $C(s)$ and σ_g described in Equations 3.5 and 3.6.

We note too, as above, that in our 2D case, where there are both stellar and planetary signals in the data, a negative a would invert the stellar absorption lines as well as the planetary lines. Our multi-epoch data have high enough S/N on the stellar lines that flipping the stellar model would produce a strong anticorrelation, which would be corrected to zero as described above. Therefore, while allowing a to vary in 1D CC routines on low S/N planetary data could certainly present challenges, 2D routines on data with high S/N stellar features would not run into the same obstacles as negative a values would be ruled out by the stellar spectrum. Thus, even without setting a to 1, the Zucker methods would not confuse planetary (and stellar) emission and absorption lines.

As in the Zucker 2003 approach, the log(L) functions from a single night are summed, then the summed log(L) for each night is converted from v_{sec} to K_p space and summed.

References

Alonso-Floriano, F. J., Sánchez-López, A., Snellen, I. A. G., et al. 2019, *A&A*, 621, A74, doi: 10.1051/0004-6361/201834339

Benneke, B. 2015, ArXiv e-prints. https://arxiv.org/abs/1504.07655

Birkby, J. L., de Kok, R. J., Brogi, M., Schwarz, H., & Snellen, I. A. G. 2017, *AJ*, 153, 138, doi: 10.3847/1538-3881/aa5c87

Boogert, A. C. A., Blake, G. A., & Tielens, A. G. G. M. 2002, *ApJ*, 577, 271, doi: 10.1086/342176

Borysow, A. 2002, *A&A*, 390, 779, doi: 10.1051/0004-6361:20020555

Brogi, M., de Kok, R. J., Albrecht, S., et al. 2016, *ApJ*, 817, 106, doi: 10.3847/0004-637X/817/2/106

Brogi, M., de Kok, R. J., Birkby, J. L., Schwarz, H., & Snellen, I. A. G. 2014, *A&A*, 565, A124, doi: 10.1051/0004-6361/201423537

Brogi, M., Giacobbe, P., Guilluy, G., et al. 2018, *A&A*, 615, A16, doi: 10.1051/0004-6361/201732189

Brogi, M., & Line, M. R. 2019, *AJ*, 157, 114, doi: 10.3847/1538-3881/aaffd3

Brogi, M., Snellen, I. A. G., de Kok, R. J., et al. 2012, *Nature*, 486, 502, doi: 10.1038/nature11161

—. 2013, *ApJ*, 767, 27, doi: 10.1088/0004-637X/767/1/27

Burrows, A., & Volobuyev, M. 2003, *ApJ*, 583, 985, doi: 10.1086/345412

Butler, R. P., Marcy, G. W., Vogt, S. S., & Apps, K. 1998, *PASP*, 110, 1389, doi: 10.1086/316287

Cutri, R. M., Skrutskie, M. F., van Dyk, S., et al. 2003, VizieR Online Data Catalog, 2246

Esteves, L. J., de Mooij, E. J. W., Jayawardhana, R., Watson, C., & de Kok, R. 2017, *AJ*, 153, 268, doi: 10.3847/1538-3881/aa7133

Feng, Y. K., Wright, J. T., Nelson, B., et al. 2015, *ApJ*, 800, 22, doi: 10.1088/0004-637X/800/1/22

Fulton, B. J., Petigura, E. A., Blunt, S., & Sinukoff, E. 2018, *PASP*, 130, 044504, doi: 10.1088/1538-3873/aaaaa8

Furtenbacher, T., Császár, A. G., & Tennyson, J. 2007, Journal of Molecular Spectroscopy, 245, 115, doi: 10.1016/j.jms.2007.07.005

Guilluy, G., Sozzetti, A., Brogi, M., et al. 2019, *A&A*, 625, A107, doi: 10.1051/0004-6361/201834615

Hawker, G. A., Madhusudhan, N., Cabot, S. H. C., & Gandhi, S. 2018, *ApJL*, 863, L11, doi: 10.3847/2041-8213/aac49d

Husser, T. O., Wende-von Berg, S., Dreizler, S., et al. 2013, *A&A*, 553, A6, doi: 10.1051/0004-6361/201219058

Kausch, W., Noll, S., Smette, A., et al. 2014, in Astronomical Society of the Pacific Conference Series, Vol. 485, Astronomical Data Analysis Software and Systems XXIII, ed. N. Manset & P. Forshay, 403

Konopacky, Q. M., Barman, T. S., Macintosh, B. A., & Marois, C. 2013, Science, 339, 1398, doi: 10.1126/science.1232003

Lockwood, A. C., Johnson, J. A., Bender, C. F., et al. 2014, *ApJL*, 783, L29, doi: 10.1088/2041-8205/783/2/L29

Madhusudhan, N., Knutson, H., Fortney, J. J., & Barman, T. 2014, in Protostars and Planets VI, ed. H. Beuther, R. S. Klessen, C. P. Dullemond, & T. Henning, 739

Martin, E. C., Fitzgerald, M. P., McLean, I. S., et al. 2018, in Society of Photo-Optical Instrumentation Engineers (SPIE) Conference Series, Vol. 10702, Ground-based and Airborne Instrumentation for Astronomy VII, 107020A

Martins, J. H. C., Santos, N. C., Figueira, P., et al. 2015, VizieR Online Data Catalog, 357

McLean, I. S., Becklin, E. E., Bendiksen, O., et al. 1998, in *Proc. SPIE*, Vol. 3354, Infrared Astronomical Instrumentation, ed. A. M. Fowler, 566–578

Nugroho, S. K., Kawahara, H., Masuda, K., et al. 2017, *AJ*, 154, 221, doi: 10.3847/1538-3881/aa9433

Öberg, K. I., Murray-Clay, R., & Bergin, E. A. 2011, *ApJL*, 743, L16, doi: 10.1088/2041-8205/743/1/L16

Piskorz, D., Benneke, B., Crockett, N. R., et al. 2016, *ApJ*, 832, 131, doi: 10.3847/0004-637X/832/2/131

—. 2017, *AJ*, 154, 78, doi: 10.3847/1538-3881/aa7dd8

Piskorz, D., Buzard, C., Line, M. R., et al. 2018, *AJ*, 156, 133, doi: 10.3847/1538-3881/aad781

Piskunov, N. E., Kupka, F., Ryabchikova, T. A., Weiss, W. W., & Jeffery, C. S. 1995, *A&AS*, 112, 525

Rothman, L. S., Gordon, I. E., Barbe, A., et al. 2009, *J. Quant. Spec. Radiat. Transf.*, 110, 533, doi: 10.1016/j.jqsrt.2009.02.013

Schwarz, H., Ginski, C., de Kok, R. J., et al. 2016, *A&A*, 593, A74, doi: 10.1051/0004-6361/201628908

Snellen, I. A. G., Brandl, B. R., de Kok, R. J., et al. 2014, *Nature*, 509, 63, doi: 10.1038/nature13253

Snellen, I. A. G., de Kok, R. J., de Mooij, E. J. W., & Albrecht, S. 2010, *Nature*, 465, 1049, doi: 10.1038/nature09111

Soubiran, C., Jasniewicz, G., Chemin, L., et al. 2013, *A&A*, 552, A64, doi: 10.1051/0004-6361/201220927

Takeda, G., Ford, E. B., Sills, A., et al. 2007, *ApJS*, 168, 297, doi: 10.1086/509763

Tennyson, J., & Yurchenko, S. N. 2012, *MNRAS*, 425, 21, doi: 10.1111/j.1365-2966.2012.21440.x

Valenti, J. A., & Fischer, D. A. 2005, *ApJS*, 159, 141, doi: 10.1086/430500

Zhang, J., Kempton, E. M. R., & Rauscher, E. 2017, *ApJ*, 851, 84, doi: 10.3847/1538-4357/aa9891

Zucker, S. 2003, *MNRAS*, 342, 1291, doi: 10.1046/j.1365-8711.2003.06633.x

Zucker, S., & Mazeh, T. 1994, *ApJ*, 420, 806, doi: 10.1086/173605

Chapter 4

PRIMARY VELOCITY AND ORBITAL PHASE EFFECTS ON PLANETARY DETECTABILITY FROM SMALL EPOCH NUMBER DATA SETS

This chapter is adapted from work previously published as

Buzard, C., Pelletier, S., Piskorz, D., Benneke, B., & Blake, G. A. 2021a, *The Astronomical Journal*, 162, 26, doi: 10.3847/1538-3881/abf7b9

4.1 Introduction

As thousands of exoplanets are being discovered through indirect methods such as transit and radial velocity surveys, astronomers have begun to consider how to follow-up on these detections and measure the planets' atmospheric properties, especially the presence and relative abundances of molecular species, the atmospheric pressure/temperature profiles, and the nature of winds and planetary rotation. High-resolution cross-correlation spectroscopy has been introduced as an effective technique to directly detect planets' thermal emission and begin to characterize their atmospheres (e.g., Brogi et al., 2012; Birkby et al., 2013; Lockwood et al., 2014). High-resolution cross-correlation spectroscopy works by allowing researchers to disentangle planetary and stellar radial velocities. By fitting the planetary radial velocities with an equation for the orbital motion, observers can constrain the amplitude of that motion, called the planetary Keplerian orbital velocity, K_p. With prior knowledge of the stellar mass and the stellar Keplerian orbital velocity K_* from optical radial velocity measurements, we can constrain the true mass and orbital inclination of the planet. Further, planetary models with different assumptions about various atmospheric properties can be cross correlated against the data and the resulting strength of the planetary detection can be used to understand the true nature of the planetary atmosphere.

Two approaches have been applied to constrain K_p from the planetary radial velocities. In one, observers target a system at times when the line-of-sight planetary acceleration is largest, e.g., near inferior/superior conjunction (e.g., Snellen et al., 2010; Brogi et al., 2012, 2013; Birkby et al., 2017; Guilluy et al., 2019). Then, by observing for many (~5–7) hours in one stretch, they can watch the planetary signal shift systematically with respect to the fixed stellar and telluric reference frames, as its line-of-sight velocity changes. The Keplerian velocity K_p is measured through a fit to this changing planetary radial velocity. While this technique has been very effective for hot Jupiters, it requires a significant change in the line-of-sight orbital velocity (tens of km/s) over the course of a single continuous observing sequence. This will preclude its application to longer period planets, including those is the nearest M star habitable zones. Another approach, first introduced by Lockwood et al. (2014), limits wall-clock observing times to ~2–3 hours to obtain measurements that do not allow the planetary signal to cross detector pixels. After building up a data set of several such measurements around the planet's orbit, the data can be fit to constrain K_p. We will call this approach the "multi-epoch" approach.

Buzard et al. (2020) used the multi-epoch approach to detect the thermal emission from the hot Jupiter, HD187123b. In that work, we introduced a simulation frame that could account for a portion of the structured noise that arose in the K_p detection space. With these simulations, we showed how beneficial many-epoch (~20) data sets are over few-epoch (~5) data sets, even if they share the same total S/N. This was because in the few-epoch simulations, structured noise resulting from unwanted correlation between the planetary spectral template and the observed stellar signal was well in excess of the shot noise readily obtainable with Keck on bright stars. Large-number epoch data sets afford more variation between the stellar and planetary signals that works to beat down this source of structured noise. However, it can be difficult to build up to such large data sets with highly over-subscribed telescopes such as Keck, especially with the current generation of high-resolution echelle spectrographs that have modest instantaneous spectral grasp in the thermal infrared, such that significant integration times are needed per epoch. In this work, we investigate whether there is a way to provide more efficient detections with few-epoch data sets by carefully selecting which nights we choose to observe. To do so, we consider the effects of the primary (stellar) velocities and orbital phases at each epoch.

At any given observation time, the stellar velocity in a system will be determined by the systemic velocity, the barycentric velocity from the component of the Earth's orbital motion in the direction of the system, and the radial velocity caused by the planetary tug on the star. The current NIRSPEC does not have the velocity precision necessary to resolve the radial velocity caused by a planet; while NIRSPEC L band velocity precision is $\sim$ 3.2 km/s, the stellar RVs caused by even the massive hot

Jupiters are $\lesssim$ 0.1–0.2 km/s. Assuming a constant systemic velocity, then, the barycentric velocity is variable and can be chosen by when the observing night is scheduled. We will consider the primary velocity at a given observation time t_{obs},

$$v_{\text{pri}}(t_{\text{obs}}) = v_{\text{sys}} - v_{\text{bary}}(t_{\text{obs}}). \tag{4.1}$$

The planetary velocity is similarly comprised of a dynamical radial velocity (which, unlike the stellar RV, is large enough to be resolved by NIRSPEC), the systemic velocity, and the barycentric velocity. The magnitude of the planetary gravitational radial velocity signature is K_p, and depends on the planetary and stellar masses, and the orbital inclination, semi-major axis, and eccentricity. The orbital phase, M, of the planet will determine the magnitude of the planetary radial velocity given K_p, and will therefore determine the planetary velocity relative to the stellar velocity. If the radial velocity parameters have been determined through optical, stellar RV measurements, M can be calculated at any time through the equation,

$$M(t_{\text{obs}}) = \frac{(t_{\text{obs}} - T_0) \mod P}{P}, \tag{4.2}$$

where T_0 is the time of inferior conjunction and P is the orbital period. As a function of t_{obs}, M can also be chosen with careful observation scheduling. With these two parameters, and assuming a circular orbit, the secondary, or planetary, radial velocity can be described as

$$v_{sec}(t_{obs}) = K_p \sin(2\pi M(t_{obs})) + v_{pri}(t_{obs}). \tag{4.3}$$

Since the primary velocity (v_{pri}) and orbital phase (M) can both be selected by the choice of observing nights, we set out to understand how different combinations of primary velocity and orbital phase epochs affect the detectability of planetary Keplerian orbital velocities, K_p, for a modest, and readily obtainable, 5-epoch data set.

The rest of this work is organized as follows. In Section 4.2, we describe the planetary spectral models used in these simulations, how the simulations are generated, and how they are analyzed. In Section 4.3, we consider the effectiveness of different groupings of orbital phases and primary velocities. We examine whether the magnitude of K_p affects the results of these primary velocity/orbital phase simulations in Section 4.4. In Section 4.5, we attempt to see whether a combination of NIRSPEC data epochs agree with these simulation results. In Section 4.6, we consider the primary velocity and orbital phase effects on larger data sets. Finally, we discuss some implications of these results in Section 4.8 and conclude in Section 4.9.

4.2 Methods

Spectral Models Used

For these simulations, we used a spectral model generated from the PHOENIX stellar spectral modeling framework (Husser et al., 2013). We interpolated the effective temperature, metallicity, and surface gravity to those of the sun-like star HD187123 (T_{eff} = 5815 K, [Fe/H] = 0.121, and $\log(g)$ = 4.359; Valenti & Fischer (2005)).

Our planetary thermal emission model was generated from the SCARLET framework (Benneke & Seager, 2012, 2013; Benneke, 2015; Benneke et al., 2019a,b) at $R = 250,000$. This framework computes equilibrium atmospheric chemistry and temperature structure assuming a cloud-free atmosphere with a solar elemental composition, efficient heat redistribution, and an internal heat flux of 75 K. We assume a solar metallicity and C/O ratio. The SCARLET model framework includes molecular opacities of H_2O, CH_4, HCN, CO, CO_2, NH_3, and TiO from the ExoMol database (Tennyson & Yurchenko, 2012; Tennyson et al., 2020), molecular opacities of O_2, O_3, OH, C_2H_2, C_2H_4, C_2H_6, H_2O_2, and HO_2 (HITRAN database by Rothman et al. (2009)), alkali metal absorptions (VALD database by Piskunov et al. (1995)), H_2 broadening (Burrows & Volobuyev, 2003), and collision-induced broadening from H_2/H_2 and H_2/He collisions (Borysow, 2002). The atmosphere does not have an inverted thermal structure in regions close to the molecular photosphere.

Generation of Simulated Data

In this work, we generated simulated data sets following the framework introduced by Buzard et al. (2020). In short, the stellar and planetary models are scaled by assumed stellar and planetary radii squared and shifted to velocities determined from Equations 4.1 and 4.3. Next, the stellar spectrum is interpolated onto the planetary wavelength axis, and the two models are added. The stellar continuum is removed with a third-order polynomial fit to the combined spectrum from 2.8 to 4 μm in wavenumber space. The spectrum is broadened with a Gaussian kernal fit to real NIRSPEC data. Finally, the spectrum is interpolated onto a NIRSPEC data wavelength axis, saturated telluric pixels from the data (where tellurics absorb more than about 40% of the flux) are masked, and Gaussian noise is added. The masking of saturated telluric removes about 40% of the data. Non-saturated tellurics are assumed to be perfectly corrected.

For these simulations, we assume a 1 $R_{\rm Jup}$ planet and a 1 $R_\odot$ star. Unless otherwise stated, these simulations approximate post-upgrade L band data. The upgraded NIRSPEC instrument was first available in early 2019 (Martin et al., 2018). Across the L band, it doubled the number of pixels per order (from 1024 to 2048), increased the number of usable orders on the chip (from 4 to 6), and nearly doubled the spectral resolution (from ~25,000 to ~40,000). The Gaussian kernals used to broaden the simulated data and wavelength axes with their corresponding locations of saturated telluric pixels were taken from the April 3, 2019 and April 8, 2019 NIRSPEC data of HD187123 presented in Buzard et al. (2020). Each epoch has six orders, covering wavelengths of approximately 2.9331–2.9887, 3.0496–3.1076, 3.1758–3.2364, 3.3132–3.3765, 3.4631–3.5292, and 3.6349–3.6962 μm. The average instrumental resolution is about 41,000. We applied the average S/N per pixel from the April 3, 2019 and April 8, 2019 data of 2860 to each epoch, which resulted in a total S/N per pixel of 6390 for the 5 epoch simulations.

Analysis of Simulated Data

The simulated data sets are analyzed analogously to the data presented in past multi-epoch detection works, e.g., Piskorz et al. (2018), Buzard et al. (2020). A two-dimensional cross correlation, TODCOR as described in Zucker & Mazeh (1994), is used to measure the stellar and planetary velocities at each epoch. Segments of data (e.g., orders and pieces of orders after saturated telluric pixels are masked) are cross correlated separately and converted to log likelihood functions in order to be combined. In this work, we use the Zucker (2003) $\log(L)$ approach to convert cross correlations to log likelihoods; the "Zucker $\log(L)$" approach is described and differentiated from the "Zucker ML" approach in Buzard et al. (2020). This approach converts cross correlations to log likelihoods as

$$\log(L) = -\frac{n}{2}\log(1 - R^2), \tag{4.4}$$

where R is the two-dimensional cross correlation and n is the number of pixels in the data segment.

Once the two-dimensional cross correlation of each epoch is converted to a two-dimensional (stellar and planetary velocity shifts) log likelihood surface, the planetary log likelihood cut is taken from the measured stellar velocity. The measured stellar velocity is always consistent with the expected stellar velocity from Equation 4.1. The planetary log likelihood curves at each epoch are converted from v_{sec}

to K_p space by Equation 4.3, and added. This planetary log likelihood vs. K_p curve is calculated from $-150 \leq K_p \leq 150$ km/s.

4.3 Primary Velocity Simulations

To study how primary velocities and orbital phases affect planetary detectability, we generate sets of simulated data with different combinations of primary velocities and orbital phases. These data sets all consider five epochs and have K_p set at 75 km/s. For these simulated data sets, we allow v_{pri} to range from -30 to 30 km/s, the rough maximum variation given by the Earth's orbital velocity, v_{bary}. We create five different groupings of primary velocities: (1) a most blue-shifted v_{pri} sample, in which the primary velocities at all five epochs are pulled from a uniform distribution from -30 to -28 km/s; (2) an even v_{pri} sample, in which the five primary velocities are evenly spaced from -30 km/s to 30 km/s; (3) a most red-shifted v_{pri} sample, in which the five epochs are pulled from a uniform distribution from 28 to 30 km/s; (4) a near-zero v_{pri} sample in which the five primary velocities are pulled from a uniform distribution from -2 to 2 km/s; and (5) a random v_{pri} sample. For the evenly spaced v_{pri} sample, the five epochs are pulled from uniform distributions covering: -30 to -29 km/s, -16 to -14 km/s, -1 to 1 km/s, 14 to 16 km/s, and 29 to 30 km/s. These slight variations in the most blue-shifted, most red-shifted, even, and near-zero primary velocity groups better resemble actual observations that could be scheduled than if all five large v_{pri} epochs had exactly 30 km/s, for example. For the randomly sampled primary velocity group, we choose the Earth's orbital position from the uniform distribution from 0 to 2π. These positions are then converted to barycentric velocities assuming the maximum barycentric velocity is 30 km/s. This results in a bimodal barycentric velocity distribution that is relatively uniform through the central velocities and increases significantly towards ±30 km/s. We consider a systemic velocity of 0 km/s, so the resulting random primary velocity distribution has the same shape as the barycentric velocity distribution ($v_{pri} = -v_{bary}$). If the systemic velocity were non-zero, the primary velocity distribution would be shifted and the probability would increase towards its maximum ($v_{sys} - \min(v_{bary})$) and minimum ($v_{sys} - \max(v_{bary})$) values. We discuss how this may affect the results of the random primary velocity simulations in Section 4.8. Realistically, systems are not observable from the Earth for the full year. A pull from half of the Earth's orbit (e.g., $v_{\rm bary} = 30\cos(x), 0 \leq x < \pi$) results in the same random primary velocity probability distribution, so we use this moving forward. We contemplate further effects of target accessibility in Section 4.8.

We split combinations of orbital phases, M, up into three groups: (1) all five epochs near conjunction, (2) all five epochs near quadrature, and (3) five epochs evenly spaced around the orbit. The five near-conjunction epochs are pulled randomly from the uniform distributions, 0 ± 0.02 (inferior conjunction) and 0.5 ± 0.02 (superior conjunction), and the quadrature epochs are pulled from the uniform distributions, 0.25 ± 0.02 and 0.75 ± 0.02. The evenly spaced M epochs have one epoch pulled from similarly wide uniform distributions centered on each of 0.05, 0.25, 0.45, 0.65, and 0.85. This is only one example of an evenly distributed set of orbital phases, and we expand the analysis to include other combinations of orbital phases in Section 4.3.

Figure 4.1 shows the results of these combinations of primary velocities and orbital phases, with the five primary velocity groups taking up different subplots, and the three orbital phase groups shown in different colors. For each primary velocity subplot, near-quadrature orbital phases are shown in dark blue, evenly spaced orbital phases in light purple, and near-conjunction phases in green.

Several notable results stand out. First, there is very little structure in any of the simulations that considered all five epochs near conjunction. These simulations show no convincing detections of K_p. This trend makes sense because when the planet is near either inferior or superior conjunction, it will have little to no line-of-sight velocity difference from its star. Regardless of what K_p is, the planet line-of-sight velocity at conjunction will simply be equal to the primary velocity. Conjunction epochs on their own are not useful for constraining the Keplerian orbital velocity through the technique that aims to measure stationary planetary velocities at multiple epochs. This is in contrast to cross-correlation techniques that aim to measure changing planetary velocities (e.g., Snellen et al., 2010; Brogi et al., 2012); they actually prefer conjunction epochs, during which the planetary acceleration is the largest. It is also useful to note that these techniques that target changing planetary velocities would also require higher spectral resolution than the technique that targets stationary planetary velocities.

The simulations with evenly spaced orbital phases and orbital phases near quadrature do have a peak at K_p in all of the primary velocity groups, but there is often large off-peak structure at the same magnitude, if not larger, than the true peak. Both Buzard et al. (2020) and Finnerty et al. (2021) found that at the S/N used in these simulations (> 2500 per pixel per epoch), shot noise has very little effect on the log likelihood surface, and the off-peak structure is due instead to non-random, structured noise.

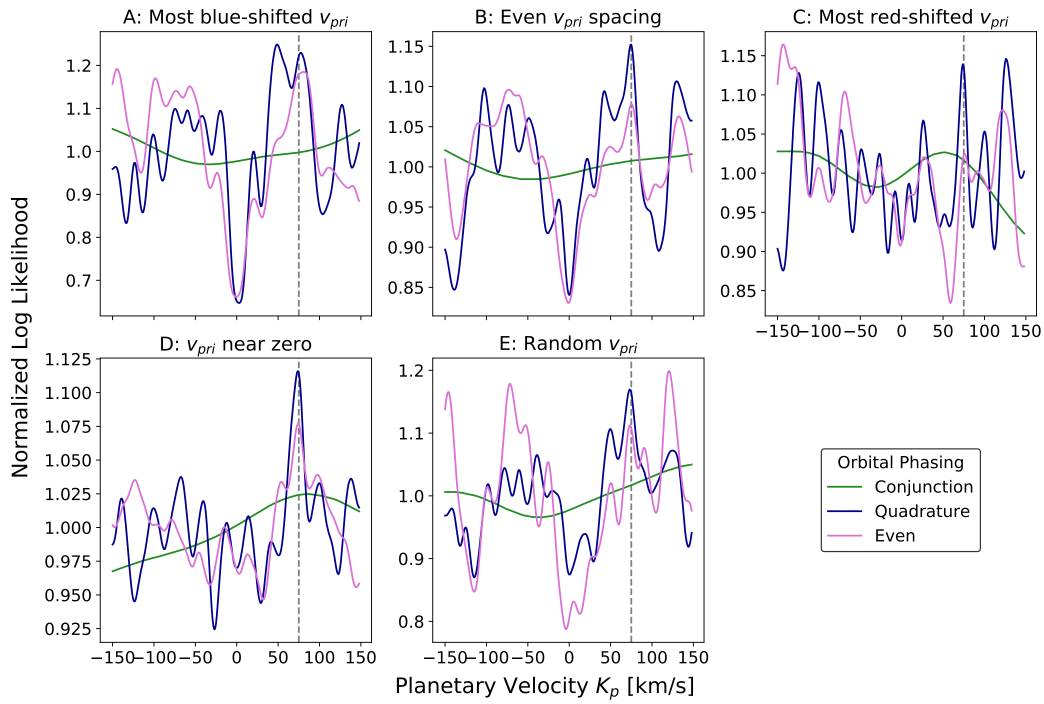

Figure 4.1: Normalized log likelihood functions vs. K_p of 5 epoch simulations with different combinations of primary velocities and orbital phases. The panels show five different groupings of primary velocities: most blue-shifted, evenly spaced, most red-shifted, near-zero, and random. The colors represent different combinations of orbital phases with near conjunction epochs in green, quadrature epochs in dark blue, and epochs evenly spaced around the orbit in light purple. The simulations with primary velocities near zero in each of the five epochs show less structured noise than do simulations with any other combination of primary velocities.

This structured noise is caused by correlation between the planetary spectral model template and the stellar features in the simulated data. Finnerty et al. (2021) removed this structure in their simulations by subtracting a stellar-only log likelihood curve, which comes from simulated data generated with no planetary signal and then cross correlated in the same two-dimensional way with a stellar and a planetary spectral model. This approach can nearly eliminate all of the off-peak structure in simulations, but it would not be as effective on data due to a variety of factors including mismatches between the real and model stellar and planetary spectra and imperfect removal of tellurics from the data. We therefore do not try to remove this off-peak structure. Instead, we look for combinations of primary velocities and orbital phases that can reduce it by design.

Interestingly, we see in Figure 4.1 that the simulations with primary velocities around 0 seem to show stronger peaks at K_p relative to the noise than for the other primary velocity groups. This appears to be true for both the evenly spaced orbital phases and the near quadrature orbital phases. While these simulations consider a planetary spectral model without a thermal inversion, simulations generated and analyzed with a planetary model with an inversion showed a similar trend in that near-zero primary velocity epochs produced the strongest detections.

Random Orbital Phases

In order to investigate whether this trend that epochs taken when the primary velocity of the system is near zero provide stronger detections is more broadly true, we generated five-epoch data sets within each of the five primary velocity sampling groups, but with orbital phases pulled from a uniform distribution from 0 to 1, i.e., the full orbit. These data sets are likely more representative of real data sets that could be obtained from systems of interest too. While the barycentric velocity changes over the course of an Earth year, the orbital phase changes on the time frame of the planet's year. For hot Jupiters, the orbital phase changes significantly from night to night, making it difficult to obtain multiple epochs with the same orbital phase (especially when trying to schedule nights which will provide useful epochs for multiple targets). The primary velocity, on the other hand, will be approximately the same on a monthly timescale. So, simulations with set primary velocities and randomly picked orbital phases might be a good approximation to data sets that could be easily obtained.

We generate 100 sets of five-epoch simulations with randomly chosen orbital phases for each of the five primary velocity groups. We define a parameter, γ, to quantify each combination of orbital phases, as follows.

$$\gamma = \frac{1}{N} \sum_i |\sin(2\pi M_i)|, \tag{4.5}$$

where N is the number of epochs. For epochs at quadrature, $\sin(2\pi M) = \pm 1$, and for epochs at conjunction, $\sin(2\pi M) = 0$. Defined this way, $\gamma = 0$ if all of the epochs are at conjunction and $\gamma = 1$ if all of the epochs are at quadrature.

After analyzing each of the 500 simulations, we attempt to fit Gaussians to the resulting normalized log likelihood curves. We first normalize the curves by subtracting the mean of the curve from -150 to 0 km/s. We choose to normalize by the mean of this range because the way that we define K_p enforces that it must be a positive value, meaning that the log likelihood curve at negative values of K_p must be completely due to structured noise, and not to any real planetary signal. Because

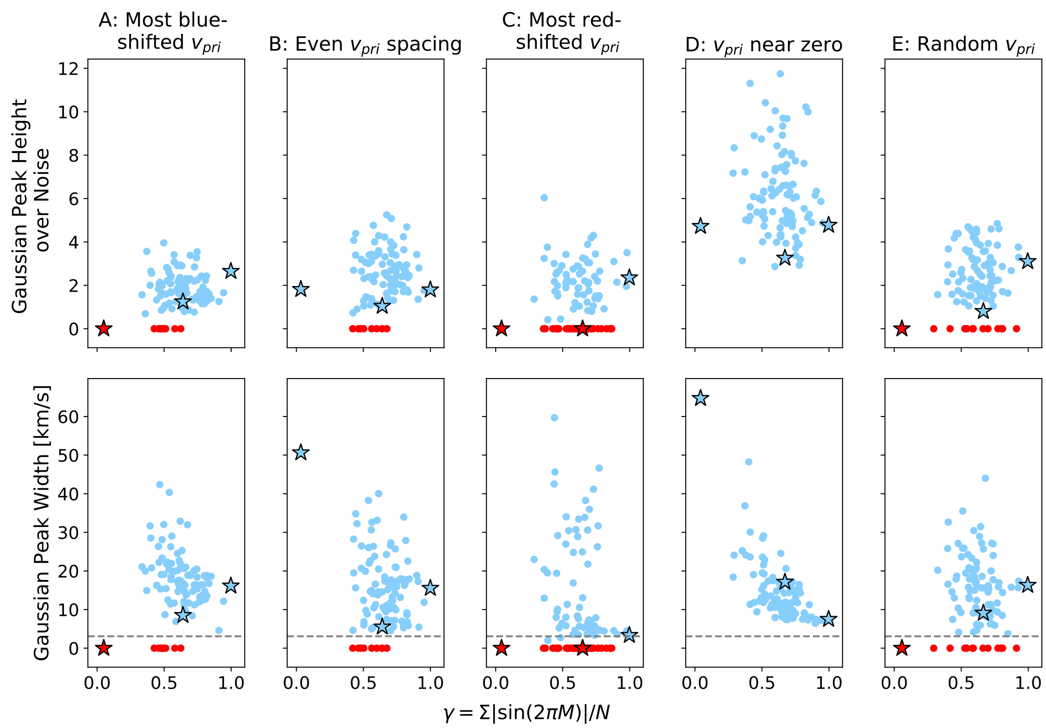

Figure 4.2: Results of Gaussian fits to 100 simulations with randomly selected orbitals phases in each of five primary velocity groups. The top panels plot the heights of the Gaussian fits over the noise level and the bottom panels plot the Gaussian widths. Light blue points represent simulations with detectable planetary peaks and red points at 0 represent simulations with non-detections, in which the Gaussian mean was more than 1σ from the set K_p of 75 km/s. The stars are the Gaussian parameters fit to the simulations in Figure 4.1. The horizontal, gray, dashed line in the Gaussian width plots shows the approximate velocity precision of post-upgrade NIRSPEC, 3.1 km/s. The planet detections made with simulated data sets with 5 near-zero primary velocity epochs are significantly stronger than those made with any other combination of primary velocity epochs. For near-zero primary velocity simulations, epochs near quadrature put much stronger constraints on K_p than do epochs far from quadrature.

the simulated data is generated with a K_p of 75 km/s, we fit Gaussians with an initial mean of 75 km/s, σ of 10 km/s, and height equal to the normalized log likelihood value where K_p = 75 km/s.

The results of these Gaussian fits are shown in Figure 4.2. In the top row, we plot the height of each Gaussian fit over the standard deviation of the curve from -150 to 0 km/s. We use this as a means to show how much stronger the true planetary peak is than the structured noise. In the bottom row are the standard deviations of the Gaussian fits. We plot a blue point for each simulation for which a Gaussian could be fit within 1σ of the true value of K_p, 75 km/s, and a red point at 0 for both of the Gaussian parameters when it could not. The stars are the Gaussian fits to the simulations shown in Figure 4.1.

These results confirm that primary velocity near 0 km/s will generally allow for stronger detections of the planetary signal and more confident measurements of K_p. The planetary peak was detected in all 100 of the near-zero primary velocity cases, but only 91 of the even primary velocity cases, 64 of the most red-shifted primary velocity cases, 90 of the most blue-shifted primary velocity cases, and 86 of the random primary velocity cases. Further, the heights of the Gaussians fits to the near-zero primary velocity cases relative to the noise are much larger, on average, than for any of the other primary velocity cases.

Interestingly, we see no obvious relationship between the γ for a simulation and its peak height over the noise for any of the primary velocity groups. We suspect that at the larger values of γ, near quadrature, the planetary peak becomes resolved, leading to a larger height, but the noise structure also becomes narrower and of larger amplitude, so the increase in the peak height and noise level balance each other out. With the lack of dependence on γ, we can consider the mean and standard deviation of the peak heights over noise. Considering only those simulations in which the planetary peak was detectable, the peak height over noise was 6.2 ± 1.9 for the near-zero primary velocity case, while it was 2.6 ± 1.0 for the even primary velocity case, 2.3 ± 1.0 for the most red-shifted primary velocity case, 1.9 ± 0.7 for the most blue-shifted primary velocity case, and 2.7 ± 1.0 for the random primary velocity case. The simulation results show a significant amount of scatter around these averages, even at a single value of γ, as seen in Figure 4.2. We found no significant relationship between Gaussian height over noise and the mean orbital phase, standard deviation of the orbital phases, or the standard deviation of the $|\sin(2\pi M_i)|$ values, though. We also ran 100 simulations with the same orbital phases (γ = 0.67) and primary velocities (near-zero) to see how much of the scatter could be explained by white noise. The Gaussian heights from these simulations had a standard deviation of only 0.3, less than the scatter in any of the five primary velocity groups. This implies that with S/N of 2860 per pixel per epoch, the structured noise related to the combination of orbital phases dominates over random Gaussian noise. This is consistent with findings from Buzard et al. (2020) and Finnerty et al. (2021).

The lower panels of Figure 4.2 show the widths of the Gaussian fits. The gray dashed line in each subplot shows the average velocity precision of the upgraded NIRSPEC data on which these simulations were based, at 3.1 km/s. The widths of the near-zero primary velocity simulations show an interesting trend. At large values of γ, the widths are quite small and do not have much variation. The widths increase toward intermediate γ values in both magnitude and degree of variation. The representative near-conjunction simulation, shown by the blue star near $\gamma = 0$, has by far the largest width. The trend in width magnitude reflects the fact the conjunction epochs have very little constraining power on K_p while quadrature epochs are the most effective for constraining K_p. The degree of variation in Gaussian width at intermediate values of γ as opposed to large or small values can also be explained. While there is only one combination of epochs each that will give a γ value of 0 (all at conjunction) or 5 (all at quadrature), there are many different combinations of epochs that could result in an intermediate value of γ. For instance, the γ values of 1000 sets of 5 epochs with orbital phases pulled from a uniform distribution from 0 to 1 form an approximately Gaussian shape with a mean of 0.64 and a standard deviation of 0.14. With more cases at intermediate values of γ, there will be more variation as some of them will provide better constraints on K_p than others.

The four primary velocity groups other than the near-zero group do not show the same strong relationship between the Gaussian widths and γ. The most blue-shifted and most red-shifted primary velocity groups do show some evidence of a corner where the widths increase below a certain γ value, but this behavior is not nearly as strong as the trend in the near-zero primary velocity case. We suspect that the higher planetary peaks in the near-zero group are better fit by a Gaussian, meaning that the widths are more representative of the true planetary detection peak than for the other primary velocity groups. This can be corroborated by the mean R^2 value of the detected planetary peaks in each v_{pri} group, which compares the goodness of the Gaussian fit to that of a horizontal line at the mean of the simulated log likelihood curve. The mean R^2 values of the near-zero, most blue-shifted, even, most red-shifted, and random primary velocity groups are 0.69, 0.25, 0.34, 0.24, and 0.36, respectively. The especially low R^2 values of the four primary velocity groups other than the near-zero one reflect the high levels of structured noise. They also support our conjecture that the widths of those four groups show less dependence on γ than the near-zero primary velocity group because the Gaussian fits are not accounting for the planetary peak structure as accurately.

Since neither the most blue-shifted (most negative) nor the most red-shifted (most positive) primary velocity groups were able to strongly detect the planetary signal, going forward, we will refer to both as the "largest absolute primary velocity group." Doing so allows us to focus on the magnitude of velocity separation between the stellar signal and the telluric frame, rather than the direction in which the stellar signal has moved.

Collectively, these results show that a set of 5 epochs with randomly selected orbital phases will have the best chance of showing a strong detection of the planet if they are taken during times when the system's velocity is canceled out by the Earth's velocity in the direction of the system. The closer these epochs are to quadrature, the better the data will be able to constrain the value of K_p. Further, we would expect that obtaining data from both quadrature positions ($M = 0.25$ and 0.75) would be better for constraining K_p than data at just one quadrature position, because having data at both quadrature positions would give us access to different velocity shifts relative to the telluric frame and so collectively more complete wavelength coverage of the planetary spectrum. Finnerty et al. (2021) showed that a larger spectral grasp can drastically increase detection significance; doubling the grasp increased the significance by nearly a factor of 2. These predictions should be useful for the planning of future multi-epoch observations.

4.4 Magnitude of K_p

All simulations presented in Section 4.3 considered data sets generated with a K_p of 75 km/s. We showed that near-zero primary velocity epochs allow for the strongest planetary detections. However, we might expect to encounter a challenge, especially as K_p decreases, with setting the primary velocity to 0, or in other words, allowing very little velocity shifting between the stellar and telluric spectra. If the stellar spectrum is not velocity shifted relative to the telluric spectrum, as K_p decreases, the planetary lines will not be able to stray much from the telluric spectrum either.

The value of K_p is set by both the semi-major axis and the orbital inclination. A decrease in K_p due to a larger semi-major axis would be accompanied by a colder planetary effective temperature, while a decrease in K_p solely due to a smaller inclination would not affect the planetary temperature. While either decrease in K_p would limit the separation between planetary and telluric lines in near-zero primary velocity epochs, cooler planetary atmospheres could further complicate the issue. While hot Jupiter L band spectra are dominated by water features, their water is much hotter ($\gtrsim$ 1000 K) than water in the telluric spectrum ($\sim$ 300 K), resulting in very different spectral line shapes, position, and relative contrast. However, as the planetary effective temperature decreases, its spectrum will more and more resemble that of the Earth's. Then, with neither very different temperatures altering the shape of the planetary spectrum from the telluric spectral shape or much velocity shifting off of the telluric spectrum, primary velocity near-zero epochs may no longer be as useful. Such cool planets will require large epoch number data sets to be detected.

To test how varying K_p affects our simulation results, we generate 100 simulations with near-zero primary velocities and randomly selected orbital phases with K_p values of 37.5, 75, and 150 km/s. We maintain a common planetary effective temperature in order to examine the effects on hot Jupiter detectability with a changing orbital inclination, not on the detectability of planets with different effective temperatures due to different semi-major axes. In analyzing these simulated data sets, we calculated the planetary log likelihoods vs. K_p from -250 $\leq K_p \leq$ 250 km/s to allow for sufficient parameter space to robustly constrain the 150 km/s detections.

Figure 4.3 shows the Gaussian heights relative to the noise and the Gaussian widths of these simulations. Of all 300 simulations, only one of the K_p = 37.5 km/s cases was unable to fit the peak within 1σ.

We used a Kolmogorov–Smirnov (KS) test to determine whether there was any statistical difference between the Gaussian heights over noise and widths of the sets of simulations with different values of K_p. Two-tailed p-values between the γ values of the 37.5, 75, and 150 km/s simulations were 0.68 (37.5 vs. 75 km/s), 0.34 (37.5 vs. 150 km/s), and 0.34 (75 vs. 150 km/s). None of these p-values are small enough to justify rejecting the null hypothesis that the 100 γ values of each of the K_p cases were pulled from the same distribution. We know the null hypothesis to be true in this case; all 300 γ values were pulled from the same distribution, the conversion of the 5 M values uniformly pulled from 0 to 1 through Equation 4.5. This result then helps to validate the use of the KS test.

The KS p-values between the Gaussian heights over noise were 0.0030 (37.5 vs.

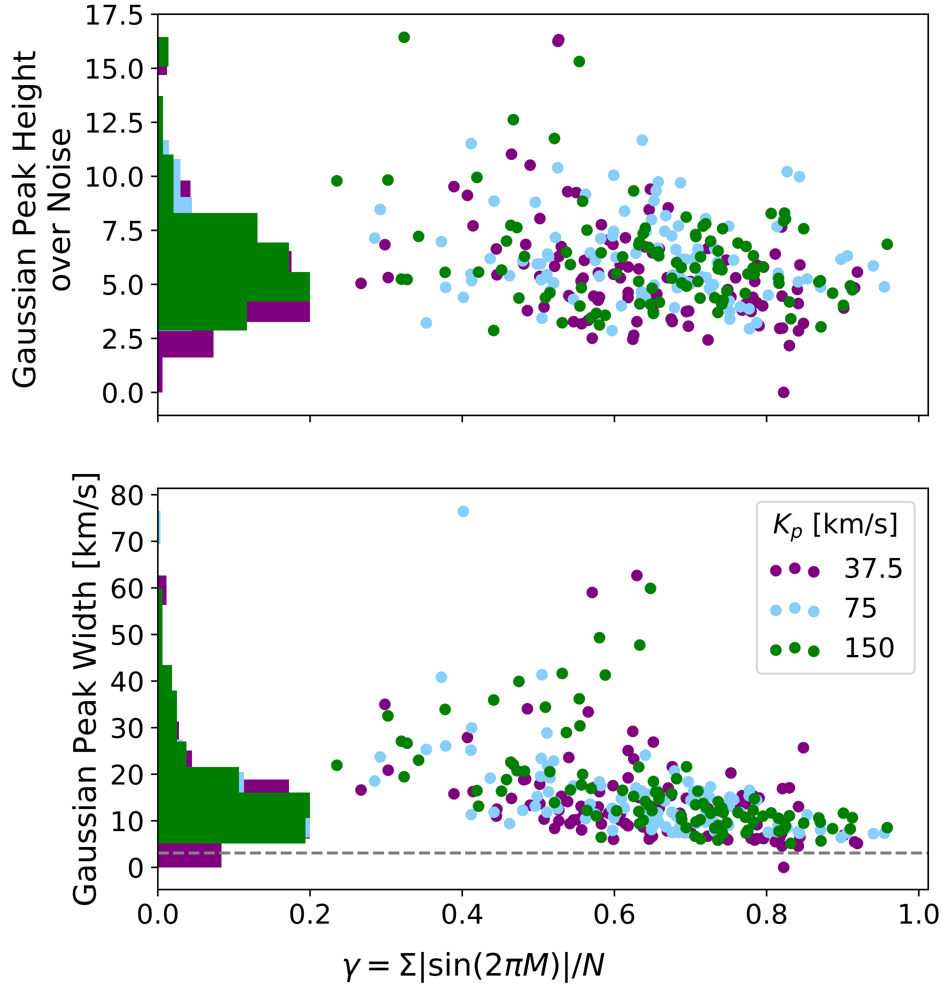

Figure 4.3: Results of Gaussian fits to simulations with near-zero primary velocities, a random selection of 5 orbital phases, and different values of K_p. Points in purple represent simulations with a K_p of 37.5 km/s, light blue points have a K_p of 75 km/s, and green points have a K_p of 150 km/s. Of the 300 simulations, only one was unable to detect the planetary signal; it was one of the K_p = 37.5 km/s simulations.

75 km/s), 0.031 (37.5 vs. 150 km/s), and 0.89 (75 vs. 150 km/s). The Gaussian width p-values were 0.031 (37.5 vs. 75 km/s), 0.069 (37.5 vs. 150 km/s), and 0.56 (75 vs. 150 km/s). The peak heights and widths of the 75 and 150 km/s cases can both be assumed to be pulled from the same parent distributions. On the other hand, KS tests reject the hypotheses that the 37.5 km/s heights are pulled from the same parent distribution as the 75 km/s heights at the 3.0σ level and from the same parent distribution as the 150 km/s heights at the 2.2σ level. They reject a common parent distribution between the 37.5 and 75 km/s Gaussian widths at the 2.1σ level and between the 37.5 and 150 km/s widths at the 1.8σ level. While these levels of statistical rejection of the null hypotheses are mostly in the "weak" to "moderate" support categories (e.g., Gordon & Trotta, 2007), when considered alongside the means and standard deviations of the Gaussian heights of each distribution, they do start to show weaker planetary detectability at lower values of K_p. The 37.5, 75, and 150 km/s sets of simulations have average Gaussian peak heights over the noise level of 5.5 ± 2.4, 6.2 ± 1.9, and 6.2 ± 2.3, respectively. While the 37.5 km/s peak heights were moderately lower than the 75 km/s and 150 km/s peak heights here, they are still on average significantly higher than the 75 km/s peak heights measured from the primary velocity groups not near zero, as described in Section 4.3.

For hot planets, we find that near-zero primary velocity epochs allow for stronger detections than other combinations of primary velocities even as K_p gets quite small. This result may be challenged as we look to cooler planetary atmospheres which will have a higher degree of spectral similarity to our own telluric spectrum.

4.5 Comparison to Data

We were interested to test whether our prediction that epochs with primary velocities near zero would give stronger detections than other samples of primary velocities would hold up against previous NIRSPEC observations. NIRSPEC has been used to obtain multi-epoch detections of exoplanets dating back to 2011; the first set of which were published by Lockwood et al. (2014) (Tau Boo b). Unfortunately, there are not enough NIRSPEC epochs for any one system to be able to test the effectiveness of different primary velocity groupings. Therefore, in order to test our predictions, we combine epochs from different targets. From our archive of NIRSPEC observations, we compile the five epochs with the primary velocities nearest zero and the five epochs with the largest absolute primary velocities (which happen to all be in the "most blue-shifted"/most negative category). These epochs are from Tau Boo b, HD187123b, 51 Peg b, and KELT2Ab. All of these planets are on orbits that can be approximated as circular.

In order to combine all epochs we need to perform a change-of-base so that the epochs reflect a single Keplerian line-of-sight orbital velocity K'_p. We denote all true parameters from the different systems without a prime, and all parameters of the fictitious combined system with a prime ($'$). The primary (v_{pri}) and secondary (v_{sec}) velocities are encoded in the data and so cannot be altered. For a single system, v_{pri} is variable because of the changing barycentric velocity in the direction of the system, but here, the variability in v_{pri} can account for both changing barycentric velocities, and the different systemic velocities of the different targets. K'_p must be large enough to account for all the values of $v_{sec} - v_{pri}$; we set it to 150 km/s. Then, rearranging Equation 4.3 for the secondary velocity, we get

$$M' = \frac{1}{2\pi} \arcsin \frac{v_{sec} - v_{pri}}{K'_p}. \tag{4.6}$$

Table 4.1 gives the true parameters (K_p, P, T_o, v_{sys}) from the four target systems. Table 4.2 gives the information about the specific dates we are considering. Because these systems have different expected stellar and planetary spectra, we use different spectral templates to cross correlate each epoch of data, and then use the new change-of-base M' values to combine the log likelihood curves generated from the two-dimensional cross correlations. The data reduction and stellar and planetary spectral template used for cross correlation for each of the sources is described in the Appendix. The five log likelihood curves that make up the two primary velocity groups are shown in Figure 4.9.

Aside from the different planetary and stellar spectral models used for each epoch, there are a few other differences between these combinations of data epochs and the predictions for the near-zero and largest absolute primary velocity groups in Section 4.3. First, all 10 of the data epochs were taken prior to the NIRSPEC upgrade, while the simulations considered post-upgrade NIRSPEC specifications. These differences affect the total S/N, the instrument resolution, wavelength coverage, and wavelength range covered (see Appendix). Second, the primary velocity groups are not defined as strictly here as they were in Section 4.3. This is simply due to the availability of data epochs. While the near-zero primary velocity group in Section 4.3 chose primary velocities from -2 to 2 km/s, the data near-zero primary velocity group have primary velocities ranging from -11.9 to 1.3 km/s. The simulated largest absolute (most blue-shifted/most negative) primary velocity group pulls v_{pri}

Table 4.1: Target Information

Target	K_p [km/s]	K_p Ref.	Period [days]	Period Ref.	T_0 [JD]	T_0 Ref.	v_{sys} [km/s]	v_{sys} Ref.
HD187123	53 ± 13	(1)	$3.0965885^{+0.0000051}_{-0.0000052}$	(1)	$2454343.6765^{+0.0064}_{-0.0074}$	(1)	-17.046 ± 0.0040	(7)
Tau Boo	111 ± 5	(2)	3.312433 ± 0.000019	(3)	2455652.108 ± 0.004	(3)	-16.03 ± 0.15	(9)
KELT2A	148 ± 7	(4)	4.1137913 ± 0.00001	(5)	$2455974.60338^{+0.00080}_{-0.00083}$	(5)	-47.4 ± 0.6	(8)
51 Peg	$133^{+4.3}_{-3.5}$	(6)	$4.2307869^{+0.0000045}_{-0.0000046}$	(6)	2456326.9314 ± 0.0010	(6)	-33.165 ± 0.0006	(7)

Note – We assume circular orbits for all of these targets.

Refs – (1) Buzard et al. 2020, (2) Lockwood et al. 2014, (3) Brogi et al. 2012, (4) Piskorz et al. 2018, (5) Beatty et al. 2012, (6) Birkby et al. 2017, (7) Gaia Collaboration et al. 2018, (8) Gontcharov 2006, (9) Nidever et al. 2002

Table 4.2: Epoch Information

Target	Obs. Date	t_{obs} [JD]	v_{bary} [km/s]	v_{pri} [km/s]	M	v_{sec} [km/s]	M'[a]
Primary Velocity Near Zero							
Tau Boo	2011, May 21	2455702.85	-17.34	1.31	0.319	102.08	0.117
HD187123	2013, Oct 27	2456592.76	-17.44	0.40	0.310	49.70	0.053
HD187123	2013, Oct 29	2456594.74	-17.50	0.45	0.949	-16.27	0.982
51 Peg	2013, Nov 07	2456603.86	-21.27	-11.90	0.455	25.46	0.040
HD187123	2017, Sep 07	2458003.77	-10.15	-6.90	0.977	-14.45	0.992
Largest Absolute Primary Velocities							
51 Peg	2011, Aug 10	2455783.96	15.77	-48.94	0.661	-161.73	0.865
51 Peg	2014, Sep 04	2456905.04	5.43	-38.59	0.643	-142.49	0.878
KELT2A	2015, Dec 01	2457357.89	11.77	-59.18	0.256	88.70	0.223
KELT2A	2015, Dec 31	2457387.97	-3.62	-43.77	0.567	-104.39	0.934
KELT2A	2016, Dec 15	2457738.10	4.79	-51.68	0.680	-185.65	0.824

[a] M' is the orbital phase, M, reflecting the change-of-base to $K_p' = 150$ km/s so that the epochs can be combined.

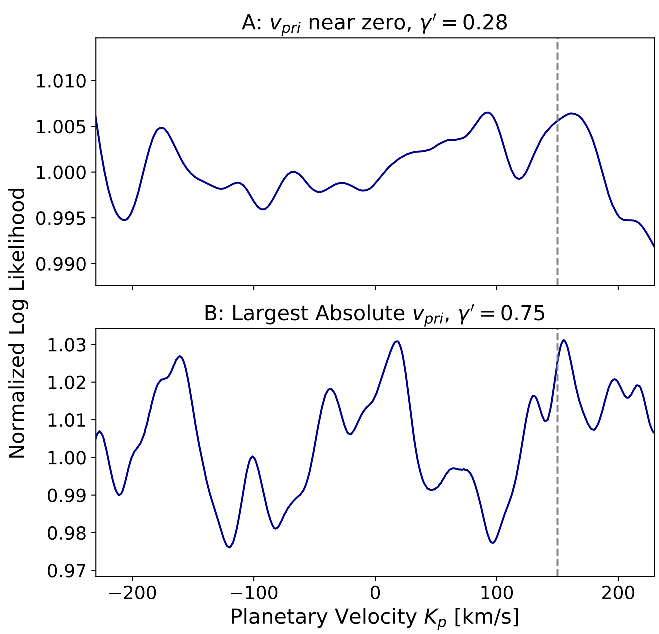

Figure 4.4: Normalized log likelihood vs. K_p from pre-upgrade NIRSPEC data epochs. The top panel shows the combination of 5 epochs with primary velocities nearest zero and the bottom panel shows the combined epochs with the largest absolute primary velocities.

values from -30 to -28 km/s, while the data's largest absolute primary velocity group ranged from -59.2 to -38.6 km/s.

In Section 4.4, we found no statistical difference between the Gaussian heights relative to the noise or Gaussian widths of the sets of simulations with K_p values of 75 vs. 150 km/s. Therefore, the fact that these data are set up with a K_p of 150 km/s should not be one of the factors differentiating these results from the K_p = 75 km/s simulations.

Figure 4.4 shows the normalized log likelihoods of the five epochs with primary velocities near zero and the five epochs with the largest absolute primary velocities. When fit with Gaussians in the same way as the analysis shown in Figures 4.2 and 4.3, the primary velocity near-zero case can be fit by a Gaussian at 157 ± 15 km/s with a height over the noise of 1.7, while the largest absolute primary velocity case fit gives a value of 180 ± 34 km/s with a height over the noise of 1.4.

We calculate γ' values for the data combinations of epochs as 0.28 for the near-zero primary velocity group and 0.75 for the largest absolute primary velocity group. While the near-zero primary velocity case has a lower γ' value, its fit is slightly more accurate and higher relative to the noise than the largest absolute primary velocity case.

We ran simulations with the exact primary velocities and Ms (and γs) from the data near-zero and largest absolute primary velocity groups to determine (1) if the primary velocity groups still showed a similar trend when they were not defined as strictly as in the simulations in Section 4.3, (2) if the near-zero primary velocity epochs were more effective with pre-upgrade NIRSPEC settings as well as with post-upgrade NIRSPEC settings, and (3) if this trend in the data is based on the different combinations of epoch orbital phases or can be assigned to primary velocity differences. For these simulations, we only consider a single planetary and stellar spectral model, defined in Section 4.2, for each epoch. Thus, we do not expect them to appropriately reproduce the off-peak structure in Figure 4.4, but they should allow us to answer the questions listed above.

The results of the simulations are shown in Figure 4.5, with the primary velocities and orbital phases of the data in the top panel. We show these simulated log likelihood curves with separate y-axes because the structured noise in the largest absolute primary velocity simulation is at a much higher level than that in the near-zero primary velocity case. Gaussian curves find fits for the near-zero v_{pri} and Ms

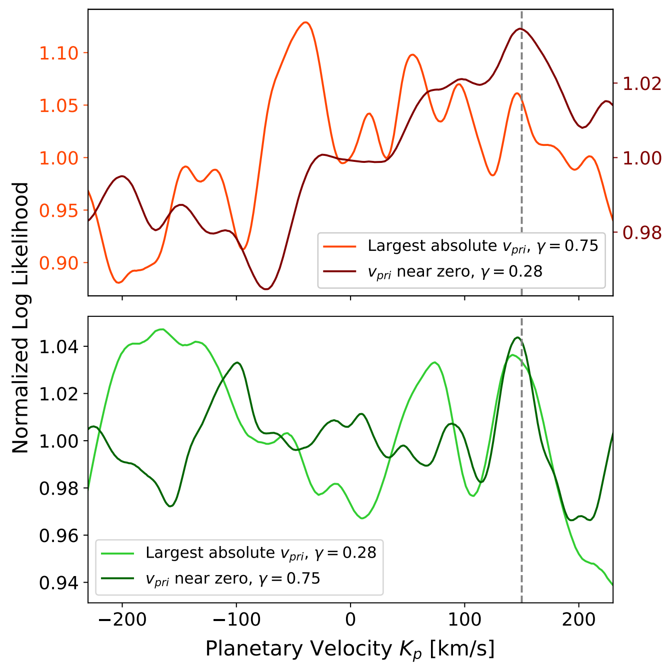

Figure 4.5: Results of simulations with the primary velocities and orbital phases of the data epochs combined in Figure 4.4. The top panel has the correct grouping of primary velocities and orbital phases and the bottom panel swaps the primary velocities and orbital phases to test whether the difference in detection strengths can be said to be mostly from the different primary velocity groups or whether the combination of orbital phases also had a large effect on the detection strengths. Unlike Figures 4.1–4.3 and 4.6, these simulations are for pre-upgrade NIRSPEC data.

(in maroon) of 138 ± 81 km/s with a height relative to the noise of 4.4 and the largest absolute v_{pri} and Ms (in orange) of 36 ± 79 km/s with a height of 1.1, which would not be considered a detection as it is more than 1σ away from 150 km/s. These simulations then do indeed agree that the data near-zero primary velocity epochs have a better chance of detecting the planet. This validated that the near-zero v_{pri} epochs are more effective with both pre- and post-upgrade NIRSPEC and that they are still preferable to larger absolute value primary velocity epochs even if not as strictly defined to $-2 \leq v_{pri} \leq 2$ km/s.

We do note that the simulations predict a much larger improvement going from the largest absolute primary velocity case to the near-zero primary velocity case (1.1 to 4.4) than was seen in the data (1.4 to 1.7). Recall that the simulated data sets are generated assuming that all non-saturated tellurics can be perfectly corrected. This is likely not the case in the real data. Because the planetary velocities are closer to the telluric frame in the near-zero primary velocity group (both because

Table 4.3: Gaussian Fits to Data

Type	v_{pri} Group	γ	μ	σ	A
Data	Near Zero	0.28	157	15	1.7
Data	Largest Absolute	0.75	180	34	1.4
Simulation	Near Zero	0.28	138	81	4.4
Simulation	Near Zero	0.75	146	9	3.3
Simulation	Largest Absolute	0.28	145	10	1.0
Simulation[a]	Largest Absolute	0.75	36	79	1.1

[a]This would be considered a non-detection because the set K_p' of 150 km/s is more than 1σ from the Gaussian mean.

of the near-zero primary velocities themselves and because of the smaller γ, see Table 4.2), the planetary spectral lines are closer to the corresponding telluric lines than in the largest absolute primary velocity group. The L band wavelengths covered are dominated by water features at hot Jupiter temperatures, and while this water is much hotter than telluric water, the closer overlap between its features and the imperfectly corrected telluric water features could be responsible for hampering the near-zero primary velocity case detection significance in the real data.

Using these simulations, we next test whether the improvement of the primary velocity near-zero epochs over the largest absolute primary velocity epochs was in fact due to the primary velocity differences, or if it was made by the different combinations of orbital phases. To do so, we ran simulations with the primary velocities and orbital phases of the data swapped. The results of these swapped simulations are in the lower panel of Figure 4.5. The simulation with the near-zero primary velocities but orbital phases of the largest absolute primary velocity epochs (in dark green) can be fit as 146 ± 9 km/s, with a relative height of 3.3 and the simulation with the largest absolute primary velocities but the near-zero orbital phases (in light green) was fit as 145 ± 10 km/s and a height over noise of 1.0. These simulations would both qualify as detections, but the one with near-zero primary velocities is stronger. Table 4.3 lists the Gaussian parameters of the two data and four simulated log likelihood curves.

Figure 4.2 saw no real trend in the Gaussian heights relative to the noise as a function of γ in any of the primary velocity groups. This is seen in the data simulations as well. The near-zero primary velocity data epochs had orbital phases corresponding to a γ of 0.28, while the largest absolute primary velocity data epochs had orbital phases corresponding to a γ of 0.75. The data near-zero primary velocities gave a Gaussian height of 4.4 when combined with the γ = 0.28 orbital phases vs. 3.3 with the γ = 0.75 epochs. The largest absolute data primary velocities showed a height relative to the noise of 1.0 with the γ = 0.28 epochs and was not detected with the γ = 0.75 epochs. These results support our finding that the primary velocities of the data epochs had a stronger effect on the detection strength than the positions of the orbital phases. It could be that the velocity separation given by epochs far from conjunction will be important though, especially for near-zero primary velocity epochs, when residual telluric features cannot be perfectly corrected from the data.

Figure 4.2 also showed a fairly significant correlation between increasing γ and decreasing Gaussian width in the near-zero primary velocity group. This too is found in these new data simulations: the near-zero primary velocities found a Gaussian width of 81 km/s for a γ = 0.28 data set and 9 km/s for γ = 0.75.

4.6 Number of Epochs

The simulations thus far have all considered 5 epochs of data. We were interested to see what increasing the number of simulations would do to the detection strengths of the different primary velocity groups. To do this, we compared the random and near-zero primary velocity groups with 5, 10, and 20 epochs. We maintain a constant total S/N per pixel in a simulation across all of the epochs. The S/N per epoch then decreases with increasing epoch number from 2860 (5 epochs), to 2020 (10 epochs), to 1430 (20 epochs). Figure 4.6 shows the results of these epoch number simulations, with near-zero primary velocity epoch simulations shown in light blue and random primary velocity epoch simulations shown in green. These Gaussian results are plotted with respect to γ.

Of the six groups (near-zero and random primary velocity groups with 5, 10, and 20 epochs), all simulations were able to detect the planetary signal except 14 of each the 5- and 10-epoch random primary velocity simulations. The mean Gaussian heights over noise of the detected planetary signals for the near-zero primary velocity groups are 6.2 ± 1.9, 8.2 ± 2.3, and 8.9 ± 2.3, for the 5, 10, and 20 epoch simulations, respectively. For the random primary velocity epochs, the means are 2.7 ± 1.1 for the 5 epoch case, 2.6 ± 1.1 for the 10 epoch case, and 2.8 ± 0.8 for the 20 epoch case. Interestingly, we see that the two populations actually appear to diverge as the number of epochs increases, rather than converge as we had expected. The random primary velocity simulations maintain a similar Gaussian height over noise as the number of epochs increases. KS statistics tell us that the 5 and 10 epoch random primary velocity results can be assumed to have been pulled from the same distribution with very high confidence ($p = 0.89$). The 20-epoch random v_{pri} group can be assumed to be pulled from a different distribution from each of the 5- and 10-epoch random v_{pri} groups at a 3.7σ confidence level. We can see in Figure 4.6, and in the reported mean, that the 20-epoch simulations have much less variance in peak height over noise than the 5- and 10-epoch random v_{pri} populations. Visually, and through the reported means, unlike the random primary velocity cases, the near-zero primary velocity heights over the noise increase from 5 to 10 epochs, and then seem to stabilize from 10 to 20 epochs. While the 5 and 10 epoch near-zero simulation heights can be said to be from different parent distributions at a 5.4σ confidence level, the 10 and 20 epoch near-zero distributions are only distinct at a 2.3σ confidence level. As we will address later, these values do not account for the fact that in addition to being generated from simulations with different numbers of epochs, these heights are apparently pulled from different γ distributions. If this were accounted for, we would expect even more commonality between the near-zero heights from 10- and 20-epoch simulations.

If we compare the Gaussian heights over the noise level from the random and near-zero primary velocity groups at 5, 10, and 20 epochs, respectively, we find that two-tailed p-values measured from the Kolmogorov–Smirnov statistic decrease from 5.1×10^{-30} with 5 epochs to 2.8×10^{-40} with 10 epochs to 9.5×10^{-44} with 20 epochs. While the heights of planetary detections resulting from the random and near-zero primary velocity groups can always be said to be pulled from statistically distinct populations, the level at which this claim can be made increases by orders of magnitude as the number of epochs in the simulation increases. The larger jump from the 5 to 10 epoch p-values versus the 10 to 20 epoch p-values reflects the leveling off of the peak heights over noise from 10 to 20 epochs.

As in Figure 4.2, the near-zero primary velocity groups widths, at every number of epochs, show a decreasing trend in both magnitude and variability with increasing γ. The random primary velocity group widths do not show this trend as strongly, likely indicative of the Gaussian models not fitting the planetary peak structure as well as in the near-zero primary velocity case.

Another thing we see in Figure 4.6 is that as the number of epochs increases, the distribution of γ values narrows. In fact, while the mean γ distribution across 1000 5-epoch simulations would be 0.64 ± 0.14, for 1000 10- and 20-epoch simulations, it would be 0.64 ± 0.10 and 0.64 ± 0.07, respectively. We might then expect the distribution of random primary velocities to be narrowing with increasing epoch number too. To see this directly, we can define a parameter β that quantifies the combination of primary velocities in a simulation, similarly to how γ quantifies the combination of orbital phases.

$$\beta = \frac{1}{30N} \sum |v_{pri}|. \tag{4.7}$$

We divide by 30 to normalize by the maximum absolute primary velocity of our simulation. Then, the mean of 1000 β values for 5, 10, and 20 epoch simulations would be 0.63 ± 0.14, 0.64 ± 0.09, and 0.64 ± 0.07 as well. This could explain why the random primary velocity simulations do not benefit from more epochs to the same extent that the near-zero primary velocity epochs do. As the number of epochs increases, the β distribution from which the random primary velocities are drawn is increasingly pulled away from the optimal near-zero case. While the heights of the Gaussian peaks from the near-zero primary velocity group increase from 5- to 10-epoch simulations, the 10-epoch random primary velocity simulations would have a slightly worse placement of primary velocities than the 5-epoch case. The larger number of epochs and worse placement balance each other out so that the Gaussian heights remain comparable at different epoch numbers.

From these analyses, we have seen that the average planetary detection from near-zero primary velocity epochs grew by a factor of 1.3 from 5- to 10-epoch simulations and nearly leveled out from 10- to 20-epoch simulations. The planetary detectability from random primary velocity epochs was nearly comparable at 5, 10, and 20 epochs, though there were no non-detections with 20-epoch simulations and a 14% non-detection rate at 5 and 10 epochs. As we saw above, the near-zero primary velocity epochs can be better modeled by a Gaussian than the random primary velocity epochs, and, as a result, their Gaussian widths show a stronger dependence on γ.

4.7 Stellar Properties

We next investigated how the properties of the host star affect the optimal primary velocity observing strategies. Could it be that the near-zero primary velocity observing strategy works well with the 5815 K stellar model assumed because this star has strong lines corresponding to strong telluric features that are removed by telluric masking when these spectra are aligned? If so, will the near-zero primary velocity observing strategy be as effective for other stellar temperatures? To test the generalizability of the near-zero primary velocity approach, we ran 100 near-zero and 100 random primary velocity simulations with five stellar models ranging from

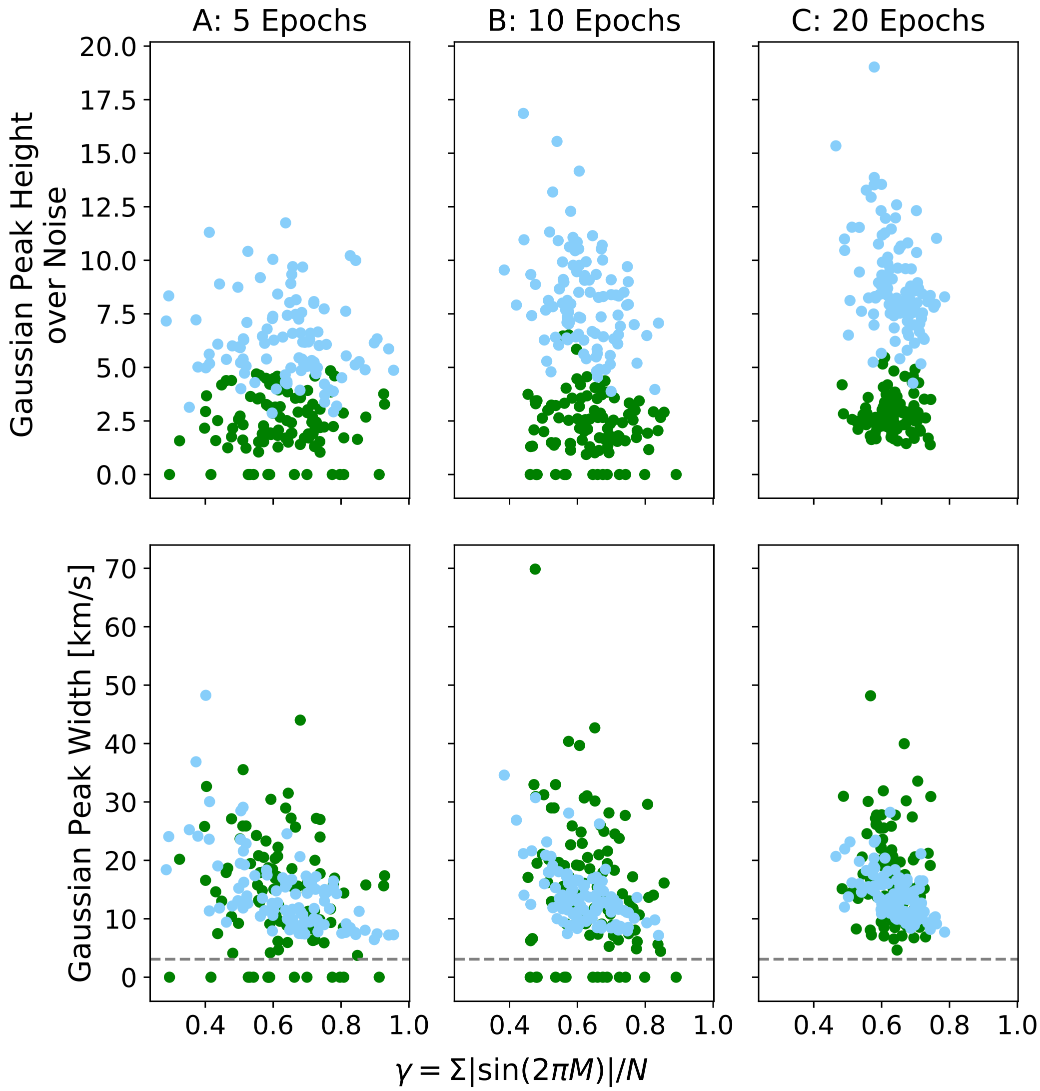

Figure 4.6: Results of Gaussian fits to 5-, 10-, and 20-epoch simulations with random and near-zero primary velocities and random orbital phases. The near-zero primary velocity simulations are shown in light blue and the random primary velocity simulations are shown in green. Of the 600 simulations, only 14 of the 5-epoch and 14 of the 10-epoch random primary velocity simulations were unable to detect the planetary signal.

5200 to 7500 K, to cover the F and G spectral types. We increased the stellar radius along with the temperature, but maintained a constant metallicity and surface gravity. We also used the same planetary model in each case. Results from these simulations are outlined in Table 4.4 and shown in Figure 4.7.

These simulations reveal some interesting trends. They show that the near-zero primary velocity approach becomes even more beneficial when targeting hot Jupiters around late G-stars with lower temperatures, but less so for hot Jupiters around hotter stars. This could be due to a number of factors. Cooler stars have much more complex spectra which could allow for more improvement from well-chosen alignments of stellar and telluric features. They also have more spectral similarity with both their planets and the Earth. Water signatures arising in cooler stars could add to the need for carefully chosen, near-zero primary velocity epochs. Hotter stars, on the other hand, with fewer lines, will not be as affected by velocity shifts relative to the telluric frame.

We also see quite a similarity between the heights derived from the random primary velocity cases across stellar temperatures and radii. This shows that there is a well-balanced trade-off between more complex stellar spectra at lower stellar temperatures and lower planet/star contrast at higher stellar temperatures.

These simulations indicate that the primary velocity trends observed in this work will be increasingly important to the study of hot Jupiters around cooler stars. We encourage future work into how more appropriate planet populations for each host stellar temperature and radius inform optimal high-resolution, cross-correlation observing strategies.

4.8 Discussion

Applicability of Near-Zero v_{pri} Observing Strategy

We have seen that epochs during which the primary velocity is near zero, or, equivalently, the systemic velocity is canceled as much as possible by the barycentric velocity in the direction of the system so there is very little velocity separation between the telluric and stellar spectra, provide the strongest planetary detections. Not all systems will have periods during which the primary velocity is near zero however. The magnitude of the barycentric velocity, determined by a system's right ascension and declination, must be large enough to cancel out its systemic velocity. The second Gaia data release DR2 (Gaia Collaboration et al., 2016, 2018) published radial velocities averaged over 22 months from 7,224,631 stars. These reported

Table 4.4: Stellar Temperature Simulation Results

Temperature [K]	Radius [$R_\odot$]	Near-zero		Random		p-value[a]	$n\sigma$[a]
		% detected	Peak Height/Noise	% detected	Peak Height/Noise		
5200	1.0	100	7.0 ± 2.4	75	2.8 ± 1.7	9.3×10^{-31}	
5775	1.1	99	5.4 ± 1.6	82	2.3 ± 1.0	5.1×10^{-30}	
6350	1.2	100	5.0 ± 2.3	84	2.4 ± 1.0	3.6×10^{-27}	
6925	1.3	96	4.8 ± 1.9	81	2.8 ± 1.4	3.7×10^{-12}	6.9
7500	1.4	75	3.5 ± 1.9	78	2.3 ± 0.9	3.2×10^{-4}	3.6

[a]The p-value and $n\sigma$ come from two-tailed KS tests run between the near-zero and random primary velocity simulations with the same stellar properties. $n\sigma$ refers to the level at which we can reject that the two groups are pulled from the same parent distribution. Below a p-value of $\sim 10^{-16}$, the confidence level that the populations are distinct approaches ∞.

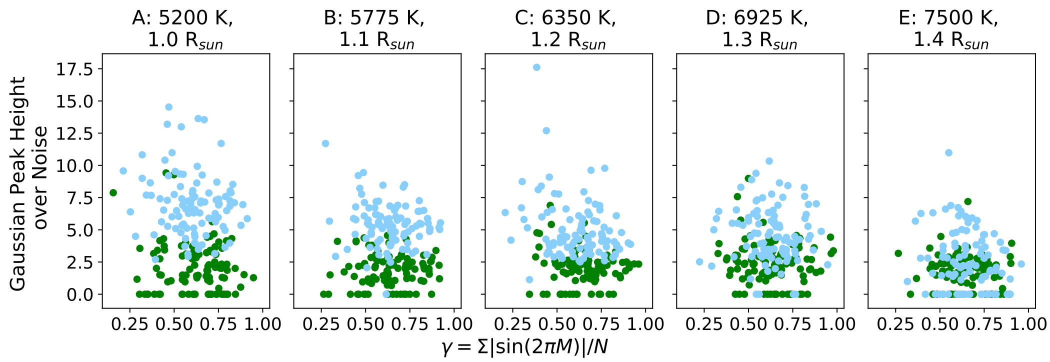

Figure 4.7: Results of 5-epoch simulations with different host stellar temperatures and radii. Near-zero primary velocity simulations are shown in light blue and random primary velocity simulations are shown in green. The numerical results are reported in Table 4.4.

radial velocities were all from sources brighter than $G_{RVS} = 14$ (the flux measured in the Radial Velocity Spectrometer G band); with a fraction of transits where the source was detected as having a double-lined spectrum less than 0.1 (to remove detected double-lined spectroscopic binaries); with an uncertainty on the radial velocity below 20 km/s; and a spectral template used to derive the radial velocity with an effective temperature from 3550 to 6900 K (Gaia Collaboration et al., 2018). This was a substantial and collaborative effort and many researchers contributed to this impressive radial velocity data set (e.g., Cropper et al., 2018; Sartoretti et al., 2018; Soubiran et al., 2018; Katz et al., 2019).

Of the 7,224,631 stars with radial velocities reported in Gaia DR2, 3,209,212, or 44.4%, have combinations of locations and systemic velocities that will allow for a near-zero primary velocity at some point during the year. This then suggests that our predicted optimal near-zero primary velocity strategy will then be applicable to nearly half of the planetary systems in the sky.

Factors Influencing the Random Primary Velocity Distribution

In this work, to define the random primary velocity distribution, we pulled uniformly from the Earth's orbit, converted the Earth's position to a barycentric velocity assuming an orbital motion of 30 km/s, and then converted to primary velocity assuming a systemic velocity of 0. This resulted in a bimodal primary velocity distribution that was relatively flat through the center and rose quickly in probability toward ±30 km/s (Figure 4.8). It was this distribution from which we pulled "random" primary velocities.

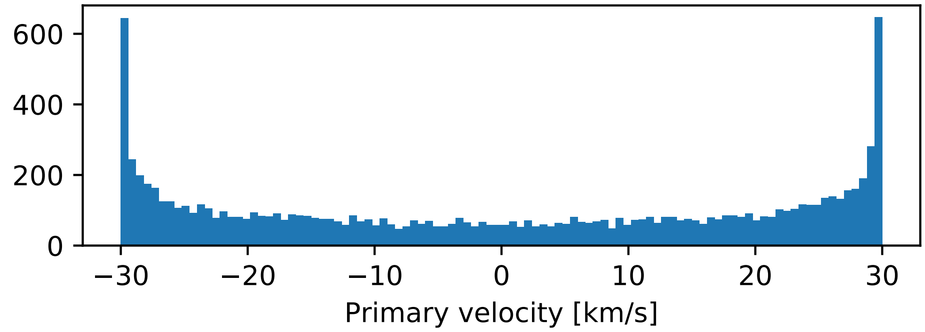

Figure 4.8: "Random" primary velocity distribution generated from 10,000 uniform pulls of Earth's orbital position.

This distribution could be different for different systems depending on their right ascensions, declinations, and systemic velocities, though. Their RAs and DECs will determine the component of the Earth's orbital motion that is in the line-of-sight to the system. While 30 km/s is about the Earth's actual orbital velocity, the barycentric velocity in the direction of a system would only vary from 30 to -30 km/s if the system were precisely on the Earth's orbital plane. Anywhere else and the range of possible barycentric velocities would shrink. A smaller range of primary velocities—if the systemic velocity was still 0 km/s and so the primary velocity range still centered around 0 km/s—might allow for slightly stronger detections than the random primary velocity simulations shown in this work. This would be because the random primary velocity distribution would have a smaller horizontal extent, so the values pulled would be nearer the optimal 0 km/s.

Systems with non-zero systemic velocities would also have a differently shaped random primary velocity distribution than the one used in this work. The center of the distribution would now be around the systemic velocity, rather than zero, and the sharp increases in probability would be at the minimum ($v_{sys} - \max(v_{bary})$) and maximum ($v_{sys} - \min(v_{bary})$) ends of the distribution. We would expect systems with systemic velocities canceled by the maximum or minimum possible barycentric velocities along their line-of-sight to show the strongest detections possible with a random primary velocity sampling strategy. This would be because one of the sharp increases towards the edges of the primary velocity distribution would be at 0 km/s, meaning that a random primary velocity strategy would offer the most near-zero primary velocity epochs if the system had this configuration of systemic and barycentric velocities (set by its RA and DEC) than any other alignment.

Another consideration for the random primary velocity observing strategy will be the location of the telescope. The location of the telescope will set if and when during the year a system is observable, and so will cut out portions of the random primary velocity distribution corresponding to barycentric velocities that arise during times the system is not observable from that telescope. The primary velocities removed could include a range around zero or a range of the largest possible absolute primary velocities. If the primary velocities around 0 were removed, we would expect a weaker detection, while if a range of the largest absolute primary velocities were removed, we would expect a stronger detection.

We do note that these predictions are all based on which selection of random primary velocities would give the most near zero. We would still expect a dedicated near-zero primary velocity observing strategy to provide the strongest detection because it would not be diluted by any of the suboptimal non-zero primary velocity epochs that could arise from a random primary velocity sampling strategy regardless of systemic velocity, magnitude of the barycentric velocity variation, or telescope location. If the combination of the telescope location and systemic and barycentric velocities are such that there is no period of near-zero primary velocities, we would recommend targeting the smallest absolute (nearest zero) primary velocities as we saw provided stronger results in our pre-upgrade NIRSPEC simulations of Section 4.5.

Random Orbital Phases

In this work, we found that the combination of orbital phases did not have a large effect on the height over noise of the planetary detection. Our simulations considered cloud-free models and did not vary the planetary spectrum as a function of orbital phase, to account for day- to night-side differences for tidally locked planets, though. If day- to night-side differences were considered, we would expect the day-side orbital phases ($0.25 \leq M \leq 0.75$), which should have higher effective temperatures, to allow for stronger detections (Finnerty et al., 2021).

While clouds have presented a challenge to low-resolution transmission spectroscopy, thermal emission spectra of the same planets show strong molecular lines (e.g., Crouzet et al., 2014; Morley et al., 2017). Gandhi et al. (2020) recently showed that high-resolution transmission spectroscopy could be used to detect water and other trace species, namely CH_4, NH_3, and CO, in cloudy atmospheres with a modest observing time from a ground-based telescope. In high-resolution emission spectra, clouds could decrease the line contrast by shifting the continuum to higher altitudes and lower temperatures, rather than by blocking stellar rays below the cloud tops as they do in transmission spectra. By decreasing line contrasts, clouds would make the planet more difficult to detect through cross correlation analysis. If, in tidally-locked atmospheres, the clouds are mainly constrained to the night-side (e.g., Demory et al., 2013; Parmentier et al., 2016), day-side epochs would be even more preferable.

For longer period planets that are not tidally-locked, neither day- to night-side temperature differences nor night-side clouds would uniformly degrade one set of orbital phases over another. Additionally, neither day- to night-side differences nor the presence of clouds should affect our predictions for the optimal primary velocity observing strategy.

Importantly, the fact that random orbital phases are sufficent, at least for non-tidally locked atmospheres, indicates that a robust detection could be made with only a fraction of an exoplanet's orbital period. Short period planets could be well detected with a selection of orbital phase epochs taken over a period when v_{pri} is near zero. With the much more quickly varying planetary orbital phase relative to Earth's orbital phase, these periods during which v_{pri} is near zero should offer a range of day- to night-side planetary epochs. Longer period planets could be targeted at multiple stretches when v_{pri} is near zero, each offering a different selection of orbital phases (as long as the orbital period is not highly commensurate with that of the Earth). Such observing strategies could be easily obtainable and should lead to strong (non-transiting) planetary detections.

Wavelength Dependence and Atmospheric Characterization

Further, while we investigated ways to strengthen detections of planetary emission through the recovery of K_p in this work, ultimately, we would be interested in constraining various planetary atmospheric properties, such as the presence and relative abundances of various molecular species and the natures of the atmospheric thermal structure, winds, and planetary rotation. Previous work has found that since there are no spectral lines from major carbon-bearing species in the L band of hot Jupiter atmospheres, this data alone is not sufficient to constrain their atmospheric C/O ratios (e.g., Piskorz et al., 2018; Finnerty et al., 2021). Such measurements may be possible for warm Jupiters ($T_{\rm eff} \approx 900$ K) from L band data alone however. At cooler effective temperatures, sufficient methane can be expected under equilibrium conditions to be detectable in L band data. With both methane and water appearing, *L* band data can provide constraints on the C/O ratios of warm Jupiters (Finnerty et al., 2021).

To make these C/O constraints for hot Jupiters would likely require additional epochs in the *K* or *M* bands, where prominent carbon monoxide bandheads exist. In this work, we found that both pre- and post-upgrade NIRSPEC *L* band simulations were better able to detect planetary signals with near-zero, rather than with random, primary velocity epochs. The pre- and post-upgrade simulations differ in both number of orders per epoch and order wavelength coverage, with no overlap between the wavelengths covered. The fact that both still preferred a near-zero primary velocity epoch strategy implies that these predictions are not completely wavelength dependent and we expect that they should hold for *L*-band observations in general. We encourage more simulation work to determine how widely generalizable these predictions will be both at other NIRSPEC bands (specifically *K* and *M*) and across the large instantaneous spectral grasp promised by upcoming and proposed instruments such as GMTNIRS (1.1–5.3 μm) and IGNIS (1–5 μm). Data covering these multiple bands would allow us to detect carbon monoxide as well as water in hot Jupiter atmospheres and allow for constraints on their atmospheric C/O ratios.

4.9 Conclusion

In this work, we aimed to determine how to best strengthen planetary detections and reduce structured noise in few-epoch data sets with careful observing strategies. The two key parameters that can be selected with the choice of observing nights are the primary velocity (because of the variable barycentric velocity) and the planetary orbital phase. We found that epochs taken during nights when the primary velocity of the system is near 0 km/s, so that there is very little relative velocity shifting of the stellar and telluric reference frames, will provide the strongest planetary detections. With a random selection of planetary orbital phases, these near-zero primary velocity epoch simulations produce planetary peaks more than two times higher relative to the noise than simulations generated with randomly selected primary velocities. Further, for near-zero primary velocity epochs, the closer their orbital phases are to quadrature, the better the constraints on K_p will be. Following these results, we recommend that observers looking to build up multi-epoch near-IR high-resolution data sets target, first, epochs with near-zero primary velocities, and second, epochs with orbital phases near quadrature to get the best constraints on the planetary detection. In this work, we demonstrated how greatly the combinations of primary velocities and orbital phases can affect a planetary detection. Moving forward, careful attention should be paid to planning observations, and all few-epoch data sets should not be assumed to have an equal probability of detecting a planet. Following these predications, observations taken from upcoming multi-echelle instruments, such as GMTNIRS and IGNIS, during periods when the primary velocity of a system is near zero, could provide both robust detections of exoplanets and constraints on their atmospheric composition in a fraction of their orbital periods.

4.10 Appendix

Notes on Epochs from Individual Sources

All of the data used in Section 4.5 is L-band data from the pre-upgrade NIRSPEC instrument. Each epoch has 4 orders, covering approximately 2.9962–3.0427, 3.1203–3.1687, 3.2552–3.3058, and 3.4026–3.4554 μm. The average spectral resolution is 20,000, and the total S/N across the 5 epochs is about 4100.

HD187123

The reduced data and PHOENIX stellar and SCARLET planetary spectral models used here were those presented in Buzard et al. (2020).

KELT2A

The reduced data and PHOENIX stellar and planetary models used here were those presented in Piskorz et al. (2018). For the planetary model, we used the best-fitting ScCHIMERA model, which had a metallicity ($\log z$) of 1.5, a C/O ratio of 0.5, and an incident solar flux f of 1.0. This parameter f accounts for day-night heat transport and an unknown albedo by scaling a wavelength-dependent incident stellar flux (from a PHOENIX stellar grid model). Defined this way, model atmospheres with $f \gtrsim 1.5$ show a temperature inversion.

51 Peg

The 51 Peg epochs were reduced in the same way as the other epochs (e.g., Piskorz et al., 2018; Buzard et al., 2020), and telluric corrected through a `Molecfit` (Kausch et al., 2014) guided principal component analysis. We used a PHOENIX stellar spectral model interpolated to an effective temperature of 5787 K, a metallicity of 0.2, and a surface gravity of 4.449 (Turnbull, 2015). The planetary spectral model we use was generated from the SCARLET framework. It does not have an inverted thermal structure, which was suggested is appropriate by Birkby et al. (2017).

Tau Boo

The Tau Boo data used here were processed using a `Molecfit` initial telluric model followed by PCA to remove residual tellurics. The stellar and planetary spectral model used here were the ones used in Lockwood et al. (2014). The stellar model was not from the PHOENIX framework. Rather, it was generated from the LTE line analysis code MOOG (Sneden, 1973) and the MARCS grid of stellar atmospheres (Gustafsson et al., 2008). Individual elemental abundances were set through fitting to well-measured lines in the NIRSPEC data. See Lockwood et al. (2014) for a full description of the stellar spectral model generation.

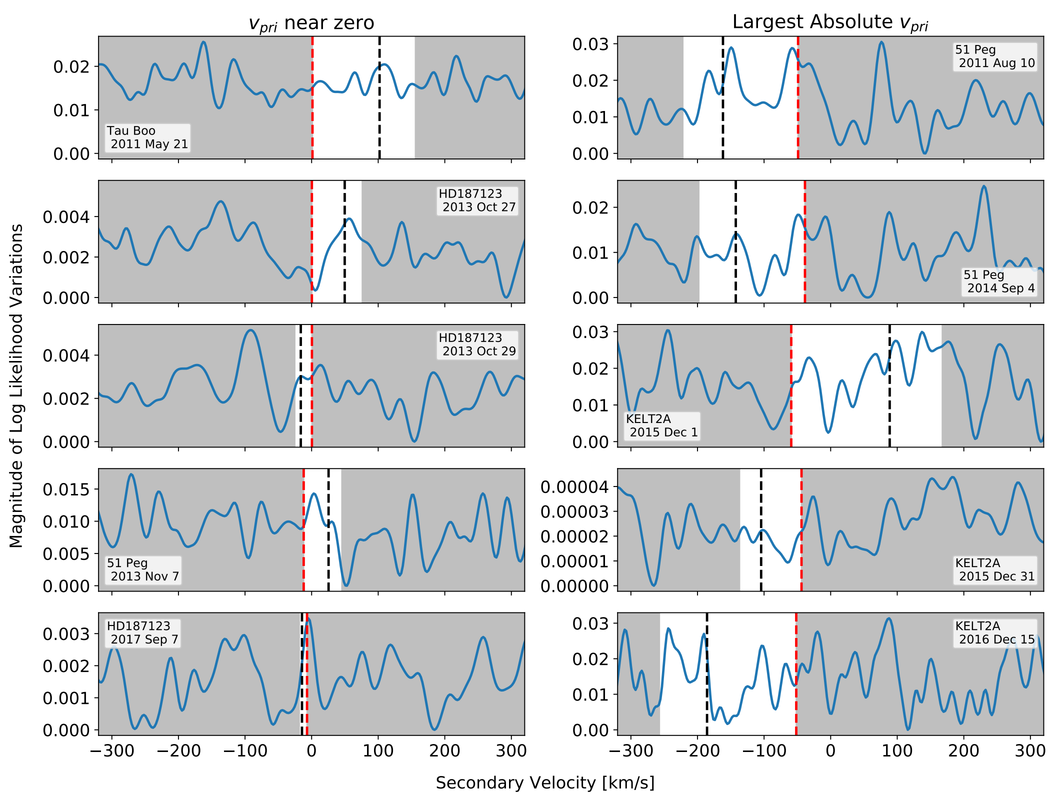

Figure 4.9: Magnitude of the log likelihood variations of each epoch in the two data primary velocity groups: near-zero and largest absolute primary velocity. Each curve has been converted to reflect a K_p of 150 km/s, rather than the underlying planets' true K_p values, which are reported in Table 4.1. These curves, converted to K_p space and summed, make up Figure 4.4. In each subplot, the red dashed line corresponds to the primary velocity at that epoch and the black dashed line corresponds to the v_{sec} given by a K_p' of 150 km/s at that each. If the fictitious combined system were face-on, with a K_p of 0 km/s, the black dashed line would coincide with the red dashed line. If, on the other hand, it were edge-on, v_{sec} would fall on the other end of the white range of possible planetary velocities. Here we have the maximum value of K_p arbitrarily set to 230 km/s.

References

Beatty, T. G., Pepper, J., Siverd, R. J., et al. 2012, *ApJL*, 756, L39, doi: 10.1088/2041-8205/756/2/L39

Benneke, B. 2015, ArXiv e-prints. https://arxiv.org/abs/1504.07655

Benneke, B., & Seager, S. 2012, *ApJ*, 753, 100, doi: 10.1088/0004-637X/753/2/100

—. 2013, *ApJ*, 778, 153, doi: 10.1088/0004-637X/778/2/153

Benneke, B., Knutson, H. A., Lothringer, J., et al. 2019a, Nature Astronomy, 3, 813, doi: 10.1038/s41550-019-0800-5

Benneke, B., Wong, I., Piaulet, C., et al. 2019b, *ApJL*, 887, L14, doi: 10.3847/2041-8213/ab59dc

Birkby, J. L., de Kok, R. J., Brogi, M., et al. 2013, *MNRAS*, 436, L35, doi: 10.1093/mnrasl/slt107

Birkby, J. L., de Kok, R. J., Brogi, M., Schwarz, H., & Snellen, I. A. G. 2017, *AJ*, 153, 138, doi: 10.3847/1538-3881/aa5c87

Borysow, A. 2002, *A&A*, 390, 779, doi: 10.1051/0004-6361:20020555

Brogi, M., Snellen, I. A. G., de Kok, R. J., et al. 2012, *Nature*, 486, 502, doi: 10.1038/nature11161

—. 2013, *ApJ*, 767, 27, doi: 10.1088/0004-637X/767/1/27

Burrows, A., & Volobuyev, M. 2003, *ApJ*, 583, 985, doi: 10.1086/345412

Buzard, C., Finnerty, L., Piskorz, D., et al. 2020, *AJ*, 160, 1, doi: 10.3847/1538-3881/ab8f9c

Cropper, M., Katz, D., Sartoretti, P., et al. 2018, *A&A*, 616, A5, doi: 10.1051/0004-6361/201832763

Crouzet, N., McCullough, P. R., Deming, D., & Madhusudhan, N. 2014, *ApJ*, 795, 166, doi: 10.1088/0004-637X/795/2/166

Demory, B.-O., de Wit, J., Lewis, N., et al. 2013, *ApJL*, 776, L25, doi: 10.1088/2041-8205/776/2/L25

Finnerty, L., Buzard, C., Pelletier, S., et al. 2021, *AJ*, 161, 104, doi: 10.3847/1538-3881/abd6ec

Gaia Collaboration, Prusti, T., de Bruijne, J. H. J., et al. 2016, *A&A*, 595, A1, doi: 10.1051/0004-6361/201629272

Gaia Collaboration, Brown, A. G. A., Vallenari, A., et al. 2018, *A&A*, 616, A1, doi: 10.1051/0004-6361/201833051

Gandhi, S., Brogi, M., & Webb, R. K. 2020, *MNRAS*, 498, 194, doi: 10.1093/mnras/staa2424

Gontcharov, G. A. 2006, Astronomical and Astrophysical Transactions, 25, 145, doi: 10.1080/10556790600916780

Gordon, C., & Trotta, R. 2007, *MNRAS*, 382, 1859, doi: 10.1111/j.1365-2966.2007.12707.x

Guilluy, G., Sozzetti, A., Brogi, M., et al. 2019, *A&A*, 625, A107, doi: 10.1051/0004-6361/201834615

Gustafsson, B., Edvardsson, B., Eriksson, K., et al. 2008, *A&A*, 486, 951, doi: 10.1051/0004-6361:200809724

Husser, T. O., Wende-von Berg, S., Dreizler, S., et al. 2013, *A&A*, 553, A6, doi: 10.1051/0004-6361/201219058

Katz, D., Sartoretti, P., Cropper, M., et al. 2019, *A&A*, 622, A205, doi: 10.1051/0004-6361/201833273

Kausch, W., Noll, S., Smette, A., et al. 2014, in Astronomical Society of the Pacific Conference Series, Vol. 485, Astronomical Data Analysis Software and Systems XXIII, ed. N. Manset & P. Forshay, 403

Lockwood, A. C., Johnson, J. A., Bender, C. F., et al. 2014, *ApJL*, 783, L29, doi: 10.1088/2041-8205/783/2/L29

Martin, E. C., Fitzgerald, M. P., McLean, I. S., et al. 2018, in Society of Photo-Optical Instrumentation Engineers (SPIE) Conference Series, Vol. 10702, Ground-based and Airborne Instrumentation for Astronomy VII, 107020A

Morley, C. V., Knutson, H., Line, M., et al. 2017, *AJ*, 153, 86, doi: 10.3847/1538-3881/153/2/86

Nidever, D. L., Marcy, G. W., Butler, R. P., Fischer, D. A., & Vogt, S. S. 2002, *ApJS*, 141, 503, doi: 10.1086/340570

Parmentier, V., Fortney, J. J., Showman, A. P., Morley, C., & Marley, M. S. 2016, *ApJ*, 828, 22, doi: 10.3847/0004-637X/828/1/22

Piskorz, D., Buzard, C., Line, M. R., et al. 2018, *AJ*, 156, 133, doi: 10.3847/1538-3881/aad781

Piskunov, N. E., Kupka, F., Ryabchikova, T. A., Weiss, W. W., & Jeffery, C. S. 1995, *A&AS*, 112, 525

Rothman, L. S., Gordon, I. E., Barbe, A., et al. 2009, *J. Quant. Spec. Radiat. Transf.*, 110, 533, doi: 10.1016/j.jqsrt.2009.02.013

Sartoretti, P., Katz, D., Cropper, M., et al. 2018, *A&A*, 616, A6, doi: 10.1051/0004-6361/201832836

Sneden, C. 1973, *ApJ*, 184, 839, doi: 10.1086/152374

Snellen, I. A. G., de Kok, R. J., de Mooij, E. J. W., & Albrecht, S. 2010, *Nature*, 465, 1049, doi: 10.1038/nature09111

Soubiran, C., Jasniewicz, G., Chemin, L., et al. 2018, *A&A*, 616, A7, doi: 10.1051/0004-6361/201832795

Tennyson, J., & Yurchenko, S. N. 2012, *MNRAS*, 425, 21, doi: 10.1111/j.1365-2966.2012.21440.x

Tennyson, J., Yurchenko, S. N., Al-Refaie, A. F., et al. 2020, *J. Quant. Spec. Radiat. Transf.*, 255, 107228, doi: 10.1016/j.jqsrt.2020.107228

Turnbull, M. C. 2015, arXiv e-prints, arXiv:1510.01731. https://arxiv.org/abs/1510.01731

Valenti, J. A., & Fischer, D. A. 2005, *ApJS*, 159, 141, doi: 10.1086/430500

Zucker, S. 2003, *MNRAS*, 342, 1291, doi: 10.1046/j.1365-8711.2003.06633.x

Zucker, S., & Mazeh, T. 1994, *ApJ*, 420, 806, doi: 10.1086/173605

Chapter 5

REINVESTIGATION OF THE MULTI-EPOCH DIRECT DETECTIONS OF HD 88133 B AND UPSILON ANDROMEDAE B

This chapter is adapted from work previously published as

Buzard, C., Piskorz, D., Lockwood, A. C., et al. 2021b, *The Astronomical Journal*, 162, 269, doi: 10.3847/1538-3881/ac2a2c

5.1 Introduction

Direct detection techniques that use radial velocity signatures from exoplanet orbital motion to detect their atmospheric thermal emission have become popular in the last decade. Two variations of such high-resolution techniques have been developed. Both aim to make a direct planetary detection through a measurement of the planetary velocity semi-amplitude, K_p. One variation targets planetary systems during periods when the change in the planetary line-of-sight motion is the greatest, typically near conjunction. By observing the system at periods of maximum planetary line-of-sight acceleration, the data contain planetary signatures that shift across the instrument's resolution elements over the course of the night, and techniques like principal component analysis (PCA) can be used to tease apart the changing planetary signal and the stationary telluric and stellar signals. A one-dimensional cross correlation routine can then be used to measure the planetary velocity. This technique was first introduced by Snellen et al. 2010 with VLT/CRIRES, and has since been applied to data from a range of instruments including Subaru/HDS (e.g., Nugroho et al., 2017), TNG/GIANO (e.g., Brogi et al., 2018; Guilluy et al., 2019), and CFHT/SPIRou (e.g., Pelletier et al., 2021).

The second variation of the high-resolution technique, which is the focus of this work, instead limits observations so that the change in the planetary line-of-sight velocity is minimized, and the planetary spectrum does not shift across the detector during the course of an observation. This variation is more technically challenging because there is no longer a velocity variation that can be leveraged to separate the planetary and stellar spectra in a single epoch. After the data is telluric corrected, a two-dimensional cross correlation is relied upon to pull apart the stellar and planetary components. Since the planetary signal is so much fainter than the stellar signal, multiple epochs must be combined before the planetary signal becomes apparent. While technically challenging, this variation is the only currently viable high-resolution method for studying the atmospheres of planets whose semi-major axes preclude both single-epoch spectroscopic detection, because they move too slowly, and direct imaging with current adaptive optics capabilities, because they are too close to the star ($\lesssim 0.1''$, e.g., Snellen et al. 2014). This gap includes planets in K dwarf and solar habitable zones. As the so-called multi-epoch technique is uniquely capable of directly studying the atmospheres of non-transiting planets in these systems, it deserves careful work and attention.

To date, the multi-epoch technique has mainly been applied to data from Keck / NIRSPEC, which is an echelle spectrograph that offered 4–6 orders in the K and L bands per cross disperser setting and R $\sim 25,000 - 30,000$ before its upgrade in early 2019. The method was first applied to Tau Boo b and was able to measure its K_p as 111 ± 5 km/s (Lockwood et al., 2014), which was in good agreement with K_p measurements from other techniques (e.g., 110.0 ± 3.2 km/s, Brogi et al., 2012). Subsequently, the non-transiting hot Jupiters HD 88133 b and Upsilon Andromedae b (ups And b) were detected at 40 ± 15 km/s (Piskorz et al., 2016) and 55 ± 9 km/s (Piskorz et al., 2017), respectively. These planets have yet to be studied via a different technique. Piskorz et al. 2018 then detected the transiting hot Jupiter KELT-2Ab with a K_p of 148 ± 7 km/s, which was in good agreement with the transit measurement of 145^{+9}_{-8} km/s (Beatty et al., 2012). Finally, Buzard et al. 2020 measured K_p of the non-transiting hot Jupiter HD 187123 b to be 53 ± 13 km/s. This detection used simulations to identify sources of non-random noise and elucidate the true planetary detection. HD 187123 b has not to date been detected via another technique.

In this work, we look back on the multi-epoch detections of HD 88133 b (Piskorz et al., 2016) and ups And b (Piskorz et al., 2017). Piskorz et al. 2016 reported the Keplerian orbital velocity of HD 88133 b as 40 ± 15 km/s using 6 epochs of NIRSPEC L band data and 3 epochs of K band data. Piskorz et al. 2017 reported the Keplerian orbital velocity of ups And b as 55 ± 9 km/s using 7 epochs of NIRSPEC L band data, 3 epochs of K_l band data covering the left-hand half of the NIRSPEC detector, and 3 epochs of K_r band data covering the right-hand half of the detector. In this work, we will focus on the L band data because the L band data provided the majority of the overall structure in both the HD 88133 b and ups And b detections.

5.2 Standard Multi-Epoch Analytic Approach

To begin, we want to give a brief description of the multi-epoch analytic process. These approaches are explained in more detail in prior publications (e.g., Lockwood et al., 2014; Piskorz et al., 2016; Buzard et al., 2020). In brief, epochs of data are obtained from hot Jupiter systems over ~2-3 hour periods during which the planetary signal is not expected to significantly shift compared to the wavelength scale of the detector. The two-dimensional echelle spectra are reduced, wavelength calibrated, telluric corrected, and run through a two-dimensional cross-correlation routine with appropriate stellar and planetary spectral models. Because the stellar signal is the major component of the data after telluric correction, the known stellar velocity, given by

$$v_{pri} = v_{sys} - v_{bary}, \tag{5.1}$$

where v_{sys} is the systemic velocity and v_{bary} is the barycentric velocity, can always be correctly measured in each epoch. A cut along the known stellar velocity gives a one-dimensional cross correlation in terms of planetary velocity shift. With a very low contrast relative to the stellar signal, the planetary signal requires the combination of multiple epochs to become clearly detectable.

To be combined, the cross correlations must first undergo two transitions. They must first be converted from functions of secondary velocity, which is dependent on orbital phase, to functions of a parameter independent of orbital phase, namely, the Keplerian orbital velocity. Second, they must be converted to log likelihoods. To convert them from functions of secondary velocity to Keplerian orbital velocity (K_p), we apply the equation,

$$v_{sec}(f) = -K_p(\cos(f + \omega_{st}) + e\cos(\omega_{st})) + v_{pri}, \tag{5.2}$$

where f is the planet's true anomaly at the observation time, ω_{st} is the argument of periastron of the star's orbit measured from the ascending node (with the Z-axis pointing away from the observer, see Fulton et al. 2018), and e is the eccentricity.

To convert the cross correlations from v_{sec} to K_p space using Equation 5.2, we need stellar radial velocity (RV) parameters (e, ω_{st}) and true anomaly (f) values at each epoch. Stellar radial velocity parameters can typically be found in the literature (e.g., Butler et al., 2006). We note that it is important that the stellar orbital parameters (e, ω_{st}) as well as those used to calculate f (t_{peri}, P) are pulled from the same literature source. This will be especially important for near-circular orbits where pericenter is not well defined because, though references can set pericenter at vastly different points on the orbit, their other parameters (mainly t_{peri} and ω) would then all be consistent to that chosen point of pericenter. A t_{peri} and ω from different references could be referring to very different points on the orbit, and so could create a large error in the derived fs and secondary velocities.

The true anomalies can be calculated using the following equations, which are described in Murray & Dermott 1999. First, the mean anomaly (M) is calculated from the observation time (t_{obs}), and the stellar radial velocity parameters, time of periastron (t_{peri}) and orbital period (P). If the orbit under study can be assumed circular, the mean anomalies can be used in place of the true anomalies.

$$M = 2\pi\left(\frac{t_{obs} - t_{peri} \mod P}{P}\right). \tag{5.3}$$

Then, the eccentric anomaly E can be calculated as follows, where e is the eccentricity. As this equation does not have a closed-form solution for E given M, E is calculated numerically.

$$M = E - e \sin E. \tag{5.4}$$

Finally, the true anomaly f is calculated as

$$f = 2 \arctan\left(\sqrt{\frac{1+e}{1-e}} \tan \frac{E}{2}\right). \tag{5.5}$$

We want to make a few important notes about Equations 5.2 and 5.3–5.5. First, the negative sign at the start of Equation 5.2, which is not present in the corresponding equation in Fulton et al. 2018, allows this equation to describe the planetary motion, rather than the stellar motion. At any given time, the planetary and stellar motions should have opposite signs. The addition of the negative sign would be equivalent to replacing ω_{st} with ω_{pl} (the argument of periastron of the planet's orbit measured from the ascending node) because $\omega_{pl} = \omega_{st} + \pi$ (for a set direction of the Z-axis). Importantly, by defining K_p this way, we specify that it must be a positive value. Second, it is important that the zero-point used to define the anomalies (t_{peri} in Equation 5.3) is consistent with the offset used in Equation 5.2. In the equations as written, f is measured from pericenter, and adding ω_{st} in Equation 5.2 brings the zero point from pericenter to the star's ascending node. The ascending node (for a circular orbit, when the star is at quadrature and moving away from the observer or when the planet is at quadrature and moving toward the observer) should have the largest negative v_{sec} possible. The negative cosine ensures this is the case. Other works that have assumed a circular orbit (e.g., Piskorz et al., 2018; Buzard et al.,

2020) use a positive sine equation with no added phase offset and with Ms centered at inferior conjunction. This is also a valid approach because the offset between the Ms and the sine equation are consistent.

Once the planetary cross correlations from different epochs are on the same K_p axis, they must be converted into log likelihoods to be combined. There are a number of ways to do so (Zucker, 2003; Brogi & Line, 2019; Buzard et al., 2020). Here, we use the approach first introduced by Zucker 2003 and termed the "Zucker ML" approach by Buzard et al. 2020 to be consistent with Piskorz et al. 2016 and Piskorz et al. 2017. The Zucker ML method converts cross correlations to log likelihoods and combines them as,

$$\log(L(s)) = \sqrt{1 - \exp\left(\frac{1}{N_{tot}} \sum_i N_i \log[1 - R_i^2(s)]\right)}, \tag{5.6}$$

where s is the velocity shift, R_i are the individual cross correlations, N_i is the number of pixels per cross correlation, and N_{tot} is the total number of pixels.

With this basis, we turn to a reinvestigation of previous multi-epoch works by Piskorz et al. 2016 and Piskorz et al. 2017.

5.3 HD 88133 b

Piskorz et al. 2016 used 6 Keck/NIRSPEC L band and 3 K band epochs to measure the planetary Keplerian orbital velocity of the non-transiting hot Jupiter HD 88133 b as 40 ± 15 km/s. To do so, they used orbital parameters from their own fit to stellar RV data. This stellar RV data set consisted of 55 RV points; 17 had been previously analyzed by Fischer et al. 2005 and the rest were new RV points taken by the California Planet Survey with HIRES at the W. M. Keck Observatory. Fitting these data with a Markov Chain Monte Carlo technique following Bryan et al. 2016, they reported the orbital parameters (velocity semi-amplitude $K = 32.9 \pm 1.03$ km/s, period $P = 3.4148674^{+4.57e-05}_{-4.73e-05}$ days, eccentricity $e = 0.05 \pm 0.03$, argument of periastron of the star's orbit $\omega_{st} = 7.22^{+31.39}_{-48.11}{}^{\circ}$, and time of periastron $t_{peri} = 2454641.984^{+0.293}_{-0.451}$).

Correction to Piskorz et al. 2016 Results

In Piskorz et al. 2016, there was a systematic error in the implementation of the time of periastron in Equation 5.3 that resulted in a 38.0% orbital offset in the mean anomalies. The anomalies used in the paper analysis and the corrected anomalies are listed in Table 5.1.

Table 5.1: HD 88133 b Epoch Positions

Date	Piskorz et al. 2016		This work	
	M^{a}	f^{a}	M	f
2012 Apr 1	5.11	5.01	1.22	1.31
2012 Apr 3	2.51	2.57	4.90	4.80
2013 Mar 10	1.52	1.62	3.91	3.84
2013 Mar 29	4.95	4.85	1.06	1.15
2014 May 14	1.03	1.12	3.42	3.40
2015 Apr 8	3.26	3.25	5.65	5.59

[a]Note, the values here are expressed from 0 to 2π, rather than from 0 to 1 as in Piskorz et al. 2016. The M and f values reported in their Table 3 also differ from these values because, while they too were affected by the systematic offset, they used Butler et al. 2006 orbital parameters rather than the newly fit parameters from Piskorz et al. 2016.

In Figure 5.1, we show the corrected log likelihood curves along with the originally published curves, analyzed with both the SCARLET and the PHOENIX planetary models. This correction causes a drastic difference in the resulting log likelihood curve. In each subplot, the red curve was the published log(L) curve and the black dashed curve is the curve reproduced with the systematic offset. Interestingly, this curve exactly reproduces the SCARLET model function, but does not reproduce the PHOENIX model function. In fact, when the data are analyzed with the PHOENIX model, Piskorz et al. 2016 orbital parameters, and the offset, the resulting function appears much more similar in shape to the corresponding SCARLET result than was originally published in Piskorz et al. 2016. This suggests that the two planetary models are much more comparable than was originally thought.

The blue and orange curves in both subplots show the corrected log likelihoods when the orbit is either treated as eccentric (blue) or assumed to be circular (orange). The similarity between these curves in both subplots shows that for low-eccentricity orbits (here $e \sim 0.05$) circular approximations do not greatly affect the shape of the resulting log likelihood surface.

We also note that the corrected log likelihood curves show no significant peaks at positive values of K_p. Remember that given how we defined the relationship between v_{sec} and K_p, only positive values of K_p are physically meaningful. Negative values of K_p would have the stellar and planetary radial velocity curves perfectly in phase rather than out of phase as they should be. This correction therefore implies that we

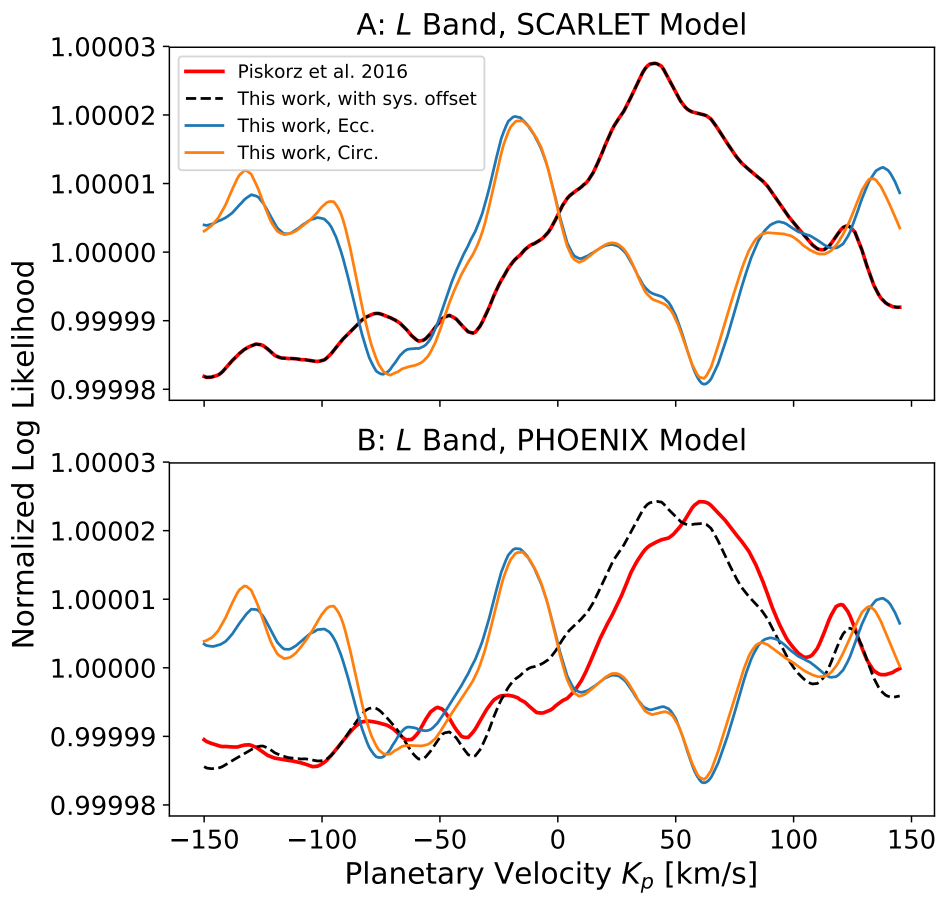

Figure 5.1: (A) The normalized log likelihood result for HD 88133 b originally published in Piskorz et al. 2016 is shown in red. The black dashed curve is able to reproduce the published curve by including a systematic offset in epoch positions. In blue and orange are the corrected log likelihood curves considering an eccentric orbit (blue) and a circular orbit (orange). (B) Same as Panel A, except using a PHOENIX planetary model rather than a SCARLET planetary model. Note here that we were unable to reproduce the published curve. However, when the same orbital parameters are used, we get a much more similar result to that of the SCARLET models than was shown in the Piskorz et al. 2016. The two different planetary spectral model frameworks do not create as significant a difference as we thought.

cannot report a measurement of the Keplerian orbital velocity of HD88133b of 40 km/s from the six L band epochs presented in Piskorz et al. 2016.

HD88133 Simulations

We ran a few sets of simulations to determine what physical or observational factors would allow for the detection of HD88133b. We note that HD88133A has a rather large stellar radius of 2.20 $R_\odot$ (Ment et al., 2018), meaning that this system has an even lower planet to star contrast than most hot Jupiters, though we cannot measure it directly because of the unknown planetary radius. Our first simulations ask how large the planetary radius would have to be for the planetary peak to be detectable in the six L band epoch observed (Section 5.3). Next, we investigate whether the same epochs taken with the upgraded NIRSPEC2.0 instrument would have been more successful than the NIRSPEC1.0 epochs (Section 5.3). Then, we consider the primary velocity. Buzard et al. 2021 found that epochs with near-zero primary velocities were more useful in damping down structured noise and revealing true planetary signatures than epochs with larger absolute primary velocities. We consider whether the observed epochs would have better revealed the planetary peak if they had smaller absolute primary velocities (Section 5.3).

Generation of Simulated Data

For these simulations, we use a stellar model generated from the PHOENIX stellar spectral model grid (Husser et al., 2013) interpolated to an effective temperature of 5438 K, a metallicity of 0.330, and a surface gravity of 3.94 (Mortier et al., 2013).

We use the PHOENIX planetary spectral model from Piskorz et al. 2016. This modeled atmosphere does not have an inverted thermal structure in regions close to the molecular photosphere.

We generated the simulated multi-epoch data using the same framework initially presented in Buzard et al. 2020 and so a full description can be found there. As a quick summary, these simulations combine the stellar and planetary models on the planetary wavelength axis after scaling them by their relative surface areas and shifting them to the desired primary and secondary velocities during each epoch. The secondary velocities are calculated by plugging the f values in Table 5.1, This work, into Equation 5.2 using Piskorz et al. 2016 orbital parameters and a K_p of 40 km/s. For these simulations, we assume a planetary radius of 1 R_{Jup} (except in the planetary radius simulations) and a stellar radius of 2.20 $R_\odot$ (Ment et al., 2018). After combination, the continuum is removed using a third-order polynomial fit from 2.8 to 4.0 μm in wavenumber space. Then, the simulated data are broadened using the instrumental profiles fit to the data, interpolated onto the data wavelength axes, and the same pixels lost to saturated tellurics in the data are removed. The data, all taken before the NIRSPEC upgrade in early 2019, contain 4 orders per epoch which cover approximately 3.4038–3.4565, 3.2567–3.3069, 3.1216–3.1698, and 2.997–3.044 μm. Gaussian white noise is added in at the same level as in the data (total S/N per pixel = 5352).

The stellar model used to generate and cross correlate the simulated data differs from the stellar model used to cross correlate the observed data in Piskorz et al. 2016 in how its continuum is removed. The stellar model used for cross correlation in Piskorz et al. 2016 was continuum corrected with a second-order polynomial fit from 2.0 to 3.5 μm in wavenumber space, while the model used here is corrected with a third-order polynomial fit from 2.8 to 4.0 μm in wavenumber space. The method of stellar continuum correction actually has a large effect on the shape of the resulting log likelihood curve; when the data are cross correlated with a stellar model corrected by a third-order polynomial fit from $2.8 - 4.0$ μm in wavenumber space, the resulting log likelihood curve much more closely resembles the simulated curves (e.g. in Figure 5.2). We use the third-order, $2.8 - 4.0$ μm approach in our simulations because this continuum correction method was validated in allowing common structure to be seen in the data and simulated log likelihoods of HD187123b (Buzard et al., 2020). Further, this approach resulted in a flatter looking stellar spectral model, and one that found the known stellar velocities in each epoch of data with higher likelihoods. We do note, however, that the seemingly strong dependence of the final log likelihood shape on the method of stellar model continuum correction is concerning and warrants deeper investigation.

Planetary Radius Simulations

Because there seems to be no clear peak at a positive K_p in Figure 5.1, we use simulations to see how much larger the planetary radius would have to be for its peak to be distinguishable. For these simulations, we set the K_p at 40 km/s and the stellar radius at 2.20 $R_\odot$ (Ment et al., 2018), and step the planetary radius up from 1 R_{Jup} to 4 R_{Jup} in increments of 0.5 R_{Jup}. Figure 5.2 shows the results of these simulations in the top panel. In the bottom panel, we show the detections that could be made if all of the structured noise (e.g., the $\mathrm{R}_{pl} = 0$ result) could be effectively removed from the results containing a planetary signal.

In this high S/N per epoch regime, we expect the contribution from structured noise to far outway the contribution from random noise (Buzard et al., 2020; Finnerty et al., 2021). The similarity between different radius simulations shows that this is still the case.

To quantify the strength of these detection peaks, we fit each with a Gaussian model and report the parameters in Table 5.2. In the non-corrected versions, the Gaussian model does not fit within one standard deviation of the input K_p until the planetary radius reaches 2.5 R_{Jup}, and the peak does not exceed 3σ until a radius of 3.5 R_{Jup}. Even at this large radius, the Gaussian model does not clearly distinguish the planetary peak from the structured noise, which can be seen in the Gaussian center offset, large Gaussian width, and relatively low R^2 value. Much more promising detections could be made if there were a way to effectively remove the structured noise from the log likelihood results. Even at 1 R_{Jup}, HD 88133 b could have been detected in the data with a significance over 3σ. These simulations take a number of liberties, though, that are not yet applicable to real data. They consider no telluric contamination outside of pixels lost to saturated telluric absorption. They also assume that the stellar and planetary spectra in the data are perfectly matched to the stellar and planetary templates used for cross correlation. Thus, while the corrected simulations shown in the bottom panel of Figure 5.2 provide an optimistic view of the possible detections with the 6 particular NIRSPEC1.0 L band epochs presented in Piskorz et al. 2016, the uncorrected versions give much more realistic estimates.

HD 88133 b has a minimum mass of 0.27 ± 0.01 $M_{\rm Jup}$ (Piskorz et al., 2016). With a radius of 3.5 $R_{\rm Jup}$, it would have a minimum density of 0.01 g/cm^3. A growing classifcation of planets with exceptionally large radii for their masses, called "super-puffs," have low densities of $\lesssim$ 0.3 g/cm^3 (e.g. Cochran et al., 2011; Jontof-Hutter et al., 2014; Vissapragada et al., 2020). While HD 88133 b ($M_p \sin i \sim 85M$) is too massive to be classified as a super-puff ($M_p \lesssim 10 - 15M$, Piro & Vissapragada 2020), by comparison of its density, we can conclude that it is highly improbably the planet's radius would be as high as 3.5 $R_{\rm Jup}$. Indeed, hot Jupiter inflation can approach 2 R_{Jup} (Thorngren & Fortney, 2018), but has not been observed to exceed it to this extent.

Our simulations therefore confirm that HD 88133 b is not detectable from the six L band epochs of data presented in Piskorz et al. 2016. These radius simulations did, however, provide useful information in telling us that the planetary signal would need to be raised by about an order of magnitude (or the structured noise lowered by the same amount), to allow for a confident detection. We now turn to simulations to ask how that order of magnitude may be made up observationally rather than by altering parameters of the physical system like the planetary radius.

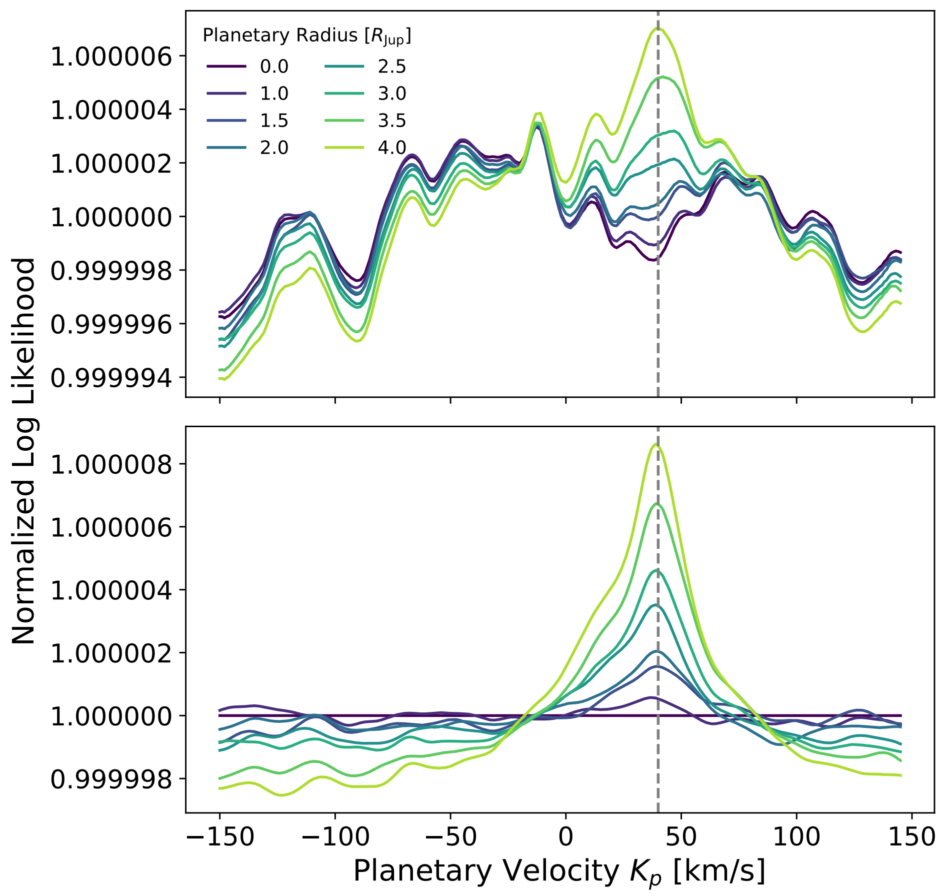

Figure 5.2: Simulated log likelihood results showing the effects of increasing HD 88133 b planetary radius. These simulations approximate NIRSPEC1.0 L band data taken with the same orbital phases (f) and primary velocities in the original data. The bottom panel shows the log likelihood results with the structured noise curve (R_{pl} = 0) subtracted off.

Upgraded NIRSPEC Simulations

The NIRSPEC instrument was upgraded in early 2019, after the Piskorz et al. 2016 publication. The upgrade would afford 6 usable L band orders per echelle/cross disperser setting as opposed to the 4 from NIRSPEC1.0. It would give twice as many pixels per order (2048 vs. 1024), a nearly doubled spectral resolution (~41,000 vs. 25,000), and a ~40% larger wavelength coverage per order (Martin et al., 2018).

We run NIRSPEC2.0 simulations with the same orbital phases and primary velocities in the original six NIRSPEC1.0 epochs to determine whether the instrument upgrade would have given the planetary signal the boost it needed to be detectable. These simulations are generated as described in Section 5.3, with the following exceptions.

Table 5.2: Gaussian Fits to HD88133 Planetary Radius Simulations

R_{pl} [R_{Jup}]	K_p [km/s]	ΔK_p [km/s]	Peak Height [σ]	R^2
Without Star Subtraction				
1.0	33	10	-0.7	2.1×10^{-3}
1.5	-33	22	1.5	0.27
2.0	-30	22	1.6	0.26
2.5	4	43	2.3	0.34
3.0	16	44	2.1	0.43
3.5	28	40	3.3	0.58
4.0	29	37	5.2	0.67
With Star Subtraction				
1.0	35	10	3.2	0.39
1.5	40	22	7.5	0.87
2.0	36	17	10.2	0.87
2.5	34	20	19.9	0.95
3.0	36	20	35.9	0.96
3.5	37	23	24.2	0.96
4.0	35	24	25.1	0.95

Note: These simulations were all run with an input K_p of 40 km/s. Prior to fitting, these log likelihood results are subtracted by the mean of their values from -150 to 0 km/s. The Gaussian model is initiated with a 40 km/s center and 10 km/s standard deviation. The Gaussian peak height is reported over σ, which is measured as the standard deviation of the log likelihood structure more than $3\Delta K_p$ above or below the best-fit Gaussian center, where ΔK_p is the standard deviation of the best-fit Gaussian model.

The six orders per epoch cover roughly 2.9331–2.9887, 3.0496–3.1076, 3.1758–3.2364, 3.3132–3.3765, 3.4631–3.5292, and 3.6349–3.6962 μm. We broaden the simulated data to an average instrumental resolution of 41,000 and assume a S/N per pixel per epoch of 2860, or a total S/N per pixel of 7000 across the six epochs. The data wavelength axes, locations of saturated telluric pixels, and Gaussian kernals used to broaden the simulated data were taken from the 2019 Apr 3 and 2019 Apr 8 NIRSPEC2.0 data of HD187123 presented in Buzard et al. 2020.

Figure 5.3 shows the results of the simulations which imagine that the HD88133 *L* band epochs had been taken with the upgraded NIRSPEC instrument. In light purple is the simulation with no planetary signal added and in darker purple is the simulation with a 1 R_{Jup} planetary signal. While the likelihood at the input K_p of

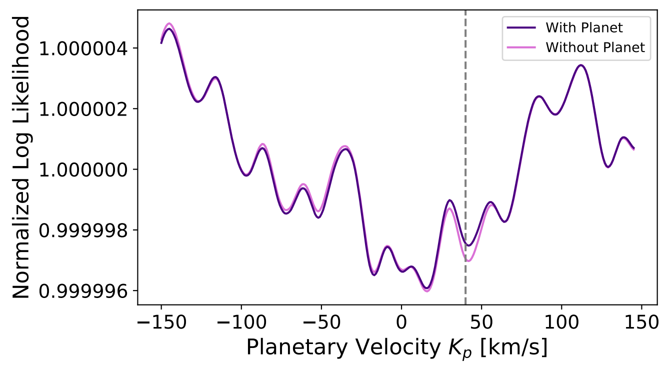

Figure 5.3: NIRSPEC2.0 simulation of HD 88133 b with same orbital phases (f) and primary velocities as in the original data. The data represented by the curve in dark purple has a 1 R_{Jup} planetary signal and the curve in light purple has no planetary signal.

40 km/s is increased from the corresponding no planet log likelihood, it does not form a peak and would not constitute a detection. The six L band HD88133 epochs were positioned such that even with the upgraded instrument, they would not have enabled a planetary detection.

Near-Zero Primary Velocity Simulations

Buzard et al. 2021 recently showed that, in the small epoch number limit, epochs taken when the primary velocity of a system is near zero are better at reducing structured noise and revealing planetary signatures than epochs taken during periods with larger absolute primary velocities. The majority of the structured noise that arises in the simulations presented here and in Buzard et al. 2021 results from correlation between the planetary spectral template and the stellar component of the simulated data. We thus suspect that the reduction of structured noise at a primary velocity of zero relates to the portion of the stellar spectrum masked by saturated tellurics when there is a minimal velocity shift between the two spectra. It could be that at this velocity shift, the stellar features that most strongly correlate with the planetary template are masked by saturated tellurics, and without them, the structured noise level decreases substantially. One must be careful in applying this prediction, though, since a primary velocity of zero would bring not just the stellar spectrum, but also the planetary spectrum, closer to the telluric rest frame. While our simulations assume perfect correction of non-saturated tellurics, any residual tellurics that make it through a correction routine could mask planetary features. In a small epoch number limit, an optimal routine might therefore include near-zero primary velocities (to reduce structured noise from star/planet correlation) and quadrature orbital positions (to maximize the planet/telluric velocity separation). With a much larger number of epochs, the structured noise from planet/star correlation may be reduced naturally by the many different combinations of primary and secondary velocities and the usefulness of near-zero primary velocity epochs may be lessened.

We can ask whether, with just the six epochs on HD88133, near-zero primary velocities might have helped. HD88133 has a primary velocity of zero twice a year: in late February and in mid-August. It would also be accessible from Keck in late February. For the following simulations, we assume epochs had been taken with the same orbital phases (f) as the original data, but in late February when $v_{pri} = 0$ km/s. The original data epochs had primary velocities of 17.4, 18.1, 8.1, 16.2, 25.7, and 19.5 km/s. We run these simulations with both the NIRSPEC1.0 and NIRSPEC2.0 configurations.

Figure 5.4 shows the results of the 0 primary velocity simulations with NIRSPEC1.0 results in the top panel and NIRSPEC2.0 results in the bottom panel. In each, we show a pure structured noise simulation (light purple), or simulation with no planetary signal in the simulated data, so that the planetary peak in the simulation with the planetary signal (darker purple) can be distinguished from the structured noise.

We first consider the NIRSPEC1.0 simulation. While the 1 R_{Jup} planetary signal definitely shows a larger peak here than when analyzed with the original primary velocities (Figure 5.2), it still does not constitute a very strong detection. We can think of a number of reasons for this. Buzard et al. 2021 showed that near-zero primary velocity epochs could raise the detection significance on average $\sim 2-3\times$ over random primary velocity epochs. From our radius simulations, we estimate an order of magnitude is needed. The gain from near-zero primary velocities then may not be sufficient. HD88133A has an effective temperature of 5438 K (Mortier et al., 2013), putting it on the cooler end of host stars considered by Buzard et al. 2021. Cooler host stars showed a stronger preference for near-zero primary velocity epochs, which means in this case, we might expect a bit more than a $3\times$ increase. On the other hand, here, we consider a K_p of 40 km/s, smaller than the 75 km/s K_p used for most of the simulations in Buzard et al. 2021. A smaller K_p brings all of the secondary velocities closer in magnitude to the primary velocity; when the primary velocity is 0 km/s, the secondary velocities are closer to 0 km/s, and the planetary spectrum is closer to the telluric rest-frame. That the near-zero primary

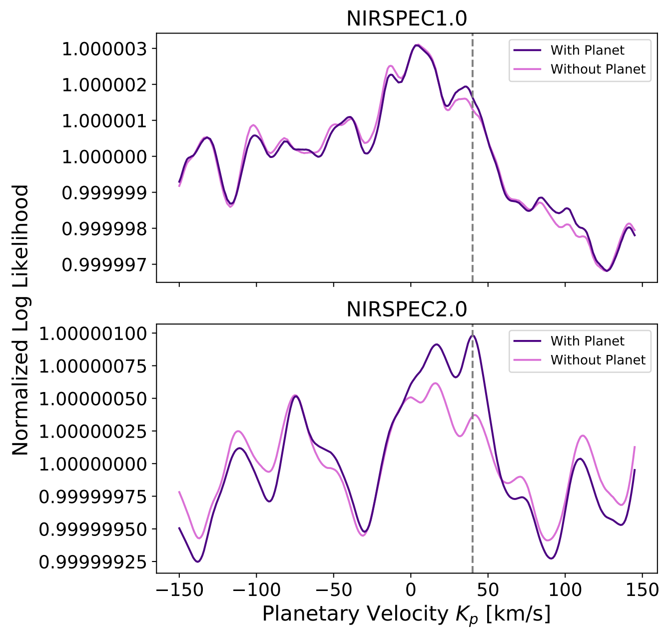

Figure 5.4: HD 88133 b simulations considering the orbital phases (f) from the six original L band epochs, but with 0 km/s primary velocities. The top panel approximated NIRSPEC1.0 data and the bottom panel approximates NIRSPEC2.0 data.

velocity approach brings the planetary spectrum closer to the telluric frame when combined with a smaller K_p could detract from its advantage over a more random set of primary velocities. Regardless of how these factors work out, Figure 5.4 confirms that a near-zero primary velocity observing strategy could not have made up for the order of magnitude needed for a strong detection of HD88133b with the orbital phases of the six L band NIRSPEC1.0 epochs obtained and presented in Piskorz et al. 2016.

The simulations considering near-zero primary velocity epochs taken with the upgraded NIRSPEC instrument, shown in the bottom panel of Figure 5.4, show the most promising chance of detection. There is a peak centered at K_p = 40 km/s. A Gaussian fit to the simulated result (dark purple) with no prior information reports a measurement of 22 ± 20 km/s, with a height of 3.2σ. If this result were from real data, and we were able to assign the peak at ∼17 km/s to noise rather than the planetary signature through either fits with simulations (e.g., Buzard et al., 2020) or because the planet had a radius inflated (e.g., Charbonneau et al., 2000) above the 1 R_{Jup} assumed here, we could expect a more refined fit.

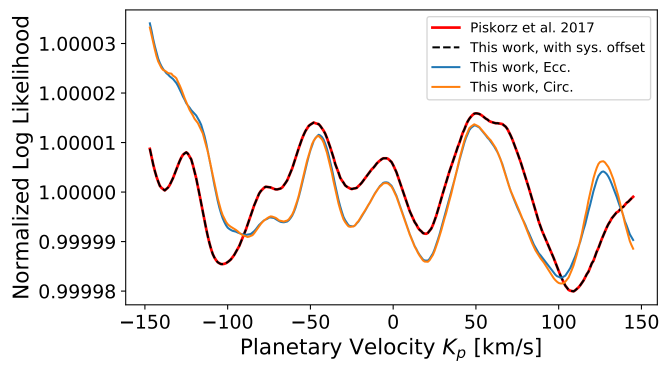

Figure 5.5: The normalized log likelihood result for ups And b originally published in Piskorz et al. 2017 is shown in red. It is reproduced, in black dashed, by including a systematic offset in the epoch positions. The corrected log likelihood curves are shown in blue (eccentric orbit) and orange (circular orbit).

5.4 Upsilon Andromedae b

Piskorz et al. 2017 reported the direct detection of upsilon Andromedae b at a K_p of 55 ± 9 km/s using 7 epochs of Keck/NIRSPEC L band data, 3 epochs of K band data covering the left-hand side of the detector, and 3 K band epochs covering the right-hand side of the detector. For this work, we will again just consider the L band epochs.

Correction to Piskorz et al. 2017 Results

Piskorz et al. 2017 approximated the orbit of ups And b as circular, and so reported mean anomaly M values, rather than true anomaly f values, because they would be the same in the circular limit. We find, however, that there was a systematic error in the calculation of the secondary velocities that stemmed from a mismatch between the zero points used in Equations 5.3 and 5.2. This resulted in a net error comparable to mean anomalies roughly -3.3% offset from their true values. Table 5.3 lists the mean anomalies used in Piskorz et al. 2017 and the corrected anomalies measured from pericenter, calculated using orbital parameters from Wright et al. 2009.

Figure 5.5 shows how these offsets affect the resulting log likelihood curve from the seven epochs of ups And NIRSPEC L band data. The originally published log likelihood curve is in red and is reproduced in black dashed. The corrected log likelihood curves are shown in blue (eccentric orbit) and orange (circular orbit). As in the case of HD 88133 b, we can see here that for low-eccentricity orbits, there is no benefit to considering an eccentric orbit rather than assuming a circular one.

Table 5.3: ups And b Epoch Positions

Date	Piskorz et al. 2017	This work	
	M	M	f
2011 Sep 6	1.54	1.33	1.36
2011 Sep 7	2.90	2.69	2.70
2011 Sep 9	5.45	5.24	5.21
2013 Oct 27	3.71	3.50	3.49
2013 Oct 29	0.13	6.20	6.20
2013 Nov 7	6.22	6.01	6.01
2014 Oct 7	1.99	1.78	1.81

Ups And Simulations

We were interested in running similar simulations to those run for HD88133 in Section 5.3 to see whether the peak at ~55 km/s can be substantiated. We are particularly curious about whether we could expect the planetary peak to be as strong as it appears in Figure 5.5 since ups And, like HD88133, has a large stellar radius ($1.7053529^{+0.1024430}_{-0.0621246}$ $R_\odot$, Gaia Collaboration et al., 2018).

Generation of Simulated Data

We generate ups And simulated data as described in Section 5.3. For these simulations, we use a stellar model generated from the PHOENIX stellar model grid (Husser et al., 2013) interpolated to an effective temperature of 6213 K, a metallicity of 0.12, and a surface gravity of 4.25 (Valenti & Fischer, 2005). We assume a stellar radius of 1.7053529 $R_\odot$ (Gaia Collaboration et al., 2018) and a planetary radius of 1.0 R_{Jup} unless otherwise stated. The simulated data are continuum corrected with a third-order polynomial fit from 2.8 to 4.0 μm in wavenumber space.

We rotationally broaden the stellar model with a stellar rotation rate of 9.62 km/s (Valenti & Fischer, 2005) and limb darkening coefficient of 0.29 (Claret, 2000). The FWHM of the instrumental kernels of NIRSPEC1.0 and NIRSPEC2.0 are about 12 and 7.3 km/s, respectively, so while rotational broadening makes little difference to data from NIRSPEC1.0, it would have a larger effect on data from the upgraded NIRSPEC instrument.

The stellar spectral model used to analyze the ups And L band data in Piskorz et al. 2017 was not from the PHOENIX grid. Instead, they used a model similar to that described in Lockwood et al. 2014. It was generated from a recent version of the LTE line analysis code MOOG (Sneden, 1973) and the MARCS grid of stellar atmospheres (Gustafsson et al., 2008). Notably, individual abundances were set by matching observed lines for elements that were well measured by NIRSPEC. While tests run on both Tau Boo and ups And NIRSPEC1.0 L band data show that stellar models generated this way are able to measure the true stellar velocities at each epoch with higher likelihoods than PHOENIX stellar models, because these models are generated without a continuum, they cannot be used to generate simulated data. Further, because they rely on fits to NIRSPEC1.0 observational data, they could not be used to generate simulated data outside of the NIRSPEC1.0 order wavelengths. Therefore, we are limited to the PHOENIX stellar model.

We use a planetary model from the SCARLET planetary spectral modeling framework (Benneke, 2015) without a thermal inversion. The planetary model used in the original work was also from the SCARLET framework, but did include a thermal inversion. We decide to run simulations with a non-inverted planetary model because most recent hot Jupiter atmospheric studies are finding non-inverted thermal structures (e.g., Birkby et al., 2017; Piskorz et al., 2018; Pelletier et al., 2021).

We use orbital positions f from the final column of Table 5.3, Wright et al. 2009 orbital parameters, and a K_p of 55 km/s in Equation 5.2 to determine the secondary velocities at each epoch. The primary velocities at each epoch are -49.7, -49.4, -48.9, -30.5, -29.6, -25.4, and -39.2 km/s.

Gaussian noise is added at the level of the data (total S/N per pixel = 18192).

Planetary Radius Simulations

As for HD88133b, we first run simulations with an increasing planetary radius. Figure 5.6 shows the results of these simulations with the planetary radius increasing from 1.0 to 4.0 R_{Jup} in increments of 0.5 R_{Jup}. Table 5.4 report the parameters from Gaussian fits to the log likelihood curves. While Gaussian models can reliably measure a peak centered around the input K_p, the R^2 values show that a Gaussian model would not be justified until at least a planetary radius of 3.5 to 4.0 R_{Jup}. While transiting hot Jupiters have been observed with radii approaching 2 R_{Jup} (e.g., KELT-26 b, Rodríguez Martínez et al., 2020), it is improbable that ups And b would have a radius larger than that. These simulations, therefore, do not suggest that, with a reasonable radius, ups And b could be well detected in the 7 original NIRSPEC1.0 L band epochs.

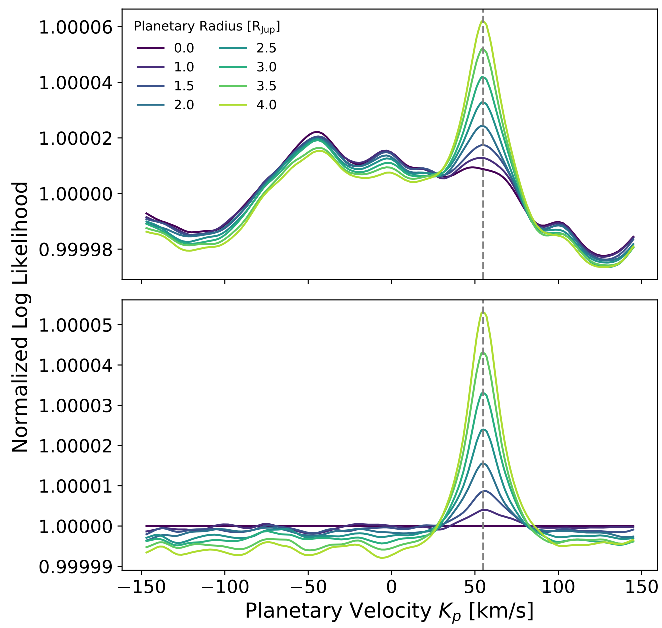

Figure 5.6: Ups And simulations showing the effects of increasing planetary radius. The simulations approximate NIRSPEC1.0 L band data with the orbital phases (f) and primary velocities from the original 7 epochs of data. The bottom panel shows each log likelihood result with the structured noise curve (R_{pl} = 0) subtracted off.

Upgraded NIRSPEC Simulations

The ups And NIRSPEC2.0 simulations are set up the same way as the HD88133 NIRSPEC2.0 simulations with one exception. Because ups And (K = 2.9) is much brighter than HD88133 (K = 6.2), we assume a S/N per pixel per epoch of 9000, or a total S/N per pixel of 23800, across the 7 epochs. At the average S/N of 6530 per pixel in the NIRSPEC1.0 data, we were already well into the regime where structured noise far outweighs white noise, so anything more should make little to no difference to the results.

Figure 5.7 shows a clear peak at the input K_p of 55 km/s. It does, coincidentally, fall at the same position as a structured noise peak (in light purple), suggesting that its significance could be overestimated. Any other value of K_p would result in a weaker peak that would need to be distinguished, through some mechanism, from the noise peak at ~ 55 km/s. With the input K_p at 55 km/s, a Gaussian model reports a fit at 57 ± 7 km/s with a height of 2.1σ.

This result is encouraging in that it implies that NIRSPEC2.0 would have allowed a multi-epoch detection of ups And b with the exact seven epochs presented in Piskorz et al. 2017 even with a planetary radius of 1 R_{Jup}.

Table 5.4: Gaussian Fits to Ups And Planetary Radius Simulations

R_{pl} [R_{Jup}]	K_p [km/s]	ΔK_p [km/s]	Peak Height [σ]	R^2
Without Star Subtraction				
1.0	50	12	0.7	0.01
1.5	52	12	1.1	0.07
2.0	53	11	1.6	0.15
2.5	53	11	2.2	0.27
3.0	54	11	2.8	0.38
3.5	54	11	3.7	0.52
4.0	54	11	4.5	0.61
With Star Subtraction				
1.0	58	12	7.4	0.81
1.5	56	12	19.6	0.96
2.0	55	11	25.1	0.97
2.5	55	11	36.5	0.98
3.0	55	11	44.3	0.99
3.5	55	12	54.3	0.99
4.0	55	12	47.2	0.98

These simulations were all run with an input K_p of 55 km/s. Prior to fitting, these log likelihood results are subtracted by the mean of their values from -150 to 0 km/s. The Gaussian model is initiated with a 55 km/s center and 10 km/s standard deviation. The Gaussian peak height is reported over σ, which is measured as the standard deviation of the log likelihood structure more than $3\Delta K_p$ above or below the best-fit Gaussian center, where ΔK_p is the standard deviation of the best-fit Gaussian model.

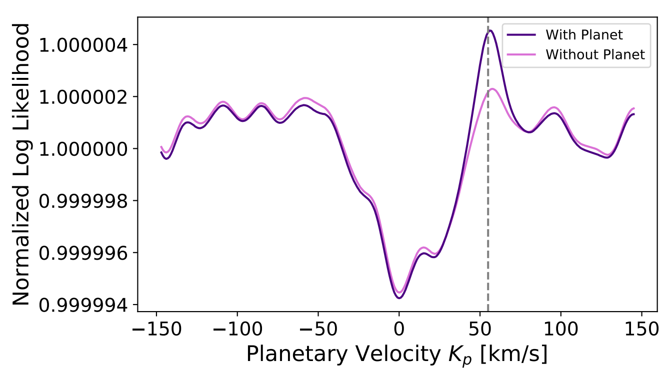

Figure 5.7: NIRSPEC2.0 simulation of ups And with the same orbital phases (f) and primary velocities as in the original data.

Near-Zero Primary Velocity Simulations

Because of its relatively large systematic velocity of -28.59 km/s (Nidever et al., 2002), ups And never reaches a primary velocity of 0 km/s. The nearest its primary velocity gets to zero is -2 km/s in late January/early February every year. During this time of year, it would be accessible from Keck during the first few hours of the night, setting, in early February, at around 7 UT. This would optimistically allow for an hour and a half on target after telescope focusing on a good night. Because ups And is a very bright source, enough S/N could be achieved to enter the regime where structured noise, rather than random noise, dominates very quickly. PCA-based telluric correction approaches, like those used in Piskorz et al. 2016 and Piskorz et al. 2017, require enough observation time to witness variation in the telluric spectrum. We run the following simulations assuming that the time before ups And sets would be enough to witness telluric variation sufficient to be picked up by PCA or that the data could be well telluric corrected by another approach. Then, these simulations are run with either the NIRSPEC1.0 or NIRSPEC2.0 set up and with the same orbital phases (f) as were in the original data, but with primary velocities at each epoch of -2 km/s.

Figure 5.8 shows the results of these simulations with the NIRSPEC1.0 results in the top panel and the NIRSPEC2.0 results in the bottom panel. Both configurations show strong features at the input K_p values, with the NIRSPEC2.0 result especially strong and unaltered, in shape, by adjacent structured noise features. A Gaussian model reports a fit to the NIRSPEC2.0 result of 56 ± 8 km/s with a height of 10.8σ. While the 7 L band epochs could have provided a confident planetary detection if taken with NIRSPEC2.0 as is, if they had been taken following the recommendations of Buzard et al. 2021, with near-zero primary velocities, they could have presented a very strong detection and a chance for further atmospheric characterization (e.g., Finnerty et al., 2021).

5.5 Discussion

In this work, we reevaluated the multi-epoch detections of HD 88133 b (Piskorz et al., 2016) and ups And b (Piskorz et al., 2017), correcting for errors in the estimated orbital positions at the observation times. Unfortunately, we find that the data is insufficient to report planetary detections or measurements of K_p in either case. Multi-epoch detections with small data sets have always been a risk; stellar radial velocity measurements are now made with tens, if not hundreds, of epochs.

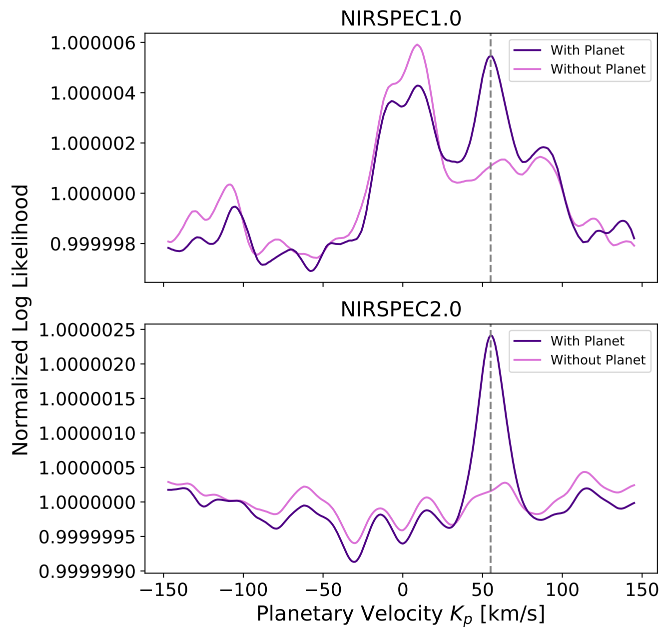

Figure 5.8: Ups And simulations with the same orbital phases (f) as the original data, but with primary velocities in each epoch equal to −2 km/s. The simulations in the top panel approximate NIRSPEC1.0 data and those in the bottom panel approximate NIRSPEC2.0 data.

HD 88133 b and ups And b were two particularly difficult planets to target. Both orbit very large stars, resulting in planet-to-star contrasts lower than those of typical hot Jupiters. At high resolution, the planet/star photospheric contrast provides an upper bound for the spectroscopic information content and thus gives only a first check on how easily detectable planets may be. Predictions of the line-to-continuum, or spectroscopic, contrasts, which can be significantly lower than photospheric contrasts, would provide a more useful guide to direct detection studies; but are highly dependent on the nature of atmospheric chemistry, in particular whether hazes are present, and thermal structure, meaning that model predictions will have large uncertainties. Here we consider photospheric contrasts as a first glimpse into why the spectroscopic detections of HD 88133 b and ups And b may have been so elusive. Measuring photospheric contrast as the mean ratio of planetary flux to stellar flux across the L band, we estimate planet-to-star contrasts for HD 88133 b and ups And b as 2.3×10^{-4} and 2.5×10^{-4}, respectively, with an assumed radius of 1 R_{Jup} for each planet. By comparison, HD 187123 b, studied in Buzard et al. 2020, has an expected L band contrast of 1.4×10^{-3}, and Tau Boo b, studied in Lockwood et al. 2014, has an expected contrast somewhere between 1.1-1.5$\times10^{-3}$, depending on whether or not water is included in its model spectrum (see Pelletier et al. 2021 for a discussion into water on Tau Boo b). Each of these planets has a contrast nearly an order of magnitude larger than do HD 88133 b and ups And b. Our radius simulations show that in each case, a planetary radius of $\gtrsim$3 R_{Jup} would have allowed for a strong detection. As planet-to-star contrast increases with R^2_{pl}, a radius of 3 R_{Jup} would increase their contrasts nearly the order of magnitude needed to be comparable to HD 187123 b and Tau Boo b.

We considered whether the upgrade to the NIRSPEC instrument (Martin et al., 2018) or the near-zero primary velocity observing strategy presented by Buzard et al. 2021 would have allowed for enough reduction in structured noise to reveal these low-contrast signals. The combination of both would offer a stronger chance of detection in both cases. Near-zero primary velocity epochs obtained with NIRSPEC2.0 would have allowed for K_p measurements of HD 88133 b as 22 ± 20 km/s with a height of 3.2σ (input K_p = 40 km/s) and of ups And b as 56 ± 8 km/s with a height of 10.8σ (input K_p = 55 km/s). Several factors could explain why ups And b could be much more strongly detected under these conditions. It was observed with 7 epochs while HD 88133 b was observed with 6. Additionally, while both stars have large radii, ups And A is not quite as large as HD 88133 A (1.7053529 vs. 2.20 $R_\odot$). Perhaps most importantly, ups And A has a higher effective temperature than HD 88133 A (6213 vs. 5438 K). The cooler a stellar effective temperature, the more complex its spectrum will be. Therefore, HD 88133 A would have a more complex spectrum that would allow for more correlation between the stellar component of the data and the planetary spectral model used for cross correlation that gives rise to the structured noise in the final log likelihood results. Additionally, ups And A not only has a less complex spectrum, but also one that is rotationally broadened. The stellar rotational broadening would also work to lessen the degree of correlation between the planetary model and the stellar component of the data. A smaller factor could be the total S/N. Ups And is a much brighter system, and so was simulated with a higher total S/N of 238000 compared to 7000 for HD88133b. Both cases are in a regime where structured noise outweighs white noise, though, so this is not likely a major contributor. Collectively, these factors all work to make ups And b more easily detectable than HD 88133 b. Though, even ups And b was below the detection limit with a small number of NIRSPEC1.0 L band epochs.

The upgrade to the NIRSPEC instrument will provide a significant advantage to multi-epoch planetary detection, due to its increases in both resolution and spectral grasp (Finnerty et al., 2021). However, in these difficult cases, it might be worthwhile to consider new observational approaches altogether. Since white noise does not appear to be the limiting factor in these multi-epoch studies, we could consider an observational campaign on a smaller telescope (for example, UKIRT) that could dedicate more nights to this work. Another approach could be to consider an instrument like IGRINS or GMTNIRS which could simultaneously afford both a higher spectral resolution than NIRSPEC and a wider wavelength coverage, both of which are beneficial for planet detectability (Finnerty et al., 2021). Many of these instruments are optimized for shorter wavelengths ($< 2.5\mu$m) than we have observed with NIRSPEC. As such, careful work into the optimal observing strategies as well as instrument settings will be crucial in the multi-epoch approach's journey beyond NIRSPEC.

Ultimately, we want to stress the importance of using simulations in multi-epoch work. Simulations are essential for understanding the origin and structure of the expected noise in high-resolution data, considering both white noise and any structured noise that may arise in cross correlation space. They can offer realistic estimates for the overall sensitivity of the data beyond expectations from a shot noise limit. As such, simulations can and should be used in many ways, e.g., for planning observations (e.g., Buzard et al., 2021), for identifying and reducing sources of structured noise (Buzard et al., 2020), and for evaluating approaches of atmospheric characterization (e.g., Finnerty et al., 2021).

Despite its challenges, the NIRSPEC multi-epoch approach has been used to characterize planetary atmospheric structure. Piskorz et al. 2018 combined the multi-epoch detection of KELT-2A b with Spitzer secondary eclipse data. They found that the multi-epoch data provided roughly the same constraints on metallicity and carbon-to-oxygen ratio as the secondary eclipse data. Further, while the secondary eclipse data provided a stronger constraint on f, the stellar incident flux which is a rough measure of energy redistribution, the multi-epoch data constrained it to low values, with a 50% confidence interval at 1.26. As models with $f \gtrsim 1.5$ show a temperature inversion, this indicates that using NIRSPEC1.0 multi-epoch data alone, Piskorz et al. 2018 were able to determine that KELT-2A b has a non-inverted thermal structure in the regions probed by $\sim$3 μm data. Finnerty et al. 2021 used NIRSPEC2.0 L band simulations to look more deeply into the atmospheric constraints that could be made with multi-epoch data and found that warm Jupiters' ($T_{\rm eq} \sim 900$ K) carbon-to-oxygen ratios could be constrained enough to differentiate between substellar, stellar, and superstellar values. While planetary detection using the multi-epoch approach can a challenging pursuit, once the true planetary peak has been identified, the approach holds potential for detailed atmospheric characterization.

5.6 Conclusion

In this work, we present and correct errors in the multi-epoch detections of HD 88133 b (Piskorz et al., 2016) and ups And b (Piskorz et al., 2017). Unfortunately, we find that the original NIRSPEC1.0 L band data presented (6 epochs for HD 88133 b, 7 for ups And b) are insufficient for planetary detections. We run simulations to determine what would have been required for confident detections. Ups And b could have been strongly detected (10.8σ) if its seven L band epochs had been taken with the upgraded NIRSPEC instrument and following the near-zero primary velocity observing strategy presented by Buzard et al. 2021. HD 88133 b would be more difficult to detect, because of its larger stellar radius and lower stellar effective temperature, and would likely have required more, carefully timed, data.

References

Beatty, T. G., Pepper, J., Siverd, R. J., et al. 2012, *ApJL*, 756, L39, doi: 10.1088/2041-8205/756/2/L39

Benneke, B. 2015, arXiv e-prints, arXiv:1504.07655. https://arxiv.org/abs/1504.07655

Birkby, J. L., de Kok, R. J., Brogi, M., Schwarz, H., & Snellen, I. A. G. 2017, *AJ*, 153, 138, doi: 10.3847/1538-3881/aa5c87

Brogi, M., Giacobbe, P., Guilluy, G., et al. 2018, *A&A*, 615, A16, doi: 10.1051/0004-6361/201732189

Brogi, M., & Line, M. R. 2019, *AJ*, 157, 114, doi: 10.3847/1538-3881/aaffd3

Brogi, M., Snellen, I. A. G., de Kok, R. J., et al. 2012, *Nature*, 486, 502, doi: 10.1038/nature11161

Bryan, M. L., Knutson, H. A., Howard, A. W., et al. 2016, *ApJ*, 821, 89, doi: 10.3847/0004-637X/821/2/89

Butler, R. P., Wright, J. T., Marcy, G. W., et al. 2006, *ApJ*, 646, 505, doi: 10.1086/504701

Buzard, C., Pelletier, S., Piskorz, D., Benneke, B., & Blake, G. A. 2021, *AJ*, 162, 26, doi: 10.3847/1538-3881/abf7b9

Buzard, C., Finnerty, L., Piskorz, D., et al. 2020, *AJ*, 160, 1, doi: 10.3847/1538-3881/ab8f9c

Charbonneau, D., Brown, T. M., Latham, D. W., & Mayor, M. 2000, *ApJL*, 529, L45, doi: 10.1086/312457

Claret, A. 2000, *A&A*, 363, 1081

Cochran, W. D., Fabrycky, D. C., Torres, G., et al. 2011, *ApJS*, 197, 7, doi: 10.1088/0067-0049/197/1/7

Finnerty, L., Buzard, C., Pelletier, S., et al. 2021, *AJ*, 161, 104, doi: 10.3847/1538-3881/abd6ec

Fischer, D. A., Laughlin, G., Butler, P., et al. 2005, *ApJ*, 620, 481, doi: 10.1086/426810

Fulton, B. J., Petigura, E. A., Blunt, S., & Sinukoff, E. 2018, *PASP*, 130, 044504, doi: 10.1088/1538-3873/aaaaa8

Gaia Collaboration, Brown, A. G. A., Vallenari, A., et al. 2018, *A&A*, 616, A1, doi: 10.1051/0004-6361/201833051

Guilluy, G., Sozzetti, A., Brogi, M., et al. 2019, *A&A*, 625, A107, doi: 10.1051/0004-6361/201834615

Gustafsson, B., Edvardsson, B., Eriksson, K., et al. 2008, *A&A*, 486, 951, doi: 10.1051/0004-6361:200809724

Husser, T. O., Wende-von Berg, S., Dreizler, S., et al. 2013, *A&A*, 553, A6, doi: 10.1051/0004-6361/201219058

Jontof-Hutter, D., Lissauer, J. J., Rowe, J. F., & Fabrycky, D. C. 2014, *ApJ*, 785, 15, doi: 10.1088/0004-637X/785/1/15

Lockwood, A. C., Johnson, J. A., Bender, C. F., et al. 2014, *ApJL*, 783, L29, doi: 10.1088/2041-8205/783/2/L29

Martin, E. C., Fitzgerald, M. P., McLean, I. S., et al. 2018, in Society of Photo-Optical Instrumentation Engineers (SPIE) Conference Series, Vol. 10702, Ground-based and Airborne Instrumentation for Astronomy VII, ed. C. J. Evans, L. Simard, & H. Takami, 107020A

Ment, K., Fischer, D. A., Bakos, G., Howard, A. W., & Isaacson, H. 2018, *AJ*, 156, 213, doi: 10.3847/1538-3881/aae1f5

Mortier, A., Santos, N. C., Sousa, S. G., et al. 2013, *A&A*, 557, A70, doi: 10.1051/0004-6361/201321641

Murray, C. D., & Dermott, S. F. 1999, Solar system dynamics

Nidever, D. L., Marcy, G. W., Butler, R. P., Fischer, D. A., & Vogt, S. S. 2002, *ApJS*, 141, 503, doi: 10.1086/340570

Nugroho, S. K., Kawahara, H., Masuda, K., et al. 2017, *AJ*, 154, 221, doi: 10.3847/1538-3881/aa9433

Pelletier, S., Benneke, B., Darveau-Bernier, A., et al. 2021, arXiv e-prints, arXiv:2105.10513. https://arxiv.org/abs/2105.10513

Piro, A. L., & Vissapragada, S. 2020, *AJ*, 159, 131, doi: 10.3847/1538-3881/ab7192

Piskorz, D., Benneke, B., Crockett, N. R., et al. 2016, *ApJ*, 832, 131, doi: 10.3847/0004-637X/832/2/131

—. 2017, *AJ*, 154, 78, doi: 10.3847/1538-3881/aa7dd8

Piskorz, D., Buzard, C., Line, M. R., et al. 2018, *AJ*, 156, 133, doi: 10.3847/1538-3881/aad781

Rodríguez Martínez, R., Gaudi, B. S., Rodriguez, J. E., et al. 2020, *AJ*, 160, 111, doi: 10.3847/1538-3881/ab9f2d

Sneden, C. 1973, *ApJ*, 184, 839, doi: 10.1086/152374

Snellen, I. A. G., Brandl, B. R., de Kok, R. J., et al. 2014, *Nature*, 509, 63, doi: 10.1038/nature13253

Snellen, I. A. G., de Kok, R. J., de Mooij, E. J. W., & Albrecht, S. 2010, *Nature*, 465, 1049, doi: 10.1038/nature09111

Thorngren, D. P., & Fortney, J. J. 2018, *AJ*, 155, 214, doi: 10.3847/1538-3881/aaba13

Valenti, J. A., & Fischer, D. A. 2005, *ApJS*, 159, 141, doi: 10.1086/430500

Vissapragada, S., Jontof-Hutter, D., Shporer, A., et al. 2020, *AJ*, 159, 108, doi: 10.3847/1538-3881/ab65c8

Wright, J. T., Upadhyay, S., Marcy, G. W., et al. 2009, *ApJ*, 693, 1084, doi: 10.1088/0004-637X/693/2/1084

Zucker, S. 2003, *MNRAS*, 342, 1291, doi: 10.1046/j.1365-8711.2003.06633.x

Chapter 6

CHOICES ALONG THE MULTI-EPOCH ANALYTIC PATHWAY

6.1 Introduction

The multi-epoch method of directly detecting exoplanet emission is a complicated technical process, and as such, requires much care and attention. In this chapter, we break up the approach into its three successive components: physical, instrumental, and analytic, and outline some of the major choices to be made in each category.

The physical component considers what set up of the exoplanet system offers the best chance of detection. The planetary orbital position and barycentric velocity, the latter of which affects the systematic velocity at the time of observation, are major physical properties to consider when planning observations.

Instrumental considerations include the wavelength band and grasp observed, the spectral resolution of the observations, and the length of each observation.

Analytic considerations, the most extensive of the three, include, for example, how the data is reduced, how the wavelength solution is determined, how telluric features are corrected, and which stellar and planetary spectral models are used for cross correlation.

6.2 Physical Considerations

Planetary Orbital Position

The choice of observation date and time will determine the position of the planet on its orbit, following the equation,

$$M(t_{\text{obs}}) = \frac{t_{\text{obs}} - t_o}{P} \mod P, \tag{6.1}$$

where t_{obs} is the observation time, reported in Julian date, t_o is a reference time, and P is the orbital period, measured in days. If t_o is set at the time of inferior conjunction, $M = 0, 0.5$ correspond to conjunction and should show $v_{sec} = v_{pri}$, and $M = 0.25, 0.75$ correspond to quadrature and should show the largest relative velocity offset between the planet and the star.

Quadrature Epochs

There are several factors to consider in selecting orbital positions. In the multi-epoch technique, a two-dimensional cross correlation uses line-of-sight velocities to tease apart the stellar and planetary signals. From this perspective, quadrature ($M = 0.25, 0.75$) epochs seem the most appealing as they provide the largest velocity separation between the stellar and planetary signals. Additionally, at quadrature, the planet's line-of-sight acceleration is the slowest. This means that at quadrature, we can afford to take slightly longer observations—to either build up a higher signal-to-noise or to obtain a longer baseline to support telluric corrections—without worrying that the planetary signal will shift across detector pixels, leading to a weaker signal overall and a broadened K_p detection.

We can estimate the change in planetary line-of-sight velocity at an epoch with the equation,

$$\Delta v_{sec} = 2K_p \sin\left(\frac{\pi h_{obs}}{P_{hr}}\right) \cos(2\pi M_{obs}^{cent}), \tag{6.2}$$

where h_{obs} is the length of the observation in hours, P_{hr} is the orbital period is hours, and M_{obs}^{cent} is the orbital phase at the center of the observation. We note that this equation measures the difference between the start and end positions of the planet. If the center of the observation is at quadrature, $\Delta v_{sec} = 0$ because the planet starts and ends at a common velocity. If an observation passes through either $M = 0.25$ or 0.75, then, this equation should be broken up into the portions before and after quadrature.

This equation makes a few assumptions. First, that the planet is on a circular orbit. Second, that the change in the barycentric velocity over the observation is negligible, which is a very reasonable assumption since the maximum change in barycentric velocity over 12 hours, longer than any ground-based observation, is around 0.3 km/s.

As an example, for a planet with a 3-day orbital period and a Keplerian orbital velocity, K_p, of 100 km/s, in an 5-hour observation centered around conjunction, the planetary line-of-sight orbital velocity would change by 43.3 km/s. The smallest change in velocity would happen during an epoch centered at quadrature, when the planetary signal would shift in one direction during half of the observation and back during the other half. For the same system, the smallest change in planetary velocity, from 2.5 hours before quadrature to quadrature itself, before the planet signal starts shifting back, would be only 2.4 km/s. The signal-to-white noise per observation and telluric correction procedures benefit from longer observations, while the instrumental resolution limits the acceptable change in planetary velocity over the observation, therefore limiting the observation length. We will discuss each of these factors in future sections. These calculation do show, though, that quadrature epochs offer not only the largest separation between planetary and stellar signals, but also an opportunity to take the longer observations without having the planetary signal diminish by shifting over detector pixels.

Day-Side Epochs

Recent high-resolution spectroscopic investigations of hot Jupiters have considered how the signatures of tidally locked planets may change versus orbital position. In other words, if their day- and night-sides show different chemical and physical properties, their day- and night-side spectra may look very different. Brogi et al. 2012, and other CRIRES-style detections, have targeted the day-side, seen at secondary eclipse, under the assumption that the brighter day-side should be easier to detect that the fainter night-side. From this perspective, day-side epochs (between $M = 0.25$ and 0.75) may allow stronger detections, though simulations could be run to determine how the increase from a larger fraction of visible day-side moving towards superior conjunction ($M = 0.5$) and the decrease from smaller relative velocity between the planetary and stellar features trade off.

Further, high-resolution spectroscopy can also be used to gain information about planetary atmospheric motion. In high-resolution CRIRES data from the hot Jupiter, HD 209458 b, Snellen et al. 2010 found hints of weak day-to-night side winds. Beltz et al. 2021 asked whether the atmosphere's three-dimensional structure could be further constrained by fitting CRIRES data of the HD 209458 b with three-dimensional atmospheric circulation models that considered temperature structure and atmospheric motion, such as winds and planetary rotation, rather than one-dimensional models. They found an increase in the detection significance of at least 1.8σ with three-dimensional models, with the primary improvement coming from the inclusion of a 3D temperature structure which varies spectral feature depths relative to what one would expect from a 1D temperature structure, and secondary improvements from chemistry and Doppler effects. The multi-epoch analysis and simulation framework has not, to date, considered differences in the planetary spectra as a function of planetary orbital phase. Inclusion of such planetary spectral variations as a function of orbital phase in the simulation framework could more strongly indicate certain orbital positions as the most effective for planetary detection, and thus support the planning of future observations. Three-dimensional atmospheric models could also be considered in cross correlating the data; we will describe how this could be done in Section 6.4.

Barycentric Velocity

The barycentric velocity is the portion of the Earth's orbital motion in the direction of the target system. It depends on the target's right ascension and declination, as well as the time of observation. We incorporate the barycentric velocity into the primary velocity, as

$$v_{pri} = v_{sys} - v_{bary}, \tag{6.3}$$

where v_{sys} is the systemic velocity, the relative velocity between the system's center-of-mass and the Solar System's center-of-mass. We do not consider the stellar reflex motion because it is below the velocity resolution of most near-infrared high resolution instruments (NIRSPEC2.0 $\sim$ 3 km/s), typically on the order of 0.1–0.01 km/s.

In Buzard et al. 2021a, we found that primary velocities near 0 km/s lead to the strongest planetary detections, on average more than twice the significance of detections made with randomly selected primary velocities. This trend grew even stronger with cooler host stars. Observing nights should be chosen then, when possible, when the barycentric velocity (nearly) cancels out the systematic velocity.

During such epochs, the host stellar spectrum is aligned with the telluric frame. These results came from simulations of a hot Jupiter-like planet with a Keplerian orbital velocity, K_p, of 75 km/s. As we look to planets on longer orbits, with smaller values of K_p, or to cooler planet temperatures, near-zero primary velocity epochs may no longer be as advantageous. Smaller values of K_p would bring the planetary spectrum closer to the stellar (and telluric) frame. This could make telluric correction more difficult, especially for cooler planets which are more spectroscopically similar to our telluric atmosphere. The suggestion of near-zero primary velocity epochs should, therefore, be taken with care as we move on to new planet populations.

6.3 Instrumental Considerations

Wavelength Region

The wavelength region covered by observations will, of course, be highly relevant to the results that can be gleaned. Notably, different molecules have features at different wavelengths, or infrared bands. Water and methane have features arising in the L band ($\sim 3-3.5$ μm), while carbon monoxide has major band heads in the K band (~ 2.3 μm) and M band (~ 4.7 μm). The peak of the planet's emission, and therefore the highest photospheric planet-to-star contrast can be estimated from the effective temperature of the planet. A black body's peak emission wavelength can be estimated as $\lambda T \approx 2900$ μmK. While hot Jupiters peak in the L band at ~ 3 μm, Earth peaks at ~ 10 μm. As we push to cooler planet populations, we will likely need to move to longer wavelengths.

There are several factors beyond the position of expected planetary features and wavelength-dependent planet-to-star contrast that could make detecting planets at different wavelengths harder or easier. Data from any ground-based telescope will be plagued by telluric contamination. While saturated tellurics remove any chance of detecting planetary features, nonsaturated tellurics could lead to significant saturated noise from correlation with the planet model. Additionally, different wavelength regions may show more or less correlation between the stellar and planetary features, the majority of noise structure we have seen in simulations. Simulations will be the best way to find optimal wavelengths regions to observe. de Kok et al. 2014 ran $1-5$ μm simulations for the CRIRES-style approach and saw that some portions of the L band offer the possibility of detecting H_2O, CH_4,CO_2,C_2H_2, and HCN a factor of $2-3$ stronger than the then-current K band detections in the same integration time. Similar full $1-5\mu$m simulations of the multi-epoch technique would be extremely helpful for planning future NIRSPEC observations. One limitation to the simulation framework presented in this thesis is that it depends strongly on the wavelength axis and position of saturated tellurics taken directly from data. We have found that running the simulations with an evenly spaced wavelength axis and with positions of saturated tellurics taken from models result in different log likelihood structures (see Figure 2.4). To extend our simulations, we observed data from bright standards on July 28, 2020 across the full L and M bands with NIRSPEC2.0. Standard observations covering nearly the full K band should be available from, for example, Piskorz et al. 2017. These observations could be used as a basis for KLM band simulations.

Moving beyond NIRSPEC, Finnerty et al. 2021 showed that doubling the spectral grasp of an observation nearly doubles the planetary detection strength. This implies that instruments like IGRINS (simultaneous HK coverage) or SPIRou (simultaneous JHK coverage) could offer significant improvements to multi-epoch detection strengths from NIRSPEC (fraction of a band at once), even on smaller, less stable telescopes. As described in Section 6.3, our current NIRSPEC observations are dominated by structured noise rather than shot noise. A smaller telescope would add to the shot noise, but broader coverage would likely decrease the structured noise. The structured noise that we have focused on comes from correlation between the stellar signal in the data and the planetary template. With broader coverage, more of both spectra are seen, and because the two spectra are different, the correlation between the two, and the resulting structured noise, will decrease. Thus, where broad simultaneous wavelength coverage is possible, it should be taken, and where not, simulations should be used to direct the choice of wavelength range.

Spectral Resolution

Instrumental spectral resolution is a crucial factor in any spectroscopic study of a planetary atmosphere. At high resolution, spectral lines do not blend, so we can measure the true depth, width, and plurality of lines (e.g., see Figure 2 in Birkby, 2018), all of which are dependent on three-dimensional atmospheric structure, including rotation and winds. Further, each IR-active molecule has a distinct rovibrational spectrum across the near-infrared wavelengths. By fully resolving the near-IR spectrum, we can elucidate the distinct signatures of each molecule, and be confident in the detection/non-detection of each molecular species.

The multi-epoch approach has been applied to data in the $R \approx 25,000 - 40,000$ range and the single-night, or CRIRES-style, approach has been applied to data from $R \approx 50,000$ (with GIANO, e.g., Guilluy et al., 2019) to $100,000$ (with CRIRES, e.g., Brogi et al., 2012). Recall that the main difference between these approaches is that the multi-epoch version utilizes observations during which the planetary signal does not shift across detector pixels, while the CRIRES-style version wants the planetary signal to move. Whether the planetary signal crosses detector pixels during an observation depends on the instrumental resolution and the change in planetary line-of-sight motion over the observation (as described in Section 6.2). The multi-epoch technique requires the change in planetary line-of-sight velocity be smaller than the velocity resolution of the instrument, and the CRIRES-style technique requires it to be larger. In fact, the CRIRES-style technique often requires the planetary signal to cross multiple pixels for principal component analysis based techniques to cleanly separate the planetary signal from the telluric and stellar spectral components. As an example, the signal from Tau Boo b crossed around 15 SPIRou pixels in a 5-hour observation (Pelletier et al., 2021). In mathematical terms, the multi-epoch approach aims for

$$\Delta v_{sec} < 1 \text{ pixel}, \tag{6.4}$$

while the CRIRES-style approach requires

$$\Delta v_{sec} \gtrsim 15 \text{ pixels}. \tag{6.5}$$

We can estimate the size of a detector resolution element as c/R, where c is the speed of light. The number of pixels per resolution element, which we will call b, varies by instrument, but is typically around $2-3$ for these near-infrared high-resolution spectrometers. Then, plugging in Equation 6.2 for the change in planetary line-of-sight velocity, we can relate the number of pixels we want the planetary signal to cross (n_{pix}) to the necessary resolution (R), given parameters of the system (K_p, P_{hr}) and observation (h_{obs}, M_{obs}^{cent}).

$$R = \frac{n_{pix}c}{\Delta v_{sec} b} = \frac{n_{pix}c}{2K_p \sin(\pi h_{obs}/P_{hr}) \cos(2\pi M_{obs}^{cent}) b}. \tag{6.6}$$

The multi-epoch approach works best when $R_{\text{instr}} < R(n_{pix} = 1)$, and the CRIRES approach works best when $R_{\text{instr}} \gtrsim R(n_{pix} = 15)$.

For a 5-hour observation of a typical hot Jupiter, such as the example we describe above, with an orbital period of 3 days and a K_p of 100 km/s, either technique could be applied. For the planet to cross 15 pixels ($b = 3$ pixels/resolution element) when it is near quadrature, the instrument would need a resolution of nearly 3×10^5. With the current maximum resolution of ground based near-infrared instruments of $\sim 1 \times 10^5$, the multi-epoch approach would be much more capable of detecting this planet near quadrature. On the other hand, near conjunction, an instrument would need a resolution below about 2.3×10^3 to prevent the planet from crossing any detector resolution elements. The CRIRES-style approach would be better suited for near conjunction epochs.

This does imply, though, that not all orbital positions for hot Jupiter-like planets could be appropriately studied via the multi-epoch technique. Epochs near quadrature would need to be broken apart and considered separate epochs. If not, significant error could arise from the uncertainty in orbital position (see Section 6.4). In the case of the HD 88133 b multi-epoch data set published by Piskorz et al. 2016, if HD 88133 b actually had a K_p of 40 km/s (see Buzard et al. 2021b), over the course of the six NIRSPEC1.0 observations, the planet would cross roughly 0.3 to 1.2 resolution elements. If it had the maximum K_p of 153 km/s (calculated with parameters from Luhn et al. 2019), which would correspond to an edge-on orbit, the planet would cross 0.8 to 4.5 resolution elements in the six observations. In this case, the planetary signal would cross pixels in all six epochs. Analyzing these epochs with the multi-epoch assumption that the planetary signal would not shift may have significantly reduced the planetary signal in two ways: by averaging it across multiple detector resolution elements and by allowing the time-variable signal to be picked up and removed by the PCA-based telluric correction routine. In short, while K_p is often not known ahead of time, researchers should take care to ensure that the planetary signal truly does not shift before analyzing the data as such.

As we move to planet populations on longer orbits, though, the CRIRES-style approach will struggle. For instance, for an Earth twin, with an orbital period of 365.25 days and a K_p of 30 km/s, in an full night observation (8 hours), even near conjunction, an instrument would need a resolution of 5.8×10^5 to allow the planet signal to cross even one pixel; 8.7×10^6 for the planet to cross 15 pixels (comparable to what has been used in CRIRES-style detections to date, e.g., Birkby et al. 2017; Pelletier et al. 2021), more than 80× larger than the instrumental resolution of current near-infrared spectrometers. For these planet populations, the multi-epoch approach is the only currently available high-resolution technique.

Figure 6.1 illustrates the number of pixels on a $R = 100,000$ spectrometer ($b = 3$ pixels/resolution element) that a signal from each of the known planets (as of October 20, 2021, exoplanets.org) would cross during an 8-hour observation centered at inferior conjunction. These estimates assume that the planets transit and that they are on circular orbits. It is important to remember, though, that most planets do not transit. Since K_p depends on orbital inclination, a non-transiting planet would have a smaller value of K_p than would a comparable mass transiting planet, resulting in the planetary signal that crosses fewer pixels than predicted by Figure 6.1. Since the value of K_p is rarely known for non-transiting planets, and in fact is typically the parameter being measured, it would be challenging to determine before observing whether a planet would cross enough pixels for the CRIRES-style technique to

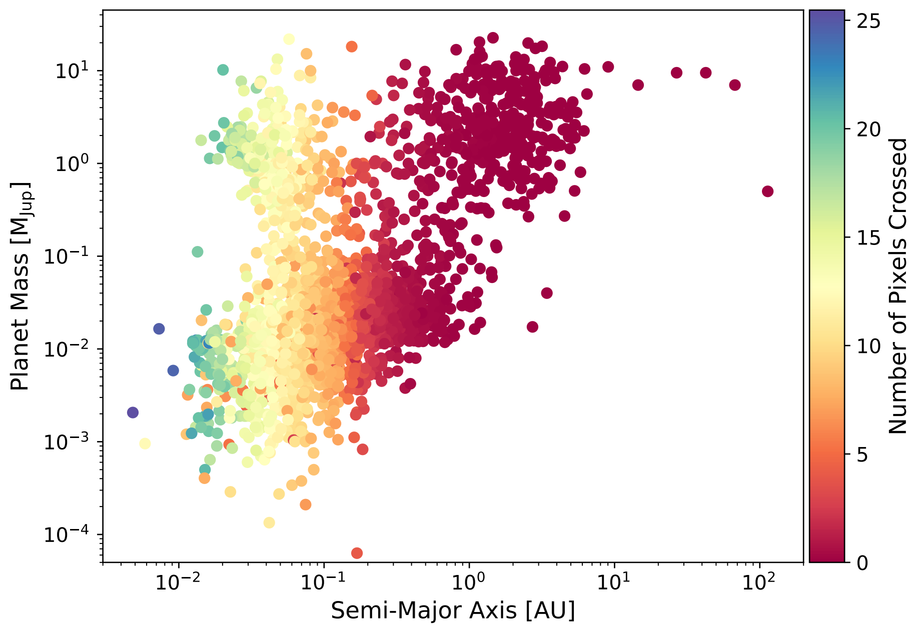

Figure 6.1: Known exoplanets from Exoplanets Data Explorer (www.exoplanets.org; Han et al. 2014) as of October 20, 2021 plotted in terms of their planet mass and semi-major axis. The colors represent the number of pixels on a $R = 100,000$ (3 pixels/resolution element) instrument each planet would cross during an 8-hour observation centered at conjunction. These estimates assume that the planets transit and that they are on circular orbits. Non-transiting systems would cross fewer pixels than estimated here, and very eccentric orbits may cross more pixels.

be effective. Very eccentric orbits, on the other hand, may cross more pixels than predicted here, but high-eccentricity orbits are much less common that non-transiting orbits. From this figure, we can see that with a $R = 100,000$ instrument, the CRIRES-style approach is really only applicable to planets within ~ 0.1 AU. The multi-epoch approach, on the other hand, with an effective telluric correction procedure and a sufficiently large number of epochs, could work for any of these systems.

While the $R \sim 25,000 - 100,000$ near-infrared spectrometers currently being used for exoplanet characterization are both applicable to hot Jupiters at different parts of the planets' orbits, as we aim to study planets on longer orbital periods and with smaller Keplerian orbital velocities, only the multi-epoch approach will suffice.

Length of Observation, e.g., Signal-to-White Noise per Observation

The length of an observation will affect the total change in planetary line-of-sight velocity seen, as described in Sections 6.2 and 6.3, the level of total shot noise, and the effectiveness of principal component analysis telluric correction procedures.

Planetary signals should increase proportionally to t_{exp} and shot noise increases as $\sqrt{t_{exp}}$, so the signal-to-shot noise should increase as $\sqrt{t_{exp}}$ as well. Through the simulations presented throughout this thesis, however, we have seen that in a small ($\lesssim$ 10) epoch limit, *structured* noise arises in the cross correlation space that far outweighs the shot noise. Buzard et al. 2020 analyzed seven L band NIRSPEC epochs on HD 187123 b, with a total signal-to-shot noise of 5874 taken over 8.9 hours. We found, both with simulations and with the data, that the signal-to-shot noise could have been reduced to 3968 overall without a significant change in the shape of the final log likelihood result. Below this level, the log likelihood curve began to change shape, implying that around a signal-to-shot noise around 4000 was the limit where shot noise contributions became comparable to structured noise. Reducing to the total signal-to-shot noise could have saved a factor of 2.2 in exposure time. Since we have also seen that many, lower S/N epochs are better at reducing structured noise than fewer, higher S/N epochs, it may be advantageous to take shorter observations rather than waste time reducing the total shot noise level when it is already far below the level of structured noise.

Piskorz et al. 2016 introduced a principal component analysis (PCA) approach for correcting telluric contamination from multi-epoch data. We will expand more on this approach in Section 6.4, but in short, it assumed the telluric atmosphere changes over the course of the observation and used PCA to remove these time-varying components from the dataset. With a longer baseline spent on a target, the telluric atmosphere would be able to vary more and so be easier for PCA to identify and remove. The time relevant to PCA is the total time spent on each target, or the full time from the beginning to the end of the observation. The exposure time relevant to the shot noise level described above is just a portion of this total time, excluding time spent between exposures or reading out frames, for instance. If a different telluric correction approach could be used that did not require the same baseline, shorter observations would be beneficial in both reducing the change in planetary line-of-sight velocity and permitting the observation of more targets per night while still remaining in the regime whether structured noise outweighs shot noise.

6.4 Analytic Considerations

Wavelength Calibration

Wavelength calibration is the process by which pixels on the detector are assigned wavelength values. It is especially important for wavelength solutions to be precise for radial velocity based approaches such as the multi-epoch one because these methods interpret offsets from expected line positions as velocity shifts. Further, if wavelength solutions from different epochs are inaccurate in different directions, together, they could work to broaden the velocity result. This broadening could be misinterpreted as having a physical origin, planetary rotation or atmospheric pressure broadening for example. An accurate and precise wavelength solution is therefore crucial to accurately measuring K_p and not artificially broadening the planetary signature.

Accurate wavelength solutions are also necessary for good telluric correction. Any telluric correction approach using a model will create large residual signatures if the telluric absorption wings in the model and in the data are misaligned due to a slight wavelength offset. These residuals can greatly exceed the strength of planetary lines in the data and lead to high levels of structured noise in cross correlation space, concealing the planetary signature all together.

For shorter wavelength studies, in the optical and very near-infrared, arc lamps (Ne, Ar, Kr, Xe) or OH sky lines can be used to align data onto a wavelength axis, but the lamps do not have enough lines out at the longer wavelengths of the L and M bands to be useful. In the past, we have used a fourth-order polynomial

$$\lambda(x) = ax^4 + bx^3 + cx^2 + dx + e, \tag{6.7}$$

with x as the pixel numbers, to align the data with a telluric absorption model. Brogi et al. 2016 describe a more refined version that cross correlates three points across an order between a telluric model and the data, varying the data wavelength guesses iteratively until the highest correlation is found. Using this approach, they were able to reach a sub-pixel precision in the wavelength solution.

Ultimately, laser frequency combs and more stable spectrographs with no moving parts will solve the problem of wavelength calibration. Laser frequency combs have been introduced to optical radial velocity instruments as researchers push to achieve the 10 cm/s stellar radial velocity limit indicative of an Earth-analogue. Laser frequency combs use femtosecond-pulsed mode-locked lasers controlled by stable oscillators such as atomic clocks to generate a series of narrow modes spaced according to the laser's pulse repetition rate (Murphy et al., 2007). With a large bandwidth set of uniformly spaced lines, with frequency precisions better than 10^{-12}, these combs are excellent for assigning wavelengths and correcting for any non-linearity across the detector. Ycas et al. 2012 used a 25 GHz comb deployed at the 9.2-meter Hobby-Eberly Telescope (HET) at McDonald Observatory to measure stellar radial velocities to a precision of $\sim$ 10 m/s. More recently, Metcalf et al. 2019 adapted a 30 GHz comb to the Habitable Zone Planet Finder (HPF) spectrograph at HET and have demonstrated an RV precision as low as 6 cm/s. This is the first time such precision has extended from the optical into the near-infrared wavelengths. At such precisions, frequency combs could revolutionize near-infrared high resolution exoplanet studies, ensuring that velocity measurements are accurate and any broadening beyond the instrumental resolution is tied to some physical phenomenon.

Instability in the wavelength solution over an observation can be as limiting as an inaccurate wavelength solution. Coupling the Keck Planet Imager and Characterizer (KPIC) with NIRSPEC could improve stability over the course of an observation. KPIC sends light into a fiber injection unit (FIU) that steers it into one of five single-mode fibers which are then connected to NIRSPEC itself (Wang et al., 2021). Some fibers can be positioned to receive only star light, while others can be positioned to receive star and planet light. When using NIRSPEC without KPIC, the wavelength solution changes across the detector, so if the object moves along the slit during the observation, the wavelength solution would vary. Because KPIC deposits the object light through a fiber, the position on the detector does not change and the wavelength solution is more stable. Morris et al. 2020 found that with KPIC, the wavelength solution was stable to the 0.1 km/s level within a night as long as the optics inside the spectrograph were not moved.

Telluric Correction

Effective telluric correction processes are crucial for deriving any results from ground-based telescopes. Most high signal-to-noise infrared telluric observations to date have been for exoplanet transit studies that obtain a long baseline of data by default that can be used for telluric correction. There are not yet effective and precise methods for telluric correcting short observations.

The current telluric correction approaches fall into three main categories: model based, data driven, and a combination of the two.

Telluric models are not accurate enough to correct data down to the level of the planetary signal. For instance, Long et al. 2011 experimentally measured air-broadened CO_2 line shapes near 1.6 μm and found deviations of 0.9–2.7% from the values found in the HITRAN 2008 database (Rothman et al., 2009), much higher than the typical 10^{-4} level of the planetary signal.

An example of a data-driven technique at its simplest is telluric correction by the subtraction of, or division by, a standard A star spectrum. This too is insufficiently accurate to enable planetary detections. To match the signal-to-noise of the data, we would need a correspondingly long standard observation, which would be a very inefficient use of telescope time. Further, a standard star observation could not account for changes in the telluric atmosphere over the course of the target observation.

Our more recent multi-epoch studies have used a combined model and data-driven approach, in which a telluric model corrects for the majority of the telluric contamination and a principal component analysis (PCA) picks up and removes time-varying aspects of the data set from, for example, changes in airmass, telluric abundances, and instrument plate scale. Unfortunately, to be effective, PCA requires enough time from the start to the end of the observation for telluric variation to become prominent. As such, current telluric correction procedures limit us from reducing observation times. Recent work has suggested that many, lower S/N epochs would allow for a more efficient planet detection than fewer, higher S/N epochs, even with the same total S/N (Buzard et al., 2020), however. Therefore, a telluric correction technique that does not require a longer observation time will be important to the progress of this technique, and to many others in infrared astronomy.

As a brief note, it is important to remember that the method of telluric (and stellar) correction is the main difference between the analytic procedures used in the multi-epoch technique and the CRIRES-style, single-night, technique. Because during the CRIRES-style observations, the planetary signal shifts across pixels, telluric correction becomes much easier. Researchers can correct each spectrum in the time series with a linear regression fit to the deepest H_2O and CH_4 lines over time (e.g., Brogi et al., 2012). Because the planetary signal is shifting across columns, this procedure should not remove it. During multi-epoch observations, the planetary signal remains stationary, so this method of telluric correction would remove the planet signal. We therefore need a scheme that can correct tellurics without removing the planet, and such an approach is much more technically challenging.

The previous multi-epoch detections have used different telluric correction procedures. Lockwood et al. 2014 used the TERRASPEC synthetic forward-modeling algorithm (Bender et al., 2012) to fit and remove telluric contamination. Piskorz et al. 2016 presented a new telluric correction framework which involved model-guided principal component analysis (PCA). To guide the PCA, they generated an initial telluric model using an RFM code (Dudhia, 2017). Piskorz et al. 2017 and Piskorz et al. 2018 followed this PCA technique. Buzard et al. 2020 used PCA, but used the ESO tool `Molecfit` (Kausch et al., 2014) to generate the initial telluric model. Beyond a reprocessing of the tau Boo b data from Lockwood et al. 2014 to validate the PCA technique in Piskorz et al. 2016, the effects of these different telluric correction routines (as well as others not yet applied to multi-epoch data sets, including the Planetary Spectrum Generator[1] and `wobble`; Bedell et al. 2019) have not been compared.

RMF + PCA vs. Molecfit + PCA Telluric Correction

Here, we briefly compare the RFM telluric model + PCA telluric correction originally used on the upsilson Andromedae data published in Piskorz et al. 2017 against a `Molecfit` + PCA routine on the same raw data. While Buzard et al. 2021b found that these data were insufficient to report a detection of ups And b, we should still be able to use them to compare telluric correction techniques. *The stellar signal can be used as a benchmark for how well each telluric correction procedure works.* Stellar velocities are typically well known, as the barycentric velocity is very well understood, and systemic velocities, especially for these systems with radial velocity detected planets, are known to within at most a few m/s. Then, whichever telluric correction technique results in a stellar correlation at the right velocity and with the highest likelihood is the most accurate.

We find that the ups And data telluric corrected by a RFM model followed by PCA (and published in Piskorz et al. 2017) sometimes struggles to detect the known stellar velocity. We re-reduced and telluric corrected the same raw data, this time using `Molecfit` (Kausch et al., 2014) to generate the initial model. It appears that the main difference between these two modelling frameworks is in how they fit the telluric model. Both use HITRAN 2008 (Rothman et al., 2009) linelists, but the Python version was set up to fit the wavelength, continuum, instrument profile, and molecular abundances,

[1]https://psg.gsfc.nasa.gov.

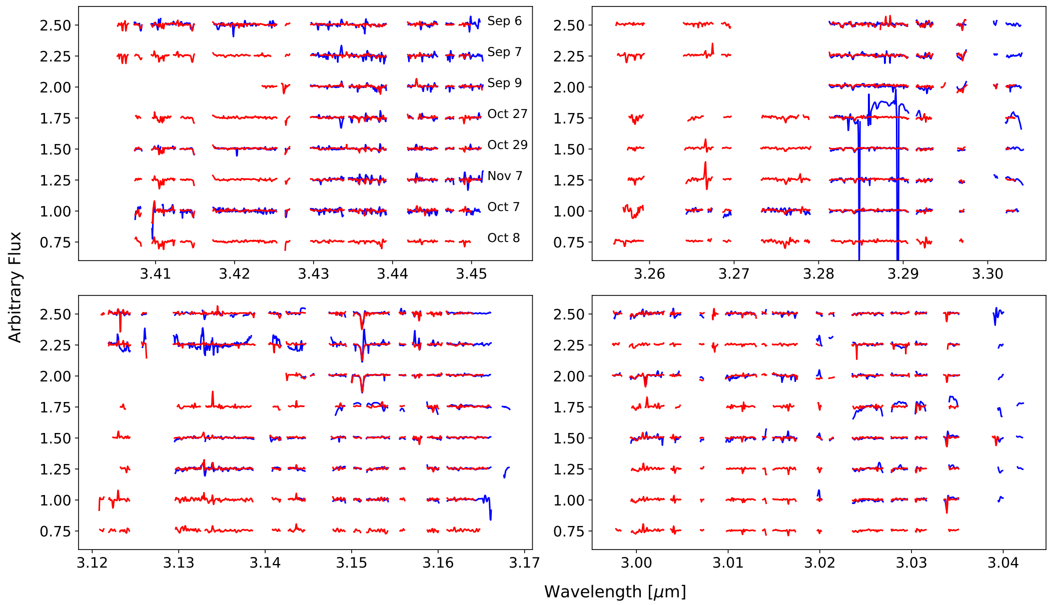

Figure 6.2: Telluric-corrected NIRSPEC data of upsilon Andromedae. The blue spectra were telluric corrected with a RFM + PCA procedure (and published in Piskorz et al. 2017), while the red spectra were corrected with an initial telluric model generated by `Molecfit` (Kausch et al., 2014), followed by PCA.

sequentially. `Molecfit` iterates in its fitting procedure between the instrument profile, continuum, and molecular abundances. The wavelength fit is still done separately, both before, and if necessary, after the `Molecfit` fitting routine.

Figure 6.2 and 6.3 show the effects of these two telluric correction frameworks in two ways. Figure 6.2 shows the RFM + PCA telluric corrected data in blue and the `Molecfit` + PCA corrected data in red. Overall, the red spectra appear less noisy than the blue spectra. Also, with `Molecfit`, we were able to recover some of the data from the left-hand side of the detector, though even in the `Molecfit`-corrected data, this half of the spectra is often noiser than the right-hand half due to bad read-out electronics that affected the left half of the detector. We analyzed an additional epoch, October 8, 2014, that had not been included in the original publication.

Figure 6.3 compares the stellar and planetary log likelihoods obtained from these differently telluric corrected data. The eight panels with stellar log likelihoods confirm that the `Molecfit` corrected data allow for stronger and more accurate measurements of the expected stellar velocity during each epoch. In these figures, the black vertical dashed lines show the expected stellar velocities ($v_{sys} - v_{bary}$) and the dotted blue and red vertical lines show the center of a Gaussian fit to the log likelihood curve of corresponding color, and the stellar velocity from which that planetary log likelihood curve was taken. That the red dotted line is closer to the black dashed line in each subplot indicates the accuracy of the `Molecfit` + PCA corrected data over the RFM + PCA corrected data. We do note that the RFM + PCA routine is very manually intensive; different manually input initial parameters and constraints could have resulted in a better fitting telluric model.

Finally, the right-hand column of Figure 6.3 shows the planetary log likelihood curves (neither including 2014 Oct 8). The top panel, in blue, is the non-detection from Buzard et al. 2021b. First, it is clear that the two curves differ in shape – differences in telluric correction can be enough to completely change the shape of the planetary log likelihood curve, making planetary detection nearly impossible. Neither the addition nor removal of 2013 Oct 27, which had a particularly noisy second order (see Figure 6.2), or 2014 Oct 8 alter the shape of either log likelihood curve significantly.

Lastly, we can consider the benefit of using PCA in addition to the initial telluric model, rather than only the model. As an example, the maximum stellar log likelihood on October 7, 2014 after only the `Molecfit` model was removed was 0.37, while after the removal of the optimal number of principal components and fringes (3 components, 15 fringes—also determined by strongest and most accurate stellar velocity), it rose to 0.49. The maximum log likelihood with 3 components but 0 fringes removed was 0.38, and with 0 components but 15 fringes removed was 0.47, indicating that the removal of fringes had more of an effect than the removal of principal components. We suspect that the accuracy of the model fit is relevant here; PCA will not fully correct for a substandard telluric model correction. Nor will PCA correct for telluric model inaccuracies (like air-broadened line shapes, e.g., Long et al. 2011) that do not vary over the observation.

Looking Forward

While this study only compares two telluric correction frameworks on a single data set, it does demonstrate an effective method for comparing techniques. We suggest using the a priori knowledge of the stellar velocity at a given epoch to determine the most effective telluric correction procedure as illustrated here.

The stellar velocity benchmark would be helpful in fully realizing the benefit

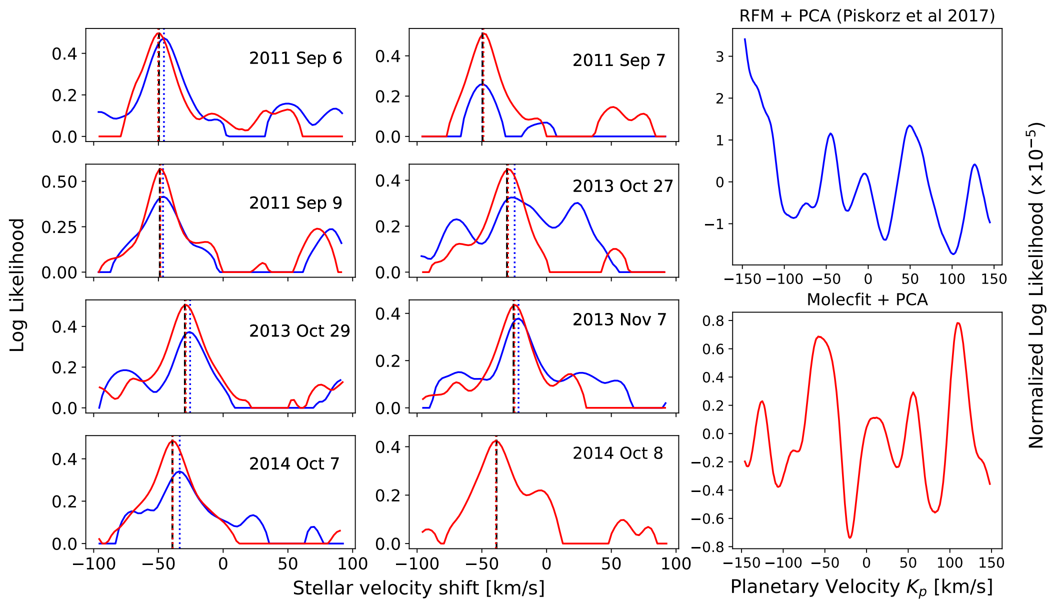

Figure 6.3: Effects of telluric correction method on resulting stellar and planetary log likelihood functions. The eight panels on the left-hand side show the stellar log likelihoods from each of the eight epochs with the RFM + PCA corrected results in blue and the `Molecfit` + PCA results in red. In each case, the `Molecfit` + PCA results find a more accurate stellar velocity with a higher likelihood. The two panels on the right-hand side show the resulting planetary log likelihoods (neither including 2014 Oct 8). Accurate telluric correction is crucial for exoplanet detection. The small differences between these two routines completely alter the shape of the planetary log likelihood curves.

of PCA. PCA-based telluric correction routines require the observer to pick the number of components and fringes to remove—the known stellar velocity can guide this choice. It should be kept in mind moving forward, too, that the multi-epoch approach combines many orders across many observing nights and each order may require a different number of components and fringes to be removed. Ideally, observers should use the stellar velocity benchmark to determine the appropriate number of components and fringes to remove from each order individually, and should not assume that the same number of components and fringes will cleanly correct each order, as has been done in the past.

An in-depth comparison of telluric modeling and data-driven frameworks (including `TERRASPEC`, Bender et al. 2012; `Molecfit`, Kausch et al. 2014; `wobble`, Bedell et al. 2019) would be be a very valuable resource. Further, moving forward, we should strive for an approach that does not require a long temporal baseline. An idea could be a machine learning algorithm that learns from the vast archive of existing NIRSPEC standard data to predict a standard telluric spectrum for any given observation night. NIRSPEC has been operational for over 20 years and must have observed all variations of the telluric atmosphere from Mauna Kea. This expansive data set could be used to generate a telluric spectrum that, because it would be completely from data and not a theoretical model, would not have theoretically estimated line shapes or positions that are prone to inaccuracies.

Stellar Spectral Model

After multi-epoch data are reduced, wavelength calibrated and telluric corrected, we use a two-dimensional cross-correlation routine with a stellar and a planetary spectral model to measure the stellar and planetary velocities. Accurate stellar models that can measure the known stellar velocities with the highest likelihoods will be necessary to push for the much lower contrast planetary signals.

Multi-epoch detections to date have used two major types of stellar models. The *L* band (non)detections of tau Boo b (Lockwood et al., 2014) and ups And b (Piskorz et al., 2017) used a stellar models generated from a recent version of the LTE line analysis code MOOG (Sneden, 1973) and the MARCS grid of stellar atmospheres (Gustafsson et al., 2008). Notably, individual abundances (Fe, Si, Mg, Na) were set by matching observed lines for elements that were well measured by NIRSPEC. Because these stellar spectra are so time consuming to produce, later works (e.g., Piskorz et al., 2016, 2017, 2018; Buzard et al., 2020) instead used stellar models interpolated to the appropriate stellar effective temperatures, metallicities, and surface gravities from the PHOENIX stellar spectral grid (Husser et al., 2013). These two stellar model frameworks have not been explicitly compared on the same data set.

Further, before stellar models are used to cross correlate data, they undergo several adjustments. Notably, the stellar continuum is removed (see Section 6.4) and, if the stellar rotational velocity is above the velocity resolution of NIRSPEC (~5 km/s pre-upgrade and ~3.1 km/s post-upgrade), the model is rotationally broadened. The stellar and planetary spectral templates are both broadened to the instrumental resolution that was fit in the telluric model as a part of the cross-correlation script. In the following section, we compare the different stellar model frameworks, the different methods of stellar continuum removal and the effects of rotational broadening. We conclude that the selection of an appropriate stellar model should be an iterative process. Because the goal of this work is to detect very low-contrast planetary emission, it is not sufficient for the stellar model to merely detect the right stellar velocity. It must detect the right stellar velocity with the highest possible likelihood. This can be used as a benchmark in selecting the best stellar model. In this way, high signal-to-noise data themselves may be used to improve stellar models.

Adjusted vs. PHOENIX Stellar Spectral Template

We first consider how the two stellar models used for multi-epoch detections compare: the model generated from the stellar synthesis program MOOG with an input linelist vetted on a very high S/N solar spectrum and with elemental abundances fit to observed lines (the "adjusted" stellar model) versus the PHOENIX model.

For this comparison, we use the adjusted *L* band upsilon Andromedae A stellar model first presented in Piskorz et al. 2017 and a PHOENIX model interpolated to an effective temperature of 6213 K, a metallicity of 0.12, and a surface gravity of 4.25 (Valenti & Fischer, 2005). The analysis is otherwise exactly the same: with `Molecfit` + PCA telluric corrected data and the SCARLET (Benneke, 2015) planetary model generated with an inverted planetary structure used in the original Piskorz et al. 2017 publication.

One immediate differences between these stellar model frameworks is that the adjusted model is generated without a stellar continuum, following from the MOOG stellar synthesis program, while the PHOENIX models do have a continuum. We will consider different methods of removing the stellar continuum from the PHOENIX model in Section 6.4, but here, we do so by dividing the model by a second-order polynomial fit from 2.8 to 3.5 microns in wavenumber space. For simplicity, for the rest of this chapter, we will call this model the [2n2835] stellar model ("2" order polynomial, waveNumber space, 2.8-3.5 μm).

Further, upsilon Andromedae A has a stellar rotation of 9.62 km/s (Valenti & Fischer, 2005), so rotational broadening should dominate over instrumental broadening. We consider the effects of rotationally broadening the stellar spectral model. To do so, we use the PyAstronomy rotational broadening algorithm with a rotational velocity of 9.62 km/s and a limb darkening coefficient of 0.29 (Claret, 2000).

Figure 6.4 shows the effects of the two different stellar models, and the effects of rotational broadening in the PHOENIX model. For each epoch, the adjusted stellar model can measure the stellar velocities with more confidence than the PHOENIX model, whether rotationally broadened or not. This creates significant differences in the shapes of the resulting planetary log likelihood curves. We can assume the red curve, corresponding to the original stellar model, is more realistic because in that case the stellar spectral template matched the stellar component of the data better.

Additionally, Figure 6.4 shows that rotationally broadening the PHOENIX stellar model before it is instrumentally broadened does not have a large effect on either its ability to detect the stellar signal or the resulting planetary log likelihood surface. At 9.62 km/s, rotational broadening does not significantly alter the spectrum beyond the instrument resolution. Nonetheless, rotational broadening could have an effect, particularly on younger systems with faster rotating stars. Comparing rotationally broadened and unbroadened models, and those rotationally broadened with ranges of rotational velocities and limb darkening coefficients would be a good strategy for identifying the best stellar model.

While the adjusted model seemed a better fit to the ups And data that either PHOENIX model, it does have some drawbacks. The generation of the adjusted models is an intensive process, carried out manually, making them inefficient. Additionally, they are generated only across the wavelength ranges of the observed data and without a continuum. This prohibits their use to simulate observations. Indeed, there is a deficit of very accurate stellar models that can also support multi-epoch simulations, and future work should focus on improved approaches that incorporate the signal-to-noise $1-5$ μm data now available.

Stellar Continuum Removal Methods

Since PHOENIX stellar models have the expected stellar continuum, we need a method to continuum normalize these models before they can be cross correlated against the data. Continuum normalization can be done by fitting a polynomial to the model and dividing it out. The range over which the polynomial is fit has been different in our past publications. The HD88133 stellar model used for cross correlation in Piskorz et al. 2016 was fit by a

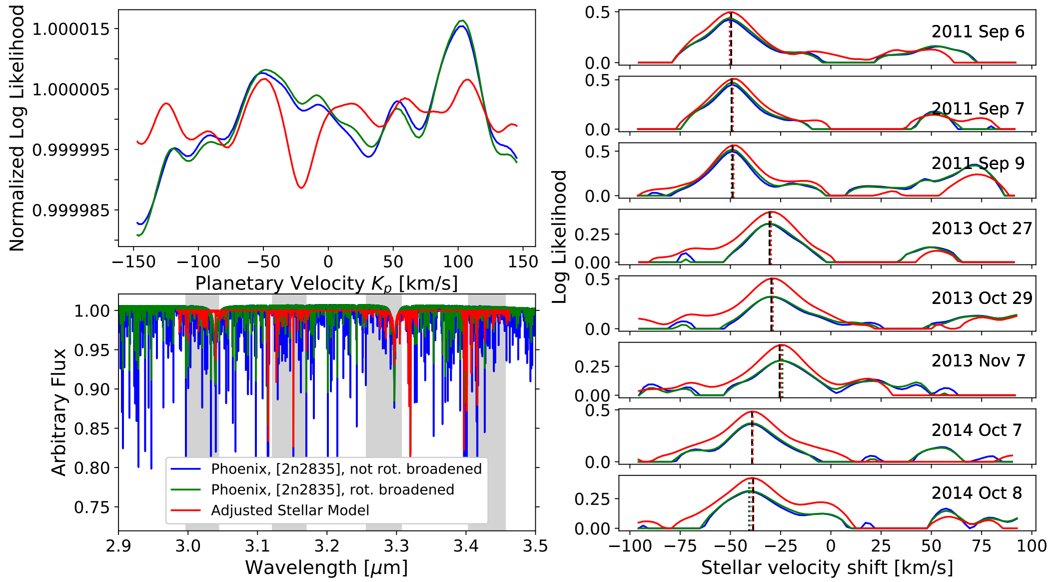

Figure 6.4: Comparison of model stellar spectra used to cross correlate the `Molecfit` + PCA corrected ups And data. PHOENIX stellar spectra are shown and used in blue and green, not rotationally broadened and rotationally broadened, respectively. The red stellar model is the adjusted one, with elemental abundances fit to the data. The same inverted SCARLET ups And b planetary spectral model and Wright et al. 2009 orbital parameters were used for the cross correlation comparisons.

second-order polynomial from 2.0 to 3.5 μm in wavenumber space [2n2035]. For KELT2Ab (Piskorz et al., 2018), a second-order polynomial was fit to the stellar model from 2.8 to 3.5 μm in wavenumber space [2n2835]. This method was shown sufficient in that it could reproduce the known K_p for the transiting system.

Figure 6.5 shows that dividing a second-order polynomial fit in wavenumber space from 2.0–3.5 μm versus 2.8–3.5 μm can significantly change the shape of the resulting planetary log likelihood curve. Everything other than the range of the continuum normalization polynomial remains the same between the red and the blue curves. Both are PHOENIX stellar models interpolated to $T_{\text{eff}} = 5438$ K, [Fe/H] = 0.330, and $\log(g) = 3.94$, the parameters for HD88133A (Mortier et al., 2013). For the log likelihood results, the same data (RFM + PCA telluric corrected, and presented in Piskorz et al. 2016 and Buzard et al. 2021b) is correlated and the same SCARLET planetary spectral model without a thermal inversion is used. In each subplot, the blue curve corresponds to a [2n2035]-normalized stellar model, while the red curve corresponds to the [2n2835]-normalized model. The bottom left panel shows the unbroadened stellar models with the NIRSPEC order wavelength ranges shaded in gray. The red model clearly has a flatter continuum across the NIRSPEC L band orders than does the blue model.

The six right-hand panels show the stellar log likelihood between each of the models and the data during each of the six L band epochs. It is clear from these panels that the red model, with the flatter continuum, results in a higher likelihood fit to the data in all of the epochs. From the six stellar log likelihood curves in the right-hand panels, it can be seen that the log likelihoods, even taken with the better fitting stellar model, do not always align perfectly with the expected primary velocities (i.e. the black dashed lines). The offset is at most ~3.6 km/s, which is less than the 12 km/s (FWHM) velocity resolution in the L band of the original NIRSPEC instrument. These sub-pixel shifts likely require a more advanced analytical technique than the fourth-order polynomial fit between the data and a telluric model that has been used for wavelength calibration of multi-epoch data to date.

The top left-hand panel shows the planetary log likelihood curves resulting from the different stellar models. There appears to be a drastic difference in the shape dependent on the method used to correct for the stellar spectral model continuum. Because the size and location of peaks at positive velocities vary so much, we can see how easily something as trivial as the polynomial used to remove the continuum from the stellar cross-correlation template could serve to obscure a planetary signal within this six epoch data set. As the multi-epoch approach is applied to larger wavelength coverage data from other high-resolution spectrometers, a question will be how to best remove the stellar continuum (wavelength range of polynomial fit, polynomial order) from the stellar model to match the data. As illustrated in Figure 6.4, this question is nontrivial and will require careful attention.

Looking Forward

As seen above, using an accurate stellar model to cross correlate the data is very important in detecting planets. As we push to even cooler and lower-contrast planets, this will be even more so the case. At these low planet contrast levels, using a single stellar model that is independent of observation time for all epochs may no longer be sufficient. Stellar activity can alter stellar

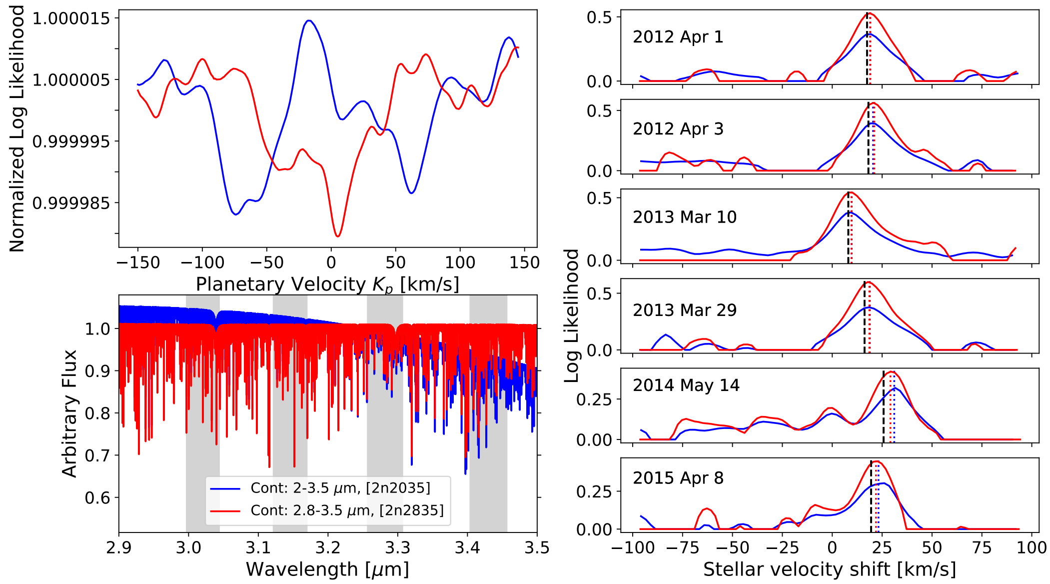

Figure 6.5: This figure shows the effects of stellar model continuum on the resulting log likelihood curve. The three log likelihood curves were all generated with the same RFM + PCA telluric corrected data (6 L band epochs), the same planetary model (SCARLET non-inverted model), and the same Piskorz et al. 2016 orbital parameters. The six stellar log likelihood curves are shown on the right-hand side, with black dashed lines indicating the expected primary velocity and the dotted lines showing the primary velocity from which the planetary cut was taken. The bottom panel shows the unbroadened stellar models used to generate the log likelihood curves in the top panel with the corresponding color. The gray shaded regions illustrate the wavelength coverage of the NIRSPEC orders. These stellar models were both corrected with a second-order polynomial fit in wavenumber space, though the wavelength range over which the fit was performed varies.

spectra as a function of time. In particular, star spots, that are typically 500–1000 K cooler than the stellar effective temperature (e.g., Frasca et al., 2005), could have a large effect on the observed stellar spectrum. If the star spots are stable, they can come in and out of our field of view as the star rotates. This can show up spectroscopically as a part of a stellar line, moving from the red-shifted to the blue-shifted end, is removed. If the star spots are not stable, or their number, suface area coverage, or temperature are unknown and varying, modeling them can become much more complicated (e.g., Barnes et al., 2017). Further, if star spots contain trace amounts of water that are not considered in the stellar spectral model template, this water could be confused for the water in the planetary spectral template, and mislead us from the true planetary velocity.

Moving forward, several approaches might allow for more realistic stellar models. An observed stellar spectrum could be constructed from the data themselves by detrending each epoch by its stellar velocity and then coadding the data. This process should, in effect, remove the planetary signal, which is much lower contrast to start and will be shifted by different amounts by detrending by the stellar velocity during each epoch. When shifted by different amounts and then coadded, the planetary signal in each epoch should essentially become random noise. This combined stellar model could then be used to correct the star signal from each data epoch, leaving behind only the planetary signal and noise. This approach is similar to how `wobble` (Bedell et al., 2019) compiles a stellar spectrum from optical radial velocity data. This approach would not correct for time-varying components of the stellar spectrum, caused by activity or spots, but may result in a stellar template that fits better than the stellar models currently being used.

Another idea could be to introduce a third-dimension to our cross-correlation analysis with a water template 500–1000 K cooler than the effective star temperature to account for star spots. If water is present in star spots that rotate into and out of our field of view, this third dimension of the correlation should correspond to the stellar rotational velocity. By attributing the star spot water signal to the star's rotational velocity, this signal would not be left to muddle the planetary water signal. As we aim to detect these tiny planetary signals, every factor counts. An appropriate stellar model is crucial, and as described above, we recommend using the stellar log likelihood curves as an indicator for which of different stellar models best fits the data.

Planetary Spectral Model

The goal of the multi-epoch technique, as with other exoplanet spectroscopic methods, is ultimately to characterize the planet's atmosphere — learn about the atmospheric composition, study physical and chemical phenomena like winds, rotation, and relative molecular abundances — not just measure its Keplerian line-of-sight velocity, K_p. To do so would involve finding the planetary model which best fits the data at the appropriate K_p.

Pelletier et al. 2021 recently published a CRIRES-style detection of tau Boo b, using 20 hours of SPIRou data. Rather than using a single planetary template, they performed a full atmospheric retrieval to constrain the abundances of all major carbon- and oxygen-bearing molecules and recover a temperature profile. They demonstrate how an atmospheric retrieval framework could allow the multi-epoch technique to go beyond the planetary model fitting it has mainly used thus far, and provide strong constraints on key atmospheric properties.

Additionally, Beltz et al. 2021 showed how considering three-dimensional atmospheric structure in planetary models could greatly increase the significance of planetary detection from CRIRES-style data. They saw that using models that accounted for three-dimensional temperature structure and atmospheric motions (e.g., winds and rotation) resulted in a $\sim 1.8\sigma$ stronger detection of HD 209458 b that any of the one-dimensional models they tested. The biggest improvements came from the use of the 3D temperature structure. The data Beltz et al. 2021 analyzed were taken with CRIRES during epochs when the planet had just passed secondary eclipse ($M = 0.51-0.57, 0.55-0.62$). One can imagine that 3D planetary templates may have an even larger effect on multi-epoch detections. While these data really only showed one view of the planetary surface, multi-epoch data, by definition, come from positions all over the planet's orbit, and so, for tidally locked planets, show a whole range of views of the planet. Then, planetary models that consider 3D structure, or even phase-dependent 1D planetary templates, may show an even larger increase in planetary detection significance with the multi-epoch technique.

While there is much room to expand our technique in terms of planetary spectral templates used, here, we consider those that have been used in multi-epoch detections to date. Specifically, planetary models have been used from different frameworks and with/without thermal inversion.

Most multi-epoch papers (e.g., Piskorz et al., 2017; Buzard et al., 2020) have used planetary models from the SCARLET framework (Benneke, 2015). Piskorz et al. 2016 compared SCARLET and PHOENIX planetary models. Piskorz et al. 2018 used a model from ScCHIMERA. In our reanalysis of Piskorz et al. 2016, Buzard et al. 2021b found that analogous PHOENIX and SCARLET planetary models give rise to analogous planetary log likelihood results.

For future works, we recommend moving beyond single planet model detections and considering the role on thermal inversions in our planet models and ability to detect planets.

Thermal Inversions?

Here, we demonstrate that the multi-epoch approach is able to distinguish between a planet with a thermal inversion and one without. Some previous multi-epoch publications have used planetary models with thermal inversions and some have not included inversions. Specifically, Piskorz et al. 2016 used a model without a thermal inversion, while Piskorz et al. 2017 and Buzard et al. 2020 used inverted models. Piskorz et al. 2018 fit a grid of planetary models from the ScCHIMERA framework to KELT-2Ab data and saw that the data preferred values of incident stellar flux f less than 1, which is consistent with no temperature inversion (models with $f \geq 1.5$ show a temperature inversion).

Thermal inversions were originally thought of as associated with TiO and VO, which both absorb strongly enough in the visible that, in solar abundances, in hot Jupiters, they should be able to cause thermal inversion (e.g., Hubeny et al., 2003; Gandhi & Madhusudhan, 2019). Inverted atmospheres have hotter layers higher up, which lead to emission features in their spectra. Non-inverted atmospheres, on the other hand, continually cool with altitude. Their spectra therefore mainly show absorption features.

Brogi & Line 2019 raised a question about whether the method that has been used in previous multi-epoch detection works to convert the cross correlations to log likelihoods would eliminate our ability to differentiate between inverted and non-inverted planetary atmospheres. The cross-correlation to log likelihood methods are discussed more deeply by Buzard et al. 2020 and Section 6.4, but, in short, previous multi-epoch detections used the framework originally presented by Zucker 2003 to convert cross correlations to log likelihoods. This can either be applied as the Zucker ML approach,

$$\log(L(s)) = \sqrt{1 - \exp\left(\frac{1}{N_{\text{tot}}}\sum_i N_i \log[1 - R_i^2(s)]\right)}, \tag{6.8}$$

or as the Zucker $\log(L)$ approach,

$$\log(L(s)) = -\frac{N}{2}\log(1 - R^2). \tag{6.9}$$

In each variation, R is the two-dimensional cross correlation. While the spectra of planetary atmospheres with and without thermal inversion are not simply inverses of each other, we would expect inverted atmospheres to show emission features and non-inverted atmospheres to show absorption features; if a non-inverted atmospheres were correlated against an inverted model, or vice versa, we would expect a negative cross correlation peak. On the other hand, if an inverted atmosphere were correlated with an inverted model, or a non-inverted atmosphere with a non-inverted model, we would expect a positive correlation peak. Brogi & Line 2019 raised concern about the R^2 term in the Zucker 2003 conversion of cross correlations to log likelihoods. The squared term could turn a negative peak into a positive peak. If so, it would make it impossible for us to gain information about the presence/absence of a thermal inversion from our data.

Buzard et al. 2020 pointed out that while this may be a concern with one-dimensional cross correlations, with the two-dimensional cross correlations used in the multi-epoch analysis, we need not worry. In our two-dimensional cross correlation, the first dimension, the correlation of the data with a stellar model, will give rise to much larger variations in cross correlation than the second, planetary, dimension. The planetary log likelihood curves come from the cuts across the peak of the stellar correlation in each data segment. The planetary correlations can then be thought of as sitting on top of a tall mountain of positive stellar correlation. Planetary anti-correlation (for instance between an inverted planet and a non-inverted model) would never be strong enough to reach down to the bottom of the stellar correlation mountain. A planetary anti-correlation squared, then, would still be distinguishable from a planetary correlation squared.

Here, we present simulations to show that in fact, the multi-epoch technique, using the Zucker 2003 ML approach, is capable of distinguishing between inverted and non-inverted planetary atmospheres. These simulations are generated as described in Buzard et al. 2020. We use a non-rotationally broadened [2n2835]-continuum normalized PHOENIX stellar model (Husser et al., 2013) approximating upsilson Andromedae A, stellar orbital parameters from Wright et al. 2009, and SCARLET models (Benneke, 2015) of ups And b, including and not including a thermal inversion.

Figure 6.6 shows the results of these simulations. The blue curves represent simulated data sets generated with the non-inverted model, the red curves were generated with the inverted model, and the black dashed curves in the top two panels were generated without any planetary contribution. The left

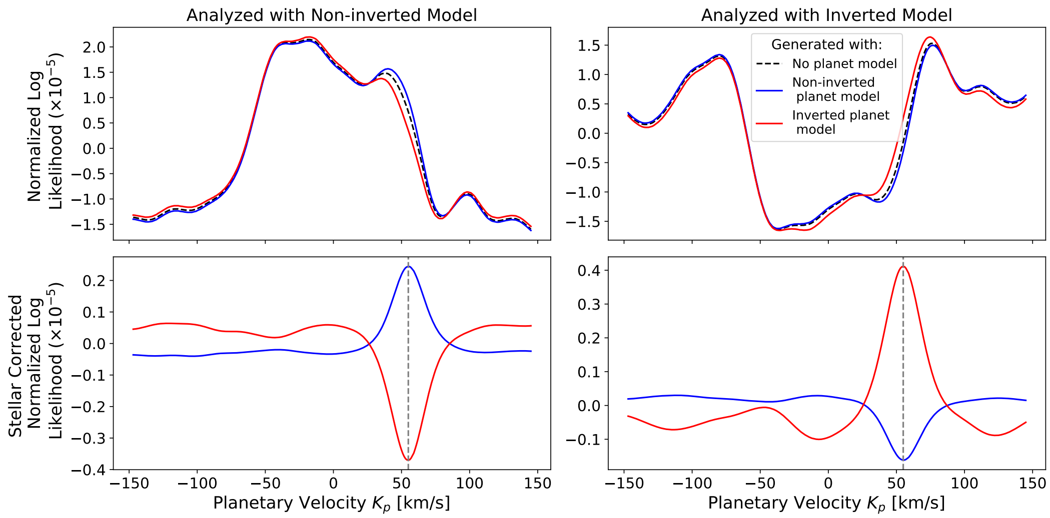

Figure 6.6: Simulations of the 7 L-band ups And epochs presented in Piskorz et al. 2017 and again in Buzard et al. 2021b, generated and analyzed with both SCARLET inverted and noninverted thermal atmosphere models. These simulations are generated with a 1.7053529 $R_\odot$ (Gaia Collaboration et al., 2018), not rotationally broadened star, no noise, and a 1.0 R_{Jup} planet. Blue curves represent the simulated data generated with the non-inverted planet model, red curves were with the inverted planet model, and the black dashed curve was from data generated without a planet model. In the bottom row, when the structured noise curve (black dashed line in top row) is subtracted off to reveal the true planetary signature, we see a peak when the planetary template used to analyze the data matches the model used to generate it, and a dip when the original model and cross-correlation template do not match. This makes sense as inverted models and non-inverted models roughly translate to spectral emission and absorption features, respectively, which should anticorrelate with each other. These simulations illustrate that the multi-epoch approach is capable of distinguishing between thermally inverted and non-inverted planetary atmospheres.

column was analyzed with the non-inverted planetary model and the right column was analyzed with the inverted planetary model. The top row shows the raw log likelihoods and the bottom row shows the log likelihoods after the "star-only" correlation (the black dashed curves) are subtracted out.

Several notable results are clear. Primarily, this figure does show that the multi-epoch technique, with Zucker 2003 conversion of cross correlations to log likelihoods, is sensitive to inverted versus non-inverted planetary thermal structure. While it is clear in the top two panels that the planetary signal is very weak (as was also shown in Buzard et al. 2021b), when the planetary signal can be isolated from the unwanted star/planet correlation structure (e.g., in the bottom two panels), it will show a peak if the thermal structure of the planet matches that of the planetary template and a dip if they do not match as we would expect. This illustrates the claim from Buzard et al. 2020 that the Zucker 2003 approach to converting cross correlations to log likelihoods can differentiate between inverted and non-inverted planetary models in the case of a 2D cross correlation where the first dimension (i.e., the stellar correlation) is of higher magnitude than the secondary, planetary, correlation.

Beyond that, we can see in the top two panels that the an inverted versus non-inverted spectral template will roughly invert the structured noise signature. This structured noise results from the correlation between the planetary spectral template and the stellar component of the simulated data. Regardless of the planetary component of the simulated data, where absorption features in the non-inverted planetary template correlate with the star model, analogous emission features in the inverted planetary template would anti-correlate with the star, and vice versa. As such, we see a roughly inverted noise structure from the two planetary templates.

Lastly, we see that the inverted planetary signal can be detected more strongly than the non-inverted planetary signal. This may be explained by their relative photospheric contrasts. Assuming a 1 R_{Jup} planetary radius, the average L band planet-to-star contrast of the inverted planetary spectrum the stellar spectrum is 6.8×10^{-4}, while that of the non-inverted planetary to stellar spectrum is 2.5×10^{-4}. The 2.7× increase qualitatively matches the difference in peak heights.

Here, we have demonstrated that the multi-epoch technique, applying the Zucker 2003 method to convert cross correlations to log likelihoods is capable of differentiating between thermally inverted and non-inverted planetary atmospheres. Looking forward, we should consider phase/epoch-dependent planetary spectral templates, especially for the close-in tidally locked planets which may show day- to night-side thermal and chemical differences. Such models would not only help to gain higher signal-to-noise planetary detections, but, through simulations, could continually offer the most efficient observing strategies.

Intensity Ratio, α

Following from the TODCOR algorithm presented by Zucker & Mazeh 1994, α is the intensity ratio between the two objects. They describe the template as,

$$g_1(n - s_1) + \alpha g_2(n - s_2), \tag{6.10}$$

where $g_1(n-s_1)$ is the stellar spectral template Doppler shifted by s_1 and $g_2(n-s_2)$ is the planetary spectral template Doppler shifted by s_2. Then, the two-dimensional cross correlation can be equated as,

$$R_{f,g_1,g_2}(s_1, s_2, \alpha) = \frac{\sigma_{g_1} C_1(s_1) + \alpha \sigma_{g_2} C_2(s_2)}{\sqrt{\sigma_{g_1}^2 + 2\alpha\sigma_{g1}\sigma_{g_2} C_{12}(s_2 - s_1) + \alpha^2 \sigma_{g_2}^2}}, \tag{6.11}$$

where $C_1(s_1), C_2(s_2)$, and $C_{12}(s_2 - s_1)$ are the cross correlations between the data and each template and between the two templates, respectively. The σs are the rms of the spectra.

The intensity ratio α can either be put into this equation if known, or if α is not known, Zucker & Mazeh 1994 describe how α can be substituted by $\hat{\alpha}$, the value of which maximizes the correlation between the data and the linear combination of the templates for each s_1 and s_2. The maximized $\hat{\alpha}$ is,

$$\hat{\alpha}(s_1, s_2) = \left(\frac{\sigma_{g_1}}{\sigma_{g_2}}\right)\left[\frac{C_1(s_1)C_{12}(s_2 - s_1) - C_2(s_2)}{C_2(s_2)C_{12}(s_2 - s_1) - C_1(s_1)}\right], \tag{6.12}$$

and, once plugged in, the two-dimensional R becomes,

$$R_{f,g_1,g_2}(s_1, s_2, \hat{\alpha}(s_1, s_2)) = \sqrt{\frac{C_1^2(s_1) - 2C_1(s_1)C_2(s_2)C_{12}(s_2 - s_1) + C_2^2(s_2)}{1 - C_{12}^2(s_2 - s_1)}}. \tag{6.13}$$

We have not found success in using the maximized $\hat{\alpha}$ yet, and have instead plugged in for α. Ultimately, it would be interesting to be able to constrain α for any given system as it should be related to the planetary radius and thermal structure. Our data have not seemed sensitive to α though. Typically, we see that increasing α by a factor of 10, within at least $\alpha \sim 10^{-3} - 10^{-9}$, increased the order of magnitude of the resulting log likelihood variations by the same amount, while the shape of the curve remains constant. This was true regardless of the method used to convert cross correlations to log likelihoods.

Cross Correlation to Log Likelihood Conversion

In order to compare how well different planetary models fit to data, we need to convert the cross correlations to likelihood functions. Converting cross correlations to likelihood functions also makes combining them straightforward.

Buzard et al. 2020 compared three different approaches of converting CC-to-logL on a NIRSPEC data set of HD 187123 b: the Zucker 2003 maximum likelihood analysis, the Zucker 2003 log likelihood analysis, and the Brogi & Line 2019 analysis. Briefly, the Zucker 2003 ML and $\log(L)$ are given by Equations 6.8 and 6.9, and the Brogi & Line 2019, rewritten by Buzard et al. 2020 to consider two-dimensional cross correlations, is given by,

$$\log(L(s)) = -\frac{N}{2}\left[\log(\sigma_f\sigma_f) + \log\left(\frac{\sigma_f}{\sigma_g} + \frac{\sigma_g}{\sigma_f} - 2R(s)\right)\right]. \tag{6.14}$$

Buzard et al. 2020 found that the Zucker 2003 $\log(L)$ conversion gave the best results for the HD 187123 b data set. In particular, we found that the Zucker 2003 $\log(L)$ approach performed better with the heterogeneous data set (5 epochs from NIRSPEC1.0, 2 from NIRSPEC2.0; so different resolutions, number of pixels per order, wavelength regions) than either the Zucker 2003 ML or the Brogi & Line 2019 approaches. Finnerty et al. 2021 also found that the Zucker 2003 $\log(L)$ approach outperformed the Brogi & Line 2019 approach of a set of simulated multi-epoch data. Further, in Section 6.4, we showed that, despite concern to the contrary, when the Zucker 2003 approach is used to convert two-dimentional cross correlations to log likelihoods, it is capable of differentiating between thermally inverted versus non-inverted atmospheres.

The Zucker 2003 ML and $\log(L)$ approaches gave very comparable results for a homogenous data set (see Figure 5 of Buzard et al. 2020). However, we saw something interesting arise with the magnitude of their variations. We have found that on a common data set, the Zucker 2003 $\log(L)$ and Brogi & Line 2019 conversions result in log likelihood functions with variations on the same order of magnitude. Meanwhile, the Zucker 2003 ML approach results in a log likelihood function with variation typically 3 orders of magnitude below the variations of the other two. Thus, while for a homogeneous data set, the Zucker 2003 $\log(L)$ and ML approaches result in a log likelihood function with the exact same shape, the ML variation is $\sim 1000\times$ below the $\log(L)$ variation.

One possible explanation comes from the derivation of the Zucker 2003 ML equation. Zucker 2003 comes across this equation by setting the log likelihood for the whole data set equal to that of the sum of the individual pieces of data. A few changes are made here for the sake of clarity:

$$\begin{aligned}
\log(L_{\text{tot}}) &= \sum \log(L_i) \\
-\frac{N_{\text{tot}}}{2}\log[1 - C^2(\hat{s})] + \text{const} &= -\frac{1}{2}\sum_i N_i \log(1 - C_i^2(s)) + \text{const} \\
N_{\text{tot}}\log[1 - \text{ML}^2(s)] &= \sum_i N_i[1 - C_i^2] \\
\text{ML}(s) &= \sqrt{1 - \exp\left(\frac{1}{N_{\text{tot}}}\sum_i N_i[1 - C_i^2]\right)}.
\end{aligned} \tag{6.15}$$

An important point, here, is that when Zucker 2003 derived this equation, they considered it to be an equation for ML, an "effective" correlation value, not an equation for the log likelihood function.

Lockwood et al. 2014 show through a χ^2 analysis that

$$\log(L) = \text{CCF} + \text{cont}. \tag{6.16}$$

We think that this was the rational used substituting $\log(L)$ into the Zucker 2003 equation for the "effective" correlation, ML. Brogi & Line 2019 considered the validity of their own conversion from CC to $\log(L)$ (Equation 6.14, but in 1D) against both the Zucker 2003 $\log(L)$ approach (Equation 6.9) and the version from Lockwood et al. 2014 (Equation 6.16). To do so, they apply Wilks' theorem (Wilks, 1938). Wilks' theorem states that the test statistic $-2\Delta\log(L)$ for an M-parameter (they used $M = 8$) estimator should follow a χ^2 distribution with M degrees of freedom. They calculated $\Delta\log(L)$ as the difference in the log likelihood between the maximum likelihood and all others within the posterior probability distribution. They found that, as expected from a statistically valid log likelihood mapping, the Brogi & Line 2019 and Zucker 2003 $\log(L)$ distributions matches the χ_8^2 distribution. The Lockwood et al. 2014 mapping ($\log(L) = \text{CCF}$) did not match the χ_8^2 distribution. Together, this piece of evidence, along with the drastic difference in likelihood variation relative to the other approaches may indicate that the Zucker 2003 ML conversion from CC to $\log(L)$, which is comprised of the Zucker 2003 conversion from individual cross correlations to an "effective" correlation (ML) and the subsequent Lockwood et al. 2014 conversion from CC to $\log(L)$, may not be statistically valid.

As such, we recommend sticking to either the Zucker 2003 $\log(L)$ method of converting cross correlations to log likelihoods, which has proven both more successful with multi-epoch data sets and capable of differentiating between inverted and non-inverted planetary atmospheres, or the Brogi & Line 2019 conversion method. Nonetheless, we recommend that these approaches be compared across a larger range of epoch combinations and instruments to determine when each will produce a better result.

Stellar Orbital Parameters

Finally, we consider the stellar orbital parameters used to predict the planet's position on its orbit during each epoch. In the multi-epoch technique, we must know the orbital position of the planet during each epoch in order to relate the planetary line-of-sight velocity (v_{sec}) to the planetary semi-amplitude (K_p). This conversion can either be carried out assuming a circular orbit (as was done in Lockwood et al. 2014; Piskorz et al. 2017, 2018; Buzard et al. 2020),

$$v_{sec} = K_p \sin\left(2\pi\left[\frac{T_{obs} - T_o}{P}\right]\right) + v_{pri}, \tag{6.17}$$

or considering an eccentric orbit (Piskorz et al., 2016),

$$v_{sec} = -K_p(\cos(f + \omega) + e\cos(\omega)) + v_{pri}. \tag{6.18}$$

When assuming a circular orbit, the time of inferior conjunction (T_o) and orbital period (P) are needed. For an eccentric orbit, accurate values of the time of pericenter (T_{peri}), argument of pericenter (ω), eccentricity (e), and orbital period are needed. Observation times can be converted into true anomalies (f) as described in Buzard et al. 2021b. Different reference times and angles could be used so long as they are consistent.

Comparison of Literature Orbital Parameters

First, we aim to show the importance of accurate stellar orbital parameters in detecting a planet. Five literature sources have published stellar orbital parameters for the HD 88133 system: Fischer et al. 2005, Butler et al. 2006, Piskorz et al. 2016, Ment et al. 2018, and Luhn et al. 2019. These sources each fit parameters to different sets of radial velocity data points. The orbital parameters from each literature source are listed in Table 6.1.

While the other four works fit HD 88133 A data with an eccentric orbit, Ment et al. 2018 set $e = 0$ and $t_{peri} = 2453014.948$. Because they assume a circular orbit, the time of periastron can be understood as corresponding to an arbitrary point on the orbit rather than having a physical meaning as in the rest of the literature sources. This is why their argument of periastron ω does not agree with the rest of the values and why its uncertainty is so much smaller than that of the other values.

Figure 6.7A shows where each of the literature sources places the HD 88133 L band epochs relative to inferior conjunction. It is clear in this figure that the parameters from Butler et al. 2006 are very different from the other four sources.

Figure 6.7B shows the how the L band orbital positions given by each of the five literature references affect the resulting planetary log likelihood curve. The difference in the Butler et al. 2006 parameters stands out here as well. These results illustrate how inaccurate orbital parameters can serve to shift the expected epoch orbital positions off of the true orbital positions and therefore have a large effect on the shape of the resulting log likelihood curve. This could shift the position of the planetary peak, resulting in an offset in the reported K_p, or even remove the peak altogether if the expected orbital positions given inaccurate orbital parameters no longer lined the appropriate per-epoch v_{sec} values up. While the estimated orbital position offset in the original HD 88133 b multi-epoch detection Piskorz et al. 2016 had a different cause (explained in Buzard et al. 2021b), the effect would have been the same as using inaccurate stellar orbital parameters. For any chance of being able to detect a planet, multi-epoch analyses must use stellar radial velocity orbital parameters that are as up-to-date and accurate as possible.

Effects of Uncertainty in Orbital Parameters

We now wish to consider how various sources of uncertainty (e.g., the uncertainty in the stellar radial velocity orbital parameters, range of observation time per epoch) affect the shape of the final planetary log likelihood curve. The uncertainty in the systemic velocity and barycentric velocity during an observation could also be considered, but we leave that for future work.

For the observation times, we have typically used the JD at the midpoint of the observation. However, our observations typically span a total of 2 – 4 hours. For the six L band epochs of HD 88133 b, the minimum observation time was about 2.2 hours and the maximum was about 4.9 hours. As we demonstrated in Section 6.3, if HD 88133 b were in a transiting geometry, in one of these epochs, the planetary signal could have crossed up to 4.5 NIRSPEC resolution

Table 6.1: HD 88133 b RV Orbital Parameters

Reference	Ref. Label	K [m/s]	P [days]	e	ω_{st} [°][a]	t_{peri} [JD]
Fischer et al. 2005	F05	35.7 ± 2.2	3.415 ± 0.001	0.11 ± 0.05	10.2 ± 162.9	2453016.4 ± 1.2
Butler et al. 2006	B06	36.1 ± 3.0	3.41587 ± 0.00059	0.133 ± 0.072[b]	349[b]	2453016.31 ± 0.32
Piskorz et al. 2016	P16	32.9 ± 1.03	$3.4148674^{+4.57e-05}_{-4.73e-05}$	0.05 ± 0.03	$7.22^{+31.39}_{-48.11}$	$2454641.984^{+0.293}_{-0.451}$
Ment et al. 2018	M18	32.7 ± 1.0	3.414887 ± 0.000045	0[c]	205.3 ± 3.3	2453014.948[c]
Luhn et al. 2019	L19	32.93 ± 0.73	3.414884 ± 0.000030	0.031 ± 0.021	43 ± 33	2453016.82 ± 0.37

[a]In this draft, we set the line-of-sight Z-axis as pointing away from the observer, as in Fulton et al. 2018. This sets the ascending node as the node at which the objects pass "behind" the sky plane. From this ascending node, ω is measured on the star's orbit. Previous works (e.g., Murray & Correia, 2010) set the Z-axis toward the observer, and therefore the ascending node is where the objects pass "in front of" the sky plane. With this sign convention, ω would be measured on the planet's orbit.

[b]When the uncertainty in e is comparable to e, uncertainties in ω and e become non-Gaussian. See Butler et al. 2006, Section 4.

[c]Ment et al. 2018 fixed $e = 0$ and $t_{peri} = 2453014.948$.

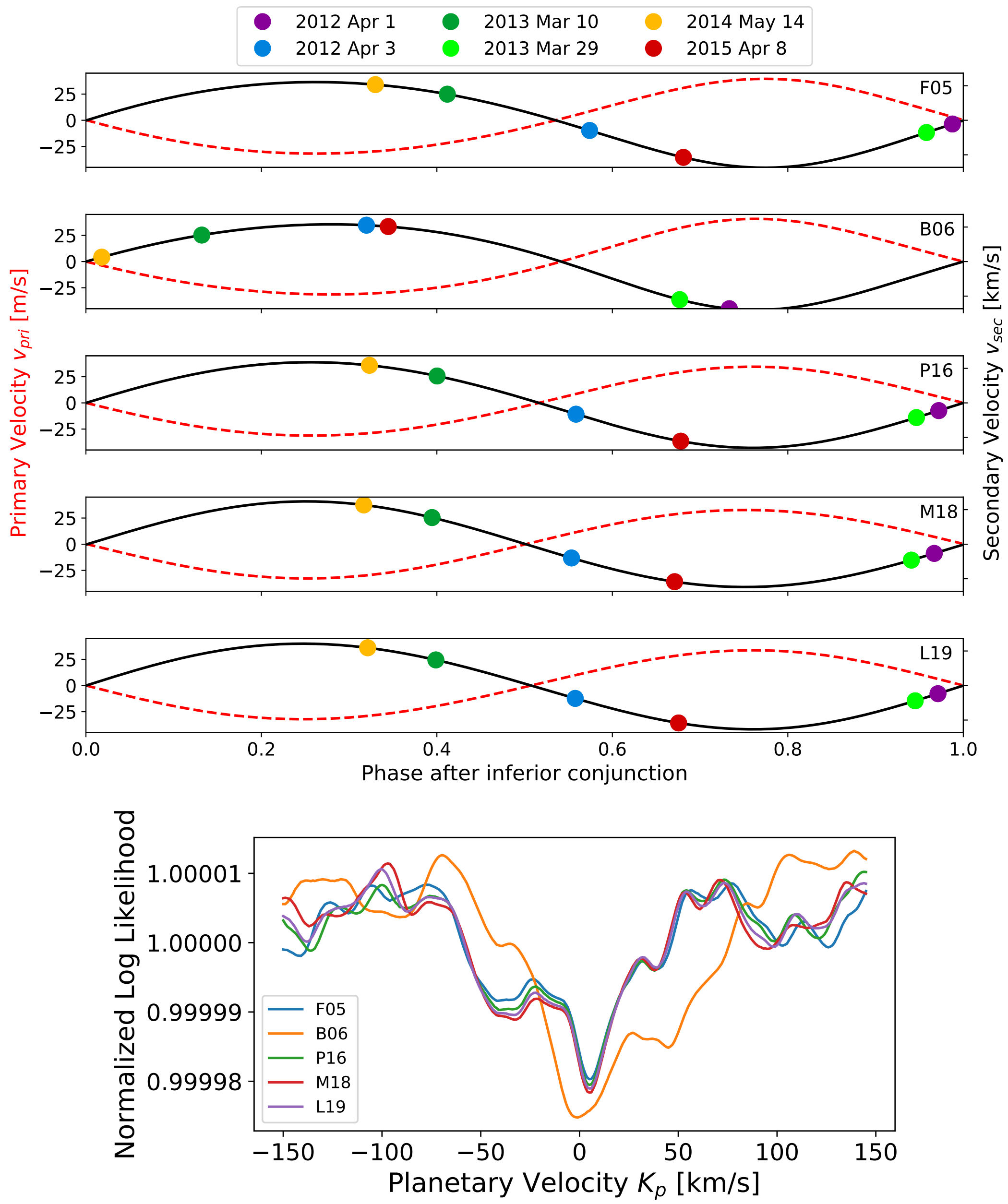

Figure 6.7: (A) RV curves for HD88133A (dashed red) and HD88133b (black) showing the positions of each data epoch given orbital parameters from the five difference references (F05 - Fischer et al. 2005, B06 - Butler et al. 2006, P16 - Piskorz et al. 2016, M18 - Ment et al. 2018, L19 - Luhn et al. 2019). The planetary curve is given an arbitrary amplitude. It is clear here that the B06 ephemeris places the epochs at significantly different positions than the ephemeri from the rest of the literature sources. (B) Normalized log likelihood for the six L band epochs of HD 88133 b using orbital parameters from different literature sources. These log likelihoods were generated by cross correlating the data with the [2n2835] stellar model and non-inverted SCARLET planetary model. The shape of the log likelihood curve generated with B06 ephemeri varies significantly from the other four, illustrating why accurate stellar RV parameters are so crucial.

elements. We first consider how the choice of observation time within the full range affects the shape of the resulting log likelihood curve. To do this, we pull 1000 draws from uniform distributions from the start to the end of the observation for each epoch. We otherwise use orbital parameters from Luhn et al. 2019 (this choice will be described shortly), the [2n2835] stellar model, and the PHOENIX non-inverted planetary model. The results of these 1000 draws are shown in Panel A of Figure 6.8 in light blue. This figure shows that the choice of observation time within the full range will not have a large effect on the shape of the log likelihood curve, which was expected because the observing times only cover $\sim$ 3 – 6% of the orbital period anyways. Furthermore, the uncertainty shown here is probably overestimated because (1) the uniform distribution puts more weighting at the boundaries of the observations times than is probably realistic, and (2) if there is an offset in the observations times, it would probably affect all epochs in the same direction rather than in different ways.

Next we look into the uncertainty in the stellar orbital parameters. We consider the Luhn et al. 2019, Piskorz et al. 2016, and Fischer et al. 2005 parameters. The Luhn et al. 2019 parameters were fit to the most radial velocity epochs and have the smallest uncertainties while the Fischer et al. 2005 parameters were fit to the fewest RV epochs and have the largest uncertainties. From each set of orbital parameters, we pull 1000 draws from the Gaussian distributions with median and 1σ values set by the orbital parameters and their uncertainties. We place a prior on the eccentricity distribution to keep its values between 0 and 1. For the Piskorz et al. 2016 parameters, because the positive and negative uncertainty values are uneven, we pull from a Gaussian centered on 0 and with a σ of 1. If the pull is negative, we multiply it by the negative error bar for each parameter and if it is positive, we multiply it by the positive error bar. Finally, we add the offset to the reported parameter value.

In addition to the parameters pulled from uncertainty distributions, we use the mid-point observation times, the [2n2835] PHOENIX stellar model, and the PHOENIX non-inverted planetary model. Panel B of Figure 6.8 shows the results of the 1000 pulls from the Luhn et al. 2019 parameters in blue, from the Piskorz et al. 2016 in green, and from the Fischer et al. 2005 parameters in gold. We see here that the variation due to uncertainty in orbital parameters is more significant than in observation time. Within the uncertainty here, the log likelihood curve is consistent with a flat line for most of the positive K_p

range, but with a significant dip near 0 km/s.

One way to reduce the uncertainty arising from the orbital parameters might be to approximate the orbit as circular, rather than using an eccentric orbit model. Buzard et al. 2021b showed that for small eccentricities ($e \sim 0.05$), assuming a circular orbit will result in planetary log likelihood curve quite comparable to the one resulting from a full eccentric orbit. However, the time and argument of periastron become very difficult to fit for small eccentricities (they are not defined for circular orbits), and this results in large uncertainties on these parameters. For instance, while the Butler et al. 2006 parameters for HD 88133 b seem off, for ups And b, Butler et al. 2006 reported a time of periastron of 2451802.64 ± 0.71 and a time of inferior conjunction of 2451802.966 ± 0.033. With its estimated period of 4.617113 days, the uncertainty on the time of periastron corresponds to 15.4% of the planet's orbit whereas the uncertainty on the time of inferior conjunction only corresponds to 0.7%. Since the time of inferior conjunction can be measured much more precisely for low-eccentricity orbits, and the planetary log likelihood curves using eccentric versus circular orbit models are equivalent at eccentricities up to at least 0.05, using a circular orbit approximation could produce a much less uncertain planetary log likelihood curve than an eccentric orbit model for these low-eccentricity systems. It should be noted, however, that for this to work, the time of inferior conjunction should be obtained through a direct fit to the stellar radial velocity data, not calculated from the uncertain time of periastron.

Finally, in Panel C of Figure 6.8, we show the jack-knife errors from this analysis. Jack-knife error has been the uncertainty shown on most of the previous multi-epoch detections (Piskorz et al., 2016, 2017, 2018; Buzard et al., 2020). Jack-knife sampling is a technique for understanding the variance in a sample that works by systematically leaving an observation (in this case, an epoch) out of a data set and recalculating the log likelihood surface. The variance of the final log likelihood surface is then calculated as the standard deviation at each velocity point among the N jack-knife samples multiplied by $\sqrt{N-1}$, where N equals the number of observations, in this case, 6. Jack-knife error is typically useful for confirming that a feature in the final log likelihood curve is not only due to a feature in one of the epochs, but rather has contributions from more of the epochs. As a general note, however, for small epoch detections, it could be the case that one or two epochs are in much

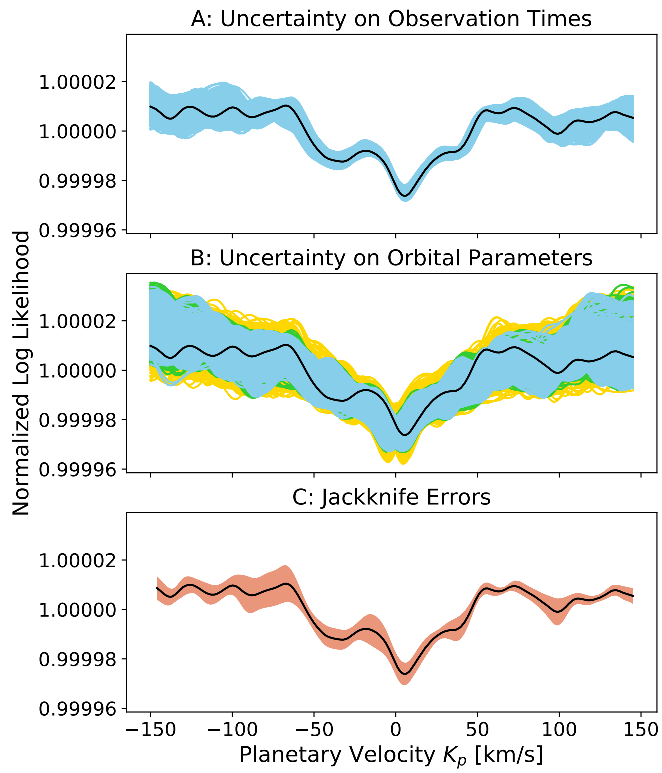

Figure 6.8: (A) Normalized log likelihoods generated by cross correlating the HD 88133 data from Piskorz et al. 2016 with a [2n2835]-normalized PHOENIX stellar model and non-inverted PHOENIX planetary model. We test the effects of the uncertainty in the time of observation by generating true anomaly f values from 1000 random pulls from the uniform distribution of observation times (JDs) from the start of the observation to the end of the observation. The other orbital parameters (P, e, t_{peri}, ω) were taken from Luhn et al. 2019. (B) We now explore the effects of the orbital parameter uncertainty. The blue log likelihood curves are generated from 1000 pulls from the Gaussian distributions of Luhn et al. 2019 orbital parameters, the green are from the Piskorz et al. 2016 orbital parameter distributions, and the gold are from the Fischer et al. 2005 orbital parameter distributions. The observation times are set constant at the observation midpoints. (C) Jack-knife errors are plotted.

better positions to constrain K_p (i.e., near quadrature), while the majority of the epochs could be in worse positions (near inferior/superior conjunction). If this were the case, the jack-knife errors, which do not discern between epochs that should be better/worse able to constrain K_p, would be overestimated and could make the planetary peak appear at a lower confidence than it truly is from the data. A more realistic error analysis would account for each epoch's expected ability to constrain K_p, which could be approximated by the epoch's orbital position.

Figure 6.8 illustrates that for the 6 L band HD 88133 b epochs, the variance among the epochs is not the only, or even the major, source of uncertainty in the final log likelihood curve. These different sources of uncertainty should all be investigated for future multi-epoch analyses.

6.5 Summary

In this chapter, we detail areas along the multi-epoch pathway where care should be taken and areas where there is much room for improvement. A few key points stand out:

- The known stellar velocity at each epoch is a very powerful indicator of what works and what does not. For instance, a better telluric correction approach should lead to higher likelihood detections of the stellar signal at its known velocity. So should a better stellar model. In this way, the stellar signal can be used as a benchmark to optimize various parts of the analysis even on data in which the planetary velocity is not yet known.

- Telluric correction approaches and stellar models are a major current limiting to the technique. An optimal telluric correction approach would be one that did not require a large baseline in each observation. Stellar models will ultimately need to consider activity and star spots.

- Planetary radial velocity parameters can only be as well known as stellar radial velocity parameters. Stellar RV parameters must be accurate and up to date.

- As long as a planetary signal is identifiable within a data set, and separable from noise features, the multi-epoch approach will be able to distinguish emission and absorption features.

- The multi-epoch approach will be applicable to a much larger population of planets than the CRIRES approach, which is essentially limited to planets on orbits less than $a \lesssim 0.05 - 0.1$ AU.

References

Barnes, J. R., Jeffers, S. V., Anglada-Escudé, G., et al. 2017, *MNRAS*, 466, 1733, doi: 10.1093/mnras/stw3170

Bedell, M., Hogg, D. W., Foreman-Mackey, D., Montet, B. T., & Luger, R. 2019, *AJ*, 158, 164, doi: 10.3847/1538-3881/ab40a7

Beltz, H., Rauscher, E., Brogi, M., & Kempton, E. M. R. 2021, *AJ*, 161, 1, doi: 10.3847/1538-3881/abb67b

Bender, C. F., Mahadevan, S., Deshpande, R., et al. 2012, *ApJL*, 751, L31, doi: 10.1088/2041-8205/751/2/L31

Benneke, B. 2015, arXiv e-prints, arXiv:1504.07655. https://arxiv.org/abs/1504.07655

Birkby, J. L. 2018, arXiv e-prints, arXiv:1806.04617. https://arxiv.org/abs/1806.04617

Birkby, J. L., de Kok, R. J., Brogi, M., Schwarz, H., & Snellen, I. A. G. 2017, *AJ*, 153, 138, doi: 10.3847/1538-3881/aa5c87

Brogi, M., de Kok, R. J., Albrecht, S., et al. 2016, *ApJ*, 817, 106, doi: 10.3847/0004-637X/817/2/106

Brogi, M., & Line, M. R. 2019, *AJ*, 157, 114, doi: 10.3847/1538-3881/aaffd3

Brogi, M., Snellen, I. A. G., de Kok, R. J., et al. 2012, *Nature*, 486, 502, doi: 10.1038/nature11161

Butler, R. P., Wright, J. T., Marcy, G. W., et al. 2006, *ApJ*, 646, 505, doi: 10.1086/504701

Buzard, C., Pelletier, S., Piskorz, D., Benneke, B., & Blake, G. A. 2021a, *AJ*, 162, 26, doi: 10.3847/1538-3881/abf7b9

Buzard, C., Piskorz, D., Lockwood, A. C., et al. 2021b, *AJ*, 162, 269, doi: 10.3847/1538-3881/ac2a2c

Buzard, C., Finnerty, L., Piskorz, D., et al. 2020, *AJ*, 160, 1, doi: 10.3847/1538-3881/ab8f9c

Claret, A. 2000, *A&A*, 363, 1081

de Kok, R. J., Birkby, J., Brogi, M., et al. 2014, *A&A*, 561, A150, doi: 10.1051/0004-6361/201322947

Dudhia, A. 2017, *J. Quant. Spec. Radiat. Transf.*, 186, 243, doi: 10.1016/j.jqsrt.2016.06.018

Finnerty, L., Buzard, C., Pelletier, S., et al. 2021, *AJ*, 161, 104, doi: 10.3847/1538-3881/abd6ec

Fischer, D. A., Laughlin, G., Butler, P., et al. 2005, *ApJ*, 620, 481, doi: 10.1086/426810

Frasca, A., Biazzo, K., Catalano, S., et al. 2005, *A&A*, 432, 647, doi: 10.1051/0004-6361:20041373

Fulton, B. J., Petigura, E. A., Blunt, S., & Sinukoff, E. 2018, *PASP*, 130, 044504, doi: 10.1088/1538-3873/aaaaa8

Gaia Collaboration, Brown, A. G. A., Vallenari, A., et al. 2018, *A&A*, 616, A1, doi: 10.1051/0004-6361/201833051

Gandhi, S., & Madhusudhan, N. 2019, *MNRAS*, 485, 5817, doi: 10.1093/mnras/stz751

Guilluy, G., Sozzetti, A., Brogi, M., et al. 2019, *A&A*, 625, A107, doi: 10.1051/0004-6361/201834615

Gustafsson, B., Edvardsson, B., Eriksson, K., et al. 2008, *A&A*, 486, 951, doi: 10.1051/0004-6361:200809724

Han, E., Wang, S. X., Wright, J. T., et al. 2014, *PASP*, 126, 827, doi: 10.1086/678447

Hubeny, I., Burrows, A., & Sudarsky, D. 2003, *ApJ*, 594, 1011, doi: 10.1086/377080

Husser, T. O., Wende-von Berg, S., Dreizler, S., et al. 2013, *A&A*, 553, A6, doi: 10.1051/0004-6361/201219058

Kausch, W., Noll, S., Smette, A., et al. 2014, in Astronomical Society of the Pacific Conference Series, Vol. 485, Astronomical Data Analysis Software and Systems XXIII, ed. N. Manset & P. Forshay, 403

Lockwood, A. C., Johnson, J. A., Bender, C. F., et al. 2014, *ApJL*, 783, L29, doi: 10.1088/2041-8205/783/2/L29

Long, D. A., Bielska, K., Lisak, D., et al. 2011, *JChPh*, 135, 064308, doi: 10.1063/1.3624527

Luhn, J. K., Bastien, F. A., Wright, J. T., et al. 2019, *AJ*, 157, 149, doi: 10.3847/1538-3881/aaf5d0

Ment, K., Fischer, D. A., Bakos, G., Howard, A. W., & Isaacson, H. 2018, *AJ*, 156, 213, doi: 10.3847/1538-3881/aae1f5

Metcalf, A. J., Anderson, T., Bender, C. F., et al. 2019, Optica, 6, 233, doi: 10.1364/OPTICA.6.000233

Morris, E. C., Wang, J. J., Ruffio, J.-B., et al. 2020, in Society of Photo-Optical Instrumentation Engineers (SPIE) Conference Series, Vol. 11447, Society of Photo-Optical Instrumentation Engineers (SPIE) Conference Series, 1144761

Mortier, A., Santos, N. C., Sousa, S. G., et al. 2013, *A&A*, 557, A70, doi: 10.1051/0004-6361/201321641

Murphy, M. T., Udem, T., Holzwarth, R., et al. 2007, *MNRAS*, 380, 839, doi: 10.1111/j.1365-2966.2007.12147.x

Murray, C. D., & Correia, A. C. M. 2010, Keplerian Orbits and Dynamics of Exoplanets, ed. S. Seager, 15–23

Pelletier, S., Benneke, B., Darveau-Bernier, A., et al. 2021, *AJ*, 162, 73, doi: 10.3847/1538-3881/ac0428

Piskorz, D., Benneke, B., Crockett, N. R., et al. 2016, *ApJ*, 832, 131, doi: 10.3847/0004-637X/832/2/131

—. 2017, *AJ*, 154, 78, doi: 10.3847/1538-3881/aa7dd8

Piskorz, D., Buzard, C., Line, M. R., et al. 2018, *AJ*, 156, 133, doi: 10.3847/1538-3881/aad781

Rothman, L. S., Gordon, I. E., Barbe, A., et al. 2009, *J. Quant. Spec. Radiat. Transf.*, 110, 533, doi: 10.1016/j.jqsrt.2009.02.013

Sneden, C. 1973, *ApJ*, 184, 839, doi: 10.1086/152374

Snellen, I. A. G., de Kok, R. J., de Mooij, E. J. W., & Albrecht, S. 2010, *Nature*, 465, 1049, doi: 10.1038/nature09111

Valenti, J. A., & Fischer, D. A. 2005, *ApJS*, 159, 141, doi: 10.1086/430500

Wang, J. J., Ruffio, J.-B., Morris, E., et al. 2021, *AJ*, 162, 148, doi: 10.3847/1538-3881/ac1349

Wilks, S. S. 1938, The Annals of Mathematical Statistics, 9, 60, doi: 10.1214/aoms/1177732360

Wright, J. T., Upadhyay, S., Marcy, G. W., et al. 2009, *ApJ*, 693, 1084, doi: 10.1088/0004-637X/693/2/1084

Ycas, G. G., Quinlan, F., Diddams, S. A., et al. 2012, Opt. Express, 20, 6631, doi: 10.1364/OE.20.006631

Zucker, S. 2003, *MNRAS*, 342, 1291, doi: 10.1046/j.1365-8711.2003.06633.x

Zucker, S., & Mazeh, T. 1994, *ApJ*, 420, 806, doi: 10.1086/173605

Chapter 7

NEAR-INFRARED SPECTRA OF THE INFLATED POST-COMMON ENVELOPE BROWN DWARF NLTT5306B

This chapter is adapted from work previously published as

Buzard, C., Casewell, S., Lothringer, J., et al. 2022, *The Astronomical Journal*, 163, 262, doi: `10.3847/1538-3881/ac6508`

7.1 Introduction

As exoplanet detecting surveys ramped up the number of known planets orbiting other stars, an interesting phenomenon arose. The "brown dwarf desert" describes the apparent lack of brown dwarf ($\sim 10-80\ M_{Jup}$) companions within ~5 AU of solar-type stars (e.g., Grether & Lineweaver, 2006). Grieves et al. 2017 estimated the brown dwarf occurrence rate around solar-type stars with periods less than 300 days to be ~0.56%. It follows that the evolved form of these rare binaries, white dwarf/brown dwarf binaries, is also quite rare; Steele et al. 2011 predicted only $0.5 \pm 0.3\%$ of white dwarfs have brown dwarf companions. To date, only eleven detached systems are known (van Roestel et al., 2021) and the number of interacting systems is equally small (e.g., Burleigh et al., 2006; Hernández Santisteban et al., 2016).

White dwarf/brown dwarf binaries are often called substellar post-common envelope binaries because of the chaotic evolutionary pathway they go through as their host star dies and evolves into a white dwarf. When the host star expands once it has exhausted its hydrogen reservoir, it overfills its Roche Lobe and eventually enters a common envelope with its brown dwarf companion. During this stage, the brown dwarf's orbit becomes unstable and it begins to spiral inward. The dying star loses its outer layers and leaves its core as a white dwarf, ending the common envelope period and retreating back within its Roche Lobe. Izzard et al. 2012 offers a nice review of the common envelope process. After the common envelope has dissipated, in the "post-common envelope binary" stage, the brown dwarf is still on an inspiraling orbit and eventually it will fill its Roche Lobe and begin to donate mass to the white dwarf. SDSS J121209.31+013627.7 (Burleigh et al., 2006; Stelzer et al., 2017) and SDSS J143317.78+101123.3 (Hernández Santisteban et al., 2016) are two examples of systems at this stage in the evolutionary process, both showing mass donation from the brown dwarf companion onto the white dwarf host.

NLTT 5306 is a post-common envelope binary with a brown dwarf companion. Details of this system are given in Table 7.1. It was first discovered by Steele et al. (2013) who searched for known white dwarfs with an infrared excess indicative of a cool companion, and it was initially thought to be a detached system. However, evidence in the form of a weak hydrogen emission feature that moves in phase with and at the radial velocity of the white dwarf and not the brown dwarf, and a sodium absorption feature moving the same way, suggests that the brown dwarf may have just begun losing mass to its host white dwarf (Longstaff et al., 2019). Non-detections in both X-rays and the radio at 6 GHz put an upper limit of this accretion at 1.3×10^{11} gs^{-1} (Longstaff et al., 2019). This low accretion rate, and the geometry of the system, suggests the brown dwarf is not, in fact, filling its Roche Lobe, and as such, the mechanism leading to accretion is unclear.

While NLTT 5306 B does not fill its Roche Lobe, near-IR spectra from SpeX on IRTF have shown evidence of intermediate gravity, with $\log(g)$ ~4.8, suggesting the brown dwarf is inflated (Casewell et al., 2020a). In exoplanets, significant levels of ultraviolet (UV) irradiation onto a planet from its host can cause the planetary atmosphere to inflate and evaporate (e.g., Demory & Seager, 2011). The white dwarf, NLTT 5306 A, however, is relatively cool (T_{eff} = 7756 ± 35 K), and so it is not possible that the brown dwarf is having its atmosphere "boiled off." In fact, there are brown dwarfs in closer orbits around hotter white dwarfs which show no evidence of either inflation or mass accretion onto the white dwarf. Two such examples are SDSS J1205-0242B (Parsons et al., 2017) and SDSS J1411+2009B (Littlefair et al., 2014), which receive ~250 and ~4.5× the irradiation of NLTT 5306B, respectively. On the other hand, NGTS-19b, a high-mass brown dwarf orbiting a K dwarf (Acton et al., 2021), and WD1032+011, a brown dwarf orbiting a 9950 K white dwarf (Casewell et al., 2020b), like NLTT 5306B, both receive relatively little UV irradiation and yet, are both inflated.

Inflation and low surface gravity have long been understood to be indicators of youth in brown dwarfs (e.g., Cruz et al., 2009; Allers & Liu, 2013). When under ~ 100 Myr, brown dwarfs are still contracting and so have larger radii than older brown dwarfs of the same spectral type (Burrows et al., 2001). Casewell et al. 2020a measured the gravity sensitive indices of Allers & Liu 2013 from their SpeX spectrum of NLTT 5306B and found that its intermediate gravity was comparable to that of a 50 – 200 Myr L5 brown dwarf. NLTT 5306B is known to be much older than that though. As a known thick-disk object (Steele et al., 2013), NLTT 5306B is at least 5 Gyr (its white dwarf's minimum cooling age) and probably much older. Youth is not a plausible explanation of the inflation seen in this dwarf.

Sainsbury-Martinez et al. 2021 considered whether a mechanism involving heating the deep atmosphere by vertical advection of potential temperature as is used to explain hot Jupiter inflation (Tremblin et al., 2017; Sainsbury-Martinez et al., 2019) could also explain brown dwarf inflation. They found that the inflation of brown dwarfs Kepler-13Ab and KELT-1b, orbiting 7650 and 6518 K main-sequence stars, could be explained this way. The highly irradiated 13000 K white dwarf companion SDSS1411B could not be inflated by vertical advection of energy into its deep atmosphere. Sainsbury-Martinez et al. 2021 suggest that the ineffectiveness of vertical advection to lead to inflation of SDSS1411B could be due to its fast rotation rate. With NLTT 5306B's slightly faster rotation rate and lower irradiation, it is unclear whether heating of its deep atmosphere could lead to inflation, or not, as in the case of SDSS1411B.

Casewell et al. 2020a proposed two alternate mechanisms that could lead to the inflation of NLTT 5306 B. Magnetic activity has been used to explain inflation in M dwarfs (Parsons et al., 2018). There is already some evidence that NLTT 5306 A has a non-negligible magnetic field, because there was no infrared excess indicative of an accretion disk (Longstaff et al., 2019), suggesting that the accretion onto the white dwarf may be following magnetic field lines, as happens in polars. Further, when Casewell et al. 2020a compared NLTT 5306 B to the 23 known brown dwarfs transiting main sequence stars (Carmichael et al., 2020), they found that CoRoT-15b and CoRoT-33b, the only two orbiting magnetically active stars, were also possibly inflated. The second contributing factor they proposed was a high-metallicity, cloudy brown dwarf atmosphere, which Burrows et al. 2011 showed could lead to larger radii. NLTT 5306 B, as mid-L dwarf, could be reasonably expected to be cloudy; however, NLTT 5306 is known to be a thick-disk object (Steele et al., 2013), which implies it is probably much older than its white dwarf minimum cooling age (> 5 Gyr). Given its old age, it is unlikely to be metal-enriched.

In this work, we obtained the highest resolution near-infrared spectrum of any white dwarf/brown dwarf binary to date. With this $R \lesssim 2000$ resolution spectrum of NLTT 5306, we aim to constrain the effective temperature, surface gravity, and metallicity of the brown dwarf's atmosphere and to determine whether there are

Table 7.1: NLTT5306 System Parameters

Property	Value	Ref.
NLTT5306A		
Temperature	7756 ± 35 K	(1)
Surface Gravity, log(g)	7.68 ± 0.08	(1)
Cooling Age	710 ± 50 Myr	(1)
Distance	71 ± 4 pc	(1)
Mass	0.44 ± 0.04 $M_\odot$	(1)
Radius	0.0156 ± 0.0016 $R_\odot$	(1)
Systemic velocity[a], v_{sys}	15.6 ± 1.8 km/s	(2)
Velocity Semi-Amplitude[a], K_{WD}	-46.8 ± 2.5 km/s	(2)
NLTT5306B		
Orbital Period	101.88 ± 0.02 min	(1)
Separation, a	0.566 ± 0.005 $R_\odot$	(1)
Time of Inferior Conjunction, T_o	2453740.1778(8)	(2)
Minimum Mass, $M \sin i$	56 ± 3 M_{Jup}	(1)
Evolutionary Radius[b]	0.095 ± 0.004 $R_\odot$	(1)
Roche Lobe Radius	0.12 ± 0.02 $R_\odot$	(2)
Spectral Type	L5	(3)

Refs: (1) Steele et al. 2013, (2) Longstaff et al. 2019, (3) Casewell et al. 2020a

[a]These values were measured from Hα absorption lines in the white dwarf.

[b]This radius was estimated from evolutionary models. Because the system is not eclipsing, a true radius measurement cannot be made.

any day- to night-side variations in these parameters that could provide clues into the mechanism of inflation. While evidence has pointed to weak accretion onto the white dwarf, we do not know precisely what could cause the accretion in this system. A closer picture of the brown dwarf, in the form of phase-resolved spectra, may offer some insight.

7.2 NIRSPEC Observations and Data Reduction

Observations

We obtained Keck/NIRSPEC (McLean et al., 1998; Martin et al., 2018) data of NLTT 5306 on three nights: October 17, 2019, January 7, 2020, and January 7, 2021. Each time, we used the NIRSPEC in its low-resolution (cross disperser-only) mode with the $42'' \times 0''.760$ slit and five-minute exposures to maximize our signal-to-noise on this faint (K_{mag} = 15.6) target. We measured a spectral resolution of $R \lesssim 2000$. On each night we observed telluric standards (HIP16322 and 31 Psc) at different airmasses to aid in telluric correcting the target data. Additional observational

Table 7.2: NIRSPEC Observations of NLTT5306

Property	2019 Oct 17	2020 Jan 7	2021 Jan 7
Filter	NIRSPEC-2	NIRSPEC-1	NIRSPEC-1
Wavelength (μm)	1.089 – 1.293	0.947 – 1.121	0.947 – 1.121
Airmass	1.02 – 1.17	1.015 – 1.075	1.0 – 1.11
N_{Nods} [a]	14	10	20
$N_{Nods,day}$	8	7	8
$N_{Nods,night}$	5	3	10
v_{bary} (km/s)	1.6	-29.6	-29.7

[a]Each nod had an exposure time of 5 minutes.

parameters are given in Table 7.2 and Figure 7.1 shows the brown dwarf orbital position at each nod. This represents the highest resolution (near-)infrared spectra ever taken of a white dwarf/brown dwarf binary system.

Reduction

With the two-dimensional images in hand, we flat-fielded and dark subtracted the data according to Boogert et al. 2002. We subtracted the A and B nods to reduce background light. Then, we used a third-order polynomial to fit and correct for any curvature of the trace, which can be quite significant in the low-resolution mode of NIRSPEC, before extracting the one-dimensional spectra.

Typically subtracting the A and B nods does not correct for telluric absorption features, which require a source of background light and so only show up, spatially separated, across the traces, but does correct for telluric emission features, which, because they do not require a source of background light, show up across the full spatial dimension of the order. Because NLTT 5306 is so faint, though, and our nods were each 5 minutes long, there was enough time for the sky emission lines to change in shape and intensity from one nod to the next. As a result, subtracting the A and B nods did not fully correct sky emission lines from our data. To compensate for this, we extracted the one-dimensional sky emission spectra off the target trace and linearly scaled them to fit the emission features in the data. We calibrated the data wavelength axes by fitting these sky emission spectra to a sky emission model from `SkyCalc`[1] (Noll et al., 2012; Jones et al., 2013) with a fourth-order polynomial fit between data pixels and model wavelengths. To correct for the sky emission lines in the data, we chose to incorporate them in our cross-correlation analysis rather than divide them out. We describe how they are included in our cross correlations in

[1]http://www.eso.org/sci/software/pipelines/skytools/skycalc.

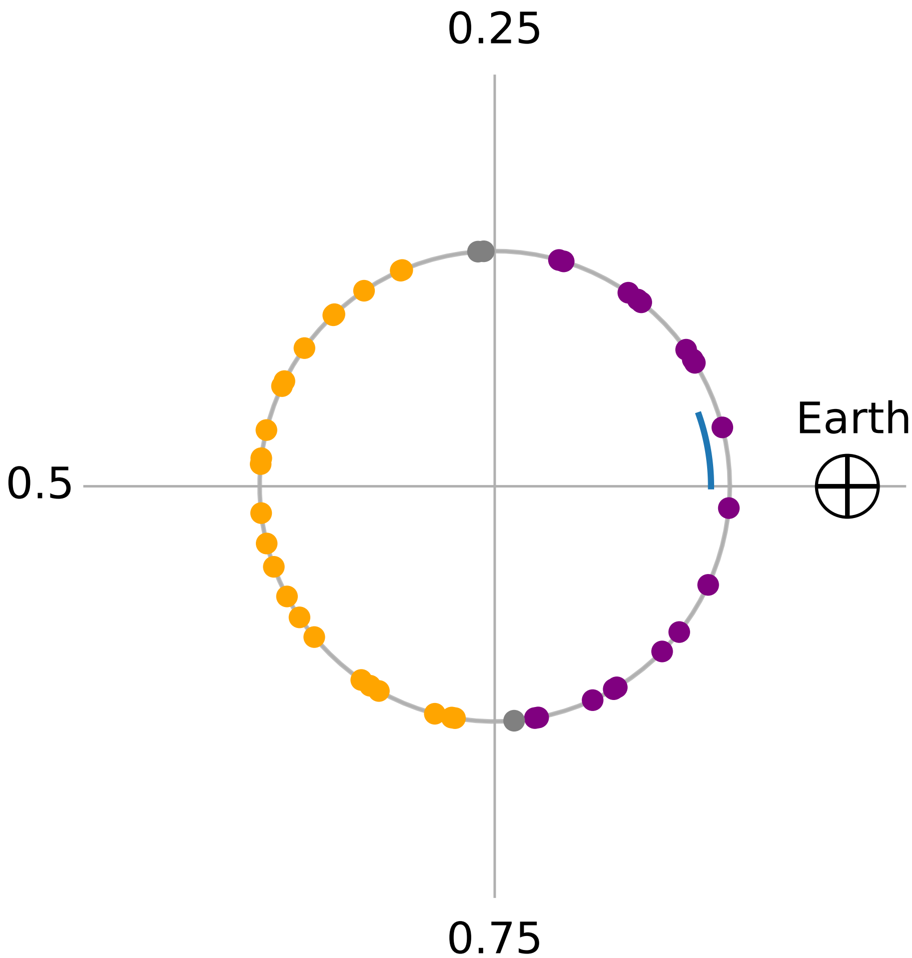

Figure 7.1: Diagram showing the center position of each of our 44 epochs. Orange points represent day-side epochs, purple points represent night-side epochs, and gray points represent observations during which NLTT5306B crossed quadrature and are therefore neither primarily day- or night-side. The blue arc starting at ϕ = 0 shows the average change in orbital position over a 5-minute exposure.

Section 7.4. We find that correcting the emission features this way reduces unwanted structure in cross correlation space.

The standard data were reduced the same way as the target data. Several Paschen series hydrogen absorption features were present in the standards, including Pa-ϵ (954 nm), Pa-δ (1005 nm), and Pa-γ (1094 nm) in the Jan 7 2020 and 2021 data taken with the NIRSPEC-1 filter and Pa-γ (1094 nm) and Pa-β (1282 nm) in the Oct 17 data taken with the NIRSPEC-2 filter. We masked out these features, interpolated between the airmasses of the standard observations to the airmass of each target observation, and divided each target nod by the appropriate airmass standard to remove telluric absorption features from the data. As seen in Figure 7.2, there is a jump between data from the two filters. This jump should not affect our cross-correlation analysis; cross correlations are sensitive to the variation in a spectrum rather than the baseline height. As will be described in Section 7.4, each nod (and so, as follows, each filter) is cross correlated separately, so the jump between filters will not be interpreted as a real absorption feature.

In order to measure the instrument profile of the data, we used the ESO tool `Molecfit` (Smette et al., 2015; Kausch et al., 2015) to fit the tellurics in the standard data from each night. With the lack of telluric features present in the wavelengths covered by the Jan 7 nights, `Molecfit` could not generate a good telluric fit. It was able to fit the Oct 17 data, however, and reported a Gaussian kernel for the instrumental profile with a σ of 1.88 cm^{-1}. This was consistent with the kernel needed to broadened a `SkyCalc` model to fit the sky emission lines in our data from all three nights. A Gaussian kernel of 1.88 cm^{-1} corresponds to R$\sim$ 2000. In the later cross-correlation analysis, we broaden each of our brown dwarf spectral models with this kernel before cross correlating.

NIRSPEC Data

The final one-dimensional spectra, shifted into the brown dwarf frame-of-reference assuming a $K_{\rm BD}$ of 333 km/s (the center of the $K_{\rm BD}$ prior described in Section 7.5) and coadded, are shown in Figure 7.2. The blue and green portions of the spectrum are from the different wavelength filters. In gray, the sky emission data extracted from off of the target traces is shifted and coadded in the same way as the corresponding trace. These wavelengths fall on the Rayleigh-Jeans side of the 7756 K white dwarf blackbody curve meaning that, while the white dwarf contributes significant flux to our data, it should not add more than a linear slope to the continuum (see Figure 5

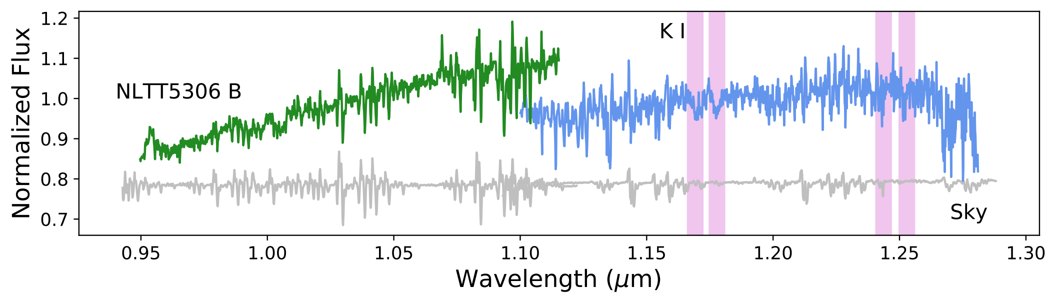

Figure 7.2: Our NIRSPEC data are shown in blue (Oct 17, 2019) and green (Jan 7, 2020 and Jan 7, 2021), shifted into the brown dwarf reference frame, assuming a K_{BD} of 333 km/s. In gray are the sky emission spectra from each epoch of data shifted in the same way as the data and vertically offset for clarity. The pink shading represents the positions of two K I doublets. Notably, the K I doublet at $\sim 1.16 - 1.17\mu$m is present in our data. The longer wavelength doublet coincides with a noisier portion of our spectrum.

from Longstaff et al. 2019), which is effectively removed by the standard correction. The white dwarf should show the same hydrogen absorption features we saw in the standard (Pa-ϵ at 0.954 μm, Pa-δ at 1.005 μm, Pa-γ at 1.094 μm, Pa-β at 1.282 μm), but we do not see strong evidence of these lines. Though, except for Pa-γ, all would fall at the noisy edges of our two orders.

Two notable features stand out. The regions shaded in pink denote the K I doublet wavelengths. The shorter wavelength doublet appears in our data. The longer wavelength doublet is less visible, but also corresponds to a noisier portion of our data.

Also, the gray sky emission spectrum can help us differentiate between signal from the target, noise, and telluric contamination. The ~1.083 μm region where metastable He emission has been detected from exoplanets with extended, eroding atmospheres (e.g., Spake et al., 2018), is dominated by sky emission, likely OH lines, in our data. It would be interesting to see whether metastable He emission lines would arise in this brown dwarf, as it does appear to be eroding at a similar rate to the canonical WASP-107b ($\lesssim 1.3 \times 10^{11}$ g/s, Longstaff et al. 2019 versus $10^{10} - 3 \times 10^{11}$ g/s, Spake et al. 2018), but as a brown dwarf, is much more dense and expresses much stronger gravitational forces on its atmosphere. Even higher resolution data, or data from a space-based instrument, would be needed to separate the telluric OH emission from any metastable He emission from the brown dwarf.

7.3 Brown Dwarf Spectral Models

To attempt to constrain NLTT 5306 B's effective temperature, surface gravity, and metallicity, we cross correlate our data with two sets of brown dwarf spectral models: the Sonora 2021 model grid (Marley et al., 2021) and a grid of irradiated brown dwarf models based on those presented in Lothringer & Casewell 2020. Before describing the cross-correlation analysis, we wish to make a few notes on the spectral models.

To test effective temperature, surface gravity, and metallicity, we use a subset of the Sonora 2021 model grid (Marley et al., 2021) that contains effective temperatures ($T_{\rm eff}$) from 200-600 K in steps of 25 K, 600-1000 K in steps of 50 K, and 1000-2400 K in steps of 100 K; surface gravity (log(g)) values of 3, 3.25, 3.5, 4, 4.5, 5, and 5.5; and metallicity ([Fe/H]) values of -0.5, 0, and 0.5. All of the models we use have a solar C/O ratio.

Effective temperature has the most dramatic effect on the morphology of these spectra. From the hottest to the coldest models, absorption features from refractory species (e.g., FeH, VO, TiO) and alkali metals (Na, K) gradually dissipate, leaving spectra shaped by only H_2O, CH_4, and NH_3 below $T_{\rm eff} \approx 1000$ K (Marley et al., 2021). Surface gravity affects the shape of the absorption features in the typical brown dwarf J band, with low surface gravity objects showing weaker FeH (0.99, 1.2 μm), Na I (1.14 μm), and K I (1.17, 1.25 μm) absorption, but stronger VO (1.06 μm) absorption, than field gravity objects (Allers & Liu, 2013). There is some commonality in the effect of high surface gravity and low metallicity on the spectral morphology. Like high surface gravity relative to low surface gravity models, low-metallicity models show stronger FeH, Na I, and K I features. However, unlike gravity, which affects both the depth and the width of the alkali features, metallicity mainly affects the depth alone.

Additionally, the Sonora models are made to replicate the spectra of non-irradiated substellar atmospheres. Zhou et al. 2022 recently found that the non-irradiated Sonora 2018 cloudless grid (Marley et al., 2018) resulted in poor fits to two other white dwarf/brown dwarf binaries, WD 0137B and EPIC 2122B. Irradiated models resulted in much better fits. These systems have substantially hotter white dwarfs than NLTT 5306 A, though. WD 0137A and EPIC 2122A are 16500 and 24900 K, respectively, compared to NLTT 5306A's 7756 K. It follows that WD 0137B and EPIC 2122B receive much higher levels of irradiation than NLTT 5306B. Indeed, both show Hα and metal emission from the surface of the brown dwarf, unlike NLTT 5306 B. Nonetheless, we also consider a grid of spectral models that do include irradiation.

Our irradiated models are based on those presented in Lothringer & Casewell 2020. The model grid spans a range of internal temperatures (T_{int} = 1000, 1500, 2000 K), surface gravities ($\log(g)$ = 4.5, 4.75, 5.0), metallicities ([Fe/H] = -0.5, 0, 0.5), and "irradiations." The irradiation cases include dayside heat redistribution ($f = 0.5$), full planet-wide redistribution ($f = 0.25$), and a high-albedo scenario ($f = 0.125$). The redistribution parameter considers both the surface area over which the object cools and the albedo. Setting the redistribution to 0 implies an albedo of 1, and so describes essentially a non-irradiated object. When irradiation is removed, these models approximate the Sonora spectra. When the redistribution is non-zero, the irradiation spectrum is determined from Koester 2010 white dwarf models. It should be noted that if there is a hot spot on the white dwarf associated with its inferred mass accretion (Longstaff et al., 2019), the flux the brown dwarf receives may exceed that predicted by the Koester 2010 models.

The internal temperatures and heat redistributions together determine the effective temperature of the irradiated brown dwarf. The following equations, originally from Lothringer & Casewell 2020, describe this conversion. First the irradiation temperature is determined from properties of the host and the brown dwarf heat redistribution and albedo,

$$T_{\mathrm{irr,BD}} = (f * (1 - A_{\mathrm{BD}}))^{1/4} * T_{\mathrm{eff,WD}} \sqrt{R_{\mathrm{WD}}/a}, \tag{7.1}$$

and then the effective temperature considers both the brown dwarf internal and irradiated temperatures,

$$T_{\mathrm{eff,BD}} = (T^4_{\mathrm{int,BD}} + T^4_{\mathrm{irr,BD}})^{1/4}. \tag{7.2}$$

Our three internal temperatures and three heat redistributions give rise to nine different effective temperature models. Using the white dwarf effective temperature and radius and the separation between the two objects from Table 7.1, and a Bond albedo A_{BD} of 0, the combinations of internal temperatures and heat redistributions give our models effective temperatures of 1077, 1140, 1241, 1525, 1549, 1593, 2011, 2021, and 2042 K. The effective temperatures are closely grouped around the internal temperatures because the irradiation is relatively mild due to the low white dwarf effective temperature. Especially at the higher internal temperatures (T_{int} = 2000 K), the internal temperature dominates the effective temperature, with irradiation playing only a minor role. As mentioned above, choosing an albedo of

1 removes the irradiation component and sets the effective temperature equal to the internal temperature.

7.4 Cross-Correlation Analysis

We cross correlate each of our nods with a brown dwarf model to determine the brown dwarf's line-of-sight velocity at that orbital position. The collection of velocities at different orbital positions can be used to measure NLTT 5306B's line-of-sight Keplerian orbital velocity $K_{\rm BD}$.

As described in Section 7.2, because our exposures were long, telluric emission features made it into our data. We decided to account for them by running a two-dimensional cross correlation. The first dimension correlates the off-trace sky emission spectra with the on-trace target spectra. These should, and do, find a maximum at 0 km/s because the data are taken from the Earth's reference frame. The second dimension of the cross correlation tests a brown dwarf spectral model against the data. We find that considering the sky emission lines in this two-dimensional cross-correlation framework allows us to better measure the brown dwarf velocity than by dividing out the emission features.

After each nod is cross correlated, we convert the cross correlations to log likelihoods so that they can be combined. To do so, we follow the formula presented by Zucker 2003,

$$\log(L(v_{\rm BD})) = -\frac{N}{2}\log(1 - C(v_{\rm BD})^2), \tag{7.3}$$

where N is the total number of pixels in the spectrum and C is the two-dimensional cross correlation. In order to avoid oversampling the likelihood surface, we calculate the likelihood in 36 km/s steps, which is approximately half of the low-resolution NIRSPEC pixel size.

Finally, the log likelihoods as a function of brown dwarf line-of-sight velocity, $v_{\rm BD}$, at each epoch can be combined into a log likelihood as a function of the line-of-sight Keplerian orbital velocity, $K_{\rm BD}$. We take the cuts along the maximum sky emission likelihood (near 0 km/s), and convert the $v_{\rm BD}$ to $K_{\rm BD}$, assuming a circular orbit, by

$$v_{\rm BD} = K_{\rm BD}\sin(2\pi\phi) + v_{\rm sys} - v_{\rm bary}. \tag{7.4}$$

The systemic velocity has been measured from the white dwarf's Hα absorption line (Table 7.1, Longstaff et al. 2019) and the barycentric velocity in the direction of NLTT 5306 can be calculated for the time of the observation. For Oct 17, 2019, Jan 7, 2020, and Jan 7, 2021, the barycentric velocity was 1.6 km/s, -29.6, and -29.7 km/s, respectively. The brown dwarf's orbital position, ϕ, is calculated as,

$$\phi = \frac{(T_{\rm obs} - T_o) \mod P}{P}, \tag{7.5}$$

where the time of inferior conjunction, T_o, and the orbital period, P, are given in Table 7.1 and ϕ runs from 0 to 1, with $\phi = 0$ corresponding to the orbital position with the brown dwarf closest to the observer (i.e., inferior conjunction).

As shown in Figure 7.1, the brown dwarf orbital position varies significantly across our 5-minute exposures. For a $K_{\rm BD}$ of 400 km/s, the change in expected $v_{\rm BD}$ could be as large as 130 km/s. This is comparable to the velocity resolution of NIRSPEC in its low-resolution mode ($\sim$ 150 km/s). As a means of accounting for this variation, we run the conversion from $v_{\rm BD}$ to $K_{\rm BD}$ 10 times, using 10 ϕ values for each nod, equally spaced from the start of the exposure time to the end. We then average the 10 resulting log likelihood functions. This should help to correct for the non-linear relationship between ϕ and $v_{\rm BD}$.

7.5 Priors on K_{BD}

We can leverage prior information from this system to get a sense of what to expect for the brown dwarf's Keplerian orbital velocity, $K_{\rm BD}$. The true brown dwarf orbital velocity ($2\pi a/P$), which sets a maximum limit on $K_{\rm BD}$, is 405 km/s. The line-of-sight velocity would equal this if the system were completely edge-in, with an inclination of 90°. However, because the system is known to be non-transiting (Steele et al., 2013), $K_{\rm BD}$ must be less than 405 km/s. Furthermore, Steele et al. 2013 saw no trace of either a full or even a grazing eclipse in phase-folded i'-band light-curves of NLTT 5306 taken with the Wide Field Camera on the Isaac Newton Telescope (INT). Given their data set-up, this is more likely explained by the system not transiting than by their missing the eclipse. The inclinations that would correspond to the minimum angles which would result in full and partial transit geometries are given by,

$$i_{\rm full} = 90^\circ - \sin^{-1}\left(\frac{R_{\rm BD} - R_{\rm WD}}{a}\right) \tag{7.6}$$

and

$$i_{\rm partial} = 90^\circ - \sin^{-1}\left(\frac{R_{\rm BD} + R_{\rm WD}}{a}\right). \tag{7.7}$$

Using evolutionary brown dwarf radius of 0.095 ± 0.004 $R_\odot$ (Steele et al., 2013), we find that any inclination above $81.9 \pm 0.4°$ would correspond to a full transit and any above $78.7 \pm 0.4^\circ$ would correspond to a partial transit. These inclinations can be converted to Keplerian orbital velocities by,

$$K_{\mathrm{BD}} = \frac{M_{\mathrm{WD}} K_{\mathrm{WD}} \sin(i)}{M_{\mathrm{BD}} \sin(i)}, \tag{7.8}$$

and give upper limits of 381 ± 45 (to exclude a full eclipse) and 378 ± 45 km/s (to exclude a partial eclipse). Using the Roche lobe radius of 0.12 ± 0.02 $R_\odot$, the full transit would extend down to $i = 79 \pm 2^\circ$ or up to $K_{\mathrm{BD}} = 378 \pm 45$ km/s and the partial transit would go down to $i = 76 \pm 2^\circ$ or up to $K_{\mathrm{BD}} = 374 \pm 44$ km/s. Assuming the brown dwarf has a radius between the evolutionary limit and Roche lobe radius, and that this system does not show even a partial eclipse, the upper limit of K_{BD} is between 378 ± 45 and 374 ± 44 km/s.

We can approximate a lower limit on K_{BD} from the expected mass of the brown dwarf. Steele et al. 2013 estimated that NLTT 5306B has a spectral type of L4-L7 based on two H_2O indices defined by Burgasser et al. 2002 measured from a near-infrared X-shooter spectrum of NLTT 5306B. Casewell et al. 2020a further refined the brown dwarf's spectral type to L5 based on a SpeX JHK spectrum. As NLTT 5306B is confidently a brown dwarf, as opposed to a star, we can set an upper limit on its mass at the hydrogen burning limit of $\sim$ 75 M_{Jup}, below which electron degeneracy pressure prevents the object's core from reaching the temperatures needed for nuclear fusion (Hayashi & Nakano, 1963; Kumar, 1963). An upper limit on the brown dwarf mass of 75 M_{Jup} would correspond to a lower limit on $K_{\mathrm{BD}} = K_{\mathrm{WD}} M_{\mathrm{WD}} / M_{\mathrm{BD}}$ of 288 ± 30 km/s.

From NLTT 5306B's expected mass and lack of even a partial eclipse, then, we can deduce K_{BD} should be in between about 288 and 378 km/s. This 90 km/s range is less than the velocity resolution of our NIRSPEC data (~150 km/s).

7.6 Results

We cross correlate the NIRSPEC data with each of the Sonora and irradiated models described in Section 7.3 and then compare their probability values. As the prior constraints on K_{BD} are stronger than we could make with our data, we compare the average of the log likelihood values between 288 and 378 km/s. We convert the log likelihoods calculated by Equation 7.3 to probabilities to compare them.

Figure 7.3 shows the results from the conditionally best-fitting Sonora and irradiated models. The left-most panel shows an example fit from the Sonora grid and from the irradiated grid to the full 44-epoch data set, each shown with jack-knife errorbars.

We also fit subsets of the data containing only day-side facing and only night-side facing epochs. Day-side epochs have ϕ values between 0.25 and 0.75, shown in orange in Figure 7.1, and night-side epochs have ϕ values between 0.75 and 0.25, shown in purple. In total, we had 23 day-side epochs and 18 night-side epochs. Three epochs crossed quadrature ($\phi = 0.25, 0.75$) during their 5-min exposures meaning they would have shown roughly 50% brown dwarf day-side and 50% night-side. We discarded these epochs from the day/night-side analysis.

The center and right-most panels of Figure 7.3 show example fits to only the day-side epochs and only the night-side epochs, respectively. When fitting the full data set, the best-fitting Sonora model results in a likelihood peak about 4× over the baseline, whereas when fitting only the day-side epochs, we see a peak around 3× over the baseline, and with only night-side epochs, a peak arises around 2× over the baseline. The irradiated models show roughly the same level fits to the full data set and day-side only subset, but shows significantly more noise than the Sonora model against the night-side only subset.

Corner plots showing the relative likelihood across the full model grids are shown in Figures 7.4 (Sonora grid) and 7.5 (irradiated grid). The left-most corner plots fit the full data set, and the center and right-most corner plots fit the day- and night-side only subsets, respectively.

Sonora Analysis

Comparisons of the full suite of Sonora 2021 models to our data sets—all epochs, day-side epochs, and night-side epochs—are shown in Figure 7.4. The marginalized, with 68% confidence intervals, and conditional best-fitting models are reported in Table 7.3 and graphed in Figure 7.3.

We first consider the effective temperatures favored by our data. The day-side epoch subset of our data prefers models with effective temperatures of 2000 K, or, when marginalized, 1900^{+200}_{-300} K. The night-side epoch subset, on the other hand, prefers the 1800 K model, or when marginalized, 1700^{+300}_{-400} K. There is substantial overlap in the marginalized effective temperature likelihoods between the day- and night-side epoch subsets, implying that there is minimal temperature difference. This is consistent with the conclusions Casewell et al. (2020a) drew from the day- and night-side brightness temperatures of NLTT 5306B in the *Spitzer* wavebands.

Figure 7.7 shows the relationship between our effective temperature measurements and the brightness temperatures from Casewell et al. (2020a). The brightness tem-

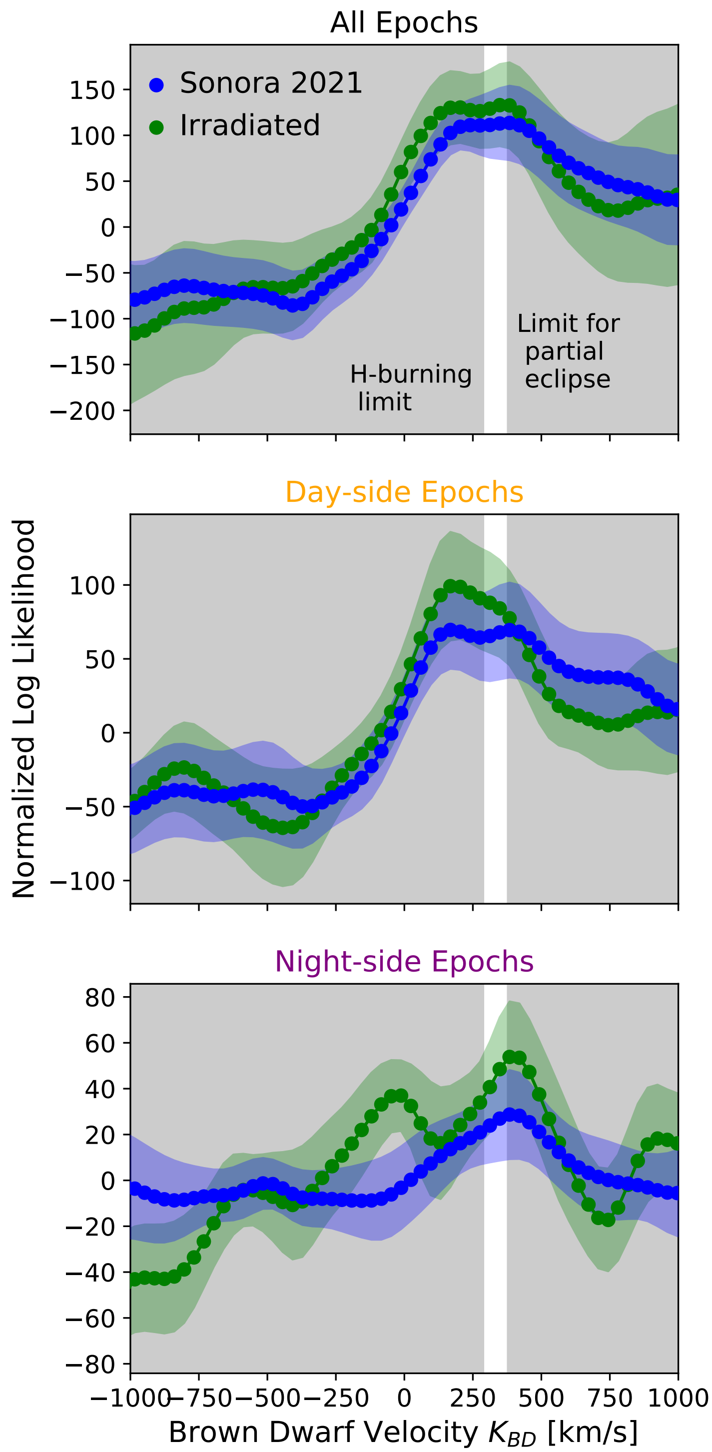

Figure 7.3: Normalized log likelihood functions generated from the cross correlation between the conditional best fitting model from each model grid to our data, shown with jack-knife error bars. The three panels represent fits to the full data set, to only the day-side epochs, and to only the night-side epochs. The blue curves come from Sonora 2021 models and the green curves are from irradiated models. The vertical white range shows the prior on K_{BD} given that the companion is a brown dwarf and does not show even a grazing transit.

peratures shown with squares were calculated under the assumption that the brown dwarf has a radius predicted by evolutionary models, while the temperatures shown with circules assumed a Roche lobe radius. If the brown dwarf is uniformly inflated, as suggested by Casewell et al. (2020a), its brightness temperatures should lie in between the two predictions. Our night-side effective temperature measurement is quite consistent with the brightness temperatures, while our day-side temperature is a bit hotter.

Our day-side epochs prefer somewhat lower gravity models than our night-side epochs. The day-side epochs prefer models with a $\log(g) = 4.5^{+1}_{-0.5}$, while the night-side models prefer $\log(g) = 5.5_{-1.0}$. The latter is a lower limit rather than a true measurement because $\log(g) = 5.5$ lies at the edge of the model grid. The two-dimensional likelihood surfaces show a more significant difference in gravities than in effective temperatures. Casewell et al. 2020a showed that an intermediate gravity ($\log(g) \sim 4.8$) template better fit a $R \sim 120$ JHK SpeX spectrum of NLTT 5306B than a field gravity ($\log(g) \sim 5.2$) template, although this spectrum was observed over roughly half an orbit of the system, which would make it impossible to detect phase variation in surface gravity.

Finally, whether we consider the day-side, night-side, or all 44 epochs, our data prefer the low metallicity, [Fe/H] = −0.5, models. This is consistent with what we would expect for an object with the > 5 Gyr system age of NLTT 5306 (Steele et al., 2013). We do see, though, especially in the corner plots of the full data set and day-side only subset, a degeneracy between high surface gravity and low metallicity models that likely arises from these parameters' common effect on spectral morphology (see Section 7.3).

Irradiated Model Analysis

Figure 7.5 shows how the irradiated model grid fits the full suite of data, as well as the day-side and night-side only subsets. To plot these results in an analogous fashion to the Sonora results, we convert the brown dwarf internal temperature and heat redistribution parameters to a brown dwarf effective temperature as described in Section 7.3.

As mentioned, there is a degeneracy between f and A_{BD}, such that the choice of A_{BD} makes little difference to our results here. Setting A_{BD} to 0 versus 1 does not affect the probability values in any way; it slightly alters the effective temperatures from the best-fitting internal temperatures depending on the magnitude of the best

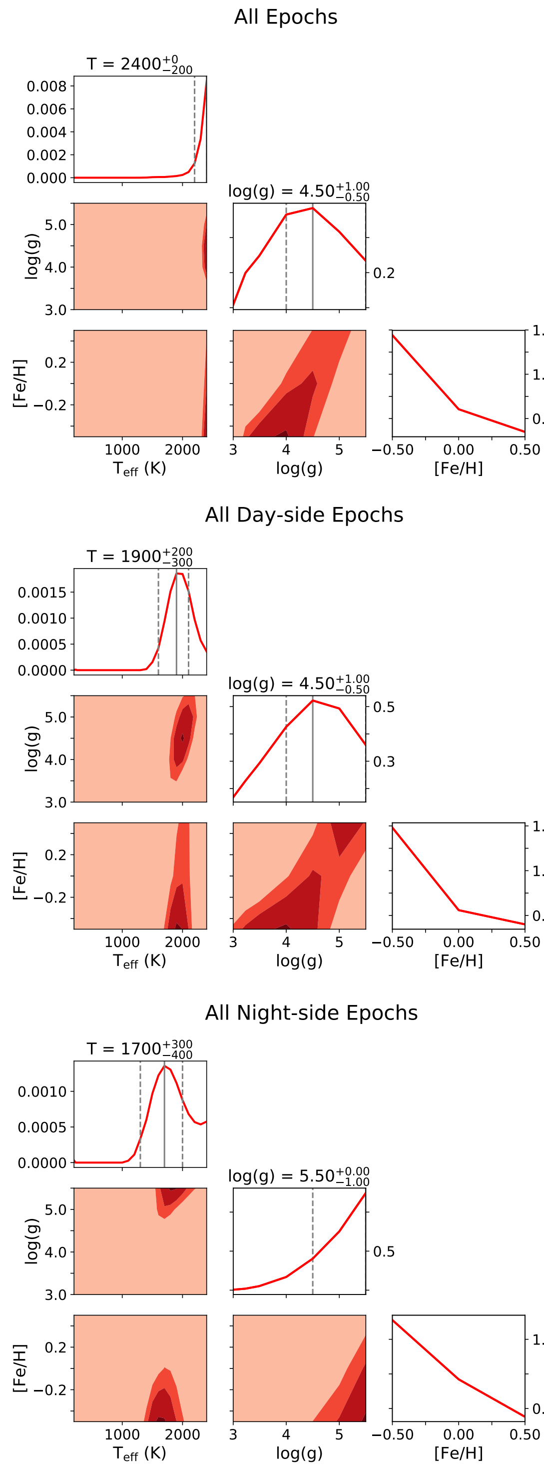

Figure 7.4: Results of Sonora model fits. The three corner plots show Sonora fits to all of the epochs, the NLTT5306B day-side epochs, and the NLTT5306B night-side epochs. The contour plots show higher likelihood with darker colors, and the line plots the marginalized results with 68% confidence intervals. Contours are at 50, 68, 95%. The log likelihood value used to compare each model is the average of the log likelihoods between K_{BD} of 288 and 378 km/s.

Table 7.3: Best-Fitting Models

Property	All epochs	Day-side	Night-side
Sonora 2021 Model Grid			
Marginalized			
$T_{\rm eff}$ (K)	2400^{+0}_{-200}	1900^{+200}_{-300}	1700^{+300}_{-400}
$\log(g)$	$4.5^{+1.0}_{-0.5}$	$4.5^{+1}_{-0.5}$	$5.5^{+0}_{-1.0}$
[Fe/H]	–	–	–
Conditional			
$T_{\rm eff}$ (K)	2400	2000	1800
$\log(g)$	4.0	4.0	5.5
[Fe/H]	-0.5	-0.5	-0.5
Irradiated Model Grid			
Conditional			
$T_{\rm int}$ (K)	2000	2000	2000
$\log(g)$	4.5	5.0	5.0
[Fe/H]	0.5	-0.5	-0.5
f	0.125	0.5	0.25

fitting heat redistribution parameters.

All subsets prefer an internal temperature of 2000 K, though disagree on the preferred heat redistribution parameter (Table 7.3), leading to slightly different effective temperatures. The full data set selects $T_{\rm eff}$ = 2011 K, while the day- and night-side subsets select 2042 and 2021 K, respectively.

Interestingly as well, the day- and night-side subsets agree on a low-metallicity ([Fe/H] = −0.5), higher gravity ($\log(g)$ = 5.0) model while the full data set selects the opposite: a high-metallicity ([Fe/H] = 0.5), lower gravity ($\log(g)$ = 4.5) model. It is surprising that with the day- and night-side subsets together making up 93% of the full data set that we see this disagreement. One explanation may be that the night-side detection is not as robust as the day-side or full data set detections or as the Sonora detections. As can be seen in Figure 7.3, the irradiated model night-side detection, while giving a higher likelihood within the desired velocity range, also shows significantly more noise structure than the Sonora night-side detection.

Comparison of Model Grids

Figure 7.6 compares the normalized probabilities from the Sonora and irradiated model grid fits. The solid curves represent the Sonora distributions and the dashed curves represent the irradiated distributions. The orange curves come from the day-side only subset of data while the purple curves come from the night-side only data.

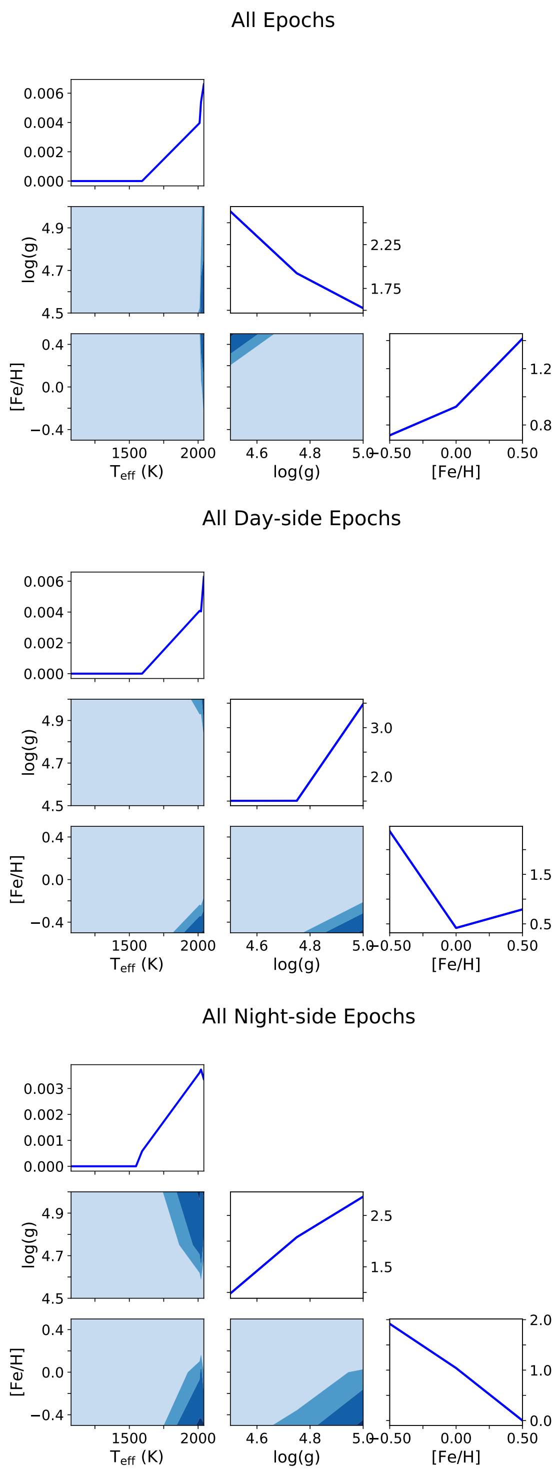

Figure 7.5: Same as Figure 7.4, but showing the results of the irradiated model fits. We convert the model internal temperature and heat redistribution parameters to brown dwarf effective temperatures using Equation 7.1 and assuming a Bond albedo of 0.

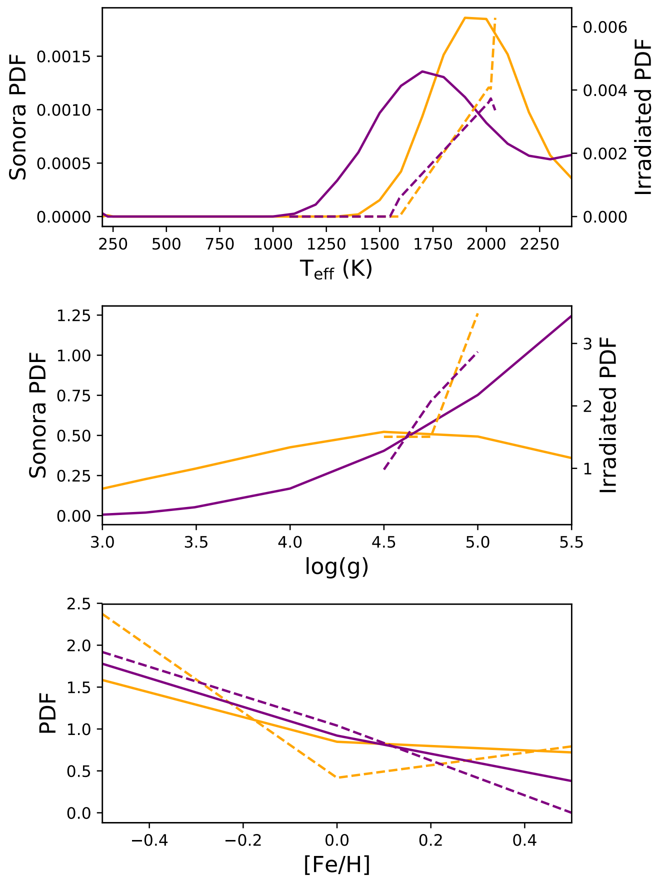

Figure 7.6: Comparison between the Sonora (solid curves) and irradiated (dashed curves) model fits to our data. The orange curves were fit to day-side epochs and the purple curves were fit to night-side epochs. Since the two model grids cover very different ranges of effective temperatures and surface gravities, we plot their normalized probability distribution functions on separate y-axes.

Because the Sonora and irradiated model grids offer different ranges of effective temperatures and surface gravities, we put their normalized posterior distribution functions on separate y-axes.

There is very good agreement in the metallicity results. The irradiated model grid tends toward higher effective temperatures and gravities than the Sonora grid, but the irradiated grid offers quite a small range of each parameter and we cannot resolve the shape of the probability distribution function as well as with the Sonora models. Future advancements in the modeling of irradiated objects like NLTT 5306B, including, for example, more detailed grids, could further our interpretation of the data.

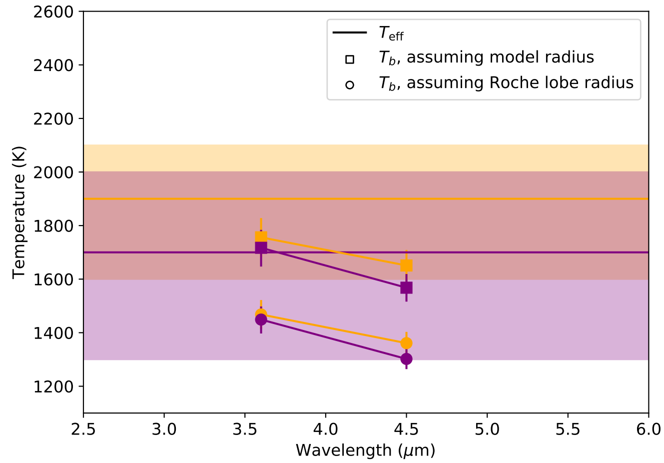

Figure 7.7: NLTT5306 B's wavelength-dependent brightness temperatures (points, from Casewell et al. 2020a) and effective temperatures (horizontal lines). Day-side measurements are in orange and night-side measurements are in purple. The brightness temperatures shown with squares were calculated assuming the evolutionary model radius, and the crosses assumed the Roche lobe radius.

7.7 Discussion

Effective Temperature and Gravity

Our Sonora 2021 analysis presented some interesting results. As illustrated in Figure 7.7, the day- and night-side effective temperatures are fairly consistent with each other, but the day-side temperature is a bit hotter. The night-side temperature was also very consistent with brightness temperature estimates from Casewell et al. 2020a. We also saw that the day-side favored lower gravity models than the night-side, though overall the night-side detection was not as strong as the day-side detection. This difference in detection strength is expected since, at these effective temperatures, our ∼1 μm data fall on the Planck side of the black body function where small drops in T_{eff} dramatically affect flux.

While our night-side effective temperature is very consistent with the brightness temperatures, if we consider the slightly raised day-side effective temperature to be significant, one explanation for it could be the presence of a hot spot. As compared to hot Jupiters, brown dwarfs orbiting white dwarfs are extremely rapid rotators, by means of their smaller orbital (and, thus, rotation) periods. This faster rotation can lead to smaller eastward-shifted hot spots, but more significant westward-shifted hot regions which arise from off-equatorial Rossby gyres (Tan & Showman, 2020). As Zhou et al. 2022 describe, while brightness temperatures measured from low resolution data are hemispherically averaged quantities, effective temperatures, which come through higher resolution spectral fitting, would be more sensitive to hot spots. As hot spots dominate spectral emission, even if they do not cover the majority of the visible surface area, they can bias effective temperature measurements to higher values than the band-averaged brightness temperatures. The day-side effective temperature being raised over both the night-side effective temperature and the brightness temperatures could be explained if the hot spot was only visible on the day-side of the brown dwarf. The day-side of the brown dwarf is the side facing the white dwarf. Perhaps then, a day-side hot spot could be related to the apparent accretion onto the white dwarf (Longstaff et al., 2019).

Our lower day-side gravity measurement may fit in to this picture. If the white dwarf were pulling some matter from the brown dwarf surface facing it (which we witness during the brown dwarf's day-side), we may expect to see a hotter and lower gravity region.

This would imply, however, that the brown dwarf surface is distorted. Casewell et al. 2020a have shown that distortion by its interaction with the white dwarf is unlikely. Using the mass ratio, separation, and assumed radius of the brown dwarf (0.095 $R_\odot$), they calculated that the tidal distortion due to the white dwarf and the tidally locked rotation, is only 2.5%. They predicted that the majority of this distortion was due to the rotation rate. While distortion could account for 2.5% difference between the equatorial and polar radii, the difference between NLTT 5306B's model radius and the radius of an intermediate gravity brown dwarf of the same mass is 22%. While with its model radius of 0.095 $R_\odot$, NLTT 5306B is filling $\approx$ 80% of its Roche lobe (Longstaff et al., 2019), if it were inflated by 22% to a radius of 0.11 $R_\odot$, NLTT 5306B would fill nearly its full ($\approx$ 96%) Roche lobe. From these calculations, Casewell et al. 2020a predicted that the lower gravity signatures they saw in SpeX low-resolution data were not likely due to distortion and more likely represented a brown dwarf which was uniformly inflated.

Our results do show day- and night-side differences in preferred surface gravity. If distortion is an unlikely cause of these differences, it may be interesting to look back on how our measurements were made. We compare the different models based on the average of their likelihoods fit to the data between a K_{BD} of 288 and 378 km/s. As described above, this velocity range prior was found on one end from the mass cut-off between stars and brown dwarfs and on the other end from the lack of a partial eclipse. For this system, the white dwarf has a line-of-sight velocity of -46.8 km/s (Longstaff et al., 2019). Material streaming from the brown dwarf to the white dwarf should start with the brown dwarf's velocity and gradually transition to the white dwarf's velocity. While the velocity range we considered is less than the velocity resolution of our NIRSPEC data, the 90 km/s range could still include the brown dwarf velocity component at a higher end of the velocity range and some of the material en route to the white dwarf towards the lower end of the range.

The non-hydrostatic material streaming between the objects could bias our measurement of the "bulk" day-side surface gravity to lower gravities. During the brown dwarf's night-side, however, the brown dwarf's cross section would likely cover the majority of the material streaming between the two and not show this same bias. That our night-side surface gravity is more consistent with the evolutionary radius matches these predictions.

While above we postulated how a hot spot could increase the day-side effective temperature, the day- and night-side effective temperatures share significant overlap. Their 68% confidence intervals do overlap between 1600 and 2000 K. In this case, a hot spot may not be needed to explain our results. This range of overlapping temperatures is closer to the brightness temperatures calculated assuming the evolutionary model radius, or higher gravity brown dwarf. Further, the overlapping temperature range is only marginally hotter than the 1581 K Filippazzo et al. (2015) would predict for an L5 field age dwarf from their sixth-order polynomial fit to 124 field age objects.

From this perspective, we might envision a non-distorted non-inflated brown dwarf with an evolutionary radius. Its day- and night-side effective temperatures are consistent, as was also seen with its brightness temperature. The brown dwarf night-side, while not overall strongly detected, prefers higher gravity values, and the effective temperatures are somewhat more consistent with the brightness temperatures derived assuming an evolutionary radius (see Figure 7.7). In this picture, the lower gravity component we seen in the day-side may rise completely from material streaming off of the brown dwarf, and so may be considered distinct from the brown dwarf itself.

However, Casewell et al. 2020a did show evidence that NLTT 5306B has an intermediate gravity surface rather than the evolutionarily expected high gravity in a low-resolution SpeX JHK spectrum. Further, WD1032B, a brown dwarf that eclipses a similarly cool white dwarf to NLTT 5306A and receives ~1.5 times the irradiation of NLTT 5306B, is inflated (Casewell et al., 2020b), as determined by its radius measurement. Could the intermediate gravity features seen in the SpeX spectrum of NLTT 5306B be consistent with a noninflated brown dwarf and lower gravity stream of material rather than a uniformly inflated object? Two pieces of information may be relevant. First, the SpeX data were taken over roughly half of NLTT 5306B's orbit, which would make it impossible to detect phase variation in surface gravity. Second, SpeX data have a resolution of $R \sim 120$, corresponding to a velocity resolution of approximately 2500 km/s. This resolution would convolve all of the velocity components of the system, from the white dwarf to the brown dwarf, together. While the white dwarf has a very different spectral shape than the brown dwarf, and could be distinguished in this way, the material streaming between the two may more closely resemble the brown dwarf spectroscopically. If so, and if the streaming material were indeed lower gravity than the brown dwarf, the intermediate gravity features Casewell et al. 2020a presented could be from a linear combination of the higher gravity brown dwarf and lower gravity material.

A final possibility could come from our observational set up. As described in Section 7.2, our 5-minute observations allow some change in the brown dwarf velocity. We can predict the expected changes in velocities across the day-side versus night-side epochs. Assuming the maximum K_{BD} = 378 km/s, the velocity change over day-side epochs varies from 6 to 164 km/s, with a mean of 87 km/s, while the night-side variation ranges from 9 to 126 km/s, with a mean of 78 km/s. With a higher mean, the day-side epochs show slightly more change in velocity. This could act to broaden out spectral features in these epochs. Allers & Liu 2013 described how low-gravity brown dwarfs show weaker FeH bands, Na I lines, and K I lines than do field gravity brown dwarfs. The velocity effects built in to our data set could work to broaden out these spectral features in our day-side data more so than in our night-side data, making them appear weaker, and thus leading to a preference for lower gravity models.

Metallicity and Magnetism

Our metallicity constraints provide a final compelling clue. We find that our data, whether considering all 44, only day-side, or only night-side epochs, prefer the [Fe/H] = −0.5 Sonora models. The day- and night-side subsets of data also prefer low-metallicity irradiated models. This is consistent with what we would expect from a thick-disk object, of a considerable age (> 5 Gyr, Steele et al. 2013). Yet, in pondering potential mechanisms for the brown dwarf's inflation, Casewell et al. 2020a cited a high-metallicity, cloudy atmosphere. Burrows et al. 2011 showed that the difference in radii between a clear, [Fe/H] = −0.5 brown dwarf and a cloudy, [Fe/H] = 0.5 one could be $\sim 0.25 R_{\rm Jup}$ at early ages and $\sim 0.1 R_{\rm Jup}$ at late ages. By these estimates, to achieve the $\sim 0.2 R_{\rm Jup}$ inflation Casewell et al. 2020a estimated from the SpeX data of NLTT 5306 B, the brown dwarf would need a metallicity near the upper end of the range ([Fe/H] = 0.5) as well as a cloudy atmosphere. Our Sonora results show that this is unlikely. Two conclusions can be drawn from this finding. As metallicity is not likely responsible for the inflation of NLTT 5306 B, either the brown dwarf is not inflated or if it is, its inflation must be a result of some other process.

We provide direct evidence that the suspected inflation of NLTT 5306 B is not due to a high-metallicity, cloudy atmosphere. This finding amplifies the evidence that magnetic evidence is at play, as was discussed in depth in Casewell et al. 2020a. High-resolution spectropolarimetric measurements could confirm this theory. We can set a prior on the strength of NLTT 5306 A's magnetic field from earlier findings. Longstaff et al. 2019 saw no evidence of an infrared excess characteristic of an accretion disk accompanying the Hα emission feature on NLTT 5306 A's surface that led to the conclusion it was accreting mass from its brown dwarf. White dwarfs called "polars" have strong enough magnetic fields that they can funnel mass along field lines, preventing the formation of an accretion disk. With the estimated accretion rate, Longstaff et al. 2019 calculated NLTT 5306 A's magnetic field must be at least 0.45 ± 0.02 kG to prevent an accretion disk forming. On the other end, there were no signs of either Zeeman splitting in NLTT 5306 A's Balmer lines or cyclotron humps in its XSHOOTER *JHK* spectrum (Longstaff et al., 2019). Typical white dwarf spectra are significantly pressure broadened, to a full width at half maximum (FWHM) of more than 1 Å, enough to blur out Zeeman splitting from fields up to $\sim 30 - 50$ kG (Landstreet et al., 2017). Even stronger fields would be needed for cyclotron emission to arise in the *J* band; the cyclotron fundamental is detectable at optical to near-IR wavelengths for fields of strength $\sim 10^5$ kG (Ferrario et al., 2020). It follows that NLTT 5306 A's magnetic field must lie in the range from 0.45 to $\sim 30 - 50$ kG.

For magnetic activity to explain the inflation of NLTT 5306B, NLTT 5306 A should show a stronger field than the white dwarfs hosting non-inflated brown dwarfs. Recall that NLTT 5306 A ($T_{\rm eff}$ = 7756 K) and WD1032+011A ($T_{\rm eff}$ = 9950 K), the two white dwarfs hosting inflated brown dwarfs, are cooler than SDSS J1205-0242 ($T_{\rm eff}$ = 23680 K) and SDSS J1411+2009 ($T_{\rm eff}$ = 13000 K), the two hosting non-inflated brown dwarfs. In fact, observations suggest that a higher fraction of white dwarfs with lower effective temperatures have strong magnetic fields. Hollands et al. 2015 found a $13 \pm 4\%$ incidence of magnetic activity in a sample of DZ white dwarfs with $T_{\rm eff} < 9000$ K, much higher than the incidence among young, hot DA white dwarfs. This could be because, at these low temperatures, white dwarfs are cool enough to be (at least partially) crystallized, which has been proposed as one method of generating magnetic fields (e.g. Isern et al., 2017).

While NLTT 5306 is a very faint source ($g' = 17.03$, Steele et al. 2013), Bagnulo & Landstreet 2018 recently published a survey of the weakest detectable magnetic fields in white dwarfs and concluded that both the European Southern Observatory's Very Large Telescope's low-resolution spectropolarimeter, FORS2, and the *William Herschel* Telescope's mid-resolution spectropolarimeter, ISIS, could search for mean longitudinal fields $\langle B_Z \rangle \sim 1$ kG in $V_{\rm mag} \lesssim 14$ DA stars. The extension to NLTT 5306 A could not only answer questions about the unique forces acting on NLTT 5306 B, covering nearly the full magnetic field strength prior, but would also expand the population of white dwarfs we can target to fill in gaps about how white dwarf magnetism scales with mass, age, and rotation, an issue described by Bagnulo & Landstreet 2018.

Heating of NLTT 5306B's deep atmosphere by vertical advection of potential temperature, as was described in Sainsbury-Martinez et al. 2021, can also not be ruled out as a mechanism responsible for radius inflation. Next-generation, fully radiative 3D global circulation models (GCMs) could test this theory.

7.8 Conclusion

Ultimately, while we have some understanding of NLTT 5306B, there is still much to learn. The results from our Sonora study could be consistent with either a hot and distorted spot on the brown dwarf day-side or with a evolutionary radius brown dwarf with no significant day- to night-side temperature difference, but some traces of the lower gravity detached material streaming to the white dwarf. Still, we do not know precisely *why* this system is interacting.

We do know that gravitational distortion is insufficient to explain the perceived inflation of NLTT 5306B. And, we know that if there is inflation, it is certainly not to the Roche lobe level, from the upper limit set on the mass accretion rate in the system (Longstaff et al., 2019). A high-metallicity, cloudy atmosphere is not likely responsible for this suspected inflation. Additionally, the atmosphere is not so hot as to be boiled off. Other, hotter brown dwarfs in equivalent systems show no signs of interaction, such as SDSS J141126.20+200911.1 and SDSS J120515.80024222.6 (Casewell et al., 2020b). Magnetic activity from the white dwarf could be inflating the brown dwarf, as is seen in M dwarfs, and would be a ripe source for future investigations.

References

Acton, J. S., Goad, M. R., Burleigh, M. R., et al. 2021, *MNRAS*, 505, 2741, doi: 10.1093/mnras/stab1459

Allers, K. N., & Liu, M. C. 2013, *ApJ*, 772, 79, doi: 10.1088/0004-637X/772/2/79

Bagnulo, S., & Landstreet, J. D. 2018, *A&A*, 618, A113, doi: 10.1051/0004-6361/201833235

Boogert, A. C. A., Blake, G. A., & Tielens, A. G. G. M. 2002, *ApJ*, 577, 271, doi: 10.1086/342176

Burgasser, A. J., Kirkpatrick, J. D., Brown, M. E., et al. 2002, *ApJ*, 564, 421, doi: 10.1086/324033

Burleigh, M. R., Marsh, T. R., Gänsicke, B. T., et al. 2006, *MNRAS*, 373, 1416, doi: 10.1111/j.1365-2966.2006.11030.x

Burrows, A., Heng, K., & Nampaisarn, T. 2011, *ApJ*, 736, 47, doi: 10.1088/0004-637X/736/1/47

Burrows, A., Hubbard, W. B., Lunine, J. I., & Liebert, J. 2001, Reviews of Modern Physics, 73, 719, doi: 10.1103/RevModPhys.73.719

Carmichael, T. W., Quinn, S. N., Mustill, A. J., et al. 2020, *AJ*, 160, 53, doi: 10.3847/1538-3881/ab9b84

Casewell, S. L., Debes, J., Braker, I. P., et al. 2020a, *MNRAS*, 499, 5318, doi: 10.1093/mnras/staa3184

Casewell, S. L., Belardi, C., Parsons, S. G., et al. 2020b, *MNRAS*, 497, 3571, doi: 10.1093/mnras/staa1608

Cruz, K. L., Kirkpatrick, J. D., & Burgasser, A. J. 2009, *AJ*, 137, 3345, doi: 10.1088/0004-6256/137/2/3345

Demory, B.-O., & Seager, S. 2011, *ApJS*, 197, 12, doi: 10.1088/0067-0049/197/1/12

Ferrario, L., Wickramasinghe, D., & Kawka, A. 2020, Advances in Space Research, 66, 1025, doi: 10.1016/j.asr.2019.11.012

Filippazzo, J. C., Rice, E. L., Faherty, J., et al. 2015, *ApJ*, 810, 158, doi: 10.1088/0004-637X/810/2/158

Grether, D., & Lineweaver, C. H. 2006, *ApJ*, 640, 1051, doi: 10.1086/500161

Grieves, N., Ge, J., Thomas, N., et al. 2017, *MNRAS*, 467, 4264, doi: 10.1093/mnras/stx334

Hayashi, C., & Nakano, T. 1963, Progress of Theoretical Physics, 30, 460, doi: 10.1143/PTP.30.460

Hernández Santisteban, J. V., Knigge, C., Littlefair, S. P., et al. 2016, *Nature*, 533, 366, doi: 10.1038/nature17952

Hollands, M. A., Gänsicke, B. T., & Koester, D. 2015, *MNRAS*, 450, 681, doi: 10.1093/mnras/stv570

Isern, J., García-Berro, E., Külebi, B., & Lorén-Aguilar, P. 2017, *ApJL*, 836, L28, doi: 10.3847/2041-8213/aa5eae

Izzard, R. G., Hall, P. D., Tauris, T. M., & Tout, C. A. 2012, IAU Symposium, 283, 95, doi: 10.1017/S1743921312010769

Jones, A., Noll, S., Kausch, W., Szyszka, C., & Kimeswenger, S. 2013, *A&A*, 560, A91, doi: 10.1051/0004-6361/201322433

Kausch, W., Noll, S., Smette, A., et al. 2015, *A&A*, 576, A78, doi: 10.1051/0004-6361/201423909

Koester, D. 2010, , 81, 921

Kumar, S. S. 1963, *ApJ*, 137, 1121, doi: 10.1086/147589

Landstreet, J. D., Bagnulo, S., Valyavin, G., & Valeev, A. F. 2017, *A&A*, 607, A92, doi: 10.1051/0004-6361/201731432

Littlefair, S. P., Casewell, S. L., Parsons, S. G., et al. 2014, *MNRAS*, 445, 2106, doi: 10.1093/mnras/stu1895

Longstaff, E. S., Casewell, S. L., Wynn, G. A., et al. 2019, *MNRAS*, 484, 2566, doi: 10.1093/mnras/stz127

Lothringer, J. D., & Casewell, S. L. 2020, *ApJ*, 905, 163, doi: 10.3847/1538-4357/abc5bc

Marley, M., Saumon, D., Morley, C., & Fortney, J. 2018, Sonora 2018: Cloud-free, solar composition, solar C/O substellar atmosphere models and spectra, nc_m+0.0_co1.0_v1.0, Zenodo, doi: 10.5281/zenodo.1309035. https://doi.org/10.5281/zenodo.1309035

Marley, M. S., Saumon, D., Visscher, C., et al. 2021, *ApJ*, 920, 85, doi: 10.3847/1538-4357/ac141d

Martin, E. C., Fitzgerald, M. P., McLean, I. S., et al. 2018, in Society of Photo-Optical Instrumentation Engineers (SPIE) Conference Series, Vol. 10702, Ground-based and Airborne Instrumentation for Astronomy VII, ed. C. J. Evans, L. Simard, & H. Takami, 107020A

McLean, I. S., Becklin, E. E., Bendiksen, O., et al. 1998, in Society of Photo-Optical Instrumentation Engineers (SPIE) Conference Series, Vol. 3354, Infrared Astronomical Instrumentation, ed. A. M. Fowler, 566–578

Noll, S., Kausch, W., Barden, M., et al. 2012, *A&A*, 543, A92, doi: 10.1051/0004-6361/201219040

Parsons, S. G., Hermes, J. J., Marsh, T. R., et al. 2017, *MNRAS*, 471, 976, doi: 10.1093/mnras/stx1610

Parsons, S. G., Gänsicke, B. T., Marsh, T. R., et al. 2018, *MNRAS*, 481, 1083, doi: 10.1093/mnras/sty2345

Sainsbury-Martinez, F., Casewell, S. L., Lothringer, J. D., Phillips, M. W., & Tremblin, P. 2021, *A&A*, 656, A128, doi: 10.1051/0004-6361/202141637

Sainsbury-Martinez, F., Wang, P., Fromang, S., et al. 2019, *A&A*, 632, A114, doi: 10.1051/0004-6361/201936445

Smette, A., Sana, H., Noll, S., et al. 2015, *A&A*, 576, A77, doi: 10.1051/0004-6361/201423932

Spake, J. J., Sing, D. K., Evans, T. M., et al. 2018, *Nature*, 557, 68, doi: 10.1038/s41586-018-0067-5

Steele, P. R., Burleigh, M. R., Dobbie, P. D., et al. 2011, *MNRAS*, 416, 2768, doi: 10.1111/j.1365-2966.2011.19225.x

Steele, P. R., Saglia, R. P., Burleigh, M. R., et al. 2013, *MNRAS*, 429, 3492, doi: 10.1093/mnras/sts620

Stelzer, B., de Martino, D., Casewell, S. L., Wynn, G. A., & Roy, M. 2017, *A&A*, 598, L6, doi: 10.1051/0004-6361/201630038

Tan, X., & Showman, A. P. 2020, *ApJ*, 902, 27, doi: 10.3847/1538-4357/abb3d4

Tremblin, P., Chabrier, G., Mayne, N. J., et al. 2017, *ApJ*, 841, 30, doi: 10.3847/1538-4357/aa6e57

van Roestel, J., Kupfer, T., Bell, K. J., et al. 2021, *ApJL*, 919, L26, doi: 10.3847/2041-8213/ac22b7

Zhou, Y., Apai, D., Tan, X., et al. 2022, *AJ*, 163, 17, doi: 10.3847/1538-3881/ac3095

Zucker, S. 2003, *MNRAS*, 342, 1291, doi: 10.1046/j.1365-8711.2003.06633.x

Chapter 8

SUMMARY AND FUTURE WORK

8.1 Summary

Chapters 2 through 6 were dedicated to a multi-epoch approach to directly detect the thermal emission of hot Jupiters at high spectral resolution. In Chapter 3, adapted from Buzard et al. 2020, we introduced a simulation framework that enabled us to identify non-random noise in our detection space and more clearly detect signal from the hot Jupiter, HD187123b. We used this simulation framework to predict optimal observing strategies, and found that many, lower S/N epochs spread across a planet's orbit would allow for a stronger detection than fewer, higher S/N epochs. In Chapter 4, we saw that, in the absence of many epochs, epochs during which the primary velocity is minimal, or when the telluric and host stellar lines are in a common reference frame, would be desirable, and would reduce the observing time needed for robust detections (Buzard et al., 2021a). Chapter 5 looked back on the multi-epoch detections of HD88133b and ups And b and found that the structure interpreted as planetary detections was more likely caused by structured noise (Buzard et al., 2021b). These results relied on data from NIRSPEC prior to its upgrade in 2019; we predict that if the same number of epochs had been taken on ups And b with the upgraded NIRSPEC and with primary velocities near 0 km/s, a strong detection (10.8σ) could have been made. HD88133b, on the other hand, would have required many more than the 6 obtained epochs to be detected, likely because of its host star's large radius and low temperature. This dissertation has demonstrated the ubiquity of noise structure that can obscure multi-epoch planetary detections, but has also presented an effective way of identifying one source of structured noise (correlation between the stellar spectrum and the planetary spectral template). In Chapter 6, we describe where other sources of non-random noise can arise along the multi-epoch pathway and what might be done to identify, and even reduce, all of these sources of noise. While challenging, the work of identifying and eliminating all sources of structured, non-random noise that prevent us from seeing down to the white noise limit of our data will be a necessary step in taking full advantage of the gains available by the next generation of high contrast imaging systems.

In Chapter 7, we take a turn from exoplanet systems to study a different type of substellar companion: a brown dwarf in a post-common envelope binary system with a white dwarf host. NLTT5306B has shown evidence of inflation and interaction with its host, but the cause of either is unknown. Using low-resolution ($R \lesssim 2000$) NIRSPEC data to directly detect the emission from the brown dwarf, we consider day- to night-side differences in effective temperature, surface gravity, and metallicity. We find a universally low-metallicity atmosphere, suggesting that the radius inflation is not due to a cloudy, high-metallicity atmosphere, a possibility described by Burrows et al. 2011. While we did not find the definitive cause for NLTT5306B's inflation, we were able to narrow the list. Future investigations into host white dwarf magnetic activity and vertical heating of the brown dwarf's interior as explanations for inflation, as described in Section 8.3, will be illuminating in our understanding the dynamics and physical states of this unique population of irradiated and high mass substellar objects.

8.2 Multi-Epoch Exoplanet Detections Beyond NIRSPEC

In Chapter 6, we detailed areas for improvements to the Keck/NIRSPEC application of multi-epoch direct exoplanet detection. The future of the multi-epoch approach will likely extend beyond NIRSPEC, though. We are coming into a time of great advancements in high-resolution near-infrared spectrometers which hold the potential to significantly improve multi-epoch exoplanet detections.

Table 8.1, adapted from the 2019 Keck White Paper for IGNIS[1], compares the specifications of several present and upcoming high-resolution near-infrared spectrographs. NIRSPEC, whether before or after its 2019 upgrade, shows among the smallest simultaneous coverage and lowest resolution. NIRSPEC was optimized for the shortest wavelengths ($\sim 0.95 - 2.5\mu$m), meaning that L and M band observations—those most important for exoplanet thermal emission studies—only offer $\lesssim 1/3$ of the band per echelle/cross disperser setting. It has long been suspected that both increased wavelength coverage and increased resolution would strengthen cross-correlation signals. As Birkby 2018 describes, cross-correlation signals increase by the square root of the number of lines detected ($\sqrt{N_{lines}}$). An instrument that allows an increased wavelength grasp in a single observation will give access to a larger number of planetary spectral lines, thereby strengthening the detection. Increased resolution, too, increases the depth of spectral lines and the dissimilarity between the planetary spectrum and stellar spectrum, both of which could be ex-

[1]Mace et al. 2019, Keck White Paper

Table 8.1: Specifications of High-Resolution Near-Infrared Spectrographs

Telescope/ Instrument	Simultaneous coverage	Spectral coverage (μm)	Resolution	AO capabilities	Year available
Keck/NIRSPEC1.0	1 band	0.95-5.5	$\sim 25,000$	Yes	1999 - 2018
Keck/NIRSPEC2.0	1 band	0.95-5.5	$\sim 37,500$	Yes	2019 -
IRTF/iSHELL	< 0.5 band	1.07-5.3	$\sim 80,000$	No	2016 -
Gemini/IGRINS	2 bands	1.45-2.5	$\sim 45,000$	No	2018 -
CFHT/SPIRou	4 bands	0.95-2.35	$\sim 75,000$	No	2018 -
VLT/CRIRES+	< 0.5 band	0.95-5.3	$\geq 100,000$	Yes	2021 -
ELT/METIS	2 bands	3-5	$\sim 100,000$	Yes	2027 -
GMT/GMTNIRS	5 bands	1.07-5.3	65-85,000	Yes	2029 -
Keck/IGNIS	5 bands	1.07-5.4	$\sim 45,000$	TBD	TBD

pected to increase the likelihood of planetary detection. Finnerty et al. 2021 showed that, across the L band, both increased wavelength grasp and increased spectral resolution strengthened planetary detection likelihoods by factors of $\sim 1.6 - 1.7$. Instruments like GMTNIRS, which offer both a wide wavelength grasp and high resolution, could open a new door to investigations of the chemical and physical properties of exoplanet atmospheres.

In addition to the advancements made possible by the increased wavelength coverage and spectral resolution of the coming near-infrared spectrometers, these instruments' connection with high-contrast imaging (HCI) facilities will bring a new realm of planets into view. High-resolution, cross-correlation exoplanet studies from the last decade (e.g., Snellen et al., 2010; Brogi et al., 2012; Lockwood et al., 2014; Piskorz et al., 2018; Buzard et al., 2020) have proven able to reach down to planets at planet-to-star contrasts of $\sim 10^{-4}$. While the multi-epoch cross-correlation technique should be furthered in the ways described in this dissertation to reliably reach these low contrast levels, it will be uniquely capable of directly detecting the majority of even lower contrast planets which fall beyond ~ 0.15 AU from their hosts. High-contrast imaging systems will support these detections by increasing planet-to-star contrasts using adaptive optics technology and coronagraphy to suppress light from the planet's star (e.g., Hinkley et al., 2021). Together, with HCI systems bringing planetary signals up by a few orders of magnitude and with analytic techniques like the multi-epoch cross-correlation approach reaching down a few orders of magnitude, a much wider range of exoplanet atmospheres, including, for example, Earth-like exoplanets with contrasts of $\sim 10^{-10}$, will slowly come into focus (illustrated in Figure 8.1). With increased insight into the known planet population, we will be able to ask and answer questions about how planets and planetary systems form, how they evolve in different environments, and, fully, what is possible, astronomically speaking.

8.3 Future Work on NLTT5306 and Other Detached PCEBs

NLTT5306 is one of only eleven detached (i.e., not showing Roche lobe overflow) post-common envelope binaries (PCEB) with a substellar secondary (van Roestel et al., 2021). There are many open questions surrounding these systems. As discussed in Chapter 7, NLTT5306B has shown evidence of radius inflation and mass loss to its host. The cause of both processes is unknown. While UV irradiation has explained the inflation of hot Jupiters (e.g., Demory & Seager, 2011), NLTT5306B and the other known inflated PCEB brown dwarf, WD1032+011 (Casewell et al.,

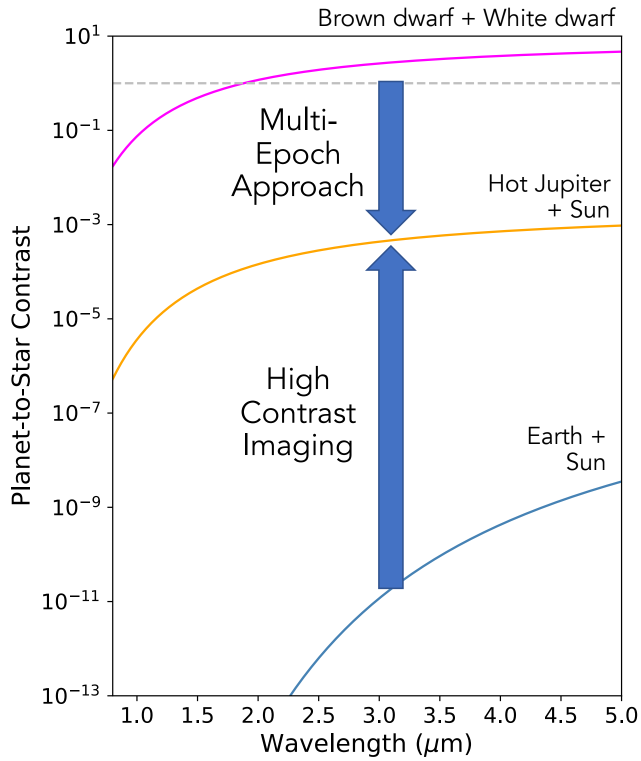

Figure 8.1: Approximate planet-to-star (or secondary-to-primary) contrast of a brown dwarf/white dwarf system like NLTT 5306 (in pink), a hot Jupiter/Sun-like star system like HD 187123 (in orange), and an Earth/Sun system (in blue). As near-infrared exoplanet spectroscopy research marches on, each blue arrow is subject to change. More efficient observing strategies and longer wavelength coverage observations will stretch the multi-epoch approach arrow down to even lower contrasts and larger telescopes with advanced optics systems will further extend the high-contrast imaging arrow. As these two arrows meet in the middle, a significant portion of the known exoplanet population will come into view.

2020b), receive less UV irradiation than two PCEB brown dwarfs known not to be inflated. Our NIRSPEC analysis also ruled out a cloudy, high-metallicity atmosphere as a potential cause of inflation. Further studies could test the two remaining proposed causes of radius inflation: magnetic activity and heating of the deep atmosphere.

Casewell et al. 2020a described magnetic activity from NLTT5306A as a potential cause for the inflation of NLTT5306B. CoRoT-15b and CoRoT-33b, the only two brown dwarfs to be orbiting magnetically active main-sequence hosts (Carmichael et al., 2020), are also inflated. NLTT5306A, itself, has shown evidence of a higher-than-average magnetic field in that there is no accretion disk accompanying the mass donation from NLTT5306B (Longstaff et al., 2019); a white dwarf with a strong enough magnetic field can funnel mass directly along field lines rather than through a disk (such an object is called a "polar"). Magnetic activity has been known to inflate M dwarfs by inhibiting convection (e.g., Parsons et al., 2018), and it is possible that the same mechanism is at play for NLTT5306B. NLTT5306A must have a magnetic field of at least 0.45 ± 0.02 kG to prevent the formation of an accretion disk (Longstaff et al., 2019), but less than ~ 50 kG to justify the lack of Zeeman splitting in its Balmer lines (Bagnulo & Landstreet, 2018; Longstaff et al., 2019). Bagnulo & Landstreet 2018 presented a spectropolarimetric study of faint DA white dwarfs using both the FOcal Reducer Spectrograph (FORS2) at the VLT ($V_{mag} = 11.4 - 13.1$) and the Intermediate dispersion Spectrograph and Imaging System (ISIS) on WHT ($V_{mag} = 12.5 - 14$) and were able to measure the mean longitudinal field $\langle B_Z \rangle$ to a precision of $220 - 310$ G (FORS2) and $180 - 710$ G (ISIS), revealing fields down to $\langle B_Z \rangle \approx 1 - 2$ kG. Such a measurement would cover nearly the full $0.45 - 50$ kG prior on NLTT5306A's magnetic field strength. While the NLTT5306A and the other PCEB white dwarfs are fainter ($V_{mag} \sim 15 - 19$) even than the WDs Bagnulo & Landstreet 2018 targeted, a similar spectropolarimetric survey could test correlations between higher white dwarf magnetic field strengths and inflated brown dwarfs, thereby testing whether magnetic activity is responsible for inflating these brown dwarfs.

Sainsbury-Martinez et al. 2021 recently considered whether deep atmosphere heating through vertical advection of potential temperature could inflate brown dwarfs as it can hot Jupiters. They found that Kepler-13Ab and KELT-1b, inflated brown dwarfs orbiting main sequence stars on $\sim 1.2 - 1.8$ day orbits (Esteves et al., 2015; Siverd et al., 2012), show signs of significant deep heating, while SDSS1411B, a non-inflated brown dwarf orbiting a white dwarf on a $\sim$ 2-hour orbit (Littlefair et al., 2014) does not. SDSS1411B's increased rotational velocity, relative to the other two objects, gives it a different zonal wind and meridional circulation pattern which could explain why, in this case, vertical advective heating is inefficient. NLTT5306B and WD1032B, the two inflated PCEB brown dwarfs, both orbit slightly cooler white dwarfs than SDSS1411B (7,756 and 9,950 K vs. 13,000 K) but have comparable rotation periods ($\sim$ 1.7 and 2.2 hours vs. 2 hours) so as of yet it is unclear whether vertical advective heating could be effective. Next generation, fully radiative 3D global circulation models (GCMs) could test whether interior heating through vertical advection of potential temperature is significant in these brown dwarfs and could explain their observed radius inflation.

A recent burst of research has investigated absorption from metastable He at ∼10833 Å. This triplet of lines was suggested as a potential tracer of upper atmospheres by Seager & Sasselov 2000 and observationally detected in an exoplanet atmosphere for the first time by Spake et al. 2018 using data from the Wide Field Camera 3 (WFC3) on the Hubble Space Telescope (HST). Metastable He I absorption is thought to be caused by the photoevaporation of the planetary atmospheres. While there are brown dwarfs that have shown signs of inflation and interaction, the He I feature has not, to date, been detected in these higher mass and gravity objects. An observational campaign to search for ∼10833 Å He I absorption in NLTT5306B could both provide us with the first detection of an eroding atmosphere on a brown dwarf and allow us to measure the mass loss rate, thereby strengthening our understanding of the system dynamics. While ground-based instruments like Keck/NIRSPEC ($R \sim 25,000$, Kirk et al. 2020) and CARMENES ($R \sim 80,000$, Allart et al. 2019) have been used to detect exoplanet metastable He I, NLTT5306's faintness presents a challenge to these instruments. To detect signal with Keck/NIRSPEC, we were forced to use the low-resolution mode ($R \lesssim 2000$) in which telluric OH emission features were broadened to cover the ∼10833 Å region. We also attempted to observe NLTT5306B using the ultra-narrowband He filter on the Hale 200″ telescope at Palomar (Vissapragada et al., 2020), but found that the brown dwarf's high velocity (∼ 330 km/s) prevents it from spending enough time in the filter to build up sufficient S/N for a detection. Therefore, a space-base instrument like HST/WFC3 or JWST/NIRSPEC would be ideal for detecting the presence of metastable He I absorption in NLTT5306B.

References

Allart, R., Bourrier, V., Lovis, C., et al. 2019, *A&A*, 623, A58, doi: 10.1051/0004-6361/201834917

Bagnulo, S., & Landstreet, J. D. 2018, *A&A*, 618, A113, doi: 10.1051/0004-6361/201833235

Birkby, J. L. 2018, arXiv e-prints, arXiv:1806.04617. https://arxiv.org/abs/1806.04617

Brogi, M., Snellen, I. A. G., de Kok, R. J., et al. 2012, *Nature*, 486, 502, doi: 10.1038/nature11161

Burrows, A., Heng, K., & Nampaisarn, T. 2011, *ApJ*, 736, 47, doi: 10.1088/0004-637X/736/1/47

Buzard, C., Pelletier, S., Piskorz, D., Benneke, B., & Blake, G. A. 2021a, *AJ*, 162, 26, doi: 10.3847/1538-3881/abf7b9

Buzard, C., Piskorz, D., Lockwood, A. C., et al. 2021b, *AJ*, 162, 269, doi: 10.3847/1538-3881/ac2a2c

Buzard, C., Finnerty, L., Piskorz, D., et al. 2020, *AJ*, 160, 1, doi: 10.3847/1538-3881/ab8f9c

Carmichael, T. W., Quinn, S. N., Mustill, A. J., et al. 2020, *AJ*, 160, 53, doi: 10.3847/1538-3881/ab9b84

Casewell, S. L., Debes, J., Braker, I. P., et al. 2020a, *MNRAS*, 499, 5318, doi: 10.1093/mnras/staa3184

Casewell, S. L., Belardi, C., Parsons, S. G., et al. 2020b, *MNRAS*, 497, 3571, doi: 10.1093/mnras/staa1608

Demory, B.-O., & Seager, S. 2011, *ApJS*, 197, 12, doi: 10.1088/0067-0049/197/1/12

Esteves, L. J., De Mooij, E. J. W., & Jayawardhana, R. 2015, *ApJ*, 804, 150, doi: 10.1088/0004-637X/804/2/150

Finnerty, L., Buzard, C., Pelletier, S., et al. 2021, *AJ*, 161, 104, doi: 10.3847/1538-3881/abd6ec

Hinkley, S., Vigan, A., Kasper, M., Quanz, S. P., & Lacour, S. 2021, in ExoFrontiers; Big Questions in Exoplanetary Science, ed. N. Madhusudhan, 5–1

Kirk, J., Alam, M. K., López-Morales, M., & Zeng, L. 2020, *AJ*, 159, 115, doi: 10.3847/1538-3881/ab6e66

Littlefair, S. P., Casewell, S. L., Parsons, S. G., et al. 2014, *MNRAS*, 445, 2106, doi: 10.1093/mnras/stu1895

Lockwood, A. C., Johnson, J. A., Bender, C. F., et al. 2014, *ApJL*, 783, L29, doi: 10.1088/2041-8205/783/2/L29

Longstaff, E. S., Casewell, S. L., Wynn, G. A., et al. 2019, *MNRAS*, 484, 2566, doi: 10.1093/mnras/stz127

Parsons, S. G., Gänsicke, B. T., Marsh, T. R., et al. 2018, *MNRAS*, 481, 1083, doi: 10.1093/mnras/sty2345

Piskorz, D., Buzard, C., Line, M. R., et al. 2018, *AJ*, 156, 133, doi: 10.3847/1538-3881/aad781

Sainsbury-Martinez, F., Casewell, S. L., Lothringer, J. D., Phillips, M. W., & Tremblin, P. 2021, *A&A*, 656, A128, doi: 10.1051/0004-6361/202141637

Seager, S., & Sasselov, D. D. 2000, *ApJ*, 537, 916, doi: 10.1086/309088

Siverd, R. J., Beatty, T. G., Pepper, J., et al. 2012, *ApJ*, 761, 123, doi: 10.1088/0004-637X/761/2/123

Snellen, I. A. G., de Kok, R. J., de Mooij, E. J. W., & Albrecht, S. 2010, *Nature*, 465, 1049, doi: 10.1038/nature09111

Spake, J. J., Sing, D. K., Evans, T. M., et al. 2018, *Nature*, 557, 68, doi: 10.1038/s41586-018-0067-5

van Roestel, J., Kupfer, T., Bell, K. J., et al. 2021, *ApJL*, 919, L26, doi: 10.3847/2041-8213/ac22b7

Vissapragada, S., Knutson, H. A., Jovanovic, N., et al. 2020, *AJ*, 159, 278, doi: 10.3847/1538-3881/ab8e34

Appendix A

NIRSPEC DATA REDUCTION

The first step of NIRSPEC data reduction is to extract one-dimensional spectra from the two-dimensional data images. This Python code was originally written by Klaus Pontoppidan and Nathan Crockett. The version described here was adapted from Danielle Piskorz's version, described in her dissertation, Piskorz 2018.

Unless otherwise stated, all NIRSPEC reduction codes can be found in `angela.gps.caltech.edu:/export/nobackup1/nirspec/Code/01_Reduction`.

Create a Conda Virtual Environment

All of the reduction codes are run within a conda virtual environment. To create the environment, enter

```
conda create -n reduction matplotlib ipython python=3.10
```

Enter the new environment with `conda activate reduction`. Within the environment, `pip install astropy lmfit PyAstronomy`. The environment should now be fully set up.

The environment only has to be set up once, and then afterwards, any time you want to run the reduction, enter the reduction virtual environment with `conda activate reduction`.

Locate Raw Data and Logs

The dates of all of our NIRSPEC exoplanet observations can be found in the Google Sheet, "Summary of All Observations," or from the Keck Observatory Archive. Likewise, all NIRSPEC2.0 protoplanetary disk observations should be listed in "Summary of Disk Observations."

All NIRSPEC raw two-dimensional spectral images can be found in `angela.gps.caltech.edu:/export/nobackup1/nirspec/data`.

Logs are stored in Caltech Box, "NIRSPEC Logs."

Set Up Initialization Files

Initialization files are generally named `nirspec_[DATE]_[TARGET].ini`; a good example is `nirspec_08apr2019_tboo.ini`. In an initialization file named with the appropriate observation date and target name, copy filter name, echelle and cross disperser values, and number of orders. The filter name and echelle and cross disperser values must match the values in the header of the fits files. For each order, input the approximate wavelengths at the start and end of the order in microns in `wrange[ORDER NUMBER]`. These can be estimated from the NIRSPEC Echelle Format Simulator. In `yrange[ORDER NUMBER]`, input pixel numbers that fully encapsulate both the A and B nods within the order and have an average between the two nods. The pixel values can be choosen from fits files of adjacent A and B nods opened in `ds9`. This is the most important part of the initialization file. The `yrange` pixel values are used to rectify the orders. If the average of the pixel values crosses one of the traces or if one of the traces leaves the defined pixel range, the rectification procedure will not work properly and the output one dimensional spectra will be inaccurate. The A, B, and C coefficients for the wavelength solution can be left as is for now.

Set Up the Run File

Run files are generally named `pl_[DATE]_[TARGET].py`; a good example is `pl_08apr2019_tauboo.py`. Input the location of the data (`path`), the observation date (`ut_date`), and the path to where you want the output save (`output_path`). Input the range of flat (`Flat_KL`), flat dark (`FlatDark_KL`), and observation dark (`ObsDark_KL`), target (`SciRanges`), and standard (`StdRanges`) frame numbers. In the `Reduction` call, write the name of the initialization file (`SettingsFile`), the base name written as "YYMMDD" of the observation date (`base`), the target name (`sci_tname`), the standard name (`std_tname`), and the NIRSPEC version, 1 or 2, of the data (`nirspec`).

This file can either be set up to run through all of the data separately and output a 1D spectrum for each of the nod pairs separately or to run through all of the data together and output a single 1D spectrum of all of the nods coadded together. Ultimately to run the PCA telluric correction, we need the data separate, but running all of the data together first can give a higher signal-to-noise spectrum to wavelength calibrate. To run the data separately, if, for example, the target frames run from $1-4$, write `SciRanges = [(1,2), (3,4)]`, and run the Reduction code in a `for` loop over the nod pairs. To run the data together, instead, set `SciRanges = [(1,4)]`.

Run the Reduction

In Python, run pl_[DATE]_[TARGET].py

The Reduction call pulls from the Class File, angela.gps.caltech.edu:/home/cbuzard/Pipeline/01_Reduction/pynirspec/pynirspec_python3.py. This is where the full reduction procedure is defined. It follows the general steps:

1. Class Reduction saves all inputs and runs full reduction procedure from _level1.

2. Class Dark opens flat darks and generates a bad pixel map.

3. Class Flat opens flats and subtracts flat darks.

4. Class Nod opens the target files, subtracts A and B nods, divides out the flats from Step 3, and removes the bad pixels identified in the darks. The A and B nods are also separately subtracted by the observation darks, divided by the dark-corrected flats, and bad pixel corrected. Images of the A – B, A, and B nods before flattening, after flattening, and after bad pixel removal are saved as fits files in [output_path]/[ut_date]/[sci_tname]/PLOTS.

5. Class Order crops the A – B images into orders by the pixel ranges defined in the initialization file under yrange[ORDER NUMBER]. The cropped orders are saved in [output_path]/[ut_date]/[sci_tname]/PLOTS. The nod pairs in analogous orders are vertically aligned and combined with a weighted average. The traces are fit in a fast Fourier transform analysis with a third-order polynomial. This polynomial is used to rectify the traces. Subtracting the median then corrects for sky emission. (Although, longer exposure times, such as the 5-minute exposures we used for NLTT5306 in Chapter 7, make correcting sky emission more complicated.) The rectified orders are saved in [output_path]/[ut_date]/[sci_tname]/SPEC2D. The procedure is repeated for the individual A and B images. Sky images are also made up by combining the off-trace halves of the individual A and B images.

6. Class Spec1D identifies the point spread functions (PSFs) of each trace and uses them to extract 1D spectra using the Horne 1986 optimal extraction algorithm. Extracted 1D A and B nod target and sky emission spectra are saved into [output_path]/[ut_date]/[sci_tname]/SPEC1D. PSF images are saved in [output_path]/[ut_date]/[sci_tname]/PLOTS.

7. The `WaveCal` class is now mostly vestigial since we perform the wavelength calibration elsewhere, but it does save the extracted 1D spectra to `[output_path]/[ut_date]/[sci_tname]/WAVE`, from where it is later drawn.

An alternate reduction code, `pynirspec/pynirspec_python3_NIRSPEC2_lamps.py`, extracts a lamp spectrum at the same position as the target traces to be used for wavelength calibration. This can be especially helpful at shorter wavelengths, e.g. in the *Y* or *J* band. An example run file that generates 1D lamp spectra is `pl_07jan2020_nltt5306.py`.

Wavelength Calibration

The wavelength calibration runs from `RunWaveCal.py`. The code functionality is drawn from the class file, `WaveCal_orig_Lband_NIRSPEC2.py`.

First, select the NIRSPEC version (1 or 2) of the data and the band. For *L* band data, we find the wavelength solution by fitting the telluric absorption in the data to a telluric model. A fourth-order polynomial converts the data pixels to wavelength in microns. *J* band data uses the lamp spectra for wavelength calibration. Here we describe the *L* band wavelength calibration routine because it is more common for exoplanet data.

Define the fits files of each order (from `[output_path]/[ut_date]/[sci_tname]/WAVE`) as `Obsfilename[ORDER NUMBER-1]`.

The *L* band wavelength calibration can be run with two different fitting methods. The `Polynomial` fitting method runs as described in the Appendix of Piskorz 2018. In this fitting method, you input the zeroth- and first-order coefficients to initiate the fourth-order fitting routine. In the `SetPoints` fitting method, which we find to run more smoothly, you instead input (pixel number, wavelength) pairs, from which the code calculates initial coefficients to run the fitting algorithm. You can input up to 5 (polynomial order + 1) pairs to initiate the fitting routine.

To run the wavelength calibration with the `SetPoints` fitting method, first generate a `.dat` file for each order with the header `Pos 0 Neg 0`. Examples of these files can be found in `WaveCalSetPoints`. Set `SetPointsName` as a list to the positions of these files.

In Python, `run RunWaveCal.py`. A prompt will arise. To fit the solution,

1. `pos` – This will generate two figures. One of your reduced positive trace data on a pixel axis and the other of the corresponding telluric model on a wavelength (micron) axis. Identify corresponding lines and input them into them into the first two columns of the WaveCalSetPoints file of the appropriate order. The two columns should be pixel number wavelength, separated by a space. Save the WaveCalSetPoints file.

2. `neg` – Repeat for the negative trace. Input (pixel number, wavelength) points into the third and fourth columns of the WaveCalSetPoints file and save it.

3. `show` – This command reads the points from WavelCalSetPoints and calculates the data wavelength by the polynomial defined by those inputs points. It overplots the model and data with its new wavelength axis, showing first the positive, then the negative, trace spectrum. Since `show` reads the WaveCalSetPoints file, new points can be added and edited without exiting the Python code. `show` must be run after a new point is input for it to be included in the initial parameters for the fit.

4. `fit` – Fits the data with a least-squares minimization routine with the initial coefficients defined by the latest set of WaveCalSetPoints points read in by `show`. First fits positive, then negative, spectrum. `Good Fit?` prompt will appear after each. Answer "yes" if satisfied with fit, answer "no" to be able to refit.

5. Repeat Steps 1 – 4 until satisfied with fit.

6. `pf` – Prints the results of the fit. Save the output to be used in the Telluric Correction routine. Examples are saved in `Wavelength_solutions`.

7. `quit` – Moves on to the next order. Repeat Steps 1 – 6 for each order.

Appendix B

TELLURIC CORRECTION WITH PRINCIPAL COMPONENT ANALYSIS

Unless otherwise stated, all telluric correction codes can be found in `angela.gps.caltech.edu:/home/cbuzard/Pipeline/02_PCA`.

This code was originally implemented by Nathan Crockett and furthered by Danielle Piskorz.

Create a Conda Virtual Environment

Create a virtual environment for running the telluric correlation procedures.

```
conda create -n molecfit matplotlib astropy wxpython python=2.7
```

Enter the environment with `conda activate molecfit`, and install `Molecfit`[1].

Now that the environment is set up, you simply need to enter it with `conda activate molecfit` before running any of the telluric correction codes.

Set Up Initialization File

Initialization files are generally called `tc_[DATE]_[TARGET].ini`; a good example is `tc_08apr2019_tauboo.ini`.

In `[FILEPATHS]`, fill in the path to the raw data (`FitsDir`), the path to the reduced data (`SpecDir`), the base name (`BaseName`, generally YYMMDD), the path to where you want the output save (`SavePath`), and the path to a stellar model (`mod_file`).

In `[CALIBRATOR DATA]`, input the standard object name (`StandName`) and range of standard frame numbers from the telescope data (`StdRanges`). In `[TARGET DATA]`, write the target name (`SciName`) and target frame numbers (`SciRanges`) as [(A_1, B_1), (B_2, A_2), ..., (B_n,A_n)].

In `[NIGHT INFO]`, choose the band, and input the Julian date (`JD`), systemic (`VRad`) and barycentric (`VBary`) velocities at the epoch. The molecular abundances are not important to change.

[1] https://www.eso.org/sci/software/pipelines/skytools/molecfit.

[GOOD ORDERS] allows you to remove erroneous nod pairs. At first, leave as is. If needed, good_order[ORDER NUMBER] can later be set to a list of nod pair indices with the bad indices removed. [PCA NOBS] sets parameters for the telluric fit. Telluric features saturated below telluriccutL will be removed from the data. Set molecfit to True to use Molecfit to fit the initial telluric model and NIRSPEC to the NIRSPEC version of the data, 1 or 2. Like [GOOD ORDERS], GoodPixels lets you cut off edges of orders that are bad. Several parameters are not relevant if Molecfit is used to fit the telluric model (refitwavelength, continuummethod, contfit1, firsttranslim1, firsttranslim2, contfit2, secondtranslim1, secondtranslim2).

In [FOR WAVELENGTH CALIBRATION], define the approximate start and end wavelengths of each order in WaveArray_L. In WaveCalCoefsArray_L, put the wavelength calibration polynomial coefficients that you saved after finding the wavelength solution (e.g., in /home/cbuzard/Pipeline/01_Reduction/Wavelength_solutions). If the first trace is from an A nod (usually the case), input the positive coefficients; if the first is a B, input the negative coefficients.

Set Up Molecfit Files

We generally use Molecfit (Smette et al., 2015; Kausch et al., 2015) to fit the initial telluric model. Molecfit input and output files can be found in angela.gps.caltech.edu:/home/cbuzard/molecfit/NIRSPEC.

Generate a parameter file for each order, called [BaseName]_[ORDER NUMBER]_[SciName].par, see 190408_3_TauBoo.par.

Within the parameter file, set filename to [BaseName]_[ORDER NUMBER]_[SciName].fits; this fits file containing the spectrum to be fit by Molecfit will be generated when running the code.

When the code is run, it will generate and save a file called [BaseName]_[ORDER NUMBER]_[SciName]_exclude_p.dat which lists all of the pixel ranges with values below the defined telluriccutL limit. To exclude these ranges from the Molecfit fit, set prange_exclude to this file name. To fit the full spectrum including saturated telluric pixel ranges, set it to none.

Create an empty directory for the Molecfit output (e.g., output_TauBoo) and point output_dir to this directory.

Define output_name as [BaseName]_[ORDER NUMBER]_[SciName].

Set `obsdate` to the modified Julian date at the observation time, the Julian date subtracted by 2,400,000.

All other values in the parameter file can be left as is. They are described in more detail in the `Molecfit` User Manual.

Set Up Run File

In `PCArunfile_v2.py`, input the initialization file name into the `allinifiles` list. You can run through multiple nights of data at once by putting all of their initialization files here.

You can run one order at a time by setting `runningindex` (near line 36) equal to the index of that order; or to run through all of the orders at once, set it equal to "all".

Remove Any Bad Data From Time Series

In `TelCorPCA_dp_fitmod.py`, uncomment `assert(1==0)` statement near line 93, after `pickle.dump...`.

In Python, `run PCArunfile_v2.py`. The fifth line of output, after a header defining the night number being run, will be a directory named with the current date and time (`[RUN TIME]`, YYYYMMDD_HHMM). All output will be saved to `[SavePath]/[RUN TIME]`, where `[SavePath]` was the directory defined in the initialization file.

In the output directory, check the two `checkspectra` figures and identify any bad nods or pixel regions. Remove these bad nods by editing the appropriate `good_order` list in the initialization file, and bad pixel regions by editing the `GoodPixel` list.

Run Full PCA Routine

`TelCorPCA_dp_fitmod.py`, comment out the `assert(1==0)` statement near line 93, after `pickle.dump...`.

In Python, `run PCArunfile_v2.py`. This command sets off the following progression.

1. `TelCorPCA_dp_fitmod.py` uses your wavelength solution for the first nod and make sub-pixel adjustments to align all of the subsequent nods to it.
2. Fits the median-normalized co-added time series using `Molecfit`. `Molecfit` fits the atmospheric abundances, instrument profile (IP), and continuum.

3. Subtracts `Molecfit` model from data time series and divides by standard deviation by column to obtain time series residuals.

4. Broadens the stellar model using the fit IP.

5. Measures PCA components from time series residuals.

6. Passes PCA components back out to `run PCArunfile_v2.py`, where principal components and fringes are sequentially removed from the data set. Data files and plots are saved to `[SavePath]/[RUN TIME]`.

7. Check the fit in the output figures. If the fit is bad, you can try including or excluding saturated tellurics from the `Molecfit` fit. Changing `telluriccutL` in the initialization file will change the depth of lines cut out. Changing `prange_exclude` in the `Molecfit` parameter file to `[BaseName]_[ORDER NUMBER]_[SciName]_exclude_p.dat` will exclude the saturated regions from the fit, while changing it to `none` will fit the full order. Significant S-shaped residuals at the edges of strong telluric lines are indicative of a bad wavelength solution. If you see them, you should refit your wavelength solution.

Appendix C

TWO-DIMENSIONAL CROSS CORRELATION

Our two-dimensional cross-correlation code runs in IDL. It was first written by Chad Bender, and edited to run without a GUI by Danielle Piskorz.

All relevant files can be found in `angela.gps.caltech.edu:/home/cbuzard/Pipeline/03_CrossCorr`. `Targets` holds all of the input, `guiless_routine` holds all of the IDL run files, and `Output` holds the outputs of the cross correlation routine.

Set Up Run File

In `master.pro`, set up an `if` statement for your target. Define `n_nights` as the number of nights, `n_orders` as a list containing the number of orders for each night, `inputdir` as the directory within `Targets` where the data are stored, `modelinputdir` as the directory within `Targets` where the stellar and planetary templates are stored, and `finalstring` as the suffix to your desired output directory. All code output will be saved to `Output/[TARGET]finalstring`. Set `combo` to "Zucker2003ML", "Zucker2003logL", "Zucker2003logL_nocorrectnegatives", or "BrogiLine2019" to set how cross correlations should be converted to log likelihoods. These naming conventions are described in Buzard et al. 2020. `versionnumber` can be used to iterate over different simulation versions.

Set Up Input Files

There are three input files: `[TARGET].dat`, `[TARGET]_ip.dat`, and `[TARGET]_nights.dat`.

1. `[TARGET].dat` has information about the target and template spectra. The first $n_{\text{night}} \times n_{\text{order}}$ lines give the locations of the spectra for each night and order of data. List by night number, then order number. The code will look for these file names in `[inputdir]`. Below these lines, write the stellar and planetary template file names (in [modelinputdir]). The following line encodes the wavelength units of the data, stellar, and planetary templates as `0` (angstroms), `1` (microns), or `2` (wavenumbers). The next two lines are the lower and upper bounds on the stellar and planetary line-of-sight velocities in km/s, respectively. The stellar velocity can range from -100 to 100 km/s. The

planetary velocity can typically range from -200 to 200 km/s, but maximum line-of-sight planetary velocities (assuming transit) can be estimated at each epoch to make sure they are never outside of the range. The final line has two instances of the spectroscopic contrast, α_{spec}.

2. `[TARGET]_ip.dat` has the instrument profiles that were fit from each night and order. The program uses these to broaden the stellar and planetary spectral templates. Instrument profiles in the appropriate format will be saved in the PCA output directory. Each line will consist of nine values: the width (σ = FWHM/2.355) of the central Gaussian, heights of four satellites to the left of the central Gaussian, and heights of four to the right. With `Molecfit`, we consider an instrumental profile with only the central Gaussian, so the last eight numbers can be 0. The order of night/order instrumental profiles must match the order of the data file names in `[TARGET].dat`.

3. `[TARGET]_nights.dat` contains information for converting the log likelihoods from planetary line-of-sight velocity space to Keplerian orbital velocity space. The first row is the orbital period (in days) and the secondary row is the time (in Julian date) at a zero-point position on the orbit. This time typically corresponds to inferior conjunction, but may also refer to pericenter. The third row has the Julian dates of each of the epochs of data. The fourth row has the barycentric velocities (km/s) at each data epoch. The last row is the systematic velocity (km/s).

Run Cross-Correlation Code

In IDL, `master`, `[TARGET]`, `[COMPONENT]`. `[COMPONENT]` can be used to run the data set with a specific number of principal components removed or to run a specific simulation version number.

The cross correlation runs in three steps. First, `sxcorr_calc2d.pro` cross correlates the stellar and planetary templates against the data. Second, `mlcombine2d.pro` converts the cross correlations to log likelihoods and combines all of the orders from each night of data. Third, `max_like_auto.pro` combines the log likelihood curves to determine the most likely Keplerian orbital velocity.

Different versions of these codes allow you to run through different data sets (either data with different numbers of principal components removed or different simulation versions) in one run, use different templates for different data epochs, assume a circular or eccentric orbit, run a jack-knife analysis, and more.

Appendix D

GENERATING MULTI-EPOCH SIMULATIONS

In this dissertation, we introduced a simulation framework to generate multi-epoch spectra from exoplanetary systems analogous to those obtained from Keck/NIRSPEC. This simulation framework is described in detail in Section 2.5.

Examples of the simulation code can be found on the Blake group server, Angela, in `angela.gps.caltech.edu:/home/cbuzard/Code`. Before running the code, enter the molecfit virtual environment, `conda activate molecfit`.

Set Up Run File

There are several different versions of the simulation run file. We will go off of `SimulateSpec_vpri.py`. This version is set up to run with `ChosenDates` (as was used in Buzard et al. 2021a), rather than `DataDates` (as in Buzard et al. 2020, 2021b), meaning all epochs will approximate either NIRSPEC1.0 or NIRSPEC2.0 (rather than some epochs from each NIRSPEC version) and instrumental profiles and positions of saturated tellurics are taken from a set of representative NIRSPEC data (rather than the data from some specific observations). `SimulateSpec_HD187123.py`, `SimulateSpec_HD88133.py`, `SimulateSpec_upsAnd.py` give an examples of the `DataDates` versions.

`SimulateSpec_vpri.py` can be set to run through many different simulation versions at once. Set `FileVersions` (near line 366) to a list of version numbers to be saved. Set `Kps` to an equal length list with the K_p for each simulation version. The `band` should remain "L". Point `SimsDir` and `NightsDir` to the directories where you want the simulated data and information about the orbital positions and primary velocities at each epoch saved. Define the `stellarradius` (in Solar radii) and `planetradius` (in Jupiter radii).

Set `planetspec` and `stellarspec` to the locations of planetary and stellar spectral models. These models should have wavelength axes (cm^{-1}) and flux axes (raw flux units). `planetfactor` and `starfactor` bring the planetary and stellar flux units to a common W m^{-3}.

Around line 396, set `NIRSPEC` to `1` or `2`, define the number of nights in each simulation (`nnights`), and the number of orders per night (`norders`).

Around line 400, pick one `VpriSelection`. This determines the primary velocity values for each night in the simulation. The different combinations of primary velocities are described in Section 4.3. "Set" allows you to define the specific primary velocities you want (Line 985).

Pick one `MSelection` to determine the orbital positions at each night in your simulation. These selections too are described in Section 4.3. With "Set", you can hardcode the orbital positions at line 952.

If you want to code to save the instrument profiles it uses for each night/order, to be used in the cross correlation routine, set `WriteIP` (line 694) to True and define `IPFileNameToWrite` as the path to the IP file.

Run the Simulation Code

In Python, `run SimulateSpec_vpri.py`. As written, this version of the simulation will assume a circular orbit.

The code will output

- `[NightsDir]/version[FileVersion]_M_nights.dat` for each version with the orbital positions (Ms) and primary velocities used.
- `[SimsDir]/version[FileVersion]_night[Night #]_order[Order #].dat` with the simulated spectrum for each night and order in each simulation.
- If you set `WriteIP` to True, a file with the instrument profiles of each night/order.

Analyze the Simulated Data

The simulation code outputs simulated data in the same form as real data after the telluric correction with PCA part of the pipeline. They can be run through the cross-correlation procedure described in Appendix C.

To set up the `[TARGET]_nights.dat` file, you can set the orbital period to 1 (day), the zero-point position to 0, the observation times to the M values, the barycentric velocities to the negative of the primary velocities, and the systematic velocity to 0.

References

Buzard, C., Pelletier, S., Piskorz, D., Benneke, B., & Blake, G. A. 2021a, *AJ*, 162, 26, doi: 10.3847/1538-3881/abf7b9

Buzard, C., Piskorz, D., Lockwood, A. C., et al. 2021b, *AJ*, 162, 269, doi: 10.3847/1538-3881/ac2a2c

Buzard, C., Finnerty, L., Piskorz, D., et al. 2020, *AJ*, 160, 1, doi: 10.3847/1538-3881/ab8f9c

Horne, K. 1986, *PASP*, 98, 609, doi: 10.1086/131801

Kausch, W., Noll, S., Smette, A., et al. 2015, *A&A*, 576, A78, doi: 10.1051/0004-6361/201423909

Piskorz, D. F. 2018, PhD thesis, California Institute of Technology, United States

Smette, A., Sana, H., Noll, S., et al. 2015, *A&A*, 576, A77, doi: 10.1051/0004-6361/201423932